Flexural Fatigue Behaviour of Corroded Pretensioned Beams and Their Repair Using Carbon Fibre Reinforced Polymer Sheets

by

Adham El Menoufy

A thesis
presented to the University of Waterloo
in fulfillment of the
thesis requirement for the degree of
Doctor of Philosophy

in

Civil Engineering

Waterloo, Ontario, Canada, 2015

AUTHOR'S DECLARATION

This thesis consists of material all of which I authored or co-authored: see Statement of Contributions included in the thesis. This is a true copy of the thesis, including any required final revisions, as accepted by my examiners.

Statement of Contributions

STATEMENT OF CONTRIBUTIONS

I would like to acknowledge the names of my co-authors who contributed to the research presented in this dissertation:

- Professor Khaled Soudki
- Professor Timothy Topper

Abstract

The study presented in this thesis investigated the flexural fatigue behaviour of non-corroded and corroded pretensioned beams and examined the use of externally bonded Carbon Fibre Reinforcement Polymer (CFRP) sheets as a repair technique aimed at restoring the loss in capacity due to corrosion. This was accomplished through an extensive experimental and analytical program.

The experimental program was comprised of a material testing phase and a beam testing phase. The material testing phase consisted of testing seventy-two (72) material samples under monotonic and cyclic axial loading, full strand testing, and corrosion measurements of prestressing strands corroded while embedded in concrete prism. Material testing achieved multiple objectives: (a) it identified the rate of accelerated corrosion of the prestressing strands, (b) it quantified the distribution of the applied nominal tensile force among the seven wires within a single 7-wire strand in a prestressed strand, (c) it determined the material fatigue properties, and the stress-strain behaviour of the strand wires, and (d) it quantified the stress concentration factor in the prestressing strand due to corrosion. The beam testing involved constructing thirty-seven (37) 3.6 m long pretensioned T-beams and testing them in a four-point bending configuration. Twelve (12) beams were tested under monotonic loading, and twenty-five (25) beams were tested under cyclic loading. The main testing variables included: the corrosion level, the applied stress range, and a repair or the lack of it.

Corrosion resulted in a significant deterioration of the monotonic and fatigue resistance of the beams in comparison to non-corroded beams, and repair using externally bonded CFRP sheet restored all or most of the monotonic and fatigue resistance lost due to corrosion. All beams

failed by rupture of the prestressing strand. Inspection of the strand's fracture surface showed signs of surface fretting. In addition, the fracture profile was similar to that reported by Toribio and Ovejero (2005) for hydrogen induced stress cracking of heavily cold drawn prestressing wires. Strands having corrosion levels of 5% and 10% by mass loss exhibited an overall section loss together with distinct deep corrosion pits.

In the analysis phase, fatigue data measured from smooth axial samples taken from the centre wire of a prestrssing strand was used to model the fatigue behaviour of the outer wires of the 7-wire prestressing strand for corroded and non-corroded pretensioned beams. Strain-based fracture mechanics was employed in all the analyses, which included the flexure fatigue behaviour of: non-corroded and corroded single prestressing wires-in-air, a full 7-wire prestressing strand-in-air, and a non-corroded and corroded 7-wire prestressing strand in a beam. The mode results correlated well with the observed experimental results.

This thesis presents extensive experimental work, along with an in depth fatigue analysis that is based on material fatigue properties obtained from simple single wire cyclic testing. The resulting modelling approach offers a mechanistic explanation of 7-wire prestressing strand failure under various conditions.

Acknowledgements

There are many people in my life that whom without I would not be where I am today, and for that I hold them at the highest regards and would like to acknowledge. First and foremost, I would like to deeply thank my wife, Mona, for her love and unwavering support; our daughters Maya and Layla, they are the source of our inspiration, strength, and motivation. I also would like to thank my parents: my mother, Heba; my father, Mohamed; and my sister, Nelly, for all of their support and encouragement throughout my life.

I am sincerely thankful to have had the opportunity to work with, and know, Professor Khaled Soudki during his life. Professor Soudki admirably cared about his students and was always there for us. He was, and remains to be an immense inspiration, a mentor, and a true friend.

I genuinely thank Professor Timothy Topper for his continuous guidance and support. His immeasurable dedication, commitment to his students, wealth of knowledge, and his love for research are a great inspiration. Thank you to Professor Giovanni Cascante for his support and guidance. I would also like to thank my committee members, Professor(s) Mark Green, Scott Walbridge, Steve Lambert and Tarek Hegazy for reviewing my thesis, evaluating my research, and for their insightful feedback.

I am grateful to the technical staff at the University of Waterloo for their expertise and support throughout my graduate studies, namely, Richard Morrison, Douglas Hirst, Rob Sluban, Ken Bowman, Terry Ridgeway, John Boldt, and Rick Forgett. Thanks to my friends and colleagues, Ayman Shihata, Amr Ezzat, Rania Al-hammoud, Rayed Alyousef, Rizwan Azam, Hisham Elhuni, Martin Noel, Mohamed Zawam, Noran Abdelwahab, and Taha Younes. Moreover, I

would like to thank the administrative staff at the Department of Civil and Environmental Engineering for all the support.

Lastly, I would like to acknowledge Hanson Pipe and Precast for their contributions to the construction of the precast-pretensioned beams. Also I would like to thank Pretium Anderson Building Engineers and the Natural Sciences and Engineering Research of Canada (NSERC) for their financial support during my PhD program.

IN MEMORY OF

PROFESSOR KHALED ADNAN SOUDKI

1966-2013

Table of Contents

Table of Contents ..... **ix**

List of Figures ..... **xiv**

List of Tables ..... **xxiii**

Chapter 1 Introduction **1**

1.1 Research objectives 3

1.2 Research methodology 4

1.3 Thesis organization 4

Chapter 2 Background and Literature Review **6**

2.1 Corrosion of Steel Reinforcement 6

2.1.1 Corrosion mechanism 6

Carbonation initiated corrosion *7*

Chloride initiated corrosion *7*

2.1.2 Types of corrosion cells 8

2.1.3 Corrosion reactions 9

2.1.4 Laboratory accelerated corrosion techniques 10

Artificial climate environment for accelerating corrosion *11*

Galvanostatic method of accelerating corrosion *11*

2.2 Prestressed Concrete 12

2.2.1 Methods of Prestressing Concrete 12

2.3 Fatigue of Reinforced Concrete Structures 14

2.3.1 Fatigue of plain concrete 14

2.3.2 Fatigue of steel deformed bars 17

Bar diameter *18*

Bar Deformation geometry *19*

Yield Strength and bending effect *19*

2.4 Fatigue of Prestressed Concrete Structures 20

2.4.1 Fatigue of prestressing reinforcements 20

Wires *20*

Strands *21*

Bars *24*

2.4.2 Fretting fatigue of prestressing strands 24

2.4.3 Fatigue of pretensioned beams 29

2.5 Corrosion of Prestressed Concrete Structures 35

2.5.1 Fracture modes of prestressing reinforcement due corrosion and cyclic loading 35

Brittle fracture *35*

Stress corrosion cracking (SCC) induced fracture *36*

Fatigue and corrosion induced fracture *42*

2.5.2 Effects of corrosion on prestressed concrete structures 43

2.6 Rehabilitation of Non-Prestressed Concrete Structures Using Fibre Reinforced Polymer (FRP) 51

2.6.1 FRP strengthening and repair of RC beams subjected to monotonic loading 51

2.6.2 FRP strengthening and repair of RC beams subjected to fatigue loading 53

2.6.3 FRP strengthening and repair of prestressed beams subjected to monotonic and fatigue loading 57

2.7 Summary 61

Chapter 3 Experimental program 63

3.1 General 63

3.2 Testing Phase 63

3.2.1 Phase I 63

3.2.2 Phase II 67
3.2.3 Phase III 67
3.3 Beams Nomenclature 68
3.4 Beam Design 69
3.4.1 Concrete 69
3.4.2 Prestressing strands 70
3.4.3 Non prestressed flexural reinforcement 70
3.4.4 Shear Reinforcement 70
3.5 Accelerated Corrosion 70
3.6 Beam Construction 71
3.7 Mass Loss Analysis 76
3.8 Carbon Fibre Reinforced Polymer (CFRP) repair 76
3.9 Test setups 79
3.9.1 Ancillary tests 79
Tensile monotonic test setup for 7-wire strands 79
Single wire fatigue test setup 80
3.9.2 Monotonic beam test setup 81
3.9.3 Fatigue beam test setup 84
Chapter 4 Experimental Results 87
4.1 Ancillary Testing – Phase I (a) 87
4.1.1 Gravimetric mass loss analysis 88
4.2 7-Wire Strand Monotonic Testing - Phase I (b) 89
4.3 Material Fatigue Testing – Phase I (c) and (d) 94
Phase I (c)-Testing of uncorroded centre wire 94
Fatigue test results 95

Phase I (d)-Testing of corroded external wire *99*

4.4 Monotonic Beam Testing 102

4.4.1 Accelerated corrosion results 102

4.4.2 Monotonic test results 104

Beams prestressed with a single 7-wire strand *106*

Beams prestressed with two7-wire strands *117*

Beams repaired with CFRP sheets *124*

4.5 Fatigue Testing 131

Chapter 5 Fatigue Analysis and Discussion 137

5.1 Nomenclature 137

5.2 Prestressing strand nominal stress 138

5.2.1 Calculation of prestress loss 138

5.3 Force Distribution for the 7-wire Strand 142

5.4 Discussion of the Stress Range or Strain Range versus Fatigue Life Results 146

5.4.1 Fatigue resistance of a non-corroded wire in air, strand in air and a strand inside a beam specimens 146

5.4.2 Fatigue resistance of a corroded single wire-in-air and a corroded strand-in-a beam 155

5.4.3 Comparison of the fatigue resistance of non-corroded and corroded strand-in-beam specimens 159

5.4.4 Fatigue resistance of corroded strand-in-beams repaired with CFRP 160

5.5 Fracture Mechanics of Fatigue Crack Propagation 162

5.5.1 Fatigue crack growth rate 165

5.5.2 Effect of the stress ratio (R) on the fatigue crack growth rate 167

5.5.3 Effect of a notch on fatigue life 170

5.6 Derivation of the Closure-free Crack Growth Rate Curve 175

5.7 Modelling of Deterioration of the Fatigue Resistance Due to Fretting Induced Flaws 181

5.8 Modelling of the Deteriorated Fatigue Resistance Due to Corrosion Pitting 187
5.8.1 Corroded single wire-in-air specimens 187
5.8.2 Corroded strand-in-beam specimens 194
5.8.3 Corroded strand-in-beam repaired with CFRP 197
5.9 Summary 202
Chapter 6 Summary, Conclusions and Recommendations 206
6.1 Summary 206
6.1.1 Beam Testing 207
Monotonic behaviour 207
Fatigue behaviour 208
Material Testing 209
Analysis and Modelling 210
6.2 Conclusions 212
6.3 Recommendations for Future Work 214
Bibliography 215

List of Figures

Figure 2-1 – Schematic of (a) micro-cell versus (b) macro-cell corrosion (Poursaee and Hansson 2009) 9

Figure 2-2 – Volume comparison of oxide of iron (Mansfeld et al. 1982)..... 10

Figure 2-3 – Prestressed concrete schematic: (a) post-tensioning, and (b) pre-tensioning 13

Figure 2-4 – Fatigue strength of plain concrete beams (Mordock 1965) 16

Figure 2-5 – Modified Goodman's diagram (ACI 215R-74 1974) 16

Figure 2-6 – Stress range vs. life curves for reinforcing bars (ACI 215R-74 1974) 17

Figure 2-7 – Fracture surface of 35M (35.7 mm diameter) deformed steel bar (ACI 215R-74 1974) 18

Figure 2-8 – 7-wire prestressing strand 22

Figure 2-9 – Strength envelopes for strand tested in United States (ACI 215R-74 1974) 22

Figure 2-10 – Complied fatigue test results for prestressing strand as an isolated element, the statistical design expression of 95% of no failure, Paulson et al. (1983) 24

Figure 2-11 – Stress range vs. fatigue life for post-tensioned beams with strands in metal ducts (Wollmann, 1996) 26

Figure 2-12 – Elliptical pressure mark on single wire and the fracture surface, Bahke (1980) ... 27

Figure 2-13 – Load range vs. fatigue life curves for non-fretted and fretted wire specimens (Cullimore, 1979)..... 28

Figure 2-14 – Comparison of the mean regression line of pretensioned beam fatigue test results to Paulson et al. (1983) lower bound strand-in-air model, Overman et al. (1984) 30

Figure 2-15 – Comparison of the mean regression line of large scale pretensioned beam fatigue tests to the Paulson et al. (1983) lower bound strand-in-air model, Overman et al. (1984) 31

Figure 2-16 – Large-scale pretensioned beams fatigue test results in comparison to Paulson et al. (1983) lower bound strand-in-air model, Overman et al. (1984) 32
Figure 2-17 – Fatigue properties of 5mm cold deformed prestressing steel in relation to the depth of local corrosion (Nurnberger 2002) 36
Figure 2-18 – Fracture profile of Hydrogen Assisted Cracking (HAC) at different level of cold drawing (Toribio and Ovejero, 2005) 39
Figure 2-19 – A comparison between stressed and unstressed corroded wires (Ngoc et al. 2009) 40
Figure 2-20 – Wire fracture plane before immersion (left) and after 96 hrs of immersion (right) in ammonium thiocyanate solution 41
Figure 2-21 – Wire surface before immersion (left) and after 96 hrs of immersion (right) in ammonium thiocyanate solution 42
Figure 2-22 – Fatigue behaviour of cold drawn prestressing steel wire tested in air, tap-water and sea-water, (Nurnberger, 2002) 43
Figure 2-23 – Fracture surface a) non-corroded wire, and b) corroded wire (Darmawan and Stewart, 2007) 46
Figure 2-24 – Distribution of cross sectional area reduction vs. time (Darmawan and Stewart, 2007) 48
Figure 2-25 – Comparison of load versus midspan deflection for beams at different corrosion levels (Rinaldi et al. 2010) 49
Figure 2-26 – Load vs. midspan deflection curves for control, corroded/non-strengthened and corroded/strengthened beams (Soudki and Sherwood, 2000) 52

Figure 2-27 – Load vs. midspan deflection curves for non-strengthened and strengthened beams subjected to no wetting and drying cycles (Soudki et al, 2007) 53
Figure 2-28 – Moment range versus fatigue life of non-strengthened and strengthened reinforced concrete beams (Heffernan and Erki, 2004) 55
Figure 3-1 – Schematic of the concrete prisms 64
Figure 3-2 – Machined single wire specimens for fatigue testing 65
Figure 3-3 – Schematic of the corrosion electrical circuit 71
Figure 3-4 – Beam dimensions and reinforcement details 73
Figure 3-5 – Beam forms along the prestressing bed 74
Figure 3-6 – Prestressing wedge anchor 75
Figure 3-7 – Salted portion of the beam 75
Figure 3-8 – CFRP sheets repair configuration 78
Figure 3-9 – Beams after application of CFRP sheet repair 78
Figure 3-10 – Monotonic test setup and instrumentation of 7-wire prestressing strand 80
Figure 3-11 – Schematic of beam test setup in four-point bending configuration 82
Figure 3-12 – LVDTs for crack opening measurements 83
Figure 3-13 – OSMOS FOS across flexure zone for average strain readings at the level of the strand 83
Figure 3-14 – Midspan deflection measurement by an external LVDT 85
Figure 3-15 – 60 mm strain gauge to monitor the concrete compressive strain 85
Figure 3-16 – External LVDTs monitoring flexure cracks width 86
Figure 4-1 - 7-wire strand (a) before and (b) after cleaning showing pitting at a 5% mass loss .. 88
Figure 4-2 – Monotonic test setup and instrumentation of 7-wire prestressing strand 90

Figure 4-3 – Applied load versus individual external wire measured tensile strain 91
Figure 4-4 – Applied load versus 7-wire strand elongation..... 91
Figure 4-5 – Applied load versus load carrying capacity per individual wire..... 93
Figure 4-6 – Average load carrying contributions per wire as a percentage of the total load 93
Figure 4-7 – Fatigue Life versus strain amplitude of uncorroded centre wire samples..... 97
Figure 4-8 – Fatigue Life versus stress amplitude of uncorroded centre wire samples..... 97
Figure 4-9 – True strain amplitude versus true stress amplitude response for uncorroded centre wire sample 98
Figure 4-10 – Stress amplitude versus life for all material samples 100
Figure 4-11 – Stainless steel tube configurations for the beams with two prestressing strands . 102
Figure 4-12 – Typical corrosion induced cracking in (a) beams with a single strand, and (b) beams with two strands..... 104
Figure 4-13 – Corrosion induced crack measurements at midspan 104
Figure 4-14 – LVDT mounted at beam end to monitor end slip of prestressing strand 105
Figure 4-15 – Experimental vs. theoretical elastic deflection response for beams with one strand 108
Figure 4-16 – Load vs. midspan deflection at different corrosion levels for beams with one strand 110
Figure 4-17 – Load vs. midspan concrete compressive strain at different corrosion levels for beams with one strand..... 110
Figure 4-18 – Cumulative crack opening within the constant moment zone vs. load 111
Figure 4-19 – Average tensile strain at the level of the strand vs. load at different corrosion levels 111

Figure 4-20 – Cracking pattern at failure for an uncorroded beam 113
Figure 4-21 – Cracking pattern at failure for a corroded beam 113
Figure 4-22 – Concrete strand interface below the strand 114
Figure 4-23 – Concrete strand interface above the strand 114
Figure 4-24 – Multi-wire rupture at the same location for the uncorroded beam..... 115
Figure 4-25 – Wires rupture at adjacent locations in a corroded beam 116
Figure 4-26 – Experimental vs. theoretical deflection response for beams with 2 strands 119
Figure 4-27 – Load vs. midspan deflection at different corrosion levels for beams with 2 strands 122
Figure 4-28 – Load vs. midspan concrete compressive strain for beams with two strand 122
Figure 4-29 – Cumulative crack opening within the constant moment zone vs. load 123
Figure 4-30 – Average tensile strand strain vs. load at different corrosion levels..... 123
Figure 4-31 – Failure by concrete crushing of beam ST-2S-10%-NW-SC 124
Figure 4-32 – Load vs. midspan deflection comparison of the repaired and unrepaired beams 127
Figure 4-33 – Load vs. concrete midspan compressive strain for corroded and repaired beams 127
Figure 4-34 – Load vs. CFRP strain at midspan for corroded and repaired beams 128
Figure 4-35 – Typical failure of a prestressed beam repaired by CFRP sheets 128
Figure 4-36 – Design repair load capacity compared to experimental response of the beam corroded to 5% by mass loss..... 130
Figure 4-37 – Design repair load capacity compared to experimental response for the beam corroded to 5% by mass loss..... 130
Figure 4-38 – Load range versus life of T-beams at different corrosion levels..... 134

Figure 4-39 –Midspan deflection versus fatigue life response of non-repaired beams with different corrosion levels 136
Figure 5-1 – Calculation flowchart for calculating the prestressing strand stress level due to moment applied on the beam 140
Figure 5-2 – (a) Schematics of 7-wire strand (b) Force diagram for an external wire, and (c) change in geometry (length and rotation) due to applied load F (Castello, 1997)..... 143
Figure 5-3 – Strain range versus fatigue life data for all the fatigue tests 146
Figure 5-4 – wire-in-air, strand-in-air, and strand-in-beam versus fatigue life 147
Figure 5-5 – Close up of a 7-wire strand as extracted from the beam after fatigue failure 150
Figure 5-6 – Close of the centre wire of a 7-wire prestressing strand at the failure location as extracted from the beam after failure..... 151
Figure 5-7 – Close-up of concrete-wire fretting damage on an external wire of the 7-wire prestressing strand as extracted from the beam after failure..... 151
Figure 5-8 – Close-up of inter-wire fretting damage on an external wire of a 7-wire prestressing strand as extracted from the beam after failure..... 152
Figure 5-9 – Close up of the fracture surface of the wire shown in Figure 5-7 & Figure 5-8.... 152
Figure 5-10 – Fatigue fracture plane of the wire shown in Figure 5-7 & Figure 5-8 153
Figure 5-11 – 200× magnification of the fretting damage circled in Figure 5-10 153
Figure 5-12 – 200× magnification of a sample the fretting damage..... 154
Figure 5-13 – Strain range-fatigue life behaviour of wire-in-air, corroded-wire-in-air & (5% & 10%) corroded strand-in-a beam..... 155
Figure 5-14 – Failure at a corrosion pit location on a wire specimen..... 157
Figure 5-15 – Failure at a corrosion pit location on a strand specimen..... 157

Figure 5-16 – Pitting cross section through the failure plain on corroded single wire specimens 158
Figure 5-17 – Comparison of the Strain range-Life behaviour of non-corroded strand-in-beam & (5% & 10%) corroded strand-in-beam 160
Figure 5-18 – Strain range versus the fatigue life data for the corroded strand-in-beam non-repaired and repaired with CFRP specimens 161
Figure 5-19 – Constant amplitude cyclic loading 163
Figure 5-20 – Graphical representation of the fatigue crack growth rate 165
Figure 5-21 – Schematic of the different stages of fatigue crack growth 167
Figure 5-22 – Schematic showing the effect of the stress ratio on the fatigue crack growth rate 168
Figure 5-23 – Effect of a notch on the fatigue resistance 171
Figure 5-24 – Load range vs. fatigue life for non-corroded and corroded concrete reinforced beams (Soudki et al., 2007) 172
Figure 5-25 – Schematic of the impact of notch/crack within a notch on fatigue resistance 173
Figure 5-26 – Fatigue behaviour of cold drawn prestressing steel wire tested in air, tap-water and sea-water, (Nurnberger, 2002) 174
Figure 5-27 – Schematic showing fitting the experimental Strain-Life data by an assumed intrinsic strain range ($\Delta\varepsilon i$) 176
Figure 5-28 – Schematic of fatigue crack growth rate versus the stress intensity factor 177
Figure 5-29 – Derived crack growth rate for 7-wire prestressing strand steel 179
Figure 5-30 – Comparison of the Strain-Life curve based on the fracture mechanics analysis of small fatigue cracks to the smooth specimen fatigue data 180

Figure 5-31 – Schematic of the fatigue crack propagation from the fretting induced flaw is presented 182
Figure 5-32 – Strain versus fatigue life comparison of experimental and modelled non-corroded-strand-in-beam specimens 183
Figure 5-33 – Experimental results from the literature for pretensioned beams and fatigue life results and modelling from the present study 184
Figure 5-34 – Comparison of the modelled Strain-Fatigue life curve to Paulson et al. (1983) data using an incremental introduction of the fretting damage 186
Figure 5-35 – Strain-fatigue life modelling using a strain-life approach (K_t=2.19 and 10) 188
Figure 5-36 – Schematic for a fatigue crack propagating from a secondary notch at the root of the primary notch 189
Figure 5-37 – Strain-fatigue life model of corroded-wire-in-air specimens 192
Figure 5-38 – Strain-fatigue life modelling of corroded-wire-in-air specimens (incremental introduction of the flaw at the notch root) 194
Figure 5-39 – Schematic showing a fatigue crack propagating from a fretting induced flaw intersecting the edge of a pit for a corroded strand-in-beam specimen 195
Figure 5-40 – Strain-fatigue life model of corroded-strand-in-beam specimens Adham correct spelling 197
Figure 5-41 – Modelled and experimental strain range vs. fatigue life data for non-repaired and repaired corroded strand-in-beam specimens 198
Figure 5-42 – Load vs. midspan deflection comparison of the repaired and unrepaired beams 200
Figure 5-43 – Modelled strange range vs. fatigue life curve non-repaired and repaired corroded strand-in-beam specimens (assuming a reduced concrete fretting damage) 201

Figure 5-44 – Summary of fatigue resistance models versus experimental behaviour 204

List of Tables

Table 3-1 –Ancillary testing program 66

Table 3-2 –Beam testing program 68

Table 3-3 - Mix proportions for a $1m^3$ batch 69

Table 3-4 – Average concrete compressive strength at transfer 76

Table 3-5 – Cured CFRP laminate properties with Sikadur® 330 epoxy 77

Table 4-1 – Breakdown of actual number of uncorroded samples tested for material properties 94

Table 4-2 – Summary of cyclic testing data of non-corroded centre wire samples 96

Table 4-3 – Cyclic material properties of low relaxation 7-wire prestressing strands 98

Table 4-4 – Summary of cyclic testing data for corroded external wire samples 101

Table 4-5 – Monotonic testing result summary of beam prestressed with single strand 107

Table 4-6 – Summary of the measured ultimate concrete compressive strength for beams with a single prestressing strand 109

Table 4-7 – Monotonic testing result summary of beam prestressed with two strands 118

Table 4-8 – Summary of measured ultimate midspan concrete compressive strain for beams with two prestressing strands 120

Table 4-9 – Test result summary for CFRP repaired, unrepaired, and control beams 126

Table 4-10 – Fatigue testing matrix 131

Table 4-11 – Summary of fatigue testing of prestressed T-beams 133

Table 5-1 – Summary of beam fatigue results and calculated nominal strand stresses 141

Table 5-2 – Fatigue crack growth rate parameters 179

Chapter 1
Introduction

Prestressing is a technique that has been widely used for decades in all sorts of concrete structures. Its ability to minimize reinforcement congestion, decrease deflection, and control cracking under service loads has made it a widely popular choice for large spans and for the precast industry. Prestressing a member can be achieved through pre-tensioning or post-tensioning of tendons/wires as the main tension reinforcement. Pre-tensioning is widely adopted by the precast industry while post-tensioning is primarily used for cast in-place concrete structures.

Bridge infrastructure in North America is aging with more than 40% percent of the bridges built in Canada and the United States being over 50 years old (Pakniat and Hammad 2008), and in need of significant maintenance, rehabilitation, or replacement. Many prestressed concrete bridge structures are subjected to corrosive environments. In addition, the Ontario highway network bridge latest inventory lists a total of 2802 bridges, out of which 1124 (40%) are prestressed concrete structures. One of the major reasons for this is the limited corrosion resistance of old structures and the continually increasing use of de-icing salts in cold regions, (PCI Bridge Design Manual Steering Committee 2011). Bridge infrastructure is also subjected to an increasing number of fatigue load cycles due to increased traffic demand.

In evaluating bridge rehabilitation options, it is very important to consider the differences between pre-stressed/pre-tensioned structures and reinforced concrete structures in the form of the higher stresses in the prestressing strand. The classical rehabilitation approach of chipping

away spalled or delaminated concrete, and cleaning reinforcement or even replacing it, is not always viable for pretensioned concrete structures because of the risk involved in exposing a highly stressed, heavily corroded steel prestressing strand. Often in pretensioned members the prestressed strands are designed as the main flexural reinforcement, making their corrosion a critical deterioration of the structure that requires immediate intervention. Although corrosion effects on the fatigue performance of steel rebars are well documented and studied; only limited studies have focused on the corrosion fatigue of prestressing strand or wire (ACI 222.2R-14).

To the author's knowledge, only very limited research is available in the literature on the fatigue behaviour of corroded pretensioned concrete members. There are no available studies that address repair techniques to restore the capacity of corroded pretensioned concrete members subjected to cyclic/fatigue loading. This topic is of critical importance and needs to be addressed because of the aging bridge infrastructure and increased load demands.

This study focuses on studying the impact of the corrosion of prestressing steel strands on the residual capacity of pretensioned concrete T-beams subjected to fatigue loading, and investigates a viable repair technique that uses Carbon Fibre Reinforced Polymer (CFRP) sheets. It consists of experimental and analytical phases. The experimental phase comprises of T-beam testing as well as material testing on 7-wire prestressing strands. The beam testing involves the construction and testing of thirty-seven (37) pretensioned concrete T-beams under monotonic and fatigue cyclic loading. The experimental variables are the corrosion level (0%, 5%, and 10% by mass loss), the repair condition (unrepaired beams and repaired beams using adhesively bonded CFRP sheets, and the fatigue stress range as a percentage of the monotonic ultimate load capacity. The material testing portion includes monotonic testing of a 7-wire strand to

experimentally quantify the stress distribution amongst individual wires, and fatigue testing of corroded and uncorroded single prestressing wires. The analytical program quantifies the material fatigue properties and analytically calculates the force distribution within a 7-wire prestressing strand to confirm experimental findings. Finally strain based fracture mechanics is used to model the fatigue life of pretensioned concrete members exposed to different corrosion levels, and to predict the life extension after CFRP repair.

1.1 Research objectives

This research aimed to investigate the monotonic and fatigue flexural behaviour of corroded pretensioned beams and their repair using CFRP sheets. Specific objectives of this study are as follows:

- Experimentally quantify the effects of corrosion on pretensioned concrete beams under monotonic and fatigue cyclic loading through a series of monotonic and fatigue tests on pretensioned beams
- Experimentally identify the material fatigue properties of 7-wire prestressing strands through a comprehensive material testing program comprised of non-corroded and corroded single wire specimens tested under fatigue cyclic loading.
- Experimentally investigate the viability of CFRP repair of corroded pretensioned beams to restore their monotonic and fatigue capacity by testing corroded then repaired pretensioned beams.
- Experimentally quantify and analytically verify the force distribution amongst individual wires forming the 7-wire prestressing strand.

- Experimentally quantify the mean stress effect on the fatigue response of prestressing strands.
- Derive the closure-free fatigue crack growth rate curve from the effective stress data based on constant amplitude fatigue test results of smooth wire specimens.
- Model the fatigue life of smooth wire specimens in air, corroded wire specimens in air, and prestressing strands in air.
- Model the fatigue life of non-corroded and corroded pretensioned concrete beams.
- Model the fatigue life extension of corroded pretensioned beams due to CFRP repair.

1.2 Research methodology

The research objectives are achieved through an extensive experimental program, which is divided in to a material testing and beam testing components that were designed with specific sub-objectives. Following the experimental program an in depth analytical program is explains the failure mechanisms of the 7-wire prestressing strand and provides a modelling approach that reasonably replicates that fatigue behaviour of non-corroded and corroded pretensioned beams.

1.3 Thesis organization

Chapter 2 presents an in-depth background and literature review of related topics and research studies. Chapter 3 presents the experimental program and details the experimental setups, variables and procedures. Experimental results are presented in Chapter 4, while Chapter 5 presents a detailed analysis of the experimental results, describing the modelling approach, and

the modelling results. Finally, Chapter 6 offers a closing summary, conclusions, and recommendations.

Chapter 2
Background and Literature Review

In this Chapter an in-depth background in relevant topics and a comprehensive literature review are presented.

2.1 Corrosion of Steel Reinforcement

Corrosion is a destructive deterioration mechanism that gradually attacks metals. When in contact with the environment (oxygen), metals undergo an electrochemical oxidation resulting in the formation of rust products (Jones 1996). Corrosion requires the presence of an anode and a cathode within a common electrolyte to produce an electrochemical reaction similar to that of a galvanic cell. Typically the rust products are oxides of the metal. In essence corrosion returns the metal to its original state from which it was extracted (Masoud 2002).

2.1.1 Corrosion mechanism

Reinforced concrete structures if designed and constructed in accordance with the best practices should be protected against the corrosion reaction. “This is counter intuitive because we know that concrete is a porous material and it contains moisture, so why should steel not corrode?” (Broomfield 2007). Reinforcing steel is protected by a passive film, which remains intact as long as the surrounding concrete maintains its alkalinity, a pH above 12.5. This passive film is a thin layer of iron oxide that significantly slows down the corrosion process by limiting the further access of oxygen to the steel. There are two ways for this protective passive film to be destroyed: carbonation of concrete or chloride penetration into the concrete. Once the passive film has been

broken, the aqueous concrete medium acts as the electrolyte, whilst the reinforcing steel will act as the electrode and corrosion continues.

Carbonation initiated corrosion

In the presence of moisture, carbon dioxide will react with calcium hydroxide after penetrating the concrete to produce calcium carbonate. Calcium carbonate reduces the concrete pH to about 8.5, which in turn destabilizes the passive protection film (Roberts 1981). Carbonation can be affected by multiple factors; a thin concrete cover, porosity, and cracking. The most aggressive environment for attacking the passive film would be the alteration between wetting and drying cycles and high temperature, with an ambient relative humidity of 60% (Tuutti 1977; ACI 222R-01 2010; Beeby 1983).

Chloride initiated corrosion

Sources for chlorides in concrete can be de-icing salts, a marine environment, contaminants, a concrete admixture, or even industrial brine. The above mentioned chloride sources make the presence of chloride ions the dominant corrosion initiation mechanism (ACI 222R-01 2010). Chlorides can be introduced in concrete either during the mixing stage by error or by chloride containing admixtures, or they can be introduced after curing by diffusion. The diffusion rate varies based on a number of factors such as the cement type, the temperature, and the age of concrete (Mehta 1980; Page et al. 1986; Goto and Roy 1981a; Goto and Roy 1981b; Schonlin and Hilsdorf 1988). When chlorides are introduced in concrete they may affect the corrosion process in multiple ways. Chlorides can reduce the resistivity of concrete and increase the rate of additional chloride ingress (Young 1988), increased conductivity of concrete thus accelerating the subsequent corrosion rate, alter the pH of concrete affecting chloride binding, and chlorides

introduced during the mixing stage can increase the corrosion rates in the plastic stages of the concrete (ACI 222R-01 2010).

Regardless of whether chlorides were added or penetrated the concrete, there is a threshold under which corrosion will not initiate. This threshold depends on several factors, some of which are contradictory. For instance a higher concrete pH means a higher level of chloride resistivity of the steel, but also means a higher chloride concentration (Stratfull et al. 1974; Clear 1974). It has been shown that the initiation of chloride corrosion depends on the chloride to hydroxide ion ratio (Cl^-/OH^-). Threshold values for this ratio are 0.3 at pH 13.3 (Evans 1961; Hansson and Sorensen 1990), and 0.29 at pH 12.6 (Page et al. 1986; Structures 1992).

2.1.2 Types of corrosion cells

There are two common corrosion mechanisms in steel; micro-cell and macro-cell corrosion, shown in Figure 2-1. Microcell corrosion refers to a corrosion process on a microscopic level. The cathode and anode exist on the same reinforcing bar. On the other hand, macro-cell corrosion indicates a separation of the anodic and cathodic sites. This occurs during a chloride attack which is associated with a high moisture content that creates a low electrical resistance allowing the anode and cathode to be further apart (Jones 1996).

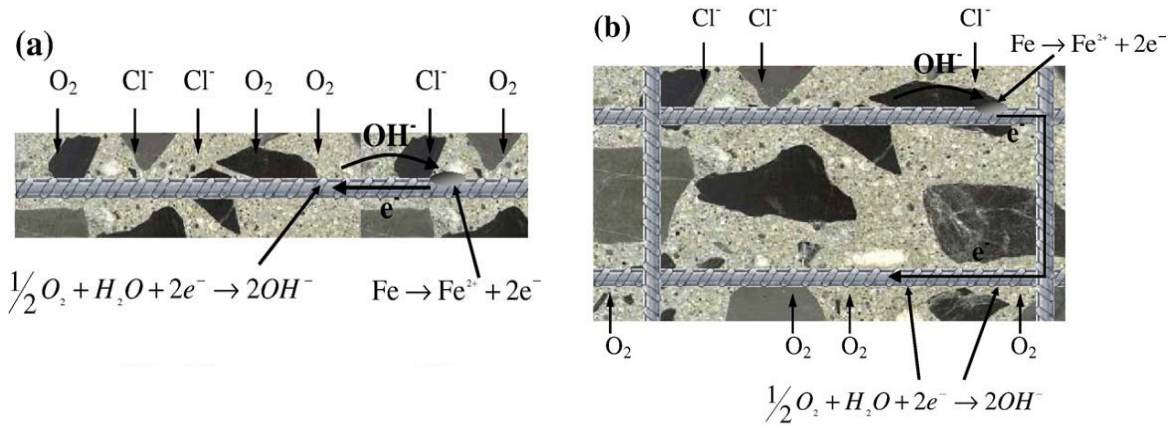

Figure 2-1 – Schematic of (a) micro-cell versus (b) macro-cell corrosion (Poursaee and Hansson 2009)

2.1.3 Corrosion reactions

Whether corrosion occurs due to chlorides or carbonation does not change the chemical reaction. As steel starts corroding it dissolves in water and releases two electrons. This is referred to as the anodic reaction, Equation (2-1). In order to preserve electrical neutrality, these electrons are consumed by the cathodic reaction, Equation (2-2). The cathodic reaction releases hydroxide ions, which increase the alkalinity, and thus preventing corrosion at the cathode.

$$Fe \rightarrow Fe^2 + 2e^- \tag{2-1}$$

$$\frac{1}{2}O_2 + H_2O + 2e^- \rightarrow 2(OH)^- \tag{2-2}$$

The hydroxide ions then migrate towards the anode through the electrolyte (moisture in the concrete). At the anodic site, the hydroxide ions react with the ferrous ions resulting in ferrous hydroxide, which then reacts with oxygen and water to form ferric hydroxide, and then finally becomes hydrated ferric oxide, Equations (2-3)-(2-5) (Jones 1996; Broomfield 2007).

$$Fe_2 + 2(OH)^- \rightarrow Fe(OH)_2 \quad (2\text{-}3)$$

$$4Fe(OH)_2 + O_2 + 2H_2O \rightarrow 4Fe(OH)_3 \quad (2\text{-}4)$$

$$2Fe(OH)_3 \rightarrow Fe_2O_3.H_2O + 2H_2O \quad (2\text{-}5)$$

The rust product can occupy up to six times the original volume of iron (Fe), Figure 2-2 (Mansfeld et al. 1982). The forms of the rust products depend on the amount of dissolved oxygen in the surrounding environment (Phillips 1993). In an oxygen deprived environment such as the submerged portion of a marine structure, a black/greenish rust product (Fe_3O_4) is observed (Bentur 1997).

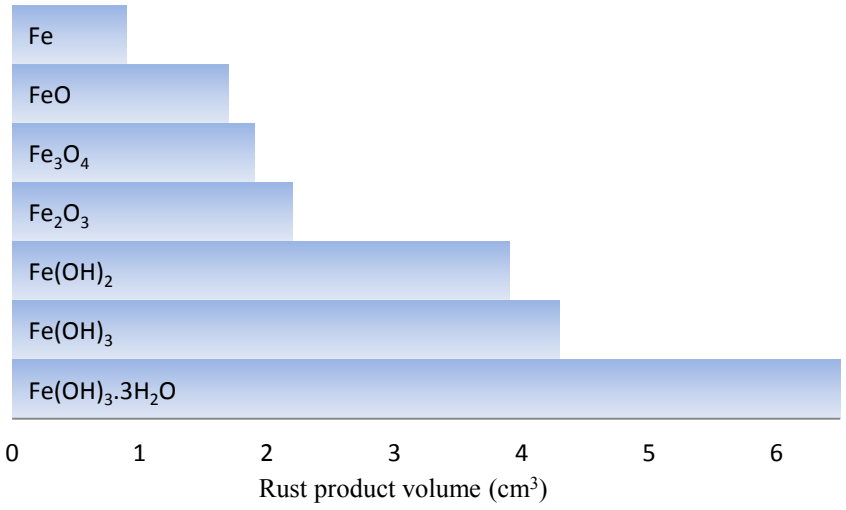

Figure 2-2 – Volume comparison of oxide of iron (Mansfeld et al. 1982)

2.1.4 Laboratory accelerated corrosion techniques

Reinforced concrete members in their natural environment corrode at very low rates ranging between 10 to 15 μA/cm^2. In the laboratory, researchers have used two methods to simulate natural corrosion in a shorter period of time.

Artificial climate environment for accelerating corrosion

In this method the corrosion process is accelerated by creating an artificially aggressive environment of high temperature, high humidity, repeated wetting and drying cycles, or wetting by spraying a salt solution (Yuan et al. 2007).

Galvanostatic method of accelerating corrosion

In this method an impressed current is introduced in the reinforcing steel while the member is exposed to salt. Impressed current densities reported in the literature have ranged from 25 up to 10400 μA/cm^2 (Andrade, C. 1993). An upper limit of 200 μA/cm^2 is recommended as higher current densities have a damaging influence on the steel/concrete interfacial bond and affect the corrosion cracking (El Maaddawy and Soudki 2003). The estimated time to achieve the required corrosion mass loss in the steel bar is calculated using Faraday's law presented by Equation (2-6) (ACI 222R-01 2010).

$$t = \frac{MzF\rho d_p}{4ai} \tag{2-6}$$

Where, t = the corrosion time (sec)

M = the mass loss of steel rebar

a = the atomic weight of steel (for Fe = 56 g)

i = the impressed current density

z = the ionic charge (+2 for steel)

F = Faraday's constant (96,500 amp-sec)

ρ = the metal density (7.86 g/cm^3 for Fe)

2.2 Prestressed Concrete

The prestressing concept is based on the application of an axial compression force, which creates a moment that counter acts tensile flexural stresses due to service loads. This in turn controls deflection and reduces or even eliminates cracking under service loads. The prestressing force is applied by an externally stressed high strength steel wires, strands, or bars, the force is then transferred to the concrete member by means of end anchorages or bond to the surrounding concrete.

2.2.1 Methods of Prestressing Concrete

There are two method of introducing a prestressing force to a concrete member: *post-tensioning*, which is used for onsite applications, and *pre-tensioning* which is used in precast plants.

Post-tensioning - Post-tensioning can be achieved by running prestressing strands (tendons) through hollow ducts prior to casting the concrete. The ducts are laid with a specific profile within a member based on the required design. After the concrete is poured the strands are stressed against the concrete by a hydraulic jack to a pre-calculated stress. The force is transferred to the concrete by anchors at the end of the strands, Figure 2-3(a). This allows post-tensioned strands to be either bonded or unbonded. If bonded, the void within the ducts is filled with grout after the strand has been stressed.

Pre-tensioning - Pre-tensioned concrete generally applies to members prefabricated in a precast plant operation. The strands are prestressed before the concrete is poured. The strands are stressed and anchored at bulkheads outside of the member's formwork. Once stressed the force is maintained by the stressing bulkhead while the concrete is poured into the formwork. After the

concrete reaches the designed strength for release the strands are cut and the force is transferred to the concrete by bond and a mechanical interlock between the strand and concrete, Figure 2-3(b).

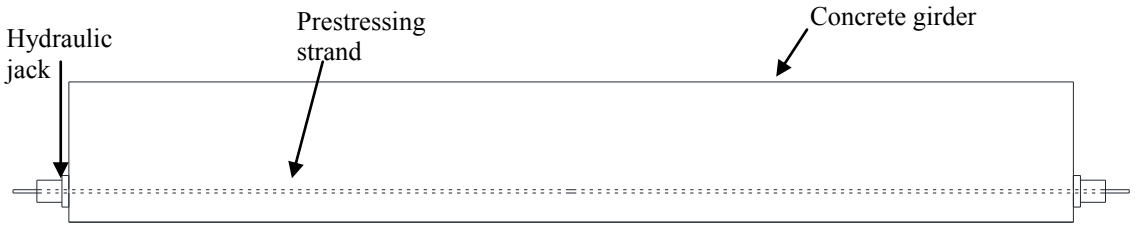

(a) Post-tensioning setup for prestressed concrete

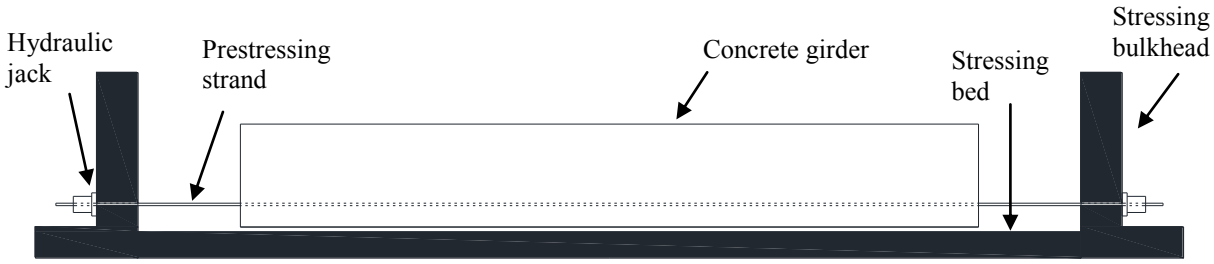

(b) Post-tensioning setup for prestressed concrete

Figure 2-3 – Prestressed concrete schematic: (a) post-tensioning, and (b) pre-tensioning

2.3 Fatigue of Reinforced Concrete Structures

Many reinforced concrete structures undergo dynamic loads. Structures such as bridges are subjected to cyclic traffic loading. Typically such structures are expected to survive 7×10^8 loading cycles during their service life (Tilly 1979). Fatigue is a form of dynamic loading consisting of repetitive loading cycles that may lead to failure (ACI 215R-74 1974). The number of load cycles to failure (fatigue life) is influenced by a number of factors, such as the stress range, the loading rate, and the mean stress (Bannantine 1990). In general, most materials exhibit a lower strength under fatigue loading than under monotonic loading. To understand the overall fatigue response of a reinforced structure, it is important to understand the fatigue behaviour of each of its components.

2.3.1 Fatigue of plain concrete

The fatigue strength of plain concrete is considered to be the fraction of its ultimate monotonic capacity that it can withstand under repeated load cycles (ACI 215R-74 1974). When subjected to cyclic loading, concrete will exhibit excessive cracks and eventually fail, this may occur even if the applied load is lower than the monotonic load capacity. In addition concrete will show softening behaviour similar to that under monotonic loading (Neville 1996). The applied stress range (maximum-minimum applied stress) is the primary variable causing fatigue of concrete. Other factors such as the water/cement ratio, the type of aggregates, and the concrete age have been found to affect the fatigue life in the same way as they affect the concrete strength. For a maximum stress level lower than 75% of the monotonic capacity, a variation in fatigue loading frequency between 1-15 Hz has little to no effect on the fatigue life of concrete (ACI 215R-74 1974; Mordock 1965).

A fatigue S-N curve (stress range versus the number of cycles to failure) for plain concrete beams is shown in Figure 2-4. The beams were loaded at 7.5 Hz. The figure shows the ratio of computed flexural tensile stress (S_{max}) to the rupture stress (f_r) on the vertical axis, and the number of cycles to failure on a logarithmic scale on the horizontal axis. The figure shows that the fatigue strength decreases with an increasing number of cycles. Also, the S-N curves are linear between 10^2 to 10^7 cycles which means that a stress limit under which concrete life is considered infinite does not exist in this life range, and it is evident that as the stress range decreases the fatigue life increases (ACI 215R-74 1974).

A modified Goodman diagram is used to predict the fatigue strength of plain concrete load in compression, Figure 2-5. This diagram presents the relationship between the stress range and the minimum applied stress in a constant amplitude compressive loading test, and the fatigue life (presented as the number of cycles). Using Figure 2-5 for a given minimum applied stress and a desired fatigue life the allowable maximum applied stress can be determined.

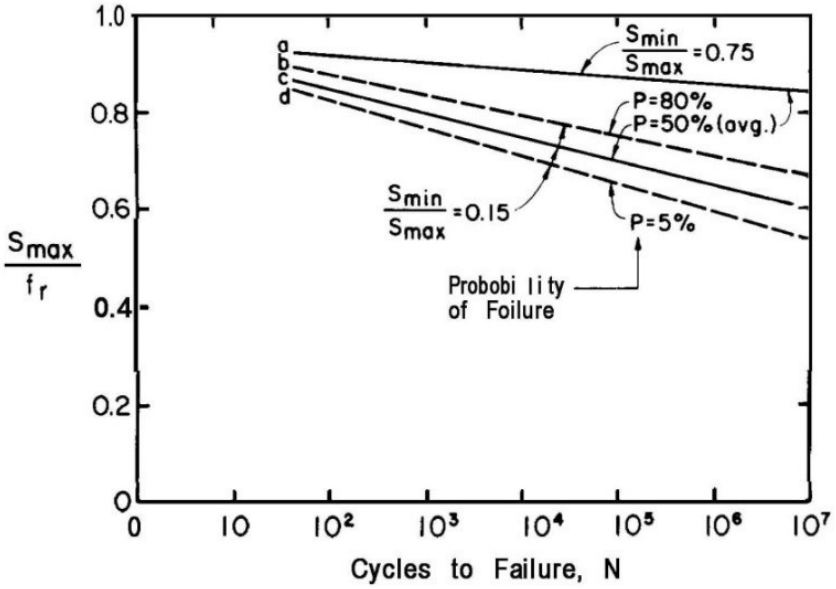

Figure 2-4 – Fatigue strength of plain concrete beams (Mordock 1965)

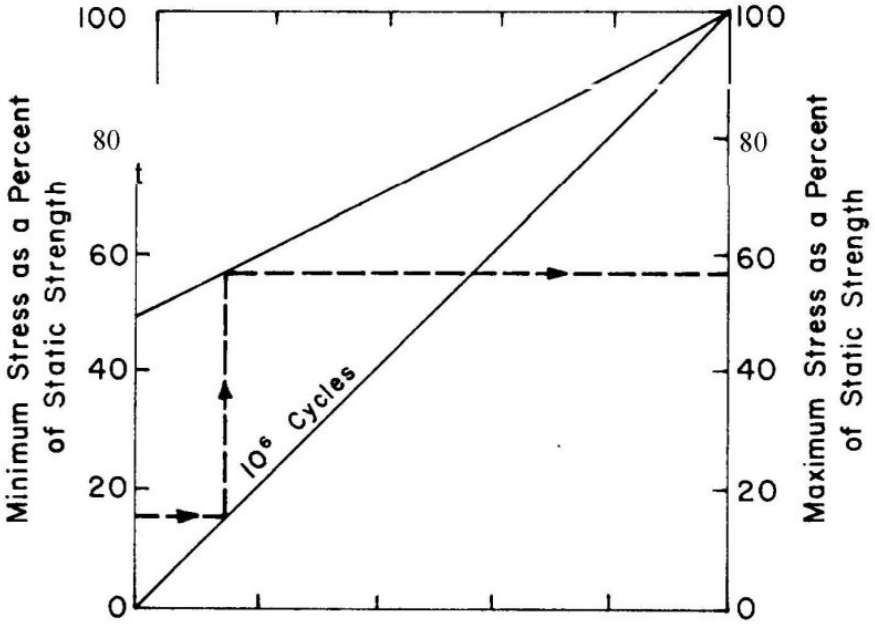

Figure 2-5 – Modified Goodman's diagram (ACI 215R-74 1974)

2.3.2 Fatigue of steel deformed bars

The S-N curves for reinforcing steel display a transition from a steep to a more flat response at around the one millionth loading cycle, Figure 2-6. This indicates that unlike plain concrete a reinforcing steel bar exhibits a practical fatigue limit stress (ACI 215R-74 1974). Figure 2-7 shows a typical failure surface of a deformed 35M steel bar (35.7mm diameter). The smooth surface is the fatigue crack surface, while the rugged surface is the fracture surface (fracture occurs after the fatigue crack has reduced the bar strength significantly). In deformed steel bars, the deformations act as stress raisers, which is why the fatigue crack in Figure 2-7 initiated at the stress raiser at the bottom of the deformation (ACI 215R-74 1974).

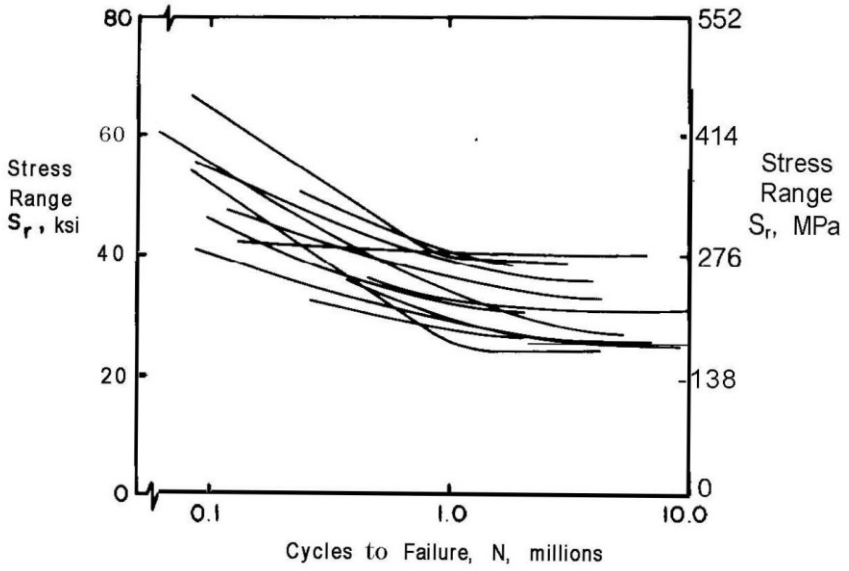

Figure 2-6 – Stress range vs. life curves for reinforcing bars (ACI 215R-74 1974)

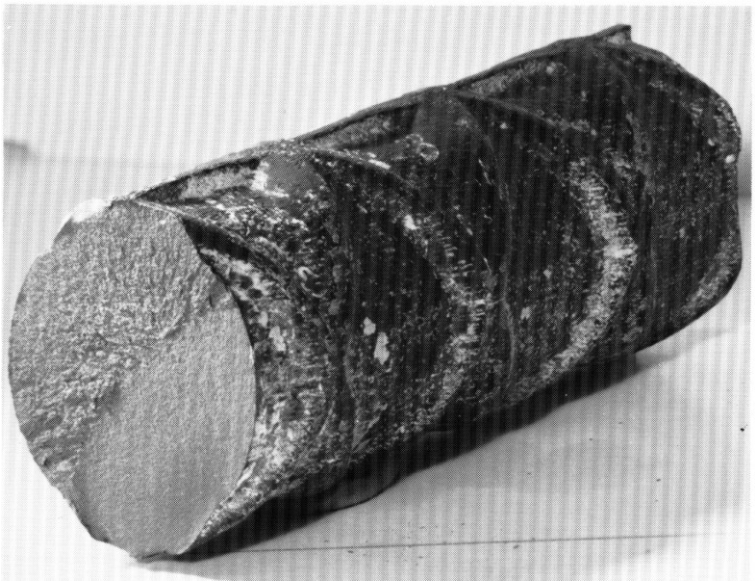

Figure 2-7 – Fracture surface of 35M (35.7 mm diameter) deformed steel bar (ACI 215R-74 1974)

Previous studies in the literature to determine whether the fatigue behaviour of steel bars tested in air resembles that of bars tested within a concrete beam are contradictory (ACI 215R-74 1974). Some studies indicate higher fatigue strength for steel embedded in concrete versus steel tested in air, while other studies report otherwise (Rehm 1967). MacGregor et al. (1971) reported that as long as the geometry of the lugs is sufficient to provide proper bond, very little difference in fracture behaviour should exist. Physical characteristics of deformed steel bars that affect the fatigue strength include: the bar diameter, the geometry of the lugs, bent bars, and the yield strength with stress concentration factors varying between 1.5 and 2.0 (ACI 215R-74 1974).

Bar diameter

It was reported that the fatigue strength of steel bars decreases as the bar diameter increases. MacGregor et al. (1971) tested bars in air in tension, while (Wascheidt 1965; Kokubu and Okamura 1965) tested bars embedded in beams. Findings from these tests were in agreement that

#5 bars (16mm nominal diameter) exhibited an 8% higher fatigue life than #8 bars (25.4mm nominal diameter)). One theory to explain the higher fatigue strength for smaller diameter bars is that the notch root at the lugs in the larger diameter bars exhibits a higher stress raiser than that found at the notch root in the lugs in the smaller bars.

Bar Deformation geometry

Deformed steel bars rely on their lugs to provide the mechanical bond with concrete; however, those lugs are also the source of the stress concentrations where fatigue fracture initiates (Burton and Hognestad 1967; Pfister and Hognestad 1964). Differences in the rolling and cutting techniques during fabrication of deformed bars lead to variations in the deformation geometry of the bars. (Derecho and Munse 1966) found in their analytical study that the variations in the geometry can significantly influence the fatigue strength by affecting the magnitude of the stress concentration factor. The stress concentration factor varies from 1.5 to 2.0 (ACI 215R-74 1974). It was reported that when the base radius of the deformation is increased from 0.1 to 1-2 times the deformation height, the fatigue strength significantly increases (MacGregor et al. 1971; Helgason et al. 1976; Kokubu and Okamura 1965; Hanson et al. 1968). However, if the base radius of the lugs on the bar is increased beyond 5 times the height of the deformation bond capacity can deteriorate (Kokubu and Okamura 1965).

Yield Strength and bending effect

The yield strength of deformed steel bars has little effect on the fatigue strength (MacGregor et al. 1971; Pfister and Hognestad 1964; Lash 1969). On the other hand, it was shown that bent bars with a 45 degrees bend angle could exhibit 29-50% less fatigue strength than straight bars,(Rehm 1967; Pfister and Hognestad 1964).

2.4 Fatigue of Prestressed Concrete Structures

A properly designed prestressed member will remain uncracked under service loads, and as such the fatigue response of prestressing strand/wire is unlikely to be critical (Bondy 1970). As a result, the fatigue behaviour of steel in prestressed concrete has not been a major issue in design guides and specifications. However, with more prestressed structures subjected to repetitive loading and a higher probability of over loading, there is a growing concern regarding the fatigue behaviour of prestressed members, especially with partially prestressed members (ACI 215R-74 1974; ACI 318-14). This concern is reflected in recent recommendations by ACI, ASCE, and PCI for unbonded construction that requires a prestressing steel and anchorage assembly to withstand a minimum of 500,000 cycles of a varying stress range from 60% to 66% of the specified ultimate strength of the assembly (ACI 318-14; ACI-ASCE 423-05).

2.4.1 Fatigue of prestressing reinforcements

Prestressing steel reinforcement can take the form of wires, strands or bars, each of which undergo different manufacturing and treatment processes, which greatly affect their fatigue strength.

Wires

Prestressing wires are usually made from drawn steel and have strengths ranging between 1720 and 1930 MPa (250 and 280 ksi). Drawing has multiple benefits: it increases the tensile strength of wires, produces a grain structure which inhibits crack nucleation and provides a smooth surface that reduces stress concentrations due to surface irregularities (ACI 215R-74 1974). Properties of wires can vary based on the manufacturing process. A study carried out on different

wires from Germany, Czechoslovakia, Belgium, and Japan showed that the fatigue strength of wire was a 30 ksi (207 MPa) stress range at a fatigue life of 4 million cycles. Testing wires of different diameters showed that their fatigue characteristics are within 5% of each other, and that similar to normal deformed steel bars the fatigue characteristics depend on the geometry of their ribs. Wires with ribs of 0.3 mm height and 45 degrees in slope and no base radius had a theoretical stress concentration factor of 2.0, and exhibited a 57% reduction in fatigue strength (Baus and Brenneisen 1968).

Strands

Similar to wires, strands are made out of drawn steel. Strands are comprised of 6 wires wrapped helically around a centre wire (often referred to as the king wire), Figure 2-8. Tests conducted on 11.1mm and 12.7mm 7-wire strands revealed a decrease in fatigue strength with increase in diameter (ACI 215R-74 1974). Figure 2-9 is a modified Goodman diagram that predicts the minimum or maximum allowable stress levels to achieve a desired number of cycles with a specific survival probability (Hilmes 1965).

Figure 2-8 – 7-wire prestressing strand

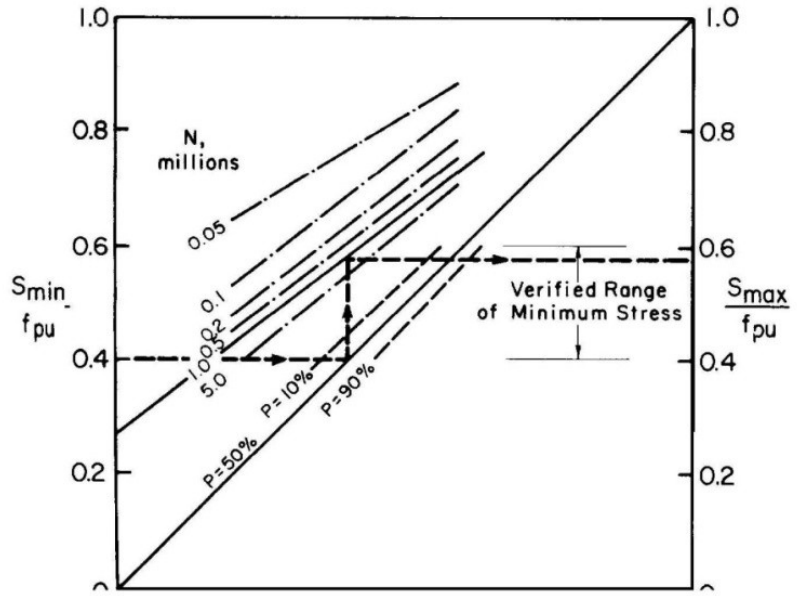

Figure 2-9 – Strength envelopes for strand tested in United States (ACI 215R-74 1974)

Paulson el at (1983) conducted an in-depth literature review and an investigation on the fatigue performance of steel prestressing strand as an isolated element as part of a research project sponsored by the Federal Highway Administration (FHWA) and the Department of Highways and Public Transportation of the State of Texas. Part of their investigation was compiling a database of available prestressing strand fatigue testing. They compiled close to 700 fatigue test results from various researchers including their own test results. They analyzed the compiled database and used a regression analysis to develop a lower bound design expression for the 95th percentile of 97.5% probability of no failure, Equation (2-7). The authors state that a stress range of 138MPa (20ksi) is a reasonable fatigue limit, and emphasized that their equation is only applicable to strands as isolated elements. Figure 2-10 shows the complied experimental data the statistical design model as presented by Paulson et al. (1983).

$$\log N = 11.0 - 3.5 \log S_r \tag{2-7}$$

Where, S_r Stress range (ksi)
N Number of cycles

Paulson et al. (1983) also noted that the fatigue behaviour of the prestressing strand varied from one manufacturer to another, and between strands from the same manufacturer. In addition, they observed that the fatigue resistance decreased with increased specimen length, which they attributed to the increased likelihood of flaws being present with a longer length.

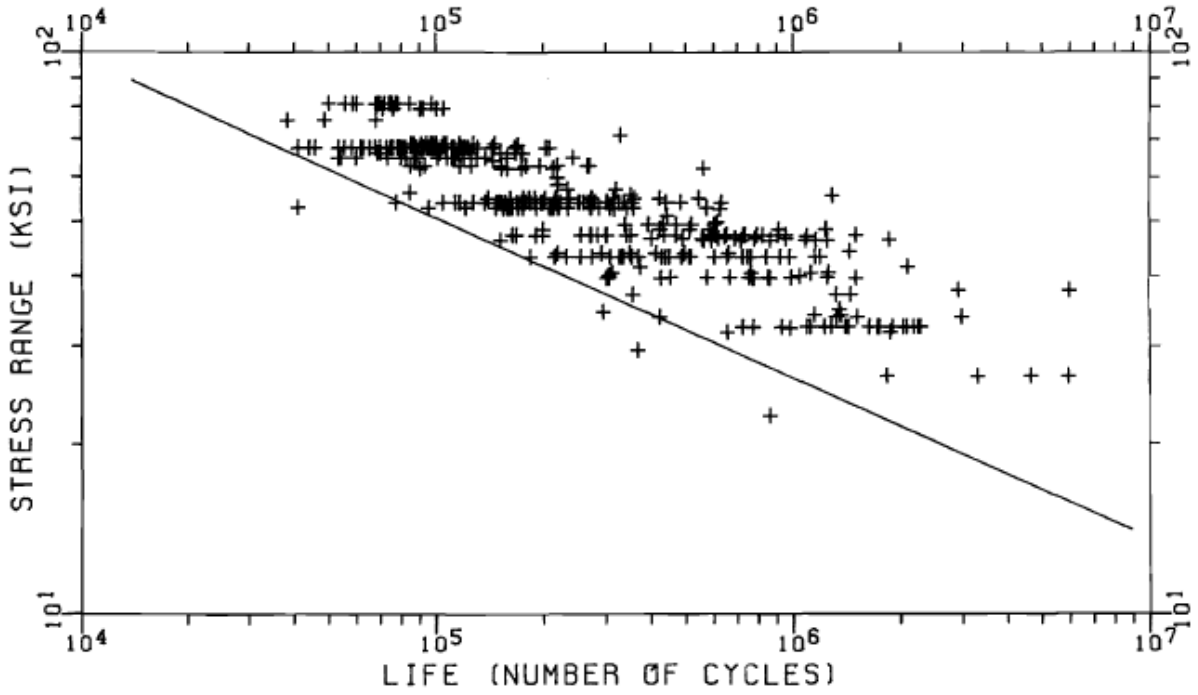

Figure 2-10 – Complied fatigue test results for prestressing strand as an isolated element, the statistical design expression of 95% of no failure, Paulson et al. (1983)

Bars

Tests on bars ranging between 25 and 35 mm in diameter have shown that the fatigue limits of these bars are in excess of 0.1 times the tensile strength of the bar for 1 x 10^6 cycles of loading with a minimum stress of 0.6 times the tensile strength (ACI 215R-74 1974).

2.4.2 Fretting fatigue of prestressing strands

Fretting fatigue occurs when two elements in contact under an applied lateral force exhibit relative movement in terms of slip or rotation under cyclic fatigue loading. This relative movement results in surface damage such as abrasive wear and corrosion. Surface abrasion results in the degradation of the protective surface oxide film, and without the oxide film the two

elements may fuse together (cold welding) at areas of local pressure exceeding the elastic limits. Furthermore, under cyclic displacement the adhesion formed between the two elements would break and another one would form; this cyclic behaviour eventually results in crack initiation, Waterhouse (1982), Wollmann et al. (1996).

Fretting fatigue of metals is a well-known phenomenon and has been extensively investigated. For prestressed concrete elements research efforts in the literature appears to have been focused on fretting in post-tensioned members due to obvious rubbing/abrasion between the prestressing strand and the strand duct, Ryals et al. (1992).

Wollmann et al. (1996) conducted an experimental investigation on fretting fatigue of post-tensioned concrete beams. The experimental program consisted of beam and strand fatigue testing. They concluded that fretting between the strand and the duct, and between the individual strands, reduced the fatigue resistance of bonded post-tensioned beams. Moreover, they compared their strand fatigue test results to the Paulson et al. (1983) model, and stated that although the strand tests were in good agreement with the Paulson model, strand-in-air data are not adequate to evaluate the allowable stress range in post-tensioned beams. They also observed that fretting between the strand and the metal duct was the predominant fretting mechanism, and recommended the use of plastic ducts and epoxy-coated strands. Figure 2-11 presents the fatigue test results for post-tensioned beams with strand in metal ducts and the strand-in-air fatigue failure zone.

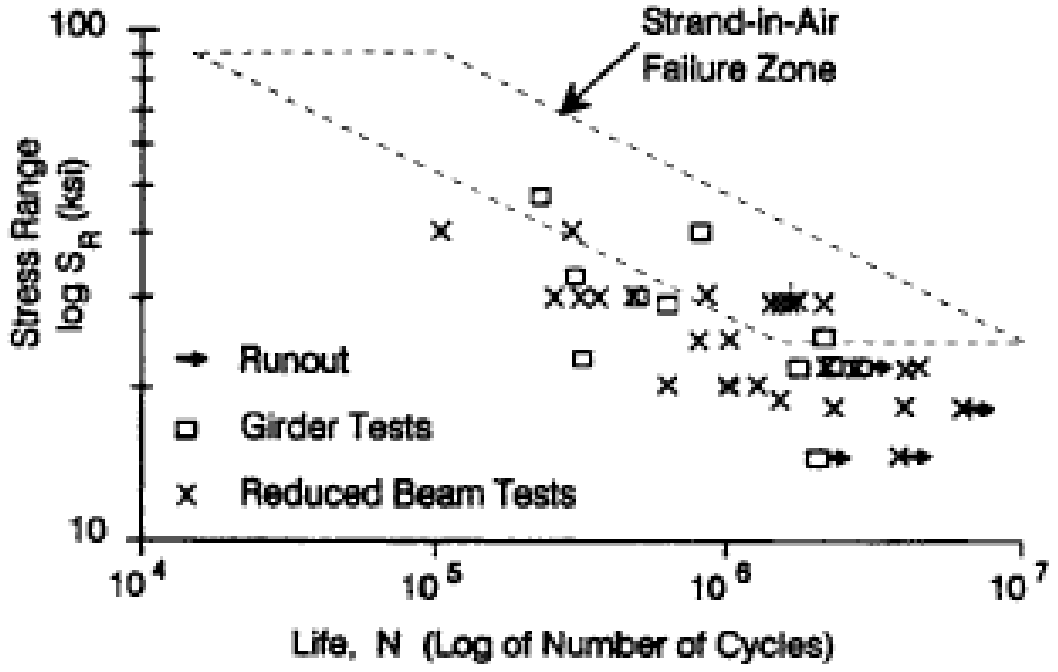

Figure 2-11 – Stress range vs. fatigue life for post-tensioned beams with strands in metal ducts (Wollmann, 1996)

Little attention has been given to fretting fatigue in pretensioned members, however, steel strands with a similar formation to concrete prestressing strands are widely used in other applications; electro-mechanical cables, anchors/tethers for deep water platforms, and cable/stayed bridges to name a few. A significant amount to studies was carried out on the fatigue of strand ropes as early as the 1970s. Although the strand rope geometry and mechanical behaviour is similar to concrete prestressing strands the metallurgy, the size of the wires and the number of layers are different which have an impact on the fatigue resistance.

For multilayered strands there are two types fretting mechanisms; longitudinal fretting and rotational fretting. Longitudinal fretting occurs between two adjacent wires with the same

lay/helix angle (inter-wire), while rotational fretting occurs at locations where two wires in different layers with opposite lay/helix angles cross each other (inter-layer). For concrete prestressing with 7-wire strands, longitudinal fretting is of concern since there is only one layer of helically wrapped wires.

Bahke (1980) reported a study conducted by Pantucek (1977) in which fatigue tests were conducted on wire ropes under combined pulsating tensile stresses and transverse pressure. The transverse pressure was increased from 600 to 3600 N. As the magnitude of the transverse pressure increased the detrimental impact on the fatigue life increased. Pantucek inspected the fracture surface under a microscope and found that cracks typically initiated at the edge of the elliptical pressure mark where high plastic deformations occurred, See Figure 2-12.

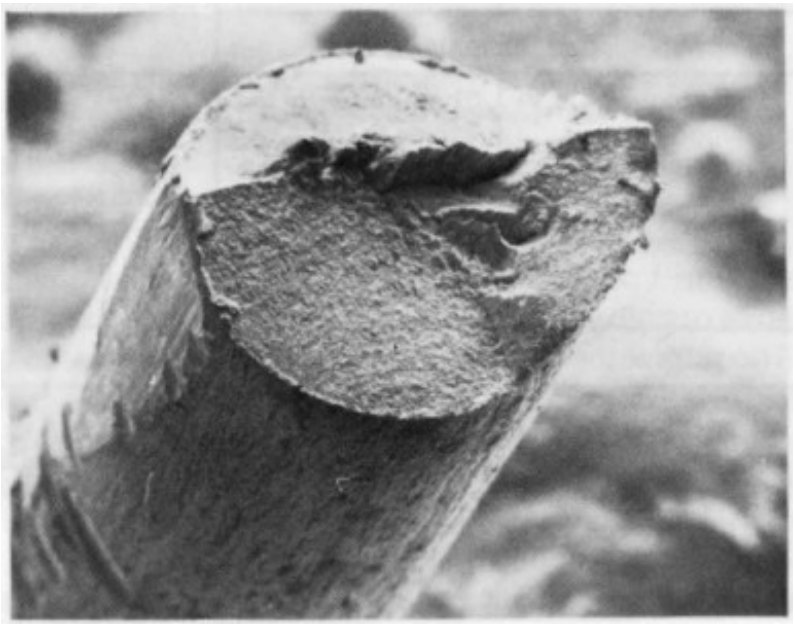

Figure 2-12 – Elliptical pressure mark on single wire and the fracture surface, Bahke (1980)

Blakeborough and Cullimore (1984) conducted a study on the fretting effects on the fatigue of 5 mm diameter galvanized bridge-wires. They used fretting rigs to simulate the fretting of galvanized steel wires due inter-wire contact in ropes, and found that longitudinal fretting causes a significant reduction in the fatigue resistance with an increasing deterioration effect beyond $1.5x10^5$ cycles, see Figure 2-13. They noted that the fretting scar had an elliptical shape and stated that as the impact is localized to the fretting area, the shape of the fretted body is of secondary importance.

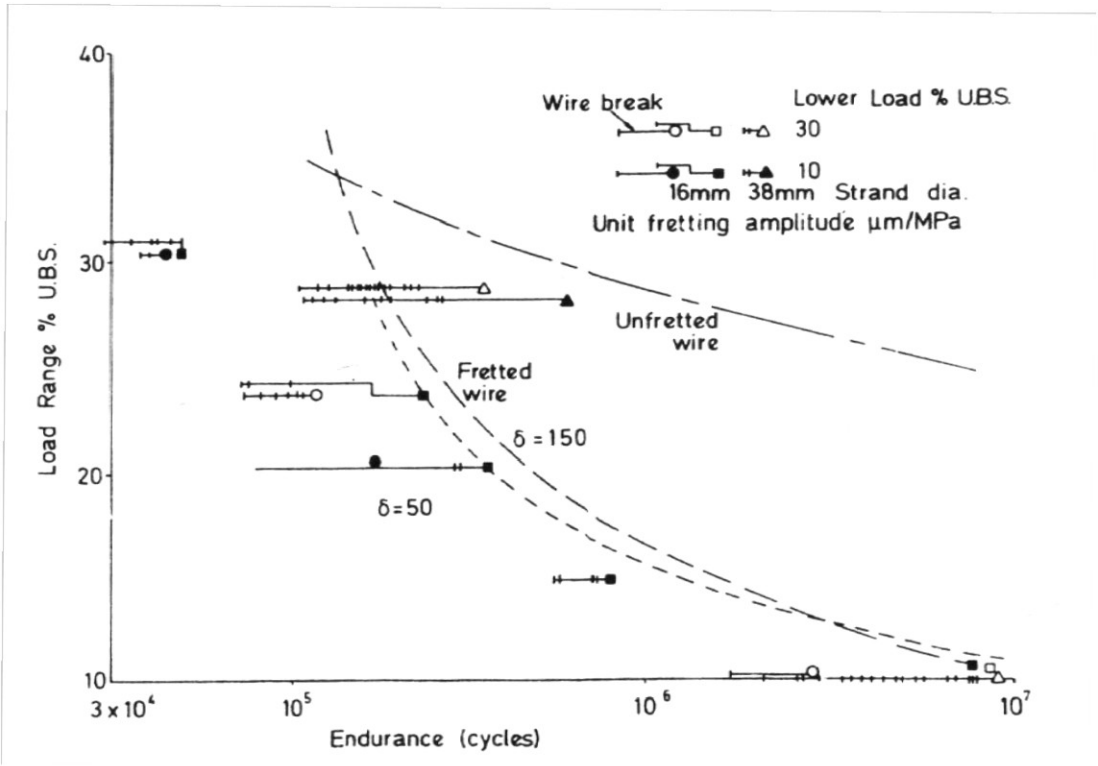

Figure 2-13 – Load range vs. fatigue life curves for non-fretted and fretted wire specimens (Cullimore, 1979)

2.4.3 Fatigue of pretensioned beams

Overman et al. (1984) conducted an investigation on the fatigue behaviour of pretensioned concrete girders. The investigation was a continuation of the research project of Paulson et al. (1983). The investigation comprised of testing eleven (11) pretensioned girders, and compared their behaviour to previous experimental results in the literature. In addition, they gave design recommendation with an emphasis on predicting their fatigue behaviour based on the fatigue behaviour of the prestressing strand. The authors cited six (6) flexure fatigue studies on pretensioned girders that reported the strand stress range or gave sufficient information to calculate it, with a total of 47 data points. They then used a linear regression analysis with the least squares method to construct the mean regression line and compared it to that by Paulson et at (1983), see Figure 2-14. The solid data points represents girders tested under a single point load, which in general had longer fatigue lives in comparison to the remaining girders tested under four-point bending (having a constant moment zone). Overman et al. note that for stress ranges below 180 MPa (26 ksi) beams exhibit shorter fatigue lives in comparison to strand-in-air lives.

Moreover, Overman et al. (1984) conducted a regression analysis on what they referred to only as large-scale beam tests, namely by Ozel (1962) and Rabbat et al. (1978), and compared the mean regression line to Paulson et al. model, see Figure 2-15. They commented that the regression lines are approximately parallel and that this type to behaviour is to be expected from a constant stress increase due to flexure cracking.

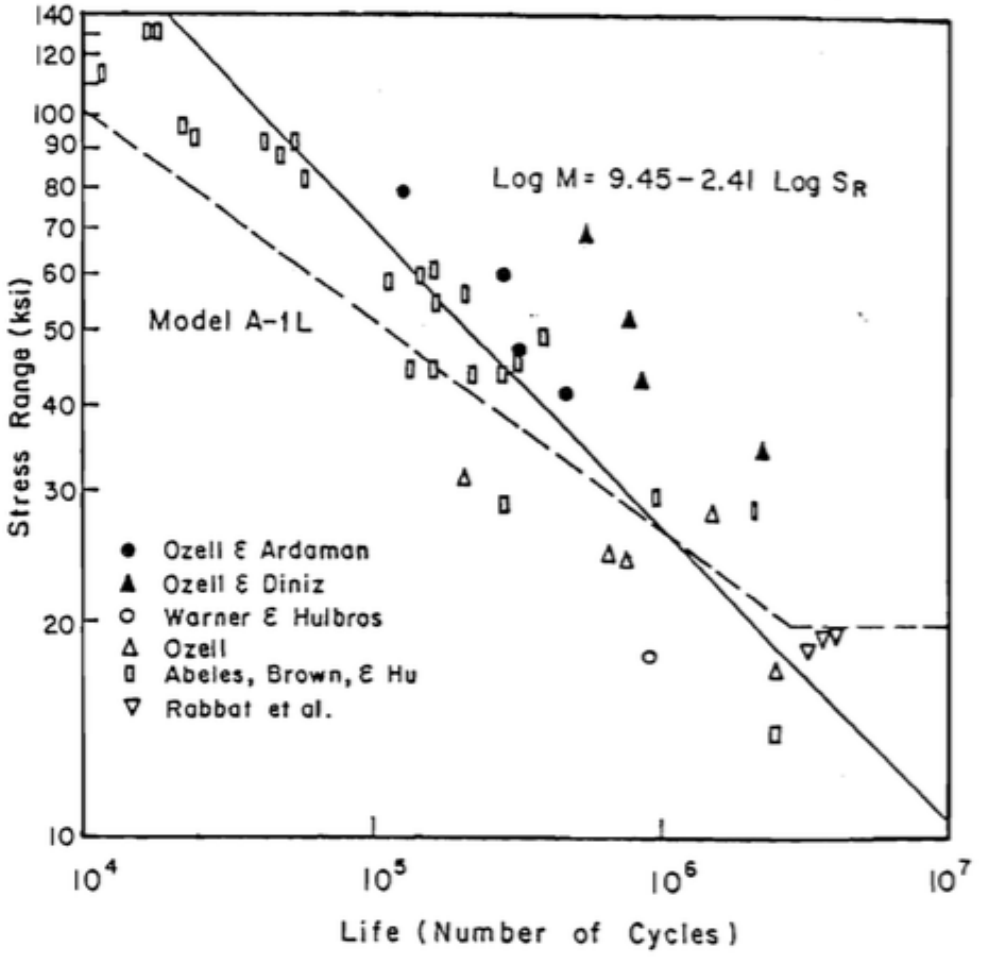

Figure 2-14 – Comparison of the mean regression line of pretensioned beam fatigue test results to Paulson et al. (1983) lower bound strand-in-air model, Overman et al. (1984)

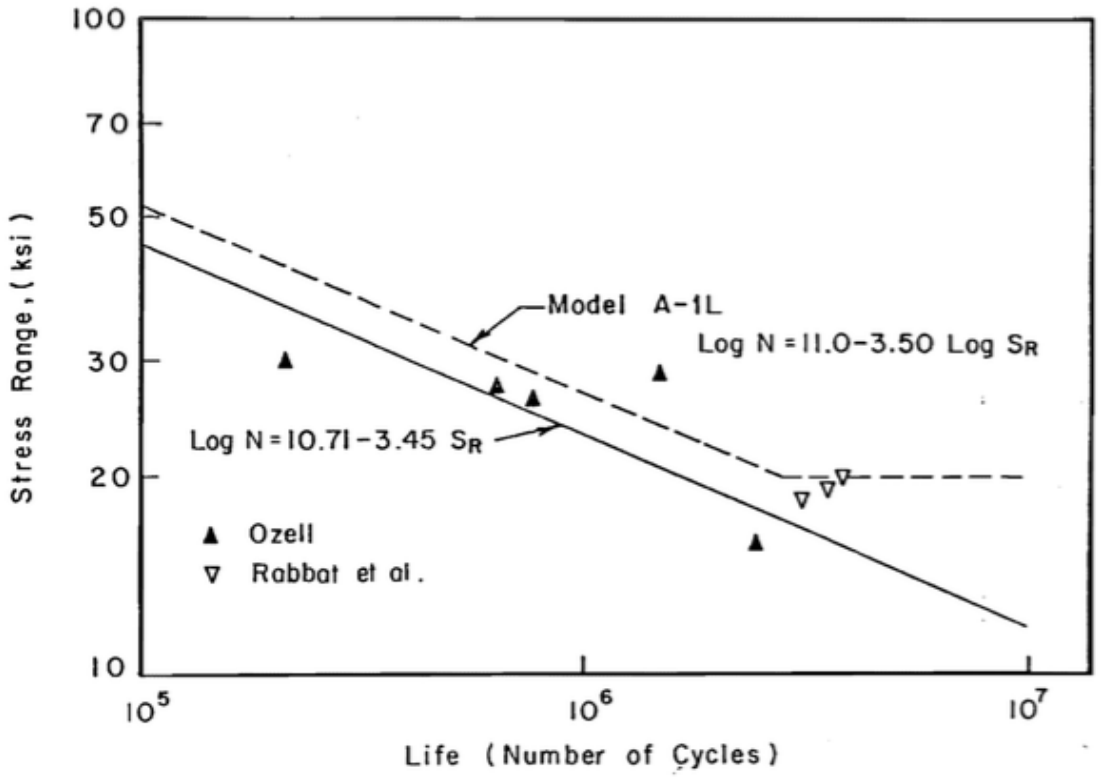

Figure 2-15 – Comparison of the mean regression line of large scale pretensioned beam fatigue tests to the Paulson et al. (1983) lower bound strand-in-air model, Overman et al. (1984)

Finally, Overman et al. (1984) tested eleven (11) large-scale beams measuring 14.65 m (48 ft) in length; four (4) beams with straight strands, four beams (4) with draped strands, and three (3) beams with supplementary crack control non-prestressed reinforcements. They compared their fatigue test results to Paulson et al. model, see Figure 2-16, and made the following notable conclusions:

- The Paulson et al. (1983) strand-in-air model can be used to predict the fatigue life of pretensioned concrete beams, with the modification that no endurance limit can be set. However, they state that a stress range below 34.5 Mpa (5 ksi) would be insignificant.

- Conservative minimum prestress forces should be used in predicted the beams fatigue life as the prestress losses have a direct influence on the strand stress range.
- The strand stress in a cracked concrete section can be calculated using an approximate manual cracked section analysis.
- Premature failures could not be correlated to draping of the prestressing strand.
- A small number of overload cycles of the order of 20 % above the applied load level can be detrimental and sharply decrease the fatigue life.

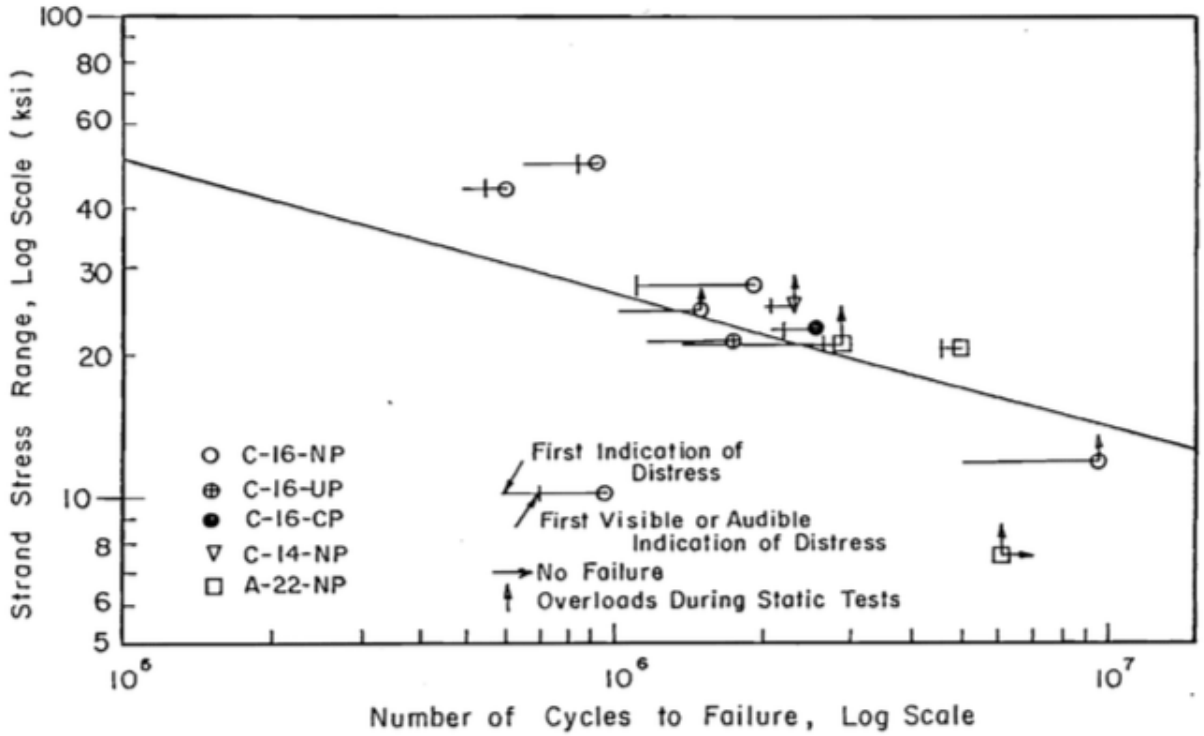

Figure 2-16 – Large-scale pretensioned beams fatigue test results in comparison to Paulson et al. (1983) lower bound strand-in-air model, Overman et al. (1984)

Naaman, A. E. (1989) conducted an experimental study that was comprised of testing a total of 38 partially and fully prestressed concrete beams. Twenty-four (24) pre-cracked prestressed concrete beams with rectangular sections were tested; twelve (12) beams were tested under monotonic loading and twelve (12) beams were tested under constant amplitude cyclic loading ranging between 40% and 60% of the monotonic beam capacity. Also fourteen (14) partially prestressed T-beams were tested under monotonic and variable amplitude cyclic loading. The beams tested under variable amplitude loading had a minimum load of 40 % of the monotonic beam capacity.

Three (3) of the rectangular fully prestressed beams failed in less than 2 million cycles and the remaining beams after surviving 5 million cycles were tested monotonically to failure. Naaman reported a correlation between an increase in the strand's stress level and the observed crack width. The beams failed in less than 2 million cycles had a crack width of 0.15 mm while the beams that survived to 5 million cycles had a crack width of 0.08 mm

Of the T-beams tested under variable amplitude cyclic loading four (4) beams failed in less than 2 million cycles. He reported that these beams had a measured crack width of more than 0.15 mm and exhibited variability in the measured stress levels between the strands and between the wires of the same strand. However, the average measured wire stress was in agreement with his analytically calculated stress. Failure of the partially prestressed beams was by fracture of the reinforcing steel or the prestressing strand.

Naaman suggested that in addition to the applied stress range, several parameters can significantly deteriorate the fatigue resistance; such as stress concentrations at anchoring

locations, fretting between adjacent wires or between the prestressing strand and the concrete. Finally he stated that the fatigue life of prestressing strands under minimal fretting conditions could be predicted by Equation (**2-8**) for stress ranges above 70MPa.

$$\frac{S}{f_{pu}} = 0.87 - 0.123 \log N \qquad (2\text{-}8)$$

Where, S The stress range

f_{pu} The ultimate strand tensile capacity

N Number to load cycles

2.5 Corrosion of Prestressed Concrete Structures

Prestressing steels are highly susceptible to corrosion attack due to the metallurgy associated with their high strength and the high stresses due to prestressing. This corrosion can significantly reduce the service life of prestressed concrete structures. Multiple factors contribute to the severity of corrosion in prestressing steels. This section presents the primary factors contributing to the corrosion of prestressing steel, and the impact of corrosion on prestressed structures.

2.5.1 Fracture modes of prestressing reinforcement due corrosion and cyclic loading

Depending on the loading condition, steel properties, and corrosion environment different fracture modes can occur in prestressing steel reinforcement (Nurnberger 2002; Ngoc et al. 2009):

- Brittle fracture.
- Stress corrosion cracking induced fracture.
- Fracture due to fatigue and corrosion influences.

Brittle fracture

Brittle failure may occur when a tensile stress is applied to high strength steels. Whether the fracture is brittle or not is influenced by general and local corrosion. In the case of general corrosion due to normal weathering, if a significant loss of cross section occurs, the residual load capacity of the high strength steel can be exceeded thus causing failure. On the other hand, if the local corrosion attack is characterized by deep pitting, the load bearing capacity can be severely affected at an early age of the structure. The latter case is more of a concern for post-tensioned ungrouted strands, where chlorides contaminated water, or bleed water can seep into ungrouted

ducts. Figure 2-17 shows the effect of pitting depth on the fatigue life of 5 mm cold deformed prestressing steel wire.

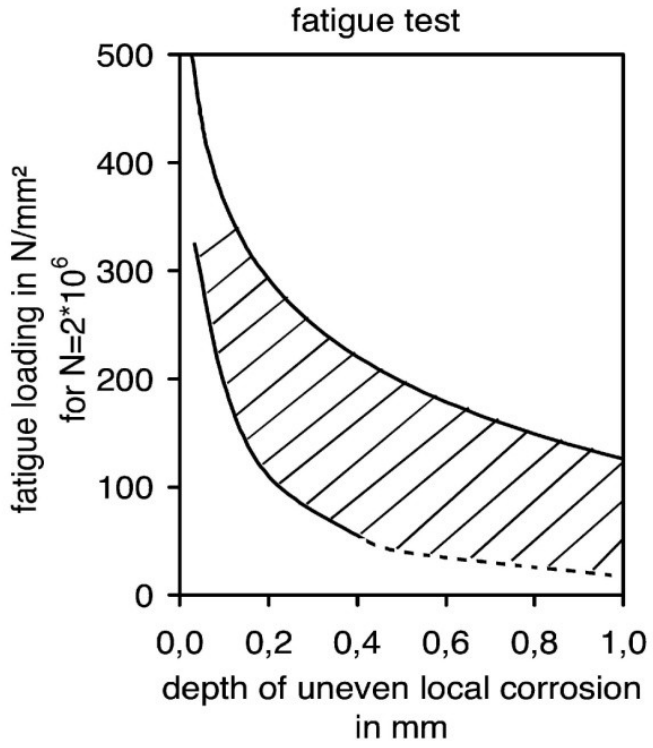

Figure 2-17 – Fatigue properties of 5mm cold deformed prestressing steel in relation to the depth of local corrosion (Nurnberger 2002)

Stress corrosion cracking (SCC) induced fracture

Stress corrosion cracking (SCC) is defined as the initiation and propagation of a crack within a material in the presence of a corrosive medium (Nurnberger 2002). This is can be either Anodic or hydrogen induced stress corrosion cracking (H-SCC). Anodic stress corrosion cracking occurs in the presence of a non-alkaline nitrate contaminate electrolyte, especially in low-carbon reinforcement. However, currently used prestressing steels are highly resistant to it.

Hydrogen induced stress corrosion cracking (H-SCC) occurs as hydrogen atoms are set free and are absorbed by the prestressing steel during the corrosion process. Coupled with the high mechanical tensile stresses due to prestressing, it can cause pre-cracks along grain boundaries. This requires the presence of hydrogen and an acidic aqueous media, which is a common attacking medium for concrete. As corrosion occurs the pH within the pit drops due to hydrolysis of the Fe^{2+} ions, creating the required acidic environment for crack initiation. The latter case is referred to as pitting induced hydrogen induced stress corrosion cracking.

Alonso et al. (1993) investigated the susceptibility of prestressing steel to stress corrosion cracking in a Sodium bicarbonate ($NaHCO_3$) solution. They conducted electrochemical and slow strain rate tests on cold drawn prestressing steel rod with a tensile strength of 1650 MPa. The rods were machined down to 2.5 mm diameter and 25 mm in length. The main variables of the study were the concentration of $NaHCO_3$, the aeration methods (air, Nitrogen or none), and the strain rate. They concluded that the prestressing steel tested was susceptible to stress corrosion cracking in $NaHCO_3$ with the greatest susceptibility being at a critical concentration of 0.1M of $NaHCO_3$. They also found that the susceptibility to cracking was affected by the solution's pH, and that a solution alkalinity with a pH of about 9.7 is required for cracking to occur.

Toribio and Ovejero (2005) studied the impact of the level of cold drawing of prestressing steel wires on their susceptibility to stress corrosion in the case of pure stress corrosion cracking (localized anodic dissolution, LAD) as well as fracture by hydrogen embrittlement (hydrogen assisted cracking, HAC).

They noted that commercial prestressing steel undergoes a heavy cold drawing that alters the microstructure and induces anisotropy in the material. This change in the microstructure although it enhances the classical material properties such as yield strength, may affect the fracture behaviour and the stress corrosion cracking (SCC) performance.

They obtained samples with different levels of cold drawing by taking samples from different stages of cold drawing from the manufacturing line, and referenced the samples by a steel designation from 0 to 6 based on the level of cold drawing, with 6 being the highest level. Samples were precracked to produce a transverse precrack with a crack depth = 0.30 × the diameter, then placed in a corrosion cell simulating the prestressing steel being surrounded by concrete. Low strain rate tests were performed on precracked steel wires with a constant displacement rate in the axial direction. The displacement rate for each test was proportional to each wire diameter, ranging from 1.7×10^{3} mm/min for the fully drawn to 3.0×10^{3} mm/min for the hot rolled bar (steel 0).

They observed the fracture plane profile for both HAC and LAD and noted an increase in anisotropic behaviour with an increase in the level of cold drawing. For lower levels of cold drawing (steel 0 and 1) the crack grows perpendicular to the loading direction while for medium levels of cold drawing (steels 2 and 3) a deflection in the fracture plane was noticed. Finally for the heavily drawn specimens (steels 4 to 6), the crack deflection had an even high deviation angle, see Figure 2-18. They noted that although heavy cold drawing helps in resisting SCC by crack tip blunting, this is countered by the mixed mode crack propagation in the direction of minimum resistance due to the anisotropic behaviour. Finally, they concluded that their observations indicate that cold drawn prestressing steels are highly susceptible to SCC.

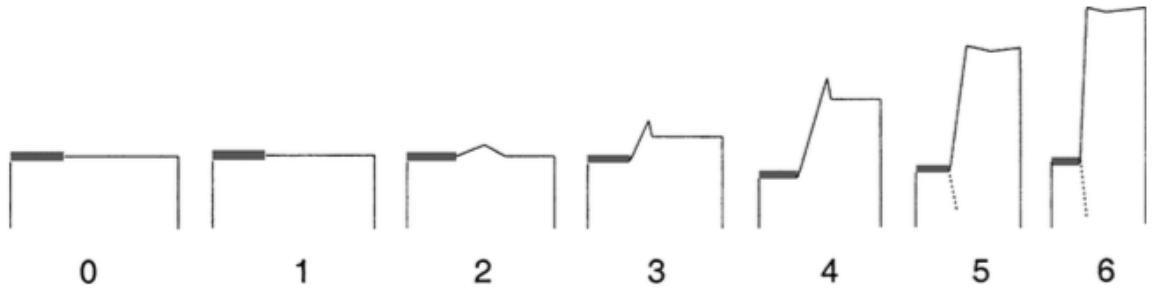

Figure 2-18 – Fracture profile of Hydrogen Assisted Cracking (HAC) at different level of cold drawing (Toribio and Ovejero, 2005)

Ngoc et al. (2009) conducted a study on the stress-strain response of 8mm prestressing wires exposed to accelerated stress corrosion cracking. The main variable considered in the study was the prestressing stress level (0, 70, 80, and 100% of the elastic limit, 1500 MPa). X-ray diffractometry was used to compare the chemical composition of the rust products resulting from corrosion at different prestressing stress levels. The average life of a wire exposed to 100%, 80%, and 70% of the elastic limit stress was found to be 164, 265, and 350 days, respectively. In addition, tensile tests were carried out on the prestressing wires at 60, 90 and 180 days of corrosion exposure. The test results showed that corrosion led a to considerable reduction in the elastic limit, elastic modulus, yield stress and the ultimate strain and also led to brittle failure of the wire, Figure 2-19.

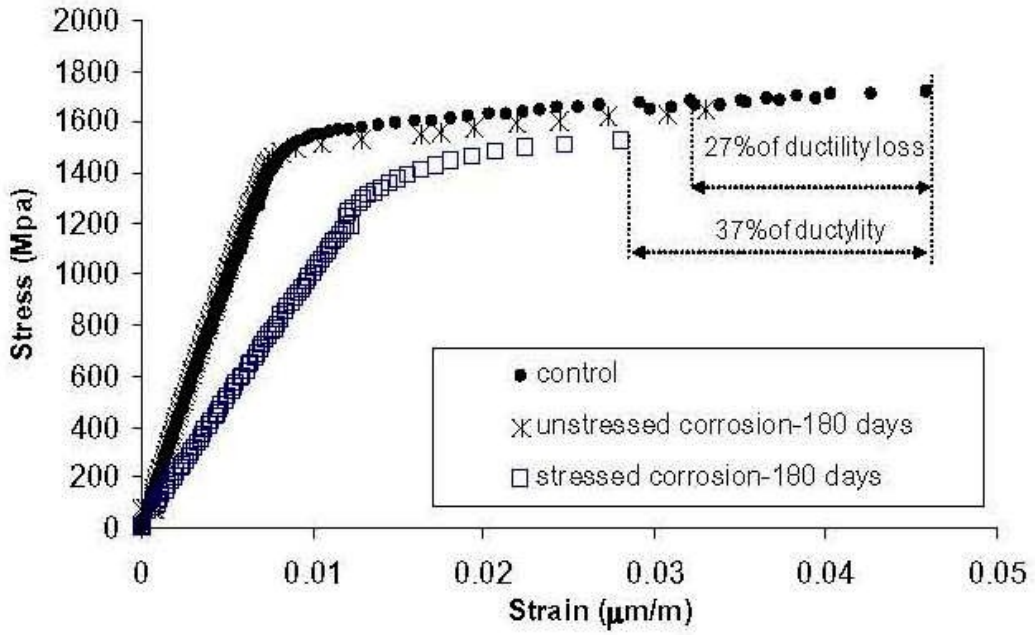

Figure 2-19 – A comparison between stressed and unstressed corroded wires (Ngoc et al. 2009)

A significant difference in corrosion pattern was noticed: as the corroded stressed wire exhibited micro cracking perpendicular to the axial direction, which was not observed in the non-prestressed wire. This is considered to be an indication of hydrogen induced stress corrosion cracking. The findings of this study highlight the impact of the prestressing stress level on the development of stress corrosion cracking, and also the influence this has on the corrosion mass loss. Highly prestressed wires can exhibit an additional 15% mass loss compared to non-prestressed wires. However, the prestressing stress level appears to have no effect on the composition of the rust products.

Perrin et al. (2010) studied the damage evolution in prestressing strands due to hydrogen embrittlement and characterized the degradation mechanism though metallographic observations. They used the centre wire of a standard monolayer (7-wire) prestressing strand. Their wire was

subjected to a corrosive solution while under a tensile force equal to 75% of the ultimate tensile strength. The corrosive solution was an ammonium thiocyanate solution (NH4SCN). The test duration was 160 hours with an interruption for metallographic observations at 24, 48 and 96 hours. Figure 2-20 shows the wire fracture plane before immersion in ammonium thiocyanate solution and after 96hrs of immersion, while Figure 2-21 shows the wire surface before an immersion in ammonium thiocyanate solution and after 96 hours of immersion. Notable observations by Perrin et al. are the change in fracture mode and the condition of the wire surface; the fracture mode changed from a ductile failure with significant necking before exposure to a brittle fracture with no necking after 96 hours of immersion, while the wire surface changed from a healthy surface elongated in the cold drawing direction before immersion to a surface with many obvious crack in the transverse direction after 96 hours of immersion.

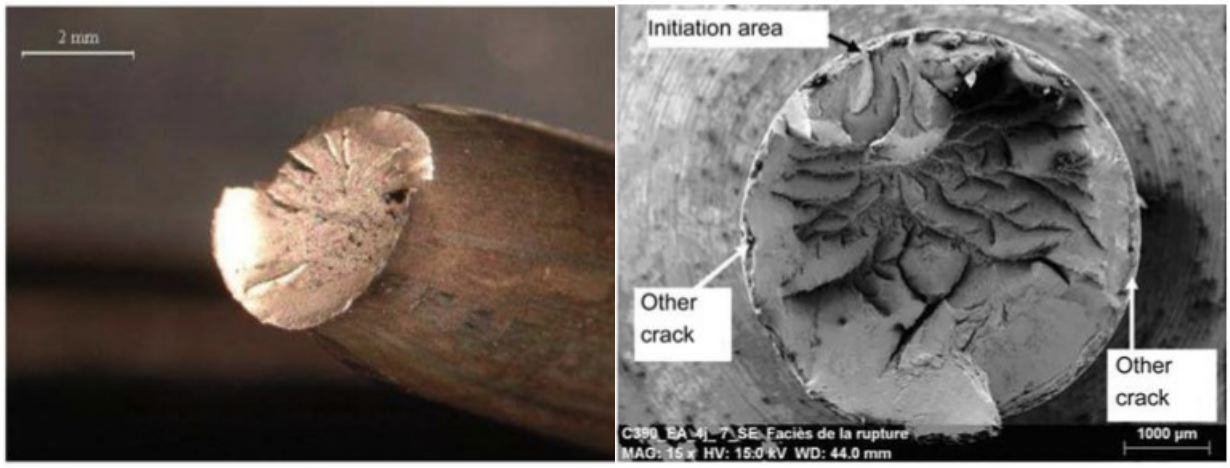

Figure 2-20 – Wire fracture plane before immersion (left) and after 96 hrs of immersion (right) in ammonium thiocyanate solution

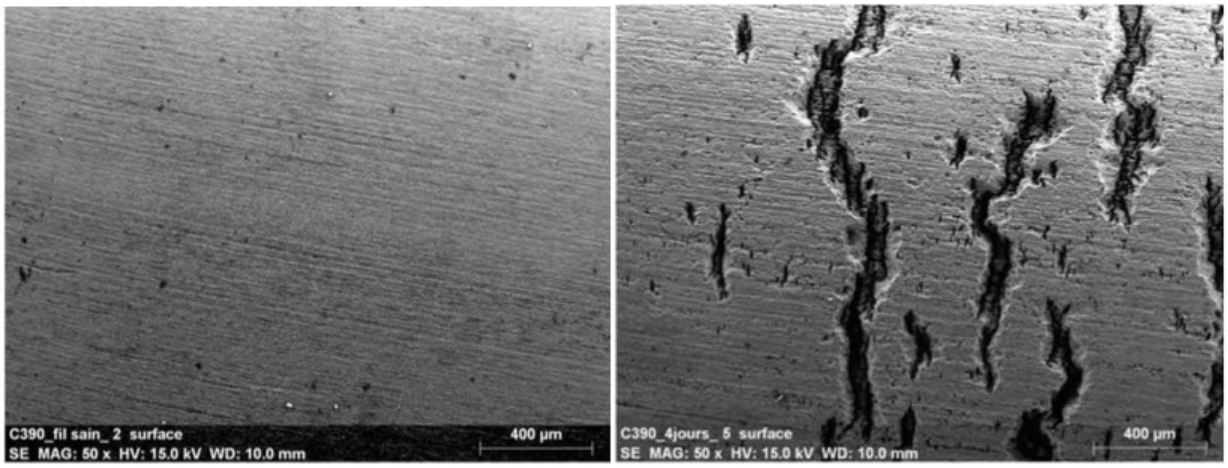

Figure 2-21 – Wire surface before immersion (left) and after 96 hrs of immersion (right) in ammonium thiocyanate solution

Fatigue and corrosion induced fracture

In prestressed members cracks can occur due to the applied fatigue stresses caused by, for example, traffic loads on a bridge. Unlike stress corrosion cracking, fatigue cracking does not require a corrosive medium for the crack to initiate. However, if the prestressed steel strand is corroded, fatigue cracking of the strand will start earlier and progress faster than fatigue cracking in air without corrosion of the prestressing steel. In addition, fretting which is defined by the disintegration of the steel surface due to oscillating friction between the adjacent wires of a single strand, the strand and the surrounding concrete and/or adjacent strand is a likely initiation mechanism for cracks. If chlorides make their way to the prestressed steel through cracks in the concrete, oxidation will take place and combine with the tensile stresses due to fretting, to deteriorate the fatigue behaviour of the prestressing steel.

Nurnberger (2002) presented a comparison between the fatigue behaviour of cold drawn prestressing steel wires tested in air and the fatigue behaviour when tested in corrosion

promoting media (tap-water and sea water). The comparison clearly shows an increasing detrimental effect on the fatigue resistance when moving from testing in air to testing in tap-water and then to testing in sea-water, see Figure 2-22.

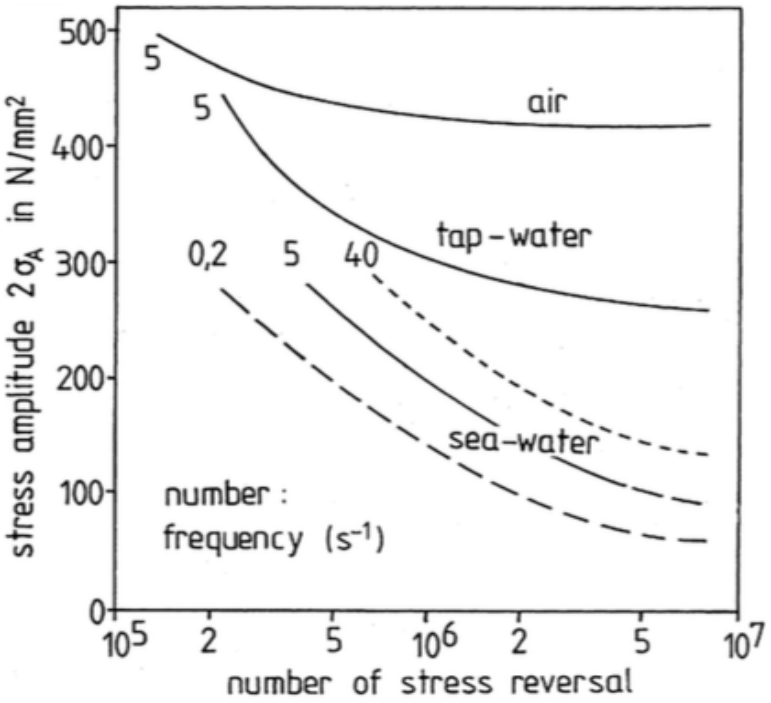

Figure 2-22 – Fatigue behaviour of cold drawn prestressing steel wire tested in air, tap-water and sea-water, (Nurnberger, 2002)

2.5.2 Effects of corrosion on prestressed concrete structures

Although corrosion induced deterioration of reinforced concrete structures has been observed throughout concrete's history, it was not until the 1980s that such deterioration was observed in prestressed concrete structures (Darmawan and Stewart 2007). Two of the recent failures attributed to corrosion are: the collapse of the Saint Stefano bridge in Italy in 1999, and the collapse of a pedestrian bridge over Lowe's Motor speedway in North Carolina in 2000 (Proverbio and Ricciardi 2000; Goins 2000).

A corrosion attack on prestressed concrete elements can present more serious consequences than on reinforced concrete elements due to the high mechanical stresses applied to the strands (Rinaldi et al. 2010). In addition, the deterioration of unbonded tendons within a structure often shows no outward signs of distress (Harder and Rogowsky 1999). Typically prestressing strands are stressed between 60-75 % of the materials ultimate stress, and as the prestressing strand corrodes it exhibits an overall loss of cross section and localized pitting creating along the strand. The severity of a stress raiser is a function of the volume of mass loss, the geometry (depth, width, and radius of a pit), and location of the pits. The prestressing steel becomes highly susceptible to local yielding and/or fracture with a reduction in cross section (Darmawan and Stewart 2007).

MacDougall and Bartlett (2002) tested six (6) - 13 mm-diameter 7-wire strands with one or two broken outer wires and subjected to accelerate corrosion by exposure to aggressive treatments. The test results indicated that corrosion significantly affected the behaviour of the unbonded 7-wire strands with broken wires in comparison to that of identical non-corroded strands. They noted that the corrosion product could increase the apparent interwire friction coefficient resulting in maintaining sufficient force in the tendon that may mask wire breaks. Finally they concluded that mechanical interlock between the broken and unbroken wires may occur which would reduce the accuracy of the screwdriver penetration test.

Darmawan and Stewart (2007) carried out a study to quantify the effects of pitting corrosion on the capacity of prestressing wires by obtaining a spatial distribution of pit depths along the prestressing wire length. Accelerated corrosion was used to simulate natural corrosion in the field. The variables considered were the type of prestressing steel (single wire and 7-wire

strands), the level of induced current used to accelerate the corrosion process, and the percentage corrosion mass loss.

The study was divided into two series; the first series focused on identifying the mode of failure of the prestressing wire (brittle, stress corrosion cracking, or yielding). The second series focused on the temporal and spatial variation pit depth along the length of the wire or strand. In series I, two 3 m × 0.3 m × 0.3 m beams were constructed with a single prestressing wire in the centre of the beam. The prestressing wire was 5.03 mm in diameter and was stressed to 74% of its ultimate strength. One beam was subjected to accelerated corrosion with an induced current density of 80 $\mu A/cm^2$ while the second beam was kept as a control without corrosion.

After 68 days, 1m sections of the prestressing wire were extracted from each beam, and tested under an axial tensile load to determine the change in the stress-strain behaviour. They measured the maximum pit depth for each 100 mm section of the 1m wires with the deepest pit measuring 1.97 mm, and reported that a corrosion pit can be typically represented by a hemispherical pit configuration. The corroded wire failed at the location of the deepest pit and exhibited an approximately 40% reduction in tensile capacity.

The fracture surface was examined using a scanning electron microscope and compared to that of a non-corroded wire, however, they go on to state that while SCC and brittle fracture were not observed in their study they cannot be ruled out as the likelihood of their occurrence depends on various variables such as; the stress level, the chemical environment and the mechanical and chemical properties of the wire. Their comparison revealed no sign of stress corrosion cracking

but showed a transition from a ductile to a less ductile mode of failure. Figure 2-23 presents a side-by side comparison of the non-corroded and corroded wires.

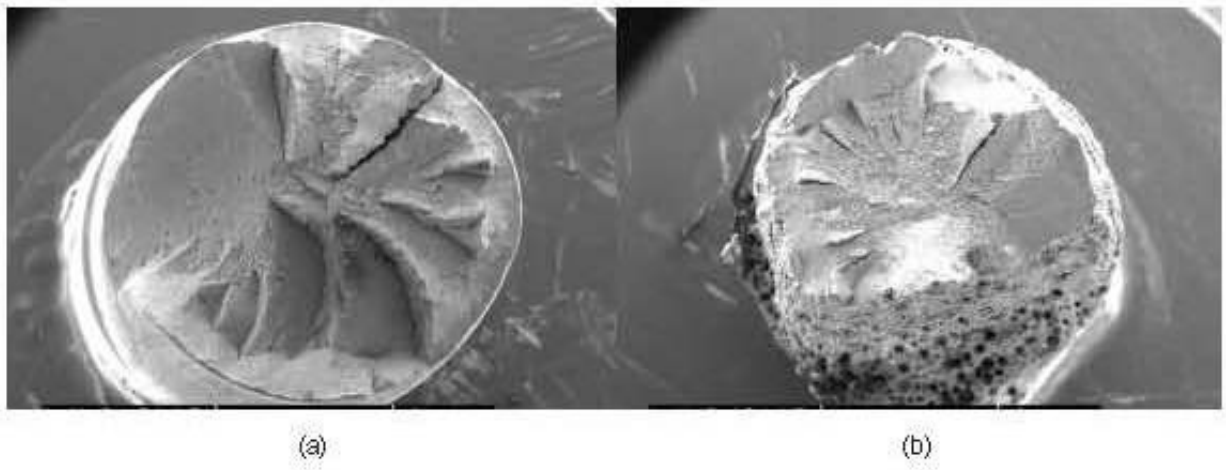

Figure 2-23 – Fracture surface a) non-corroded wire, and b) corroded wire (Darmawan and Stewart, 2007)

For Series II, six (6) concrete slabs 1.5 m × 1.0 m × 0.25 m in dimensions, were constructed and subjected to accelerated corrosion with an induced current density ranging from 150 to 418 $\mu A/cm^2$ for up to 56 days. Nine (9) wires/strands were placed in each slab but were not stressed. After the accelerated corrosion exposure, the wires/strands were extracted, cleaned and weighed. Statistical data were collected from the samples and found to be best represented by the Gumbel EV-Type I distribution. The authors used the data to formulate a probabilistic model to predict the maximum pit depth, along any length of wire at any time during its service life, Equation (2-9).

Darmawan and Stewart stated that the model is slightly conservative as it assumes that the pit has a fixed length/width, thus over predicting the pit depth. They used this model, Equation (2-9), to

simulate a real life corrosion scenario at a current of 1 μA/cm^2 for 20 years and found that the mean loss of cross section can exceed 30%, and there is a 5% chance of reductions in the cross section up to 45%. Also, after 10 years of corrosion there is a 15% chance of at least a 20% reduction in cross-sectional area. These results highlight the effect of pitting corrosion on the monotonic capacity of a prestressing strand. Figure 2-24 presents the distribution of the reduction in cross sectional area for a 20 m prestressing wire at a corrosion rate of 1 μA/cm^2 in relation to time in years.

$$f_a(T, i_{corr}, L) = \frac{\alpha}{\lambda^{0.54}} e^{-\alpha(\frac{a}{\lambda^{0.54}}-\mu)} e^{-e(\frac{a}{\lambda^{0.54}}-\mu)} \quad (2\text{-}9)$$

Where,

f_a	The probability distribution of maximum pit depth a
T	Exposure duration of accelerated corrosion (years)
i_{corr}	Corrosion rate (μA/cm^2)
L	Length of wire/strand
a	Pit depth
α, μ	Constants based on the Gumbel distribution parameters
λ	Ratio of increase in volume of corrosion products

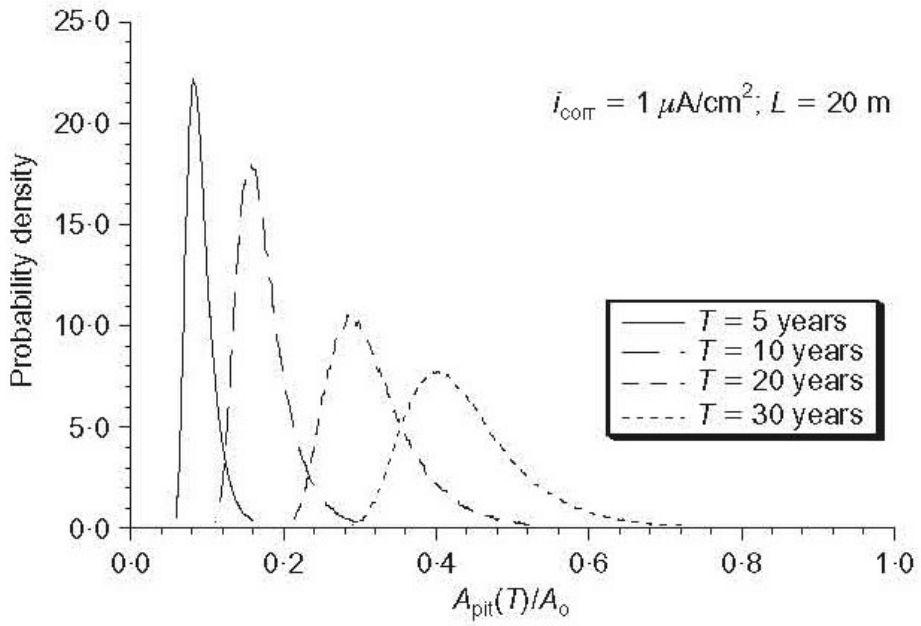

Figure 2-24 – Distribution of cross sectional area reduction vs. time (Darmawan and Stewart, 2007)

Rinaldi et al. (2010) conducted an experimental investigation to study the flexural behaviour of corroded prestressed concrete beams. The study comprised of 9 beams measuring 3 m × 0.3 m × 0.2 m. The main variables of the study were the corrosion or mass loss level (7%, 14%, and 20%) and concrete strength (34, 42, 47.4 MPa). All beams were partially prestressed with 3 7-wire stands (12.7 mm in diameter), stressed to 66% of their ultimate stress. An induced current of 400 mA was used to accelerate the corrosion process in the presence of a 5% NaCl solution. Two beams were left un-corroded to serve as reference control beams. After the strands reached the desired corrosion level, all beams were tested monotonically up to failure in four point bending. The load, midspan deflection, and end-slip measurements were all recorded.

Test results revealed that corrosion of the prestressing strand significantly affected the behaviour the prestressed members in terms of load bearing capacity, ductility, and failure mode. The

control beams failed by concrete crushing of the overly reinforced section, while the beams corroded to a 7% mass loss exhibited a combined failure of localized rupture accompanied by concrete crushing. Beams corroded to 14% and 20% mass loss failed by localized strand rupture. Figure 2-25 presents a comparison of load versus midspan deflection of an uncorroded beam and corroded beams at 14% and 20% mass loss. Results show a reduction in monotonic capacity of 55%-65%, but no significant effect on the member stiffness.

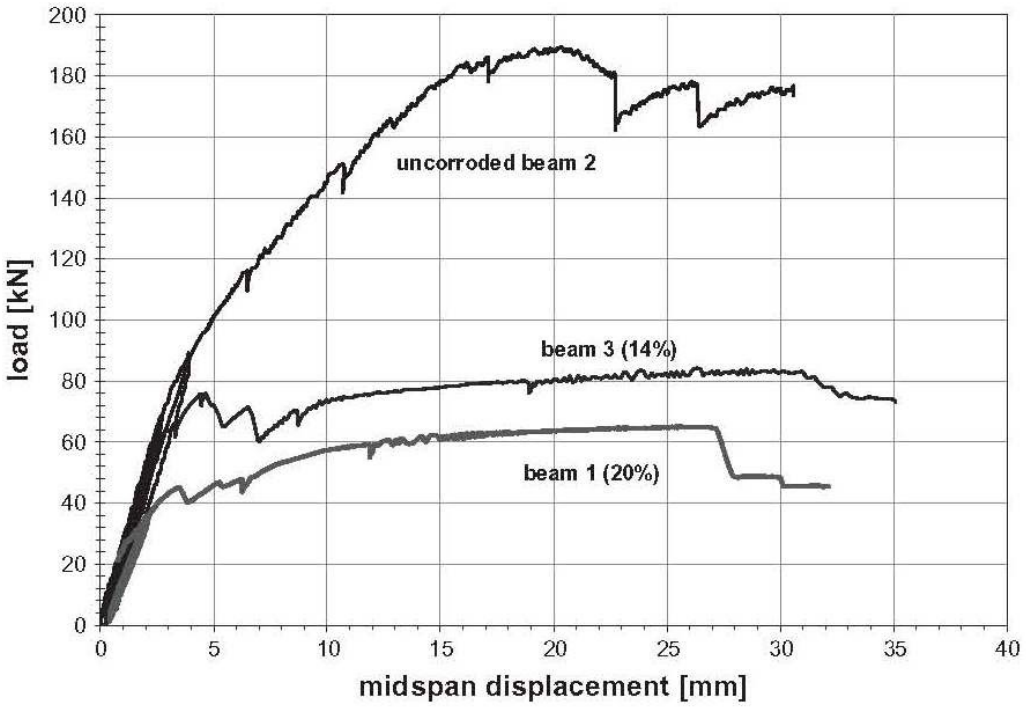

Figure 2-25 – Comparison of load versus midspan deflection for beams at different corrosion levels (Rinaldi et al. 2010)

Rinaldi et al. attempted to predict the beam capacity based on the average mass loss of the prestressing strand by using the stress block approach. They found that uniformly reducing the cross sectional area (average mass loss) over the length of the strand contradicts the observed

pattern of localized pitting corrosion, and therefore over estimates capacity. When the corroded prestressing strand was extracted from the beam it was observed that the king wire (centre wire) was often undamaged while the remaining six (6) wires were severely corroded. Based on this observation the authors concluded that for uncorroded beams and beams with a low level (7%) of corrosion, the simplified stress block approach would suffice; however, for higher corrosion levels, 14% and 20%, predictions of the beam capacity can be made by assuming that only one or two wires out of the seven wires are intact.

In summary, this section presented the available literature on the effects of corrosion on the monotonic capacity and ductility of prestressed members. The importance of these effects is evident, with prestressing strands being susceptible to corrosion of up to a 45% mass loss in 20 years (Darmawan and Stewart 2007), and exhibiting a loss of monotonic capacity of up to 65% at a 20% mass loss (Rinaldi et al. 2010).

2.6 Rehabilitation of Non-Prestressed Concrete Structures Using Fibre Reinforced Polymer (FRP)

The detrimental effects of corrosion on conventional concrete reinforced structures have been scrutinised by the research community for decades. However, for over two decades now Fibre Reinforced Polymers (FRP) have been gaining an ever increasing acceptance as a strengthening/rehabilitating method to restore degraded member capacity due to corrosion damage. The drive behind the increasing popularity of using FRP is the numerous researchers who have investigated their use in repairing corroded steel reinforced concrete beams. In this section a brief review of recent studies that have focused on the effectiveness of FRPs for repair purposes is presented.

2.6.1 FRP strengthening and repair of RC beams subjected to monotonic loading

Bonacci and Maalej (2001) compiled and analyzed an experimental database compiled from the literature of reinforced concrete beams strengthened by externally bonded Fibre Reinforced Polymers (FRP). The database contained 127 specimens from 23 different studies. All beams were simply supported with rectangular and T-cross-section and conventional reinforcement. Externally applied FRP strengthening were all glass (GFRP) or carbon (CFRP) fibres designed for flexural strengthening. The authors observed that almost one-third of the sample size exhibited a strength increase of at least 50%, however, it was evident that all the studies focused on strengthening and not rehabilitation. They concluded that future research should focus on the application of rehabilitation under conditions that resemble field conditions such as sustained loading and environmental attack.

Soudki and Sherwood (2000) conducted an experimental program comprised of constructing and testing 10 reinforced concrete beams. Beams had chloride levels varying from 0% to 3% and were subjected to accelerated corrosion to 5%, 10% and 15% corrosion by mass loss. Six beams were strengthened with external epoxy bonded CFRP laminate while the remaining four (4) remained non-strengthened. All beams were tested to failure under four-point bending. Strengthened beams exhibited an increased stiffness, yield and ultimate monotonic strength. Beams corroded to 15% by mass loss and strengthened using CFRP were able to regain their uncorroded monotonic capacity. Figure 2-26 presents load versus midspan deflection curves for the control non-corroded beam, the corroded non-strengthened beam, and corroded and strengthened beams.

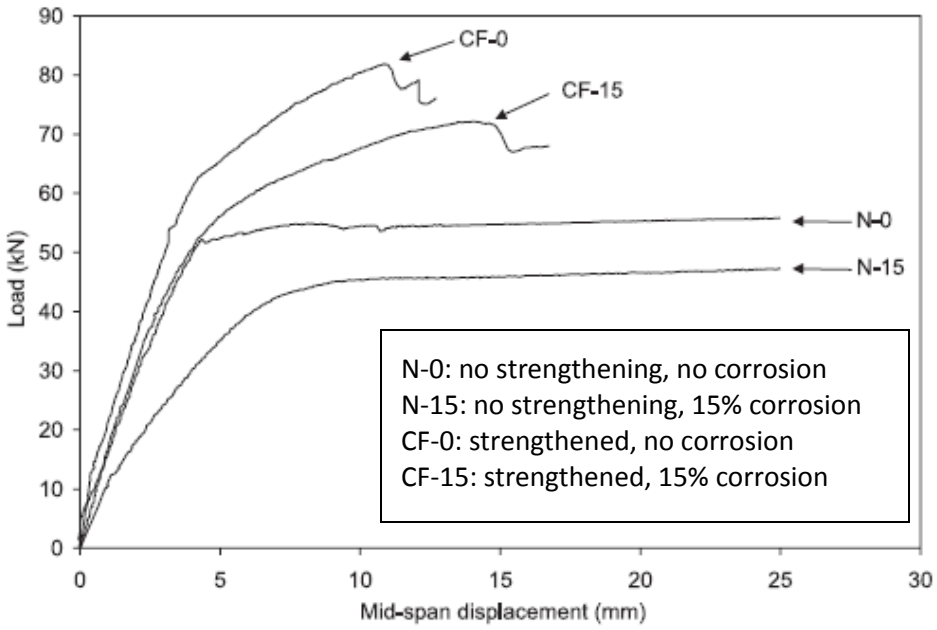

Figure 2-26 – Load vs. midspan deflection curves for control, corroded/non-strengthened and corroded/strengthened beams (Soudki and Sherwood, 2000)

Soudki et al. (2007) investigated the behaviour of CFRP-strengthened concrete reinforced beams in a corrosive environment. The investigation comprised of constructing and testing eleven (11) concrete reinforced beams. Beams where subjected to 300 cycles of wetting and drying in a corrosive solution (3% NaCl), and repaired using CFRP sheets. Test results showed that CFRP strengthening significantly enhanced the performance of reinforced concrete beams, and restoring them to 1.25 to 2 times the maximum monotonic load capacity of the non-corroded beams depending on the number corrosive cycles the beam was exposed to.

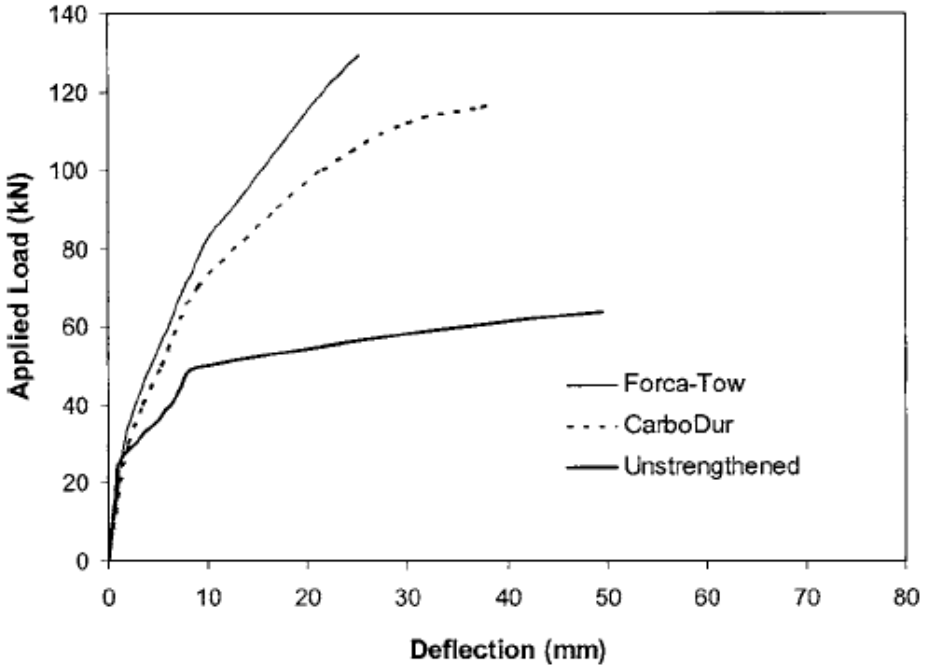

Figure 2-27 – Load vs. midspan deflection curves for non-strengthened and strengthened beams subjected to no wetting and drying cycles (Soudki et al, 2007)

2.6.2 FRP strengthening and repair of RC beams subjected to fatigue loading

Shahawy and Beitelman (1999) tested 16 T-beams with different repair schemes to investigate the monotonic and fatigue performance of reinforced concrete beams strengthened with carbon-

fibre-reinforced polymer (CFRP) laminates. The beams were under-reinforced 6 m (20 ft) long T-beams; ten (10) beams were tested under monotonic loading, while the remaining six (6) beams were tested under fatigue loading. Results showed that CFRP strengthening increased the monotonic load capacity by up to 70% with four layers of CFRP laminate, while the ductility decreased with the increased number of layers. In addition, results indicated that fatigue-critical beams could be effectively rehabilitated using CFRP laminates.

Masoud et al. (2001) constructed and tested eight (8) reinforced concrete beams measuring 120 x 175 x 2000 mm. Seven (7) beams were subjected to accelerated corrosion, and six (6) were strengthened with CFRP sheets. One (1) beam remained non-corroded and non-strengthened. All beams were tests to failure in a four-point bending configuration. Three specimens were tested under monotonic loading and five specimens were tested under cyclic loading. Beams strengthened using CFRP sheets had a fatigue life ranging from 2.5 to 6 times the fatigue life of an equivalent corroded but non-strengthened beam, but did not achieve the fatigue life of the control beam (non-corroded and non-strengthened). They concluded that CFRP strengthening is technique of capable of improving the structural behaviour of corroded reinforced concrete beams.

Heffernan and Erki (2004) experimentally studied the fatigue behaviour of steel reinforced concrete beams strengthened with externally bonded CFRP laminates. The authors tested a total of 26 beams (20 - 3 m long and 6 - 5 m long) under monotonic and cyclic loading, and observed that all the fatigue failures were initiated by the fracture of one of the steel rebars. Moreover, the fatigue life of beams strengthened with CFRP increased in comparison to non-strengthened beams, with no significant degradation of the CFRP laminate. Finally, the authors concluded that

externally bonded CFRP strengthening is an appropriate method of extending the fatigue life of steel reinforced concrete when rehabilitation is required. Figure 2-28 compares the moment range versus fatigue response of non-strengthened and strengthened reinforced concrete beams.

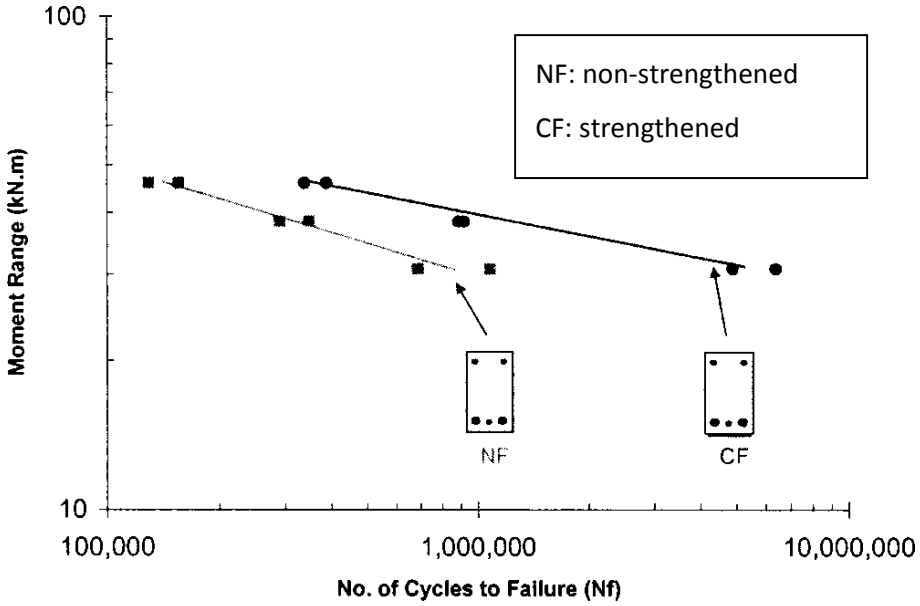

Figure 2-28 – Moment range versus fatigue life of non-strengthened and strengthened reinforced concrete beams (Heffernan and Erki, 2004)

Aidoo el at. (2004) constructed and tested eight (8) 5.6 m long reinforced T-beam under constant amplitude cyclic loading to investigate the effects of externally bonded CFRP sheets and laminates on their flexural fatigue performance. They conclude that FRP repairs can extend the fatigue life of a reinforced concrete beam by reducing the stresses resisted by the steel. However, the fatigue performance is governed by the fatigue behaviour of the reinforcing steel and the bond between the carbon FRP and concrete substrate.

Al-Hammoud el al. (2011) constructed thirty (30) steel reinforced concrete beams measuring 152 mm x 254 mm x 2000 mm; all beams were tested to failure in a four-bending configuration. One

(1) beam was tested under monotonic loading while the remaining twenty-nine (29) beams were tested under cyclic loading. The beams tested under fatigue loading were divided into; non-corroded and non-repaired, corroded and non-repaired, and corroded and repaired using CFRP.

Beams subjected to accelerated corrosion had an actual mass loss varying from 4.65% to 14.3%, and corrosion pitting was not observed below the corrosion level of 7% by mass loss. Corrosion resulted in decreases in the fatigue resistance of the beams that increased with corrosion level. The authors concluded that repairing with CFRP sheets increased the fatigue capacity of the beams with corroded steel reinforcement beyond that of the control unrepaired beams with uncorroded steel reinforcement, and stated that this conclusion was only applicable to medium corrosion levels (9% by mass loss) and for fatigue lives between 100,000 and 500,000 cycles.

Oudah and El-Hacha (2013) conducted a comprehensive literature review on the fatigue performance of Reinforced Concrete (RC) beams strengthened using Fibre Reinforced Polymers (FRP) reinforcement. They reviewed the fatigue properties of the constituent materials, the effects of pre-damage, and environmental exposure on the fatigue behaviour of Reinforced Concrete (RC) beams strengthened using (FRP) and made recommendations for future research, which included but were not limited to: (1) revisiting into the fatigue limits provided by the design codes include the effects of other fatigue test variables on the fatigue life of tension steel such as the R ratio and the mean cyclic stress, (2) investigations on types of FRP other than CFRP, (3) further experimental testing to investigate the effects of existing pre-damage and the environmental conditions/exposures, (4) examine the effect of various/variable amplitude loading on the fatigue performance of RC beams strengthened using different types of FRPs and strengthening systems.

2.6.3 FRP strengthening and repair of prestressed beams subjected to monotonic and fatigue loading

Takács and Kanstad (2000) obtained two (2) 11.2m long double-T bridge girders from the decommissioned Isakveien Bridge in Oslo, Norway. The two double-T girders were cut along the longitudinal direction to form four (4) T-beams. All beams were tested monotonically to failure in a four-point bending configuration. Two beams remained non-strengthened while the other two were strengthened using CFRP plates in the longitudinal direction. CFRP strengthening resulted in an increase in flexural moment capacity of up to 37%, and the observed failure by debonding of the CFRP plate from wide crack locations. They concluded that strengthening prestressed beams using CFRP plates is effective, however, they cautioned of the possibility of brittle failure due to a reduction in member ductility.

Hassan and Rizkalla (2002) investigated the flexural behaviour of post-tensioned bridge slabs strengthened with various techniques. They constructed three (3) slabs with a centre span and two cantilevers (one on each side). Each slab underwent three monotonic tests under single point loading. The centre span was tested as a singly supported slab and the ends were tested as cantilevers. The strengthening techniques used were near surface mounted Leadline bars, CFRP bars and strips, and surface mounted sheets and strips.

They reported that strengthening using CFRP increased the post-crack stiffness by at least 1.5 times, and decreased crack opening in comparison to non-strengthened slabs. In addition, CFRP strengthening provided a substantial increase in monotonic load capacity of up to 50% depending on the type and configuration of strengthening. They concluded that externally bonded CFRP sheets were the most effective of the five (5) strengthening techniques in terms of strength

improvement, and that future research should investigate the impact of other parameters such as fatigue loading and temperature effects.

Ford (2004) investigated the effects on fatigue behaviour of prestressted concrete beams when strengthened using externally bonded prestressed CFRP sheets. Five (5) rectangular beams measuring 3.6 m long were constructed and strengthened using CFRP sheets prestressed to 20% to 50% of their ultimate capacity. In addition three (3) were also subjected to 80 freeze/thaw cycles to assess the impact of the harsh exposure environment on the fatigue performance. Ford noted that the freeze/thaw and fatigue cycling may result in concrete softening, reduction the monotonic ultimate capacity and an increased ultimate deflection, concluded that the strengthening technique was effective and behaved adequately under fatigue loading.

El-Hacha et al. (a) & (b) (2004) investigated the performance of partially prestressed concrete beams strengthened with post-tensioned CFRP sheets under sustained loading at room (+22 °C) temperature or at low (-28 °C) temperatures. They constructed and tested eight (8) – 4.5 m long T partially prestressed T-beams. The strengthened beams showed significant increases in flexural stiffness and ultimate capacity in comparison to the unstrengthened beams. The concluded that the long-term and low temperature effects did not adversely affect the strength of the beams indicating that strengthening by bonded prestressed CFRP sheets could be used to on damaged prestressed concrete girders under extreme environmental conditions.

Larson et al. (2005) stated that although favourable results about FRP as strengthening technique are increasingly being reported in the literature, its impact on the fatigue behaviour of prestressed concrete members remains to be adequately evaluated. They conducted an experimental program

to study the fatigue behaviour of pretensioned T-beams strengthened with CFRP sheets. Five (5) 5 m (16.5 ft) long pretensioned T-beams were constructed and tested in a four-point bending configuration. One beam was remained unstrengthened and was tested to failure under monotonic loading. Two beams were strengthened and then monotonically tested to failure, while the remaining two beams were strengthened and tested under fatigue loading, one to 1million cycles and the other to 3 million cycles before being tested monotonically to failure.

When the experimental results for identical beams tested under monotonic loading were compared to those tested under fatigue loading and then under monotonic loading to failure they found that the global beam stiffness remained the same while the load capacity was reduced for the beams subjected to fatigue loading. They stated that fatigue loading deteriorates the strength but not the stiffness of the beams. Finally they concluded that externally bonded FRP sheets were effective for strengthening concrete beams prestressed with straight strands.

Rosenboom and Rizkalla (2006) and Rosenboom et al. (2006) investigated the monotonic and fatigue behaviour of strengthened partially prestressed bridge girders. They conducted an experimental program that consisted of strengthening and testing fifteen (15) decommissioned girders from two bridges in Eastern North Carolina. The girders were 9.14 m (30 ft) long C-channel girders that had both straight and harped prestressing strands. They used multiple CFRP strengthening systems designed to achieve strengthening levels of a 20%, a 40% and a 60% increase in the monotonic capacity. The strengthening systems used were near-surface-mounted bars and strips, and externally bonded strips and sheets.

They stated that the near surface mounted CFRP systems were the most effective of the strengthening systems. They reported that CFRP strengthening achieved an up to 73% increase in the monotonic capacity and reduced the crack widths and spacing, and reduced the stress range in the prestressing strands under service loading conditions. However, the prestressing strand remained as the most fatigue critical component in a CFRP strengthened prestressed concrete bridge girder.

2.7 Summary

A review of the literature on the corrosion effects on the fatigue behaviour of prestressed members was presented. Key findings are as follows:

- Corrosion of a prestressed concrete member can be fatal, and can manifest itself in prestressed members without external signs of distress. Recent bridge collapses mentioned in Section 2.5.2 were attributed to corrosion of prestressing strands.
- Corrosion induced failures in prestressed members are more severe than those in reinforced concrete members due the stored high mechanical energy.
- Stress corrosion cracking could evolve from corrosion pitting, which would lead to the development of both micro cracking and micro-voids in the steel bulk.
- The effects of corrosion on the monotonic capacity of prestressed concrete members are significant, and can lead to a major reduction in the member's monotonic load capacity.
- Cyclic loading significantly reduces the strength of reinforced and prestressed concrete members.
- Repair of reinforced concrete beams using Carbon Fibre Reinforced Polymer is an effective technique for restoring monotonic and fatigue capacity to that of the non-deteriorated beam.
- Repair of prestressed concrete beams using Carbon Fibre Reinforced Polymer is an effective technique for restoring monotonic capacity, but its effectiveness under cyclic loading requires further evaluation.

- Repair of concrete beams using Carbon Fibre Reinforced Polymer techniques increases the post-cracking stiffness and reduces the crack opening.

To the author's knowledge only limited studies addressing the impact of corrosion on the monotonic and fatigue behaviour of pretensioned concrete beams, reported in Section 2.5.2, are available in the literature. Also no research was found that addresses repair using externally bonded CFRP sheets to restore the fatigue capacity of corroded pretensioned concrete members, but rather literature found and reported in this chapter focused on strengthening of non-corroded members. The study presented in this thesis addresses this gap in the literature by investigating the flexural monotonic and fatigue behaviour of corroded pretensioned beams and their repair with CFRP sheets. This topic is of importance to extending the life of our aging bridge infrastructure.

Chapter 3
Experimental program

3.1 General

In this chapter, a description of the experimental program is given including: specimen fabrication, accelerated corrosion, CFRP repair, material testing, and monotonic and fatigue beam testing.

3.2 Testing Phase

Table 3-1 and Table 3-2 summarize the experimental program. The experimental program consists of the three phases described below.

3.2.1 Phase I

In Phase I ancillary tests were conducted with four objectives, (a) to investigate the rate of accelerated corrosion of the prestressing strands, (b) to quantify the distribution of the applied nominal tensile force among the seven wires within a single 7-wire strand, (c) to identify the material fatigue properties and the stress-strain behaviour of strand wires, and (d) to quantify the stress concentration factor in the prestressing strand due to corrosion.

To achieve Objective (a), strands were embedded in prisms (100 mm × 150 mm × 300 mm) constructed from 30 MPa concrete mixed with NaCl salt solution at a 2.1% chloride concentration by weight of cement. The strands had a 50 mm cover, and were not prestressed, Figure 3-1. Nine prisms were constructed and corroded to three corrosion levels (2.5%, 5%, and 10%). The galvanostatic accelerated corrosion approach was used, and the expected time to achieve the desired corrosion levels was calculated using Faraday's law. When the theoretical

corrosion levels were reached, the corroded strands were extracted from the prisms and a gravimetric mass loss analysis was conducted to determine the actual corrosion level achieved. Based on the difference between the theoretical and actual corrosion levels a correction factor was computed to account for the variation in the required time to achieve a specified corrosion in the strands.

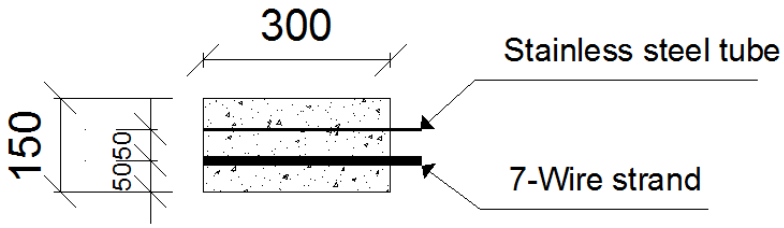

Figure 3-1 – Schematic of the concrete prisms

For the Objective (b), two 1 m long uncorroded 7 wire strands were tested under monotonic tensile loading with 2 mm strain gauges mounted on the six external wires at the same location along the strand's length (a total of 6 strain gauges per strand). Using the strain measurements, the force distribution between the external helical twisted wires and centre king wire were determined.

For the Objective (c), uncorroded 7-wire strands were unravelled and the centre wire was cut in 130mm long samples. A total of 23 samples were prepared and tested in fatigue under fully reversed loading (R = -1). To avoid buckling of the wire due to fully reversed loading, a ratio of diameter to free wire length of 2:1 was used. Moreover the free length was machined down gradually to 2 mm diameter to prevent buckling, ensure failure in the free length zone, and avoid

anchor failure by avoiding stress concentrations due to the sudden change in diameters, Figure 3-2. The samples were tested under different strain ranges. The results of the non-corroded samples are used to plot a strain versus number of cycles to failure (ε-N curve), which is used as the baseline data and is used to identify the material fatigue properties, and a stress versus strain curve that is used to describe the stress-strain behaviour of the wires.

Figure 3-2 – Machined single wire specimens for fatigue testing

For Objective (d) 60 corroded wire samples were divided into two groups of 30 samples per corrosion level. The samples were obtained as follows; four prisms (100 mm × 200 mm × 1000 mm) were constructed from 30 MPa concrete mixed with NaCl chloride solution at 2.1% chloride concentration by weight of cement. Each prism contained a single non-stressed prestressing 7-wire strand. Each prism was subjected to accelerated corrosion to achieve two corrosion levels (5% and 10% by mass loss). Upon completion of the corrosion process, the strands were extracted from the prisms, and the actual corrosion level was determined by gravimetric mass loss analysis. The corroded strands were unravelled to separate individual wires. A single one (1) metre of corroded strand when unravelled results in six (6) meters of corroded external helical wire. The corroded helical wire was cut into smaller samples. The centre (king) wire was disregarded as the more severe corrosion occurs on the external wires making them more critical to fatigue failure.

Table 3-1 –Ancillary testing program

Phase		Specimen Type	Number of Specimens	Corrosion Level	Testing Type
I	(a)	Prism (100 × 150 × 300 mm)	3	2.5%	Mass loss analysis
			3	5.0%	
			3	10.0%	
	(b)	7-wire strand (1000 mm)	2	0.0%	Monotonic (tensile)
	(c)	Single centre wire (200 mm)	14	0.0%	Fatigue (R = -1)
			9		+500 MPa mean stress
	(d)	Single external wire (200 mm)	30	5.0%	Fatigue (tension-tension)
			30	10.0%	

3.2.2 Phase II

Phase II aimed to quantify the effect of corrosion of a 7-wire steel strand on the monotonic capacity of pretensioned beams. This phase comprised of 12 T-beams. Details of the specimen design are given in Section 3.4. To facilitate the corrosion process the bottom central region (1 m × 0.15 m) of the beams was cast using salted concrete with 2.1% chloride concentration by weight of cement, while the rest of the beam was cast using unsalted concrete. This ensured that only the central tension region (1 m portion of the beam) corroded. The beams were subjected to accelerated corrosion to achieve three corrosion levels: low 2.5%, medium 5%, and high 10% of mass loss. Two beams were kept as controls (i.e. not corroded). Four beams were repaired using CFRP sheets following the medium and high corrosion exposure levels to examine the feasibility of using CFRP repair to restore the capacity of corroded pretensioned beams. All beams were tested under monotonic loading in four-point bending to failure to assess their flexural behaviour.

3.2.3 Phase III

Phase III investigated the fatigue behaviour of 25 pretensioned T-beams. The beams were constructed with the same beam dimensions and reinforcement details as those in Phase II (Details on specimen design are given in Section 3.4). The beams consisted of 15 non-repaired and 10 repaired beams. Five beams were left non-corroded and non-repaired to act as control beams. The remaining 20 beams were corroded to two corrosion levels (5% and 10% by mass loss) with 10 beams per corrosion level. At each corrosion level, five beams were corroded and were non-repaired, and five beams were corroded and repaired using CFRP sheets. Each set of five beams was tested in four point bending under fatigue loading at different stress ranges. The

data from this experimental phase is used to construct S-N curves under the different corrosion levels, and to verify the modelling results.

Table 3-2 –Beam testing program

Phase	Specimen Type		Number of Specimens	Corrosion level	Testing Type
II	12 × T-beam	8× non-repaired	2	0.0%	Monotonic (flexural)
			2	2.5%	
			2	5.0%	
			2	10.0%	
		4× repaired	2	5.0%	
			2	10.0%	
III	25 × T-beam	15× non-repaired	5	0.0%	Fatigue (flexural)
			5	5.0%	
			5	10.0%	
		10× repaired	5	5.0%	
			5	10.0%	

3.3 Beams Nomenclature

The beam nomenclature will consist of 5 parts, the first part refers to the test loading condition (ST: monotonic loading, FT: fatigue loading). The second part indicates the number of prestressing strands (1S: 1 strand, 2S: 2 strands), while the third part refers to the corrosion level in mass loss percentage (2.5%, 5%, and 10%). The fourth part specifies whether the member in repaired by CFRP sheets or not (NW: not wrapped, W: Wrapped). The fifth part indicates the configuration of the cathode (stainless steel tube), (SC: straight cathode, LC: L-shaped cathode). For example, S-2S-10%-W-SC, would indicate a beam tested monotonically prestressed using 2 strands, with a straight cathode corroded to 10% by mass loss, and then wrapped with CFRP sheets.

3.4 Beam Design

The beams had a T-beam cross section with the following dimensions: a flange of 400 mm width by 50mm thickness, a web height of 250 mm and a thickness of 100 mm. The T-beam cross section was chosen to represent a scaled down single-T standard bridge girder section from the (CPCI 2008). The beams were designed with a prestressing force of 70% of the ultimate tensile strength of the strand with an allowance for an estimated 10% losses in accordance with (CPCI 2008). Two configurations were designed; the first had a single strand at 60 mm from the bottom, while the second had two strands above one another with a 50 mm vertical spacing in-between. The prestressing force was transferred to the beams at a nominal concrete strength of 26 MPa. Figure 3-4 shows the beam dimensions and reinforcement details.

3.4.1 Concrete

Beams were constructed from 40 MPa concrete, with the concrete mix proportions presented in Table 3-3. The beams were manufactured at Hanson Pressure Pipe plant in Uxbridge, Ontario. The plant facilitated the use of their 40-foot long prestressing bed for pretensioning the strands and casting the T-beams.

Table 3-3 - Mix proportions for a 1m^3 batch

Cement (kg/m^3)	Sand (kg/m^3)	Coarse aggregate (kg/m^3)	HRWA (l/m^3)	Water (L)	w/c ratio
475	729	1009	2.8	184	0.39

3.4.2 Prestressing strands

Standard 7-wire low relaxation strands with a nominal diameter of 12.7 mm were used for prestressing. The strands were made from cold drawn steel and conform to (ASTM A416M 2010) with yield strength at a 1% extension equal to 90% of the specified minimum tensile strength. Strands in all beams had 60 mm of concrete cover, and for beams with two (2) prestressing strands; the vertical spacing was 50 mm. All beams were prestressed to 70% of the ultimate tensile strength of the 7-wire low relaxation strand. Beams were all designed in accordance to the Canadian Precast Prestressed Concrete Institute (CPCI) Design Manual 4. The beams design satisfied all the stress requirements at transfer to avoid cracking as the prestress was applied.

3.4.3 Non prestressed flexural reinforcement

Shrinkage and temperature steel were placed in the flange. Five-8 mm plain bars were placed in the longitudinal direction in the compression zone, and 8 mm bars at 150 mm o/c were placed in the transverse direction.

3.4.4 Shear Reinforcement

Single legged 15M (16 mm diameter) epoxy-coated stirrups at 75 mm spacing were used in the shear zones to prevent shear failure. No stirrups were placed in the constant moment zone.

3.5 Accelerated Corrosion

The accelerated corrosion used the galvanostatic approach. This approach applies an impressed constant electrical current due to an external power supply, which maintains a constant current during the corrosion period. To form an artificial corrosion cell, a stainless steel hollow tube with

8mm diameter was also embedded in the concrete and ran parallel to the prestressing strand. The prisms were connected to the external power supply, with the stainless tube connected to the negative terminal thus acting as the cathode, and the 7-wire strand connected to the positive terminal acting as the anode, as shown in Figure 3-3. In order to achieve a closed electrical circuit, the beam must be subjected to a moist environment to facilitate the conductivity between the anode and cathode. The impressed current density was set at 200 $\mu A/cm^2$ as recommended in the literature (El Maaddawy and Soudki 2003).

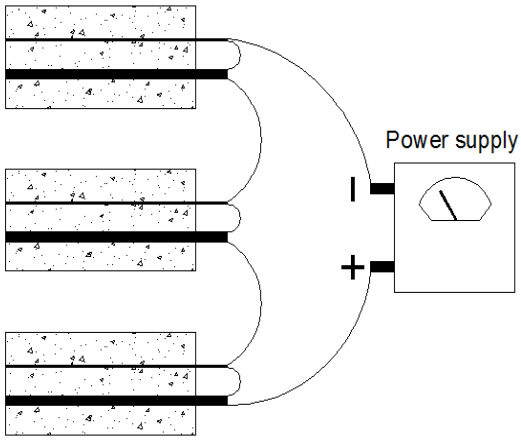

Figure 3-3 – Schematic of the corrosion electrical circuit

3.6 Beam Construction

Thirty-seven (37) pretensioned beams were constructed in an off-campus precast plant that offered the use of their prestressing equipment for pretensioning the beams. Five steel forms were fabricated for casting; as a result four pours were carried out to cast all twelve beams. The beams had the same concrete dimensions; however, six beams had one prestressing strand and six beams had two strands. The prestressing strands were low relaxation 7-wire strands with a

nominal diameter of 12.7 mm, and a nominal tensile capacity of 1860 MPa. All strands were prestressed to 70% of their ultimate tensile capacity (128.9kN or 1302 MPa). The reinforcement configuration was described in Section 3.4 and shown in Figure 3-4.

The steel forms were put together along the prestressing bed, then the steel cages were dropped in and the 7-wire strand was fed through the three forms, Figure 3-5. The strand was then prestressed and the prestressing force was locked by prestressing wedge anchors, see Figure 3-6. The middle 1000 mm long × 150 mm high portion of the beams were cast first using the salted concrete mixed with NaCl solution to achieve a 2.1% chloride concentration by cement weight. Once the salted portion of the beams (1000 × 150 mm) were cast, the rest of the beams were cast with regular concrete and consolidated and then the plastic dividers used to confine the salted concrete were removed, Figure 3-7.

Beams were steam cured for 24 hours after which standard concrete cylinders (100 mm × 200 mm) were tested for compressive strength. At a nominal compressive strength of 26 MPa after 24 hours the prestressing force was transferred to the beams by cutting the strand. Table 3-4 summarises the compressive strength at transfer for each pour.

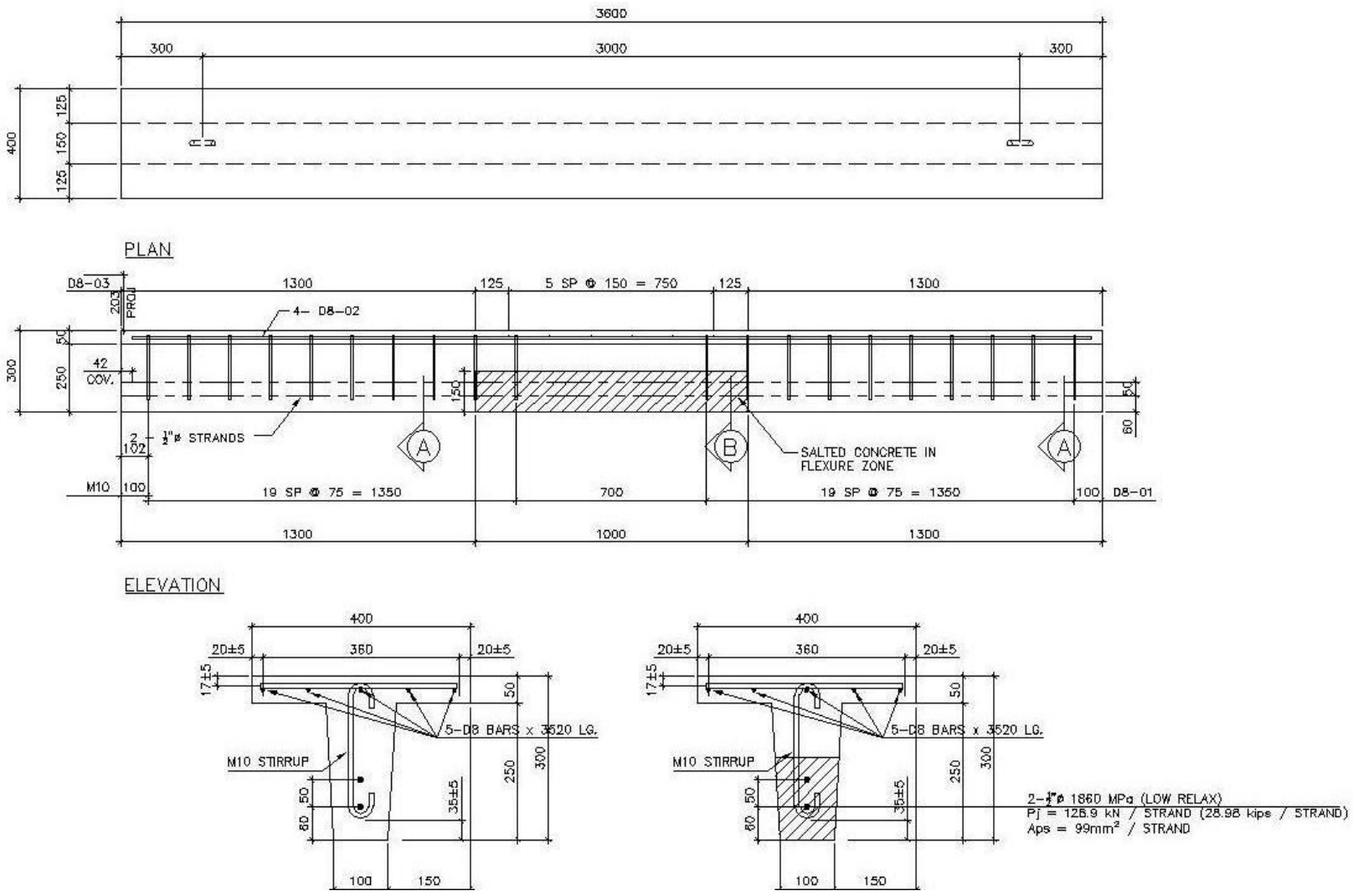

Figure 3-4 – Beam dimensions and reinforcement details

Figure 3-5 – Beam forms along the prestressing bed

Figure 3-6 – Prestressing wedge anchor

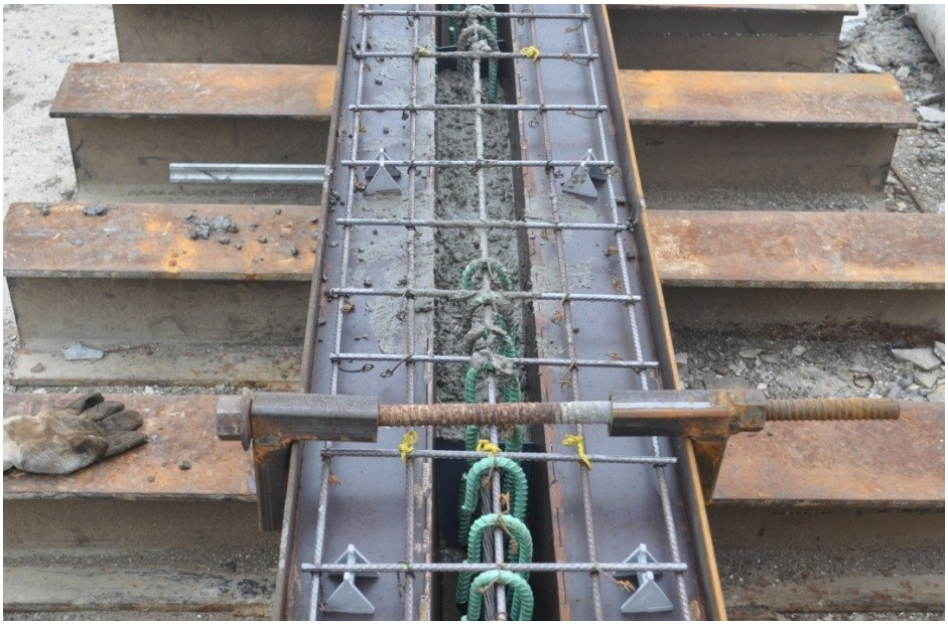

Figure 3-7 – Salted portion of the beam

Table 3-4 – Average concrete compressive strength at transfer

	Concrete compressive strength at transfer (MPa)	
1st pour	28.20 ± 1.12	Beams prestressed with a one strand
2nd pour	26.35 ± 0.49	
3rd pour	30.10 ± 1.56	Beams prestressed with a two strand
4th pour	28.15 ± 0.07	

3.7 Mass Loss Analysis

Gravimetric mass loss measurements were carried out in accordance to (ASTM G1 2003). This was done following testing of the beams to determine the actual corrosion level reached in the strands versus the theoretical corrosion level imposed using accelerated corrosion. This is a destructive approach as it requires the beam to be broken and concrete removed to expose the corroded steel strands. Then samples are cut from the corroded strand. The samples were weighed and cleaned; the difference in weight before and after corrosion gives the percentage of mass loss.

3.8 Carbon Fibre Reinforced Polymer (CFRP) repair

Fourteen beams were repaired using CFRP sheets after the completion of the accelerated corrosion duration and prior to load testing. The type of CFRP sheet used was SikaWrap® Hex 230C, a unidirectional Carbon Fibre fabric that is used in conjunction with Sikadur® 330 epoxy resin.

Table 3-5 gives the mechanical properties of cured SikaWrap® Hex 230C laminate with Sikadur® 330 epoxy as published by the manufacturer.

Table 3-5 – Cured CFRP laminate properties with Sikadur® 330 epoxy

	Tensile strength (MPa)	Modulus of elasticity (MPa)	Tensile elongation (%)	Thickness (mm)
SikaWrap® Hex 230C	894	65,087	1.33	0.381

All 14 repaired beams had the same CFRP repair configuration. The unrepaired beams were expected to fail in flexure, and corrosion was expected to cause a reduction in load bearing capacity. The repair configuration was designed to restore the reduction in load bearing capacity. A 100mm wide×0.38mm thick flexural CFRP sheet was applied to the soffit of the beam in the longitudinal direction. In addition, two U-wraps were applied at the location of the loading points to provide confinement to the concrete in the corroded zone, and two more U-wraps were placed at the beam-ends to prevent delamination of the flexure sheet. The orientation of the fibres of the flexure sheet was in the longitudinal direction (parallel to the prestressing strand), while for the U-wraps the fibres were oriented in the direction transverse to the prestressing strand. Figure 3-8 shows a schematic of the CFRP repair configuration, while Figure 3-9 shows the beams after CFRP repair application.

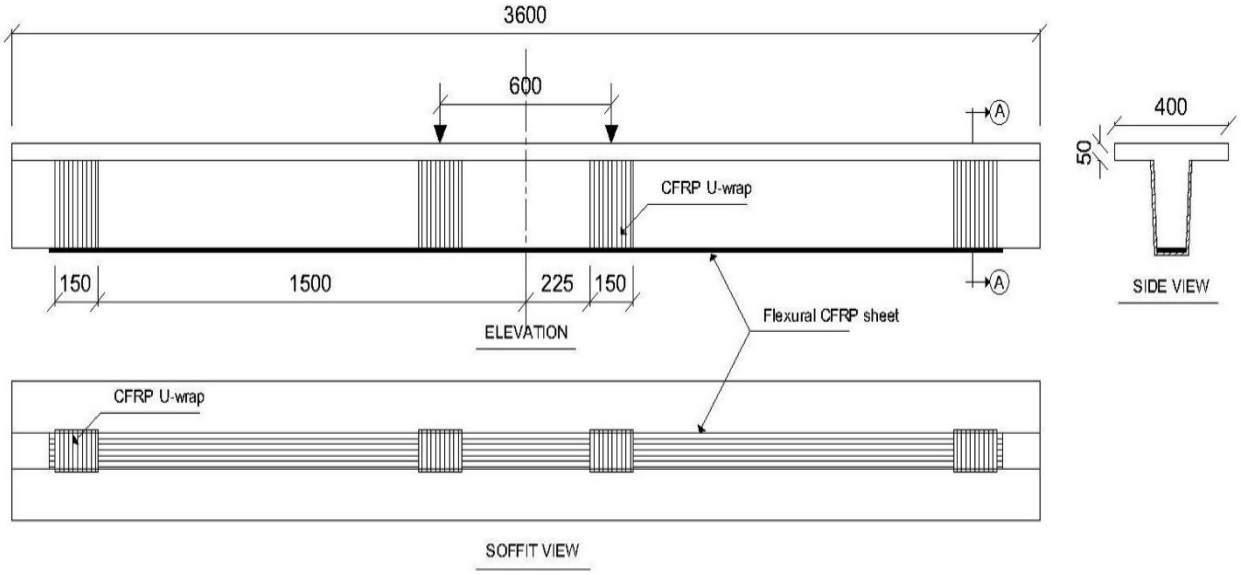

Figure 3-8 – CFRP sheets repair configuration

Figure 3-9 – Beams after application of CFRP sheet repair

3.9 Test setups

This section describes the test equipment, instrumentation, and test procedure for each test.

3.9.1 Ancillary tests

Tensile monotonic test setup for 7-wire strands

Standard monotonic tension test standards for multiwire strands (ASTM A1061M 2009; ASTM A931 2008) were adopted for the test setup and gripping of the strand. The strands were tested under tensile monotonic load in a closed loop servo-hydraulic MTS test frame equipped with the MTS controller-Flextest GT and a double ended MTS-244 actuator with 500 mm (20 inches) of stroke and a capacity of 500 kN (112 Kips). The strands were tested in load control at a rate of 40 kN/min. A total of 12 - 2 mm strain gauges were mounted on 6 external wires of a strand at two different locations. The tests were controlled using a Multipurpose TestWare (MPT) environment with TestStar control software. Figure 3-10 shows the test setup and instrumentation for tensile monotonic test setup of 7-wire strands.

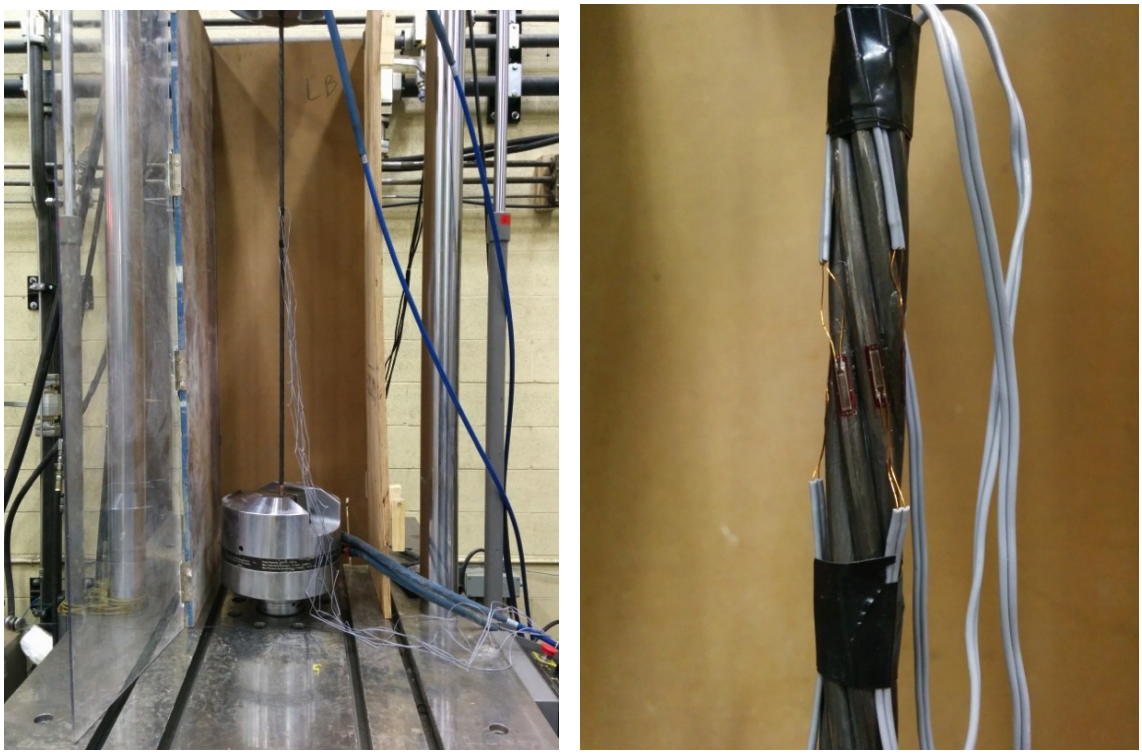

(a) (b)

Figure 3-10 – Monotonic test setup and instrumentation of 7-wire prestressing strand

Single wire fatigue test setup

These tests were carried out to determine the effect of corrosion on the fatigue life of a single prestressing wire characterised by the notch factor (K_t). Fatigue tests were carried out using an MTS servo-controlled closed-loop electro-hydraulic testing machine with a process control computer controlled by FLEX software to output constant strain and stress amplitudes in the form of sinusoidal waves. This setup was used for testing Phases II and (d). Phase II tests on samples of uncorroded centre wires was carried out in fully reversed strain control. At the beginning of each test it was determined whether the cyclic stress- strain response of the material was elastic for the specified strain range. If it was elastic the test was run in load control. If it was

not the test was run in strain control. The stress-strain limits for each specimen were recorded at logarithmic intervals throughout the test via a peak reading oscilloscope. Phase I (d) tests on corroded external wires were in stress control under tension-tension cyclic loading. Failure of a specimen for strain control was defined as a 50 percent drop in the tensile peak load from the peak load observed at one half the expected specimen life. Failure of a specimen for stress control was defined as the separation of the specimen into two pieces. Run-out tests were limited to 5 million cycles (10 million reversals). The loading frequency varied from 0.5 Hz to 3 Hz for strain control and from 40 to 80 Hz for load control.

3.9.2 Monotonic beam test setup

All beams were tested in four-point bending in a four post testing frame. The load was applied by a servo-hydraulic actuator of 280 kN capacity with a stroke of 250 mm, and controlled by a 407 Material Testing System (MTS) controller. Figure 3-11 shows a schematic of the test setup. The monotonic loading was applied in displacement control at a rate of 1mm/min. Failure during monotonic beam tests was defined by prestressing strand rupture or concrete crushing accompanied by a 20% drop in load.

Instrumentations for the monotonic beam tests included a Linear Variable Differential Transducer (LVDT) to measure the midspan deflection. Crack opening measurements within the constant moment zone were monitored using LVDTs mounted across three cracks, Figure 3-12. This was achieved as follows; the beams were loaded to initiate cracking; the first three cracks within the constant moment zone were marked. The beams were then unloaded and three - ½ inch (12.7 mm) LVDTs were placed, one across each crack. The beams were then reloaded to failure at a rate of 1 mm/min while the LVDTs captured crack opening measurements. The

concrete compression strain was measured by a 60 mm concrete strain gauge mounted onto the top concrete surface at midspan.

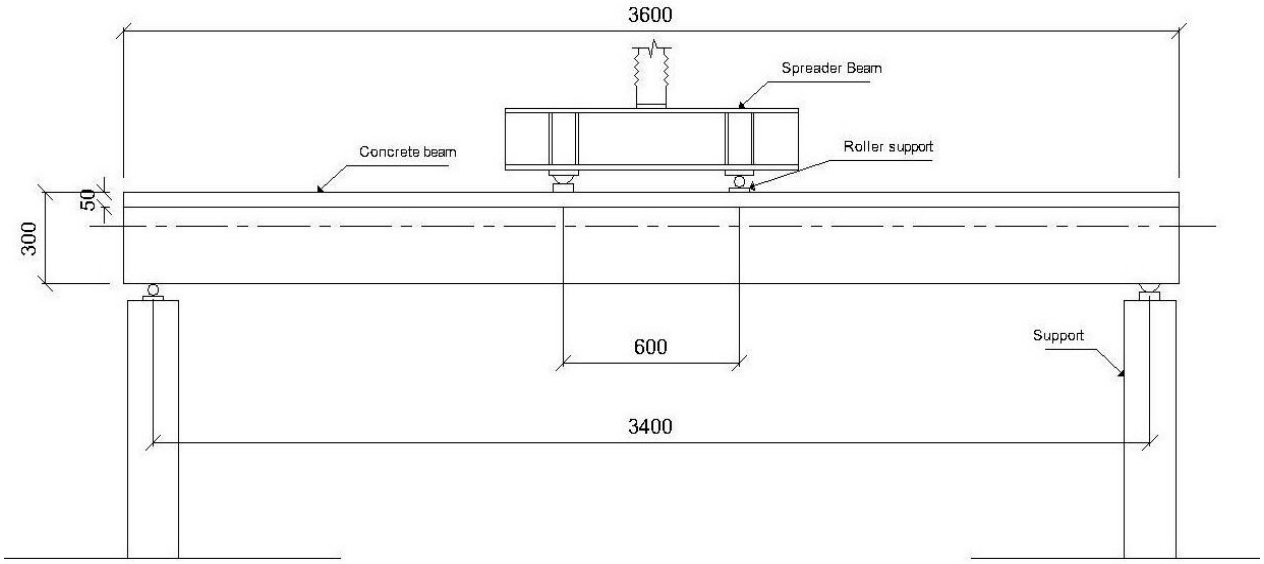

Figure 3-11 – Schematic of beam test setup in four-point bending configuration

The average tension strain at the concrete surface was also measured using a 500 mm long OSMOS fibre optic sensor (FOS) placed on the web at the location of the embedded prestressed strand, Figure 3-13. For beams wrapped with CFRP sheets, two 5 mm strain gauges were installed on the flexural CFRP sheet at midpoint in the longitudinal direction. A National instruments data acquisition system was used to acquire all measurements.

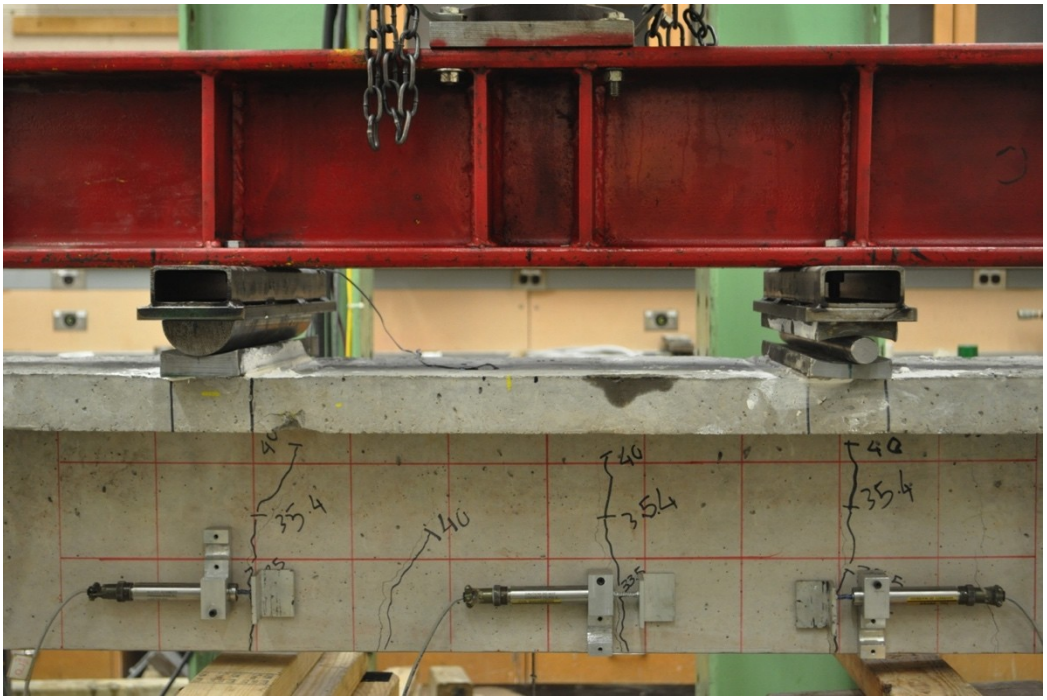

Figure 3-12 – LVDTs for crack opening measurements

Figure 3-13 – OSMOS FOS across flexure zone for average strain readings at the level of the strand

3.9.3 Fatigue beam test setup

The test setup for the fatigue test was identical to that of the monotonic test, however, the fibre optic sensors were not used during the fatigue testing.

In this study the fatigue loading was applied as a load range between maximum and minimum load values that were calculated as a percentage of the ultimate monotonic load capacity. Fatigue tests were conducted in load control at a frequency of 1 Hz for the higher load ranges (short fatigue lives) and 2.5 Hz for the lower load ranges (long fatigue lives). The reason for lower cycling frequencies for short fatigue lives was to allow the hydraulics actuator to accurately meet the specified higher load range; however, the difference in cycling frequencies from 1 to 2.5 Hz does not have any impact on the testing results. At the start of the test the maximum load was applied manually then decreased to the mean load, after which the 407 Material Testing System (MTS) controller took over and started cycling at the chosen frequency. The load range and cycling frequency for each test after the first were selected based upon the result of the fatigue test. The aim was to have a uniform logarithmic distribution of fatigue lives with only the lowest load range as a run out, i.e. no failure at 1 million cycles.

Instrumentation for the fatigue beam test included: external LVDT(s) monitoring the midspan deflection (Figure 3-14) and the flexure crack opening widths (Figure 3-16), a 280 kN load cell to monitor the applied load, a 60 mm strain gauge that monitored the compressive strain at the concrete's top fibre (Figure 3-15), and two 10 mm strain gauges at mid-span to monitor the tensile strain in the CFRP sheets. A national instruments data acquisition system (DAQ) was used to record all the instruments' readings. Fatigue tests were stopped upon rupture of the prestressing strand, concrete crushing, or after recording more than one million cycles.

Figure 3-14 – Midspan deflection measurement by an external LVDT

Figure 3-15 – 60 mm strain gauge to monitor the concrete compressive strain

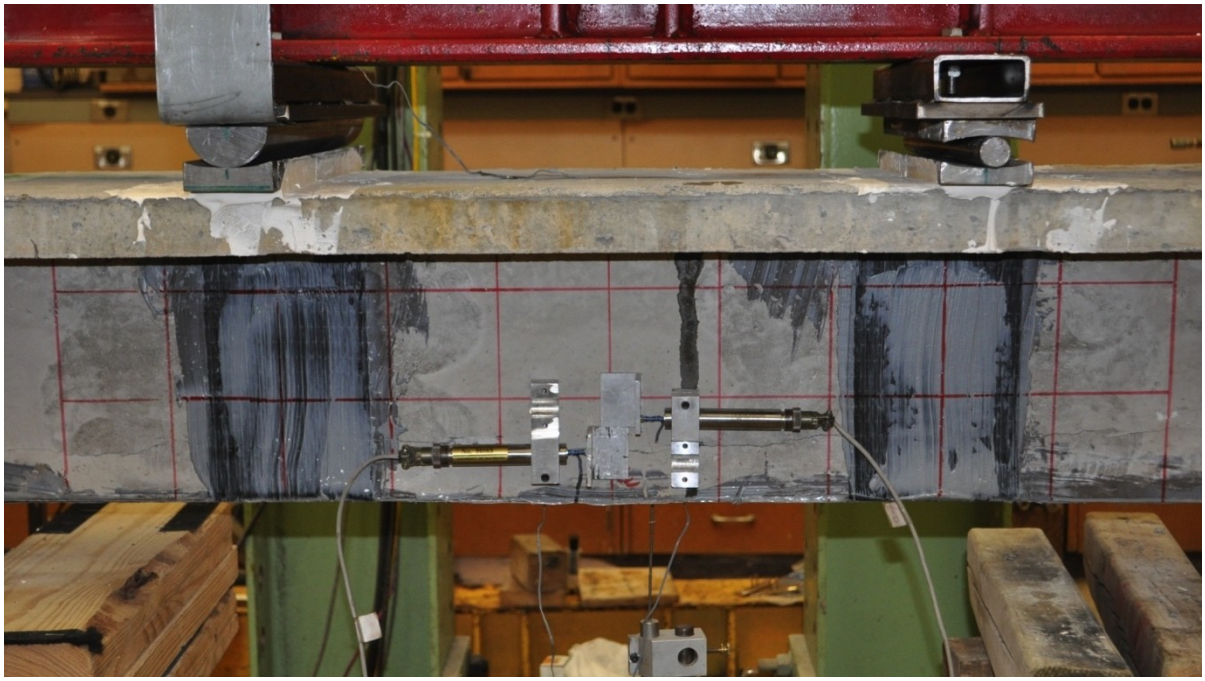

Figure 3-16 – External LVDTs monitoring flexure cracks width

Chapter 4

Experimental Results

This chapter details the experimental results of the present study.

4.1 Ancillary Testing – Phase I (a)

This series of tests aimed at investigating the relationship between the experimental and the theoretical corrosion mass loss based on Faraday's law. The test series comprised of 9 concrete prisms measuring 100 mm × 150 mm × 300 mm with one embedded non-stressed prestressing 7-wire strand with a nominal diameter of 12.7 mm, Figure 3-1. The prisms were constructed from 30 MPa concrete, mixed with a NaCl salt solution to achieve a 2.1% chloride concentration by cement weight. They were constructed and subjected to galvanostatic accelerated corrosion with an impressed current density of 200 $\mu A/cm^2$ as described in Section 3.5.

The prisms were placed inside an enclosed corrosion chamber with misting nozzles located at the top of the chamber to ensure the presence of moisture and oxygen during the accelerated corrosion process. The nozzles were connected to water and pressurized air supplies to create the misting effect. Three corrosion levels (2.5%, 5%, and 10% mass loss) were used, and the time required to reach those levels with an induced current density of 200 $\mu A/cm^2$ was calculated using Faraday's law. Upon completion of the accelerated corrosion process, the 7-wire strands were extracted from the prisms and a gravimetric mass loss analysis was conducted to determine the actual corrosion level achieved.

4.1.1 Gravimetric mass loss analysis

A mass loss analysis was carried out in accordance with (ASTM G1 2003). The standard specifies six cleaning procedures for steel and iron, out of which only two are applicable at room temperature. Procedure C.3.5 was used, which uses a solution of 500 mL hydrochloric acid with 3.5 g of hexamethylenetetramine and 500 mL of reagent water. The samples are submerged in the solution for a minimum of 10 minutes, then cleaned with water and wire brushed. The cleaning cycles are repeated with the samples being dried and weighted after each cleaning cycle until the weight remains constant, and the mass loss percentage is then calculated. It is worth noting that there was no significant difference in the actual mass loss due to corrosion between the cleaned strand as a whole and the cleaned strand as individual wires. This is explained due the vast majority of the rust products are accumulated on the external surface of the strand. Adham clarify Figure 4-1 shows a corroded 7-wire prestressing strand before and after cleaning as part of the gravimetric mass loss analysis.

(a) Extracted strand (b) Strand after mass loss analysis

Figure 4-1 - 7-wire strand (a) before and (b) after cleaning showing pitting at a 5% mass loss

The results of the mass loss analysis showed that Faraday's law over estimates the duration required for a 2.5% mass loss, but can reasonably predict the duration for a 5% mass loss, and underestimates the duration for a 10% mass loss. Based on these findings it was decided to decrease the corrosion duration for the 2.5% specimens and increase the corrosion duration of the 10% specimens by 25% of the theoretical required corrosion duration given by Faraday's law. The 25% change in corrosion duration is equal to the difference between the theoretical and actual corrosion levels observed.

4.2 7-Wire Strand Monotonic Testing - Phase I (b)

The purpose of this testing was to quantify the variation in stress distribution amongst the individual wires of the 7-wire strand. This variation occurs as a result of the inter-wire friction and the helical twist angle. The testing procedures were carried out as described in Section 3.9.1 of this thesis. Standard monotonic tension tests of multi-wire strands (ASTM A1061M 2009; ASTM A931 2008) were adopted for the test setup and gripping of the strand. The strands were tested in load control at a rate of 40 kN/min.

Quantifying the individual wire load carrying contribution is important as beam failure initiates by single wire(s) rupture inside the concrete beam. This is more common in corroded beams due stress concentrations at pitting locations, which is discussed in further detail in the beam test results Section 4.4. The knowledge of the individual wire load carrying contributions, primarily that of the external wires versus the centre/internal one is important to identify the stresses in each wire, which is important when modelling their behaviour.

To acquire this data, individual external wire strains were monitored and recorded via 2mm strain gauges mounted on each wire. Figure 4-2 shows the test setup and instrumentation for the tensile monotonic test setup for the 7-wire strands. By knowing individual wire strain, wire diameter, and modulus of elasticity the load carrying distribution amongst individual wires can be calculated.

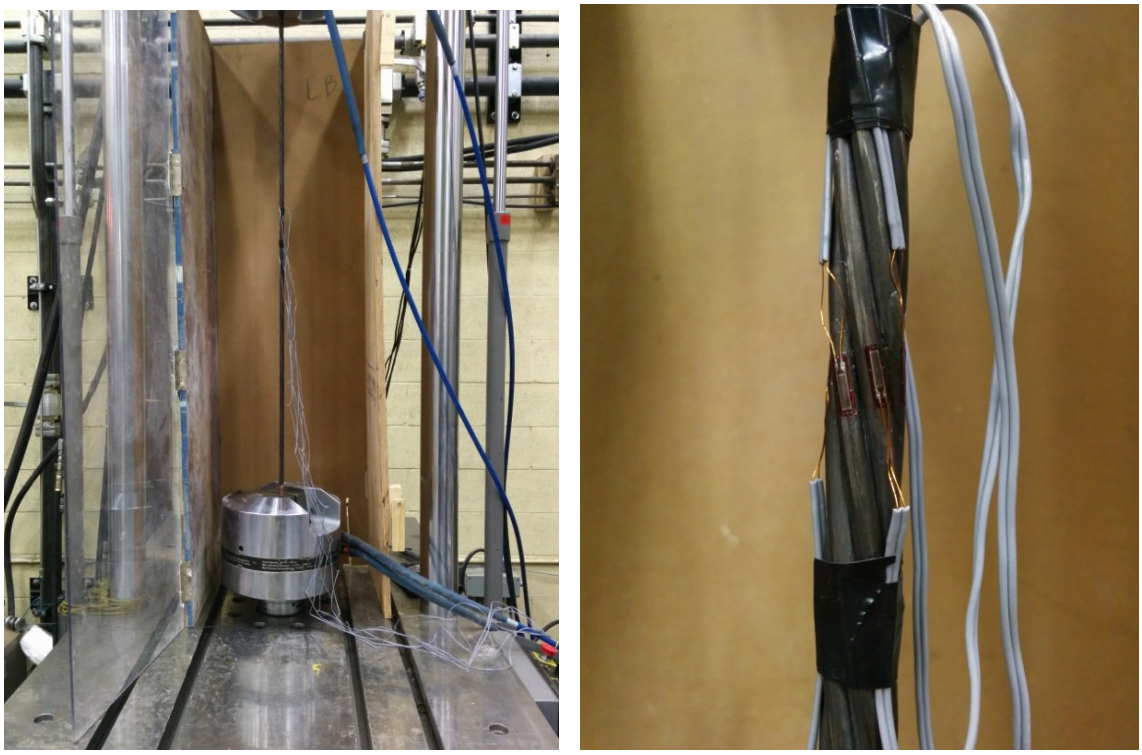

(a) (b)

Figure 4-2 – Monotonic test setup and instrumentation of 7-wire prestressing strand

The following figures present the measured and observed response from individual wires and the strand as a whole. All external six (6) wires responded in a similar fashion. Figure 4-3 shows the load versus measured tensile strain for each external wire. The strain distribution amongst the six external wires was fairly uniform with no significant variations. In addition, the overall strand

elongation was measured, which when used to calculate the overall strand strain would yield a slightly higher value than the local strain readings for the individual wires, this is possibly due to unaccounted for seating in the gripping anchor. Figure 4-4 presents the applied load versus measured overall strand elongation.

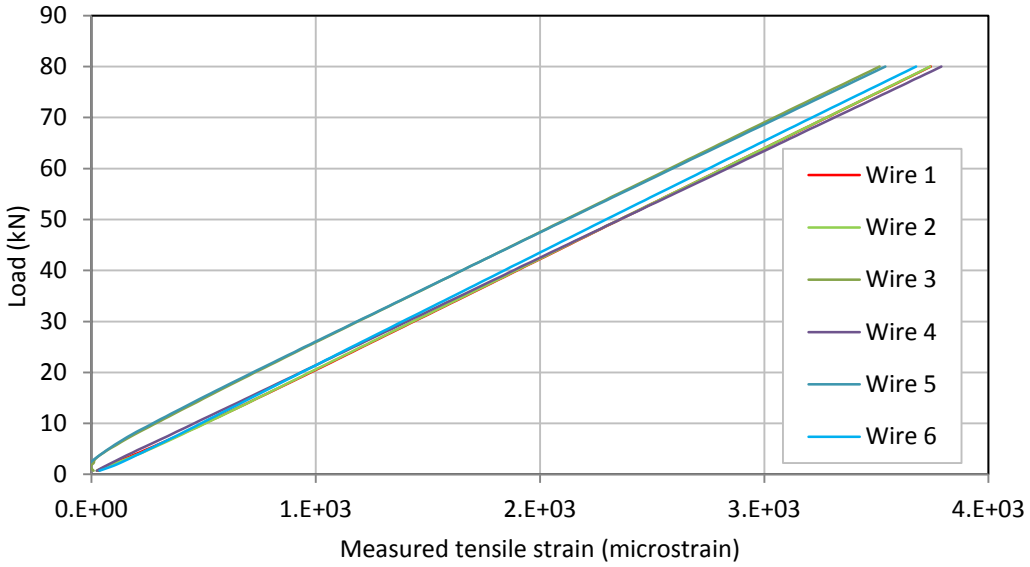

Figure 4-3 – Applied load versus individual external wire measured tensile strain

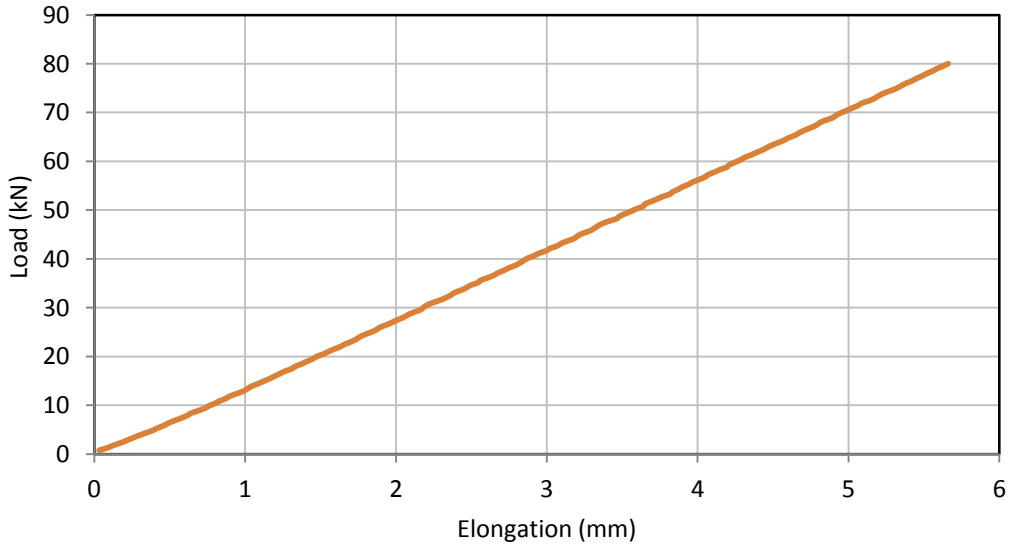

Figure 4-4 – Applied load versus 7-wire strand elongation

The measured strain for each individual external wire was used to calculate the applied stress in each wire, which in turn was used to calculate the load carrying contribution of individual wires. It is worth noting, that this does not account for twisting of the external wires or bending stress induced by elongation of the helix, however, their impact on the longitudinal tensile strains is not expected to be significant.

The load carrying contribution of the centre (king) wire was calculated by simply subtracting the summation of the external wires' load carrying capacity from the total applied load. Figure 4-5 presents curves of the applied wire load versus individual load carrying contributions as a percentage of the total applied load versus the applied load. It is observed that initially almost 35% of the load is carried by the centre wire, while two of the external wires combined only contributed to less than 20%. As the applied load is increased the load carrying contributions of the external wires converges on an average value of 12-13%. This is caused by the seating, elongation, and change in helix angle of the helically wrapped external wires as they become fully engaged. Figure 4-6 presents the average load carrying contribution of individual wires.

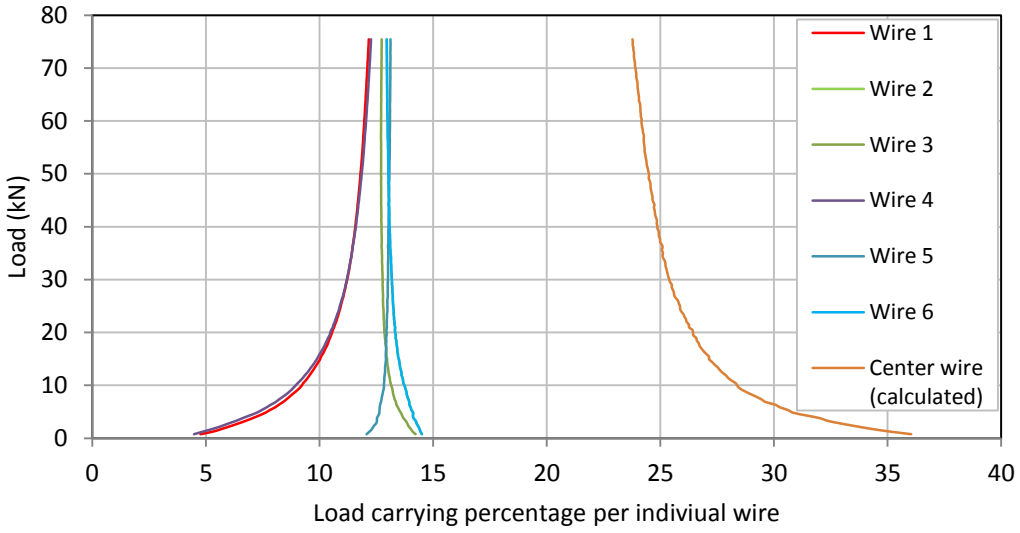

Figure 4-5 – Applied load versus load carrying capacity per individual wire

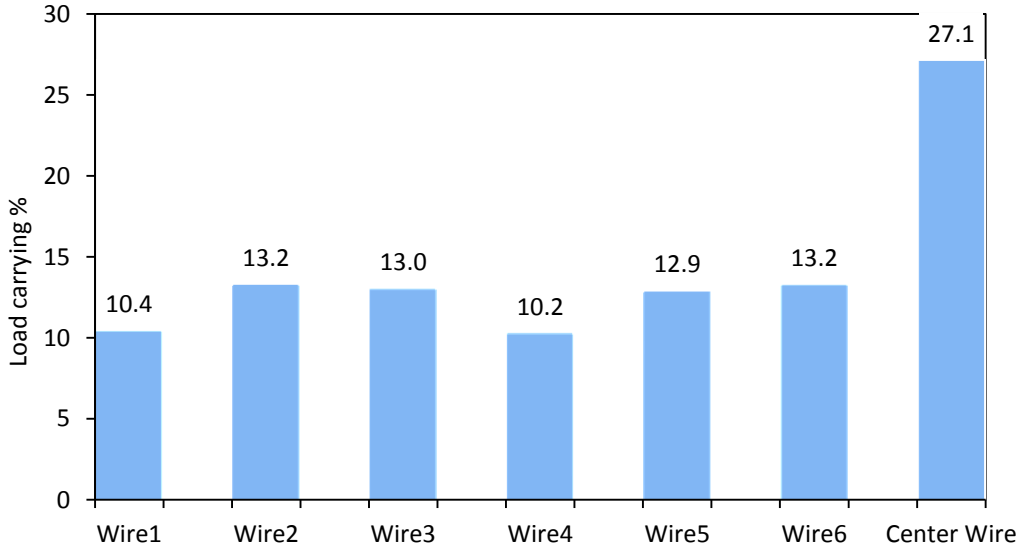

Figure 4-6 – Average load carrying contributions per wire as a percentage of the total load

4.3 Material Fatigue Testing – Phase I (c) and (d)

These tests were carried out to determine the fatigue properties as well as the effects of mean stress and corrosion on the fatigue life of a single prestressing wire. Fatigue tests were carried out using the test setup described in Section 3.9.1. Phase II, testing of uncorroded centre wire specimens were carried out in strain controlled fully reversed cycling loading, in addition, a set of specimens were tested with a positive mean stress to evaluate the effect of mean stress on the material fatigue behaviour. Phase I (d) testing on corroded external wires was run in load control under tension-tension cyclic loading. Tests for both testing Phases II and (d) ran at cyclic frequencies varied from 0.5 Hz to 3 Hz for strain controlled tests and from 40 to 80 Hz for load controlled tests.

Phase I (c)-Testing of uncorroded centre wire

A total of (25) uncorroded centre wire samples where machined as described in Section 3.2.1. Two (2) samples where monotonically tested in tension to identify the monotonic material response and identify elastic and plastic loading zones. Twenty-three (23) specimens were tested under cyclic loading; fourteen (14) samples were tested under fully reversed (R=-1, zero mean stress) cyclic loading, and nine (9) samples were tested with an average positive mean stress of 500Mpa.

Table 4-1 – Breakdown of actual number of uncorroded samples tested for material properties

25 samples	2	Monotonic tension tests
	14	Zero mean stress cyclic loading
	9	Positive mean stress cyclic loading

Monotonic tension test results

The monotonic response was typical of ductile metals, with an initial linear elastic zone, followed by yielding of the material, and a nonlinear plastic zone. The recorded ultimate capacity was approximately 2150 MPa, which is higher than the nominal ultimate capacity of 1860 MPa reported by the manufacturer. Also Rockwell Hardness Test was done and the average material hardness was found to be 53 HRC.

Fatigue test results

A total of 23 samples were test under cyclic loading with variable strain ranges to produce a strain range versus number of cycles (ε-N) curve. The fatigue behaviour of the uncorroded samples showed no significant scatter. Moreover, the set of nine (9) specimens tested with an average applied positive mean stress of 500 MPa showed no significant variation from the fourteen (14) samples tested at zero mean stress. Figure 4-7 presents a fatigue life versus strain amplitude curve, while Figure 4-8 shows the fatigue life versus stress amplitude curve for both sets of fatigue test specimens.

Table 4-2 summarizes the testing parameters and test results for uncorroded centre wire specimens. Specimens were tested to cover a range of fatigue lives between 500 and 10 million reversals (250 to 5×10^6 cycles). Based on the cyclic/fatigue testing data the cyclic material and fatigue properties for low relaxation 7-wire prestressing strands were calculated and are presented in Table 4-3. Figure 4-9 presents the experimental monotonic and cyclic true stress/strain response of the material, along with a fitted cyclic response. As expected the monotonic and cyclic responses are the same within the elastic region, and diverge beyond it due to cyclic softening the of the material.

Table 4-2 – Summary of cyclic testing data of non-corroded centre wire samples

#	Diameter	Life		Stress Amplitude	Mean Stress	Strain Amplitude	Notes
	(mm)	Cycles	Reversals	(MPa)	(MPa)	(%)	
1	2.01	755	1510	1532	57	1.263	
2	1.97	3673	7346	1339	39	0.861	
3	2.00	5000000	10000000	821	0	0.411	Runout
4	1.95	5000000	10000000	864	0	0.432	Runout
5	1.93	619021	1238042	882	0	0.441	
6	2.02	5000000	10000000	936	0	0.468	Runout
7	2.05	40882	81764	1154	9	0.577	
8	2.01	8263	16526	1276	9	0.727	
9	2.01	10517	21034	1248	0	0.757	
10	2.03	13597	27194	1205	37	0.602	
11	1.97	647	1294	1476	177	1.460	
12	1.93	15981	31962	1169	144	0.585	
13	2.04	5000000	10000000	1028	0	0.514	Runout
14	2.04	1480	2960	1487	55	1.172	
15	1.96	99491	198982	1014	398	0.507	
16	1.98	208477	416954	955	507	0.477	
17	1.94	114724	229448	822	619	0.411	
18	1.91	5000000	10000000	785	555	0.393	Runout
19	2.04	5000000	10000000	835	523	0.418	Runout
20	1.95	4580	9160	1266	301	0.732	
21	2.05	5006	10012	1073	600	0.729	
22	2	252	504	1275	559	0.769	
23	1.91	4183	8366	1236	524	0.618	

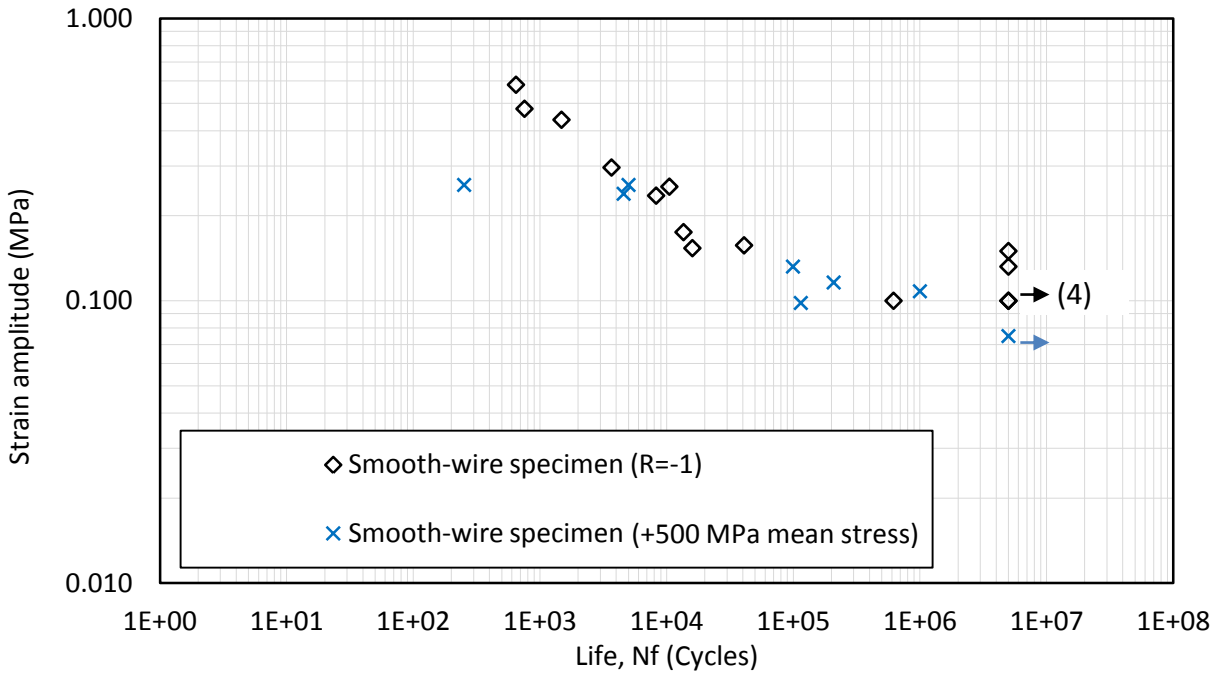

Figure 4-7 – Fatigue Life versus strain amplitude of uncorroded centre wire samples

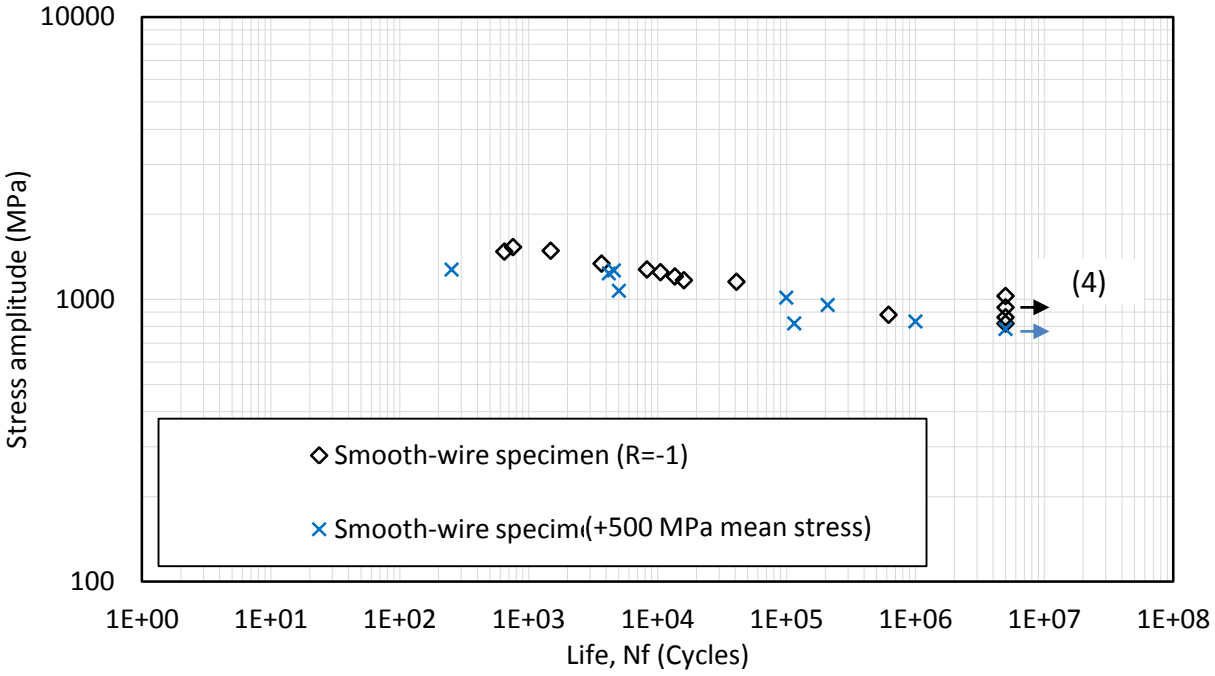

Figure 4-8 – Fatigue Life versus stress amplitude of uncorroded centre wire samples

Table 4-3 – Cyclic material properties of low relaxation 7-wire prestressing strands

Cyclic Properties	
Cyclic Yield Strength, (0.2% offset)	1338.5
Cyclic Strength Coefficient, K'	2415.6
Cyclic Strain Hardening Exponent, n'	0.095
Fatigue Strength Coefficient, (σ')	2329
Fatigue Strength Exponent, b	-0.061
Fatigue Ductility Coefficient, (ε')	1.09
Fatigue Ductility Exponent, c	-0.707
Cyclic Elastic Modulus (MPa)	196000

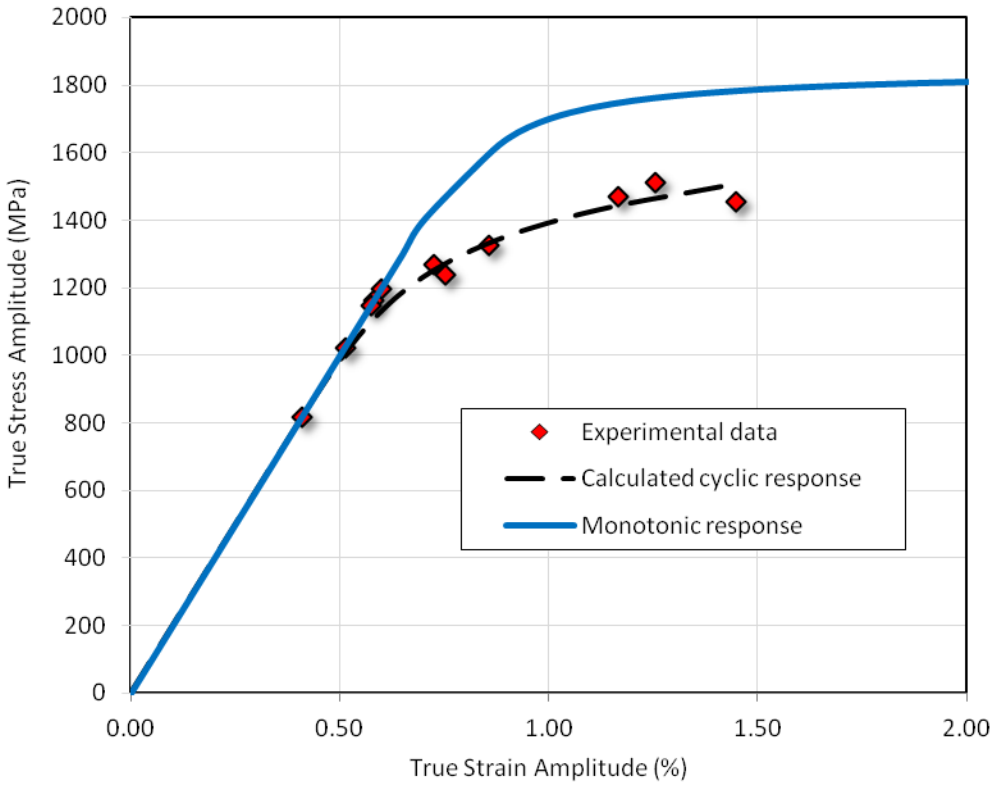

Figure 4-9 – True strain amplitude versus true stress amplitude response for uncorroded centre wire sample

Phase I (d)-Testing of corroded external wire

All corroded external wire samples were prepared as described in Section 3.2.1. Initially a total of 30 samples per corrosion level were planned to be tested, however, after a mass loss analysis was conducted on an extracted corroded sample it was noted that the targeted corrosion levels were not achieved. The set of samples that aimed to achieve 5% corrosion by mass loss had exhibited a higher average corrosion level of 8% by mass loss, while the second set achieved the required average 10% corrosion by mass loss. This presented the problem of two corrosion levels that were too close to each other that the inherent scatter of the amount of corrosion may result in an overlap between results. Therefore the complete set of thirty (30) specimens at an 8% corrosion were tested, followed by testing of enough specimens of the 10% corrosion level set to verify our expectation that the two corrosion levels were close enough that the fatigue results would overlap/

A total of twenty-nine (29) specimens corroded to 8% by mass loss, and seven (7) samples corroded to 10% by mass loss were tested. The two sets of experimental results (for the specimens at an 8% and a 10% corrosion by mass loss) did not exhibit a significant difference, between them as the 10% corrosion specimens' results fell close to the scatter band of the 8% corrosion results but with a slightly higher mean level at long fatigue lives – an unexpected result.

At short fatigue lives the effect of the corrosion was not evident as the high stress amplitude governs the life of the material due to global high plastic strains. However, for medium to long life tests the effect of corrosion is apparent. This is attributed to stress raisers due to corrosion pitting which amplifies the lower nominal applied stress amplitude. The observation described

above can be clearly identified when comparing the fatigue response of non-corroded and corroded specimens. Figure 4-10 compares the stress amplitudes versus fatigue life curves for the entire life range of the specimens tested; including both corroded and uncorroded samples. Table 4-4 summarizes the testing parameters and results for corroded external wire samples tested under cyclic fatigue loading.

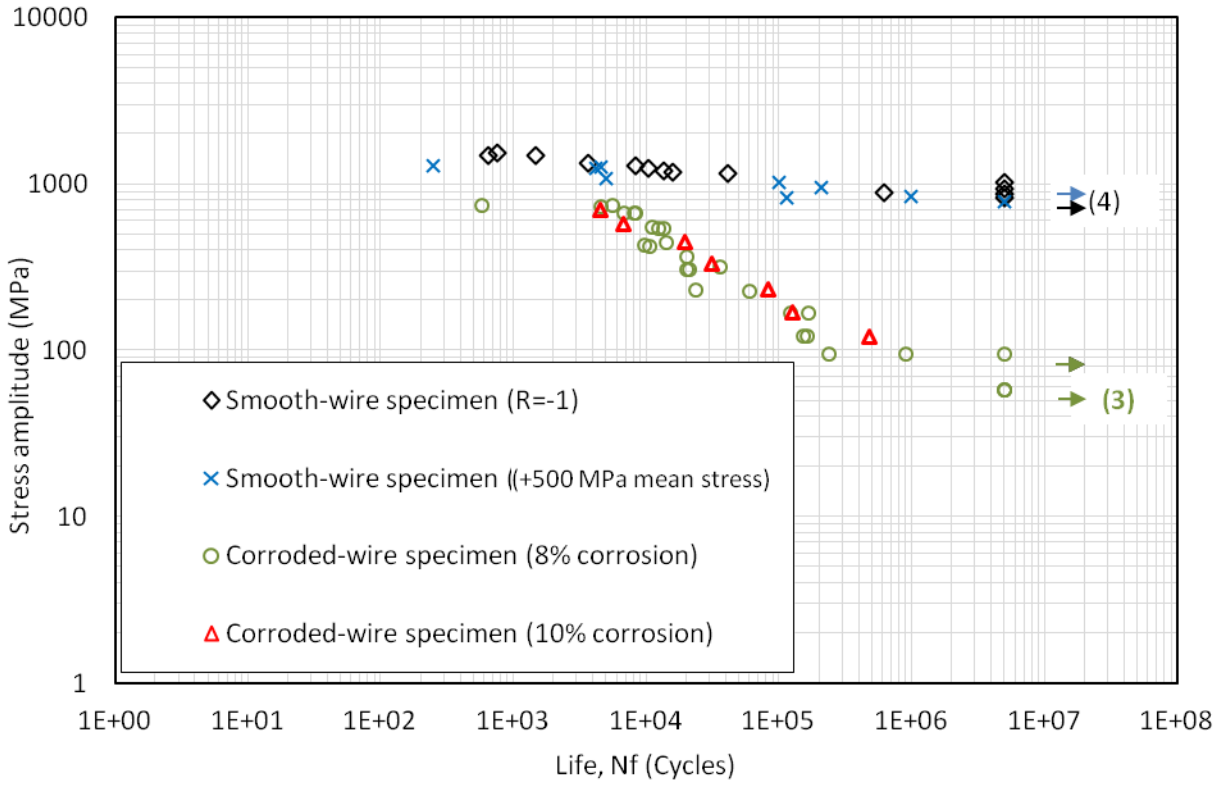

Figure 4-10 – Stress amplitude versus life for all material samples

Table 4-4 – Summary of cyclic testing data for corroded external wire samples

	SP #	Dia.* (mm)	Life (cycles)	Reversals	Stress				Notes
					Max (MPa)	Min (MPa)	Amplitude (MPa)	Mean (MPa)	
8% Corrosion by Mass Loss	1	3.8	5582	11164	1394	38	678	716	
	2	3.8	8402	16804	1413	191	611	802	
	3	3.8	6793	13586	1413	191	611	802	
	4	3.8	10740	21480	1394	630	382	1012	
	5	3.8	20288	40576	1413	745	334	1079	
	6	3.8	35973	71946	1423	850	286	1136	
	7	3.8	60242	120484	1413	1003	205	1208	
	8	3.8	154590	309180	1423	1203	110	1313	
	9	3.8	5000000	10000000	1413	1241	86	1327	Runout
	10	3.8	13550	27100	1394	411	492	902	
	11**	3.8	0.5	1	1413	1241	86	1327	
	12	3.8	581	1162	1413	57	678	735	
	13	3.8	14077	28154	1413	611	401	1012	
	14	3.8	21144	42288	1413	859	277	1136	
	15	3.8	23790	47580	1413	993	210	1203	
	16	3.8	162224	324448	1423	1203	110	1313	
	17	3.8	8175	16350	1413	191	611	802	
	18	3.8	9753	19506	1394	611	392	1003	
	19	3.8	20485	40970	1413	859	277	1136	
	20	3.8	168174	336348	1404	1098	153	1251	
	21	3.8	121646	243292	1404	1098	153	1251	
	22	3.8	238535	477070	1413	1241	86	1327	
	23	3.8	909585	1819170	1413	1241	86	1327	
	24	3.8	5000000	10000000	1413	1308	53	1361	Runout
	25	3.8	12349	24698	1385	411	487	898	
	26	3.8	5000000	10000000	1413	1308	53	1361	
	27	3.8	11140	22280	1404	401	501	902	
	28	3.8	5000000	10000000	1413	1308	53	1361	Runout
	29	3.8	4620	9240	1385	48	668	716	
10% Corrosion by Mass Loss	1	3.7	19329	38658	1394	611	392	1003	
	2	3.7	30795	61590	1404	821	291	1112	
	3	3.7	81800	163600	1366	955	205	1160	
	4	3.7	6643	13286	1375	372	501	874	
	5	3.7	470596	941192	1451	1241	105	1346	
	6	3.7	4468	8936	1380	162	609	771	
	7	3.7	125497	250994	1385	1089	148	1237	

**Reduced average diameter based on mass loss analysis*

***Outlier*

4.4 Monotonic Beam Testing

The monotonic testing phase of the experimental program (Chapter 3) was comprised of 12 T-beams. It is worth noting that the location of the stainless steel tube (cathode) differed in the first pour from the remaining three. The first and second pours were for prestressed beams using two strands. The first pour consisted of three beams with a straight stainless steel tube running in between and parallel to the prestressing strands; the cathode was inserted from one beam end and terminated at the opposite end of the corrosion zone. For the remaining pours all beams had an L-shaped stainless steel tube that entered the beam vertically from the top just before the corrosion zone, then ran horizontally above and parallel to the prestressing strand(s), and terminated at the opposite end of the corrosion zone, see Figure 4-11.

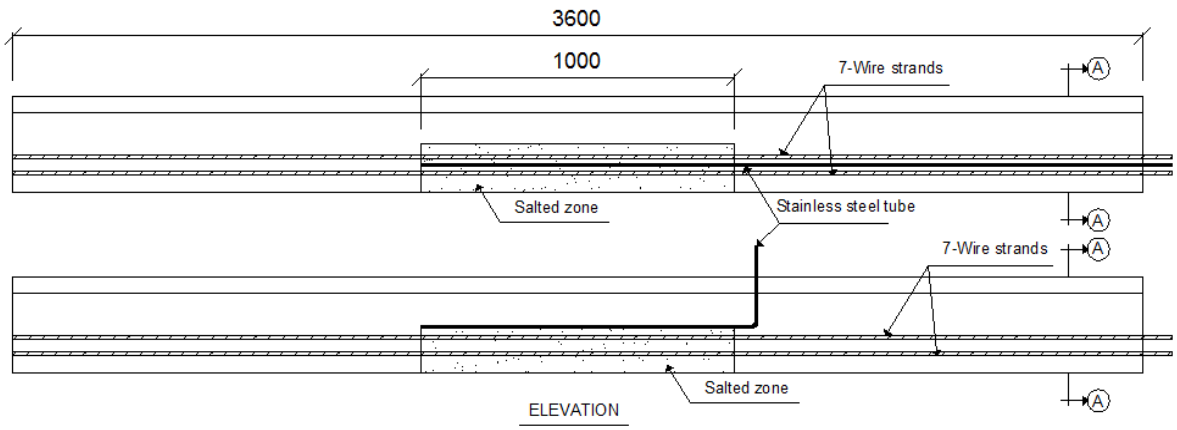

Figure 4-11 – Stainless steel tube configurations for the beams with two prestressing strands

4.4.1 Accelerated corrosion results

The beams were transported back to the structure's laboratory at the University of Waterloo where they were placed in an enclosed corrosion chamber 28 days after casting. Ten (10) beams where connected to power supplies in the same manner as described in Section 3.5, with an

impressed current density of 200 $\mu A/cm^2$. Three corrosion levels of 2.5%, 5%, and 10% were targeted. Two control beams remained uncorroded, one prestressed beam had a single strand while the other beam had 2 prestressing strands. Figure 4-12 shows the typical corrosion induced crack pattern for beams with one and two strands. The width of corrosion cracks at midspan was monitored and recorded during the corrosion period; Figure 4-13 shows the corrosion induced crack width measurements at midspan for beams with one and two strands. It is apparent that the variation of corrosion crack width is nonlinear with mass loss. As expected, higher crack widths were measured for the two strand beams versus the one-strand beams. Cracks were stable (no significant increase in width) up to 2.5% mass loss and then exhibited a sharp increase in rate of growth in width between 2.5% and 6%, and grew in width at a decreased rate afterwards.

During the accelerated corrosion process it was noticed that the corrosion cracking for beams with two prestressing strands varied from one beam to the other, indicating that the beams were not corroding uniformly. Based on the observed cracking width, and by comparison to crack width for beams with a single prestressing strand, it was deduced that the targeted theoretical 5% corrosion level was not achieved. As a result of this observation it was decided that all remaining beams with the 2 strands would be exposed to accelerated corrosion with a targeted 10% mass loss. After completion of the corrosion process the six beams with 2 strands had reached the following actual corrosion levels; 1 beam at 0%, 1 beam at 2.5%, and 4 beams at 10%.

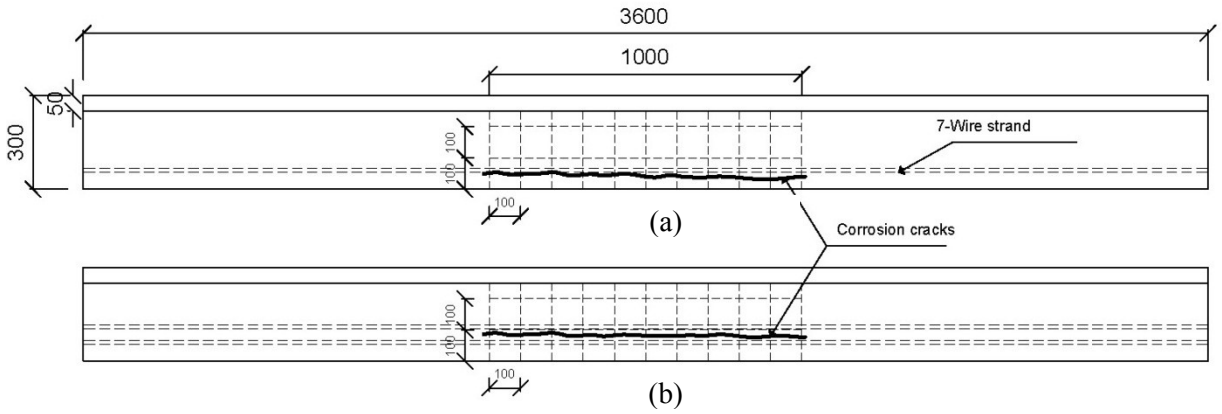

Figure 4-12 – Typical corrosion induced cracking in (a) beams with a single strand, and (b) beams with two strands

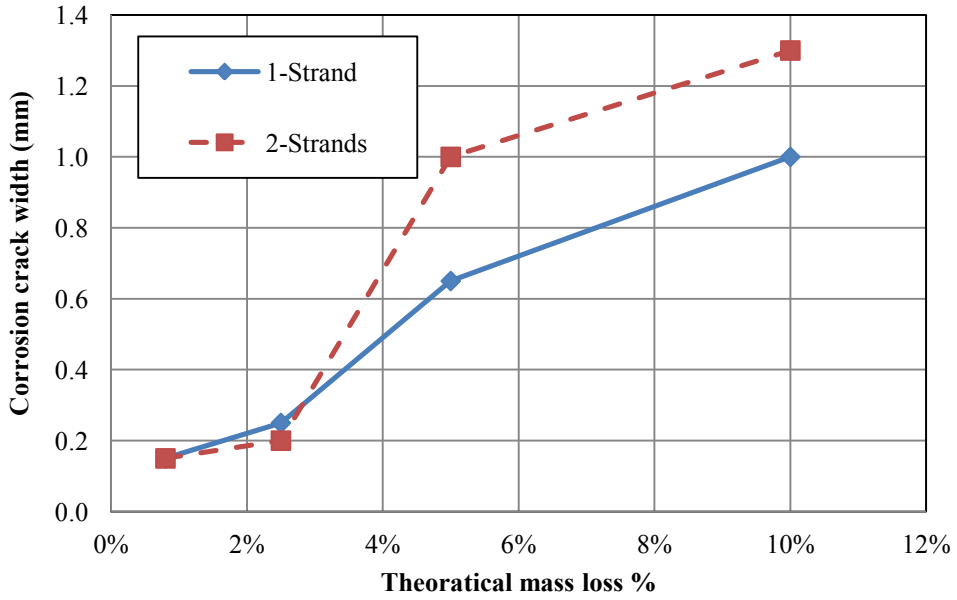

Figure 4-13 – Corrosion induced crack measurements at midspan

4.4.2 Monotonic test results

Twelve (12) beams were divided into two groups; six beams were prestressed using one 7-wire strand, and six beams were prestressed using two strands. The purpose of having two sets of

specimens with different prestressing configurations was to examine the effect of the number of strands, if any, on the corrosion mechanism. Prior to monotonic testing, concrete cylinders were tested for compressive strength. The beams were tested under monotonic loading in four point bending. The tests were carried out in displacement control at a loading rate of 1mm/min. During testing the applied load, the mid span deflection, the crack opening, and the concrete compressive strain were recorded. In addition to the monitored testing parameters listed above, LVDTs were mounted on the prestressing strand at the beam-ends, Figure 4-14, to confirm that no end slip occurred during testing. All beams failed in flexure by strand rupture, except for one (1) beam prestressed by two (2) prestressing strands that failed by concrete crushing. A detailed discussion of the failure modes in presented later in this chapter.

Figure 4-14 – LVDT mounted at beam end to monitor end slip of prestressing strand

Beams prestressed with a single 7-wire strand

Six beams were prestressed with a single 7-wire strand: one uncorroded (control beam) and five corroded beams. The experimental results for their monotonic tests were reported by El Menoufy and Soudki (2014). Table 4-5 summarizes the test results for beams prestressed with a single strand. The load deflection response of the control (uncorroded) beam was typical of a prestressed beam with a distinct change in stiffness beyond the cracking load.

The load versus deflection curve of the control beam agreed well with the theoretical elastic response calculated based on the effective moment of inertia (ACI 318M-08 2008; CPCI 2008), Figure 4-15. The control beam had an internal linear load-deflection response with a distinct change in slope (stiffness) at cracking, followed by a gradual transition into a non-linear response. The beam did not exhibit a distinct yield plateau; this was expected, as prestressing strands do not have a yield plateau. On the other hand, the corroded beams had an initial linear load-deflection response that transitioned into a non-linear one with no distinct change in slope (stiffness) at the cracking load.

Figure 4-16 shows load versus midspan deflection results for beams prestressed with a single strand at different corrosion levels (0%, 2.5%, 5%, and 10%). The stiffness of the beams was not affected by corrosion. However, the cracking load, the ultimate load and the midspan deflection at failure of the beams decreased as the corrosion level increased. The ultimate load capacity and deflection of the corroded beams were compared to those of the control beam. The beam with a 2.5% corrosion level exhibited a 6.56% reduction in ultimate load and a 26.39% reduction in midspan deflection at failure, while the beam with a 5% corrosion level had a 9.93% and a 44.43% reduction in ultimate load and midspan deflection, respectively. The beam with a 10%

corrosion level had a reduction of 26% in the ultimate load and a 76% reduction in ultimate midspan deflection.

Table 4-5 – Monotonic testing result summary of beam prestressed with single strand

Corrosion level	Concrete Strength (MPa)	Cracking		Ultimate			
		Load (kN)	Deflection (mm)	Load (kN)	% Reduction in load	Deflection (mm)	% Reduction in deflection
0.0%	48.69 ± 3.49	33.6	3.0	65.3	-	141.4	-
2.5%	48.69 ± 3.49	31.4	2.9	61.0	6.6%	104.1	26.4%
5.0%	49.89 ± 4.66	24.0	2.0	58.8	9.9%	78.6	44.4%
10.0%	49.89 ± 4.66	23.0	1.8	48.3	26.0%	33.3	76.4%

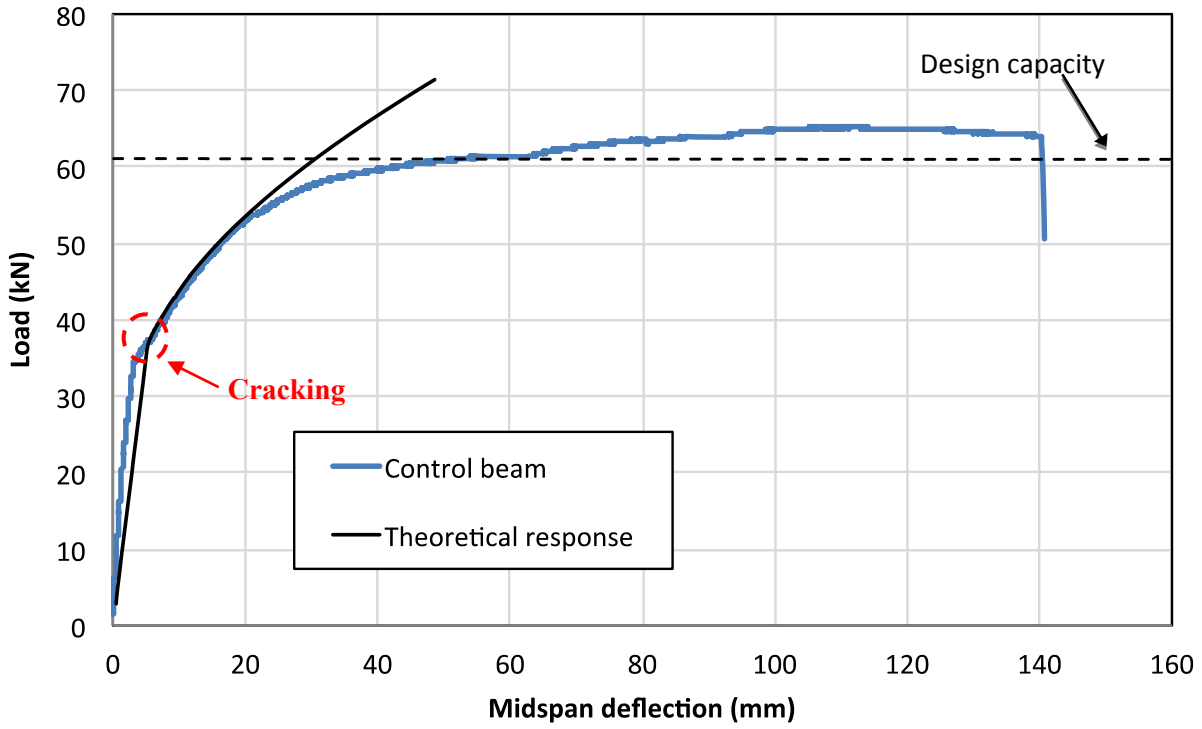

Figure 4-15 – Experimental vs. theoretical elastic deflection response for beams with one strand

The concrete midspan compressive strain was recorded and had a typical trend; increasing as the midspan deflection increased. In addition, the ultimate midspan deflection and the concrete compressive strain at failure decreased with higher corrosion levels. Beams with 2.5% and 10% corrosion levels exhibited a 26.87% and a 53.79% reduction in concrete compressive strain at failure respectively, which correlates well with the reduction in midspan deflection. However, the beam with a 5% corrosion level exhibited a reduction of 19.67% in concrete compressive strain versus a 44.43% decrease in midspan deflection. Figure 4-17 presents the applied load versus measured midspan concrete compressive strain for beams with different corrosion levels. Table 4-6 summarizes the measured ultimate concrete compressive strain.

Table 4-6 – Summary of the measured ultimate concrete compressive strength for beams with a single prestressing strand

Corrosion level	Ultimate			
	Compressive strain	% Reduction in concrete compressive strain	Deflection (mm)	% Reduction in deflection
0.0%	2069	-	141.4	-
2.5%	1513	26.9%	104.1	26.4%
5.0%	1662	19.7%	78.6	44.4%
10.0%	956	53.8%	33.3	76.4%

The crack opening widths of the first three (3) flexure cracks were measured, and the cumulative crack opening width versus load results are presented in Figure 4-18. In addition, the average tensile strain within the centre 600 mm constant moment zone was measured by an OSMOS Fiber Optic Sensor (FOS) and is plotted against the applied load in Figure 4-19. The FOS was damaged during testing of the control beam and no average tensile strain was recorded. As anticipated the average tensile strain at the prestressing strand level decreased with an increased corrosion level, due to the decrease in monotonic load capacity.

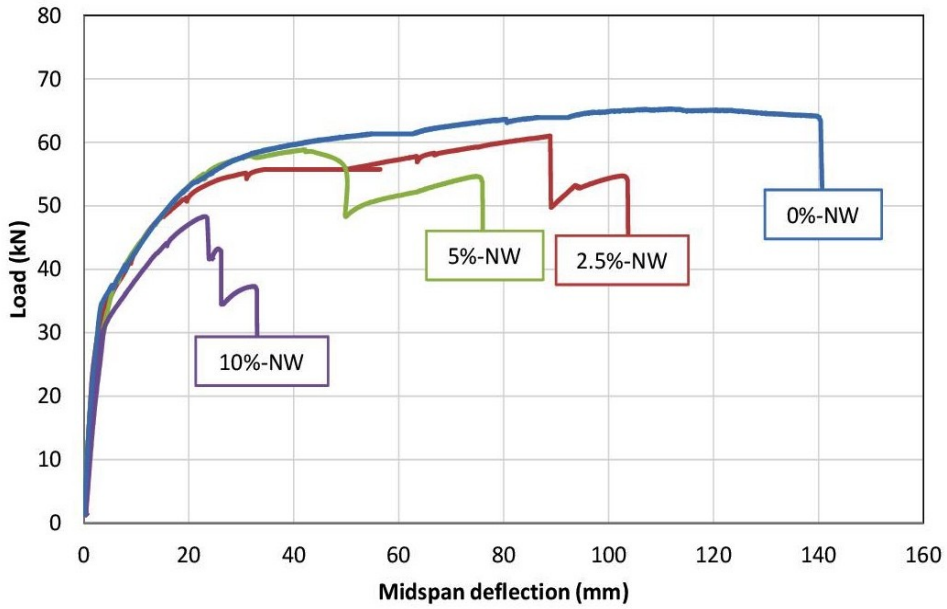

Figure 4-16 – Load vs. midspan deflection at different corrosion levels for beams with one strand

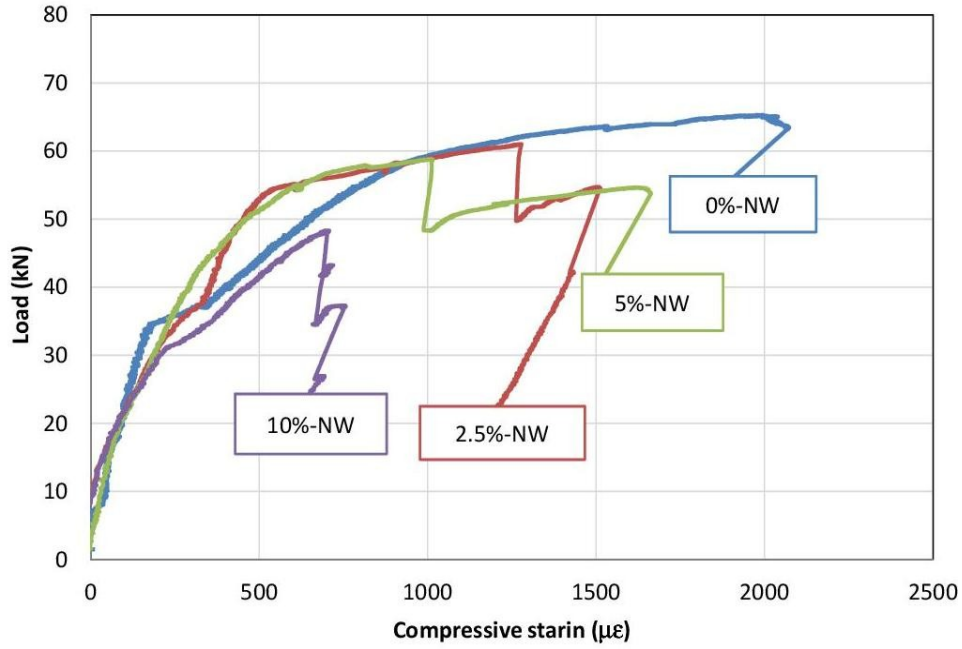

Figure 4-17 – Load vs. midspan concrete compressive strain at different corrosion levels for beams with one strand

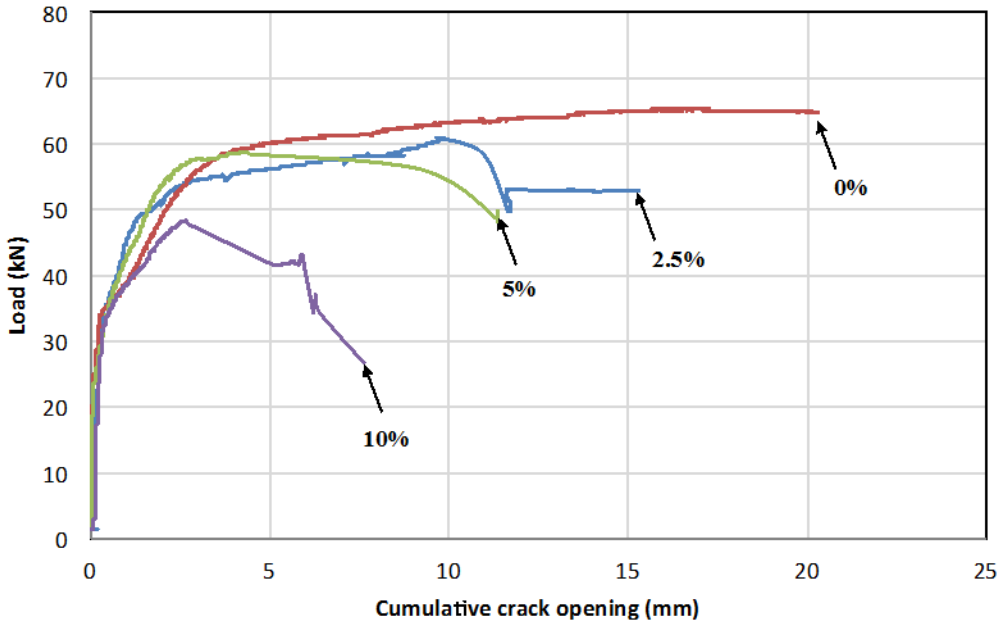

Figure 4-18 – Cumulative crack opening within the constant moment zone vs. load

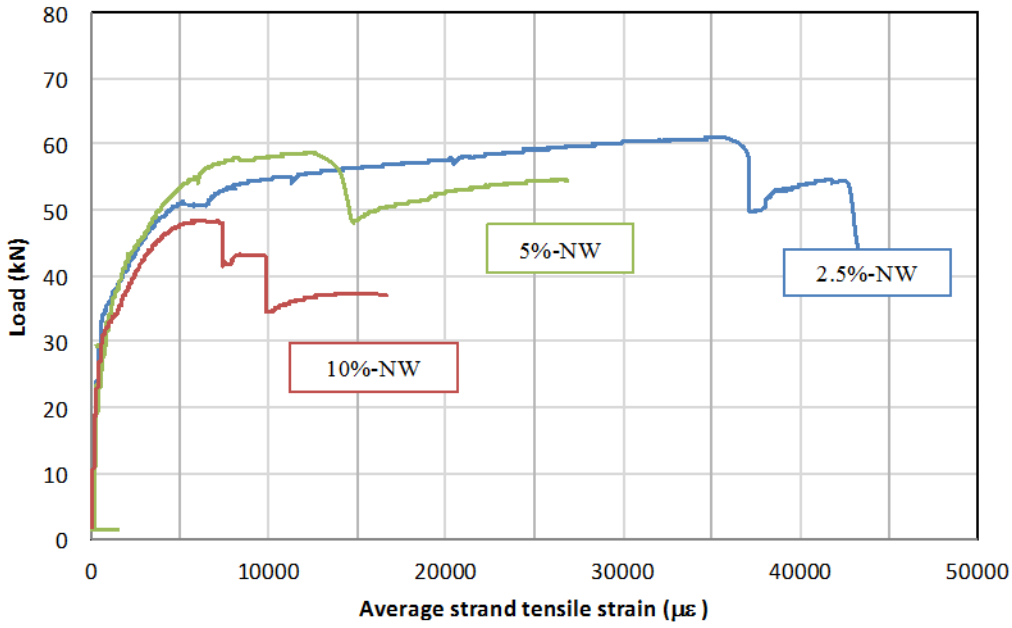

Figure 4-19 – Average tensile strain at the level of the strand vs. load at different corrosion levels

It is worth noting that the cracking pattern was observed to be a fairly uniform and equally spaced flexural cracking along the beam in the uncorroded beams, Figure 4-20. A similar pattern was observed for the corroded beams with the addition of a distinct corrosion induced longitudinal crack along the location of the prestressing strand. However, flexure cracks were not vertically continuous, as they shifted location below and above the horizontal corrosion crack, Figure 4-21.

This indicates slip/movement between the strand and concrete along the horizontal plane of the corrosion crack. This can also be observed when comparing the interfacial concrete/steel surface above and below the prestressing strand. The concrete below the strand separates (spalls off) from the strand upon loading and therefore the strand imprint can be seen to be intact, Figure 4-22, on the other hand, the concrete above the strand remains in contact with the strand and differential movement along the interface causes the imprint to be reduced to a smooth surface, Figure 4-23.

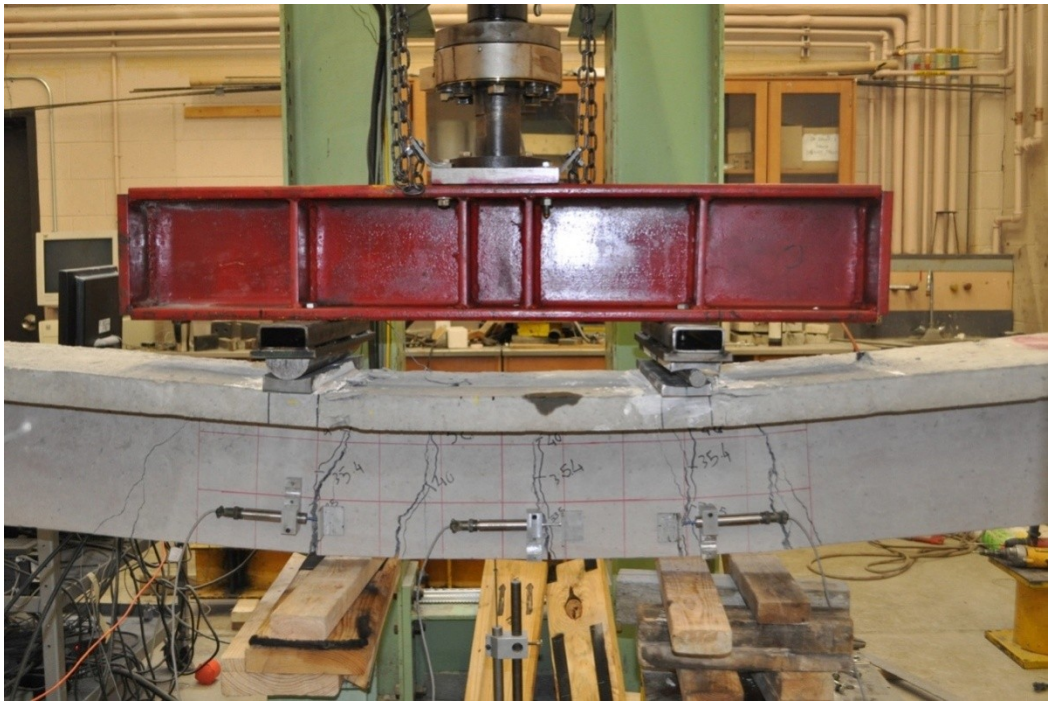

Figure 4-20 – Cracking pattern at failure for an uncorroded beam

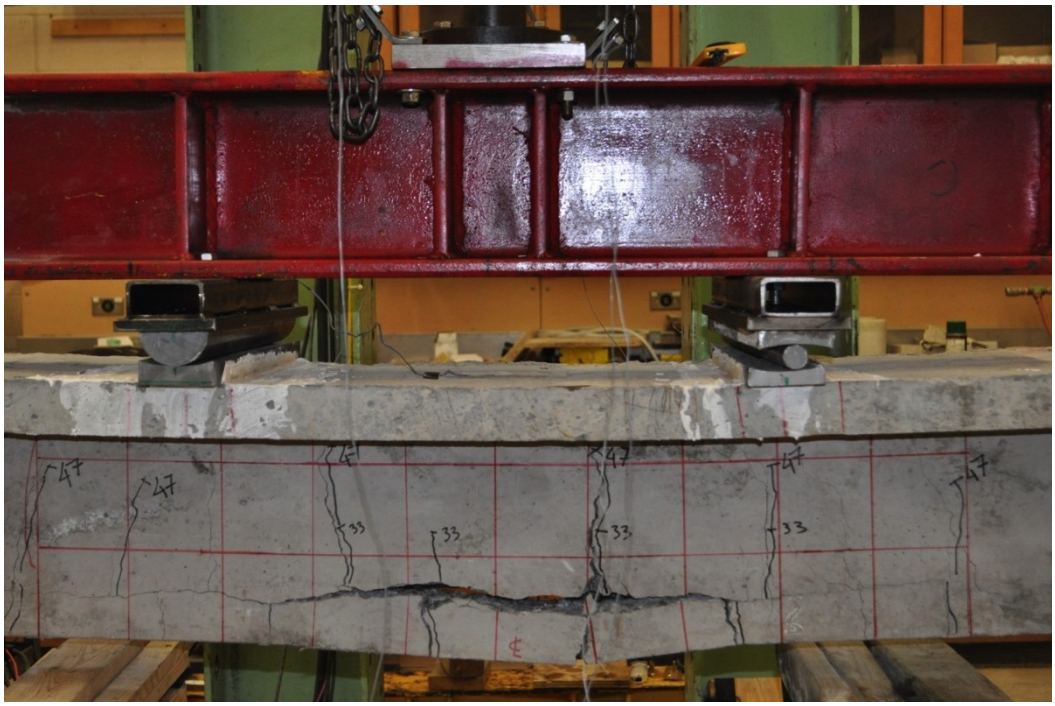

Figure 4-21 – Cracking pattern at failure for a corroded beam

Figure 4-22 – Concrete strand interface below the strand

Figure 4-23 – Concrete strand interface above the strand

Beam failures were defined by complete strand rupture or by a 20% drop in load, whichever occurred first. The control-uncorroded beam failed by strand yielding followed by multiple wire ruptures at one location, Figure 4-24. The failure pattern of the corroded beams differed. Failures were initiated by rupturing of one or two wires at a single location accompanied by a drop in load, shortly thereafter another wire ruptured at a nearby location, Figure 4-25. This second wire failure at a different location than the first is attributed to the varying location of the most severe pitting stress concentration locations for different wires.

Figure 4-24 – Multi-wire rupture at the same location for the uncorroded beam

Figure 4-25 – Wires rupture at adjacent locations in a corroded beam

Beams prestressed with two7-wire strands

Six beams were prestressed with two 7-wire strands: One beam was kept as control and five beams were subjected to accelerated corrosion. Table 4-5 summarizes the test results for beams prestressed with two strands. Similar to beams prestressed with one strand the load deflection curve of the control beam agrees well to the theoretical elastic response calculated based on the effective moment inertia (ACI 318M-08 2008; CPCI 2008), see Figure 4-26.

The control beam had an initial linear load-deflection response with a distinct change in slope (stiffness) at cracking, and then gradually transitioned into a non-linear response with no distinct yield plateau. On the other hand, the corroded beams had an initial linear response that transitioned into a non-linear one with no distinct change in stiffness at the cracking load.

Figure 4-27 shows load versus midspan deflection curves for all four beams prestressed with two strands at different corrosion levels (0%, 2.5%, and 10%). As shown in the slope of the curves the beams stiffness was not affected by the corrosion. However, the effect of the corrosion on the cracking load, the ultimate load, and the midspan deflection were similar to those for beams with a single strand with a 2.5% corrosion level, but significantly less pronounced at a corrosion level of 10%.

The beam with a 2.5% corrosion level exhibited 6.13% and 24.55% reductions in load capacity and midspan deflection respectively compared to the control beam. At a 10% corrosion the load carrying capacity of the beam decreased by 10.63% and the midspan deflection decreased by 38.8% for the beam with the L-shaped cathode (ST-2S-10%-NW-LC) compared to the control

beam. The beam with a straight cathode (ST-2S-10%-NW-SC) exhibited only 2.39% and 15.43% decreases in the load carrying capacity and midspan deflection of the beam respectively.

Table 4-7 – Monotonic testing result summary of beam prestressed with two strands

Corrosion level	Concrete Strength (MPa)	Cracking		Ultimate			
		Load (kN)	Deflection (mm)	Load (kN)	% Reduction in load	Deflection (mm)	% Reduction in deflection
0.0%	41.26 ± 3.49	48.0	4.1	107.6	-	104.0	-
2.5%	48.33 ± 3.67	40.8	3.4	101.0	6.1%	78.5	24.6%
10.0%-LC	48.33 ± 3.67	43.0	4.4	96.1	10.6%	63.7	38.8%
10.0%-SC	41.26 ± 3.49	40.2	2.8	105.0	2.4%	88.0	15.4%

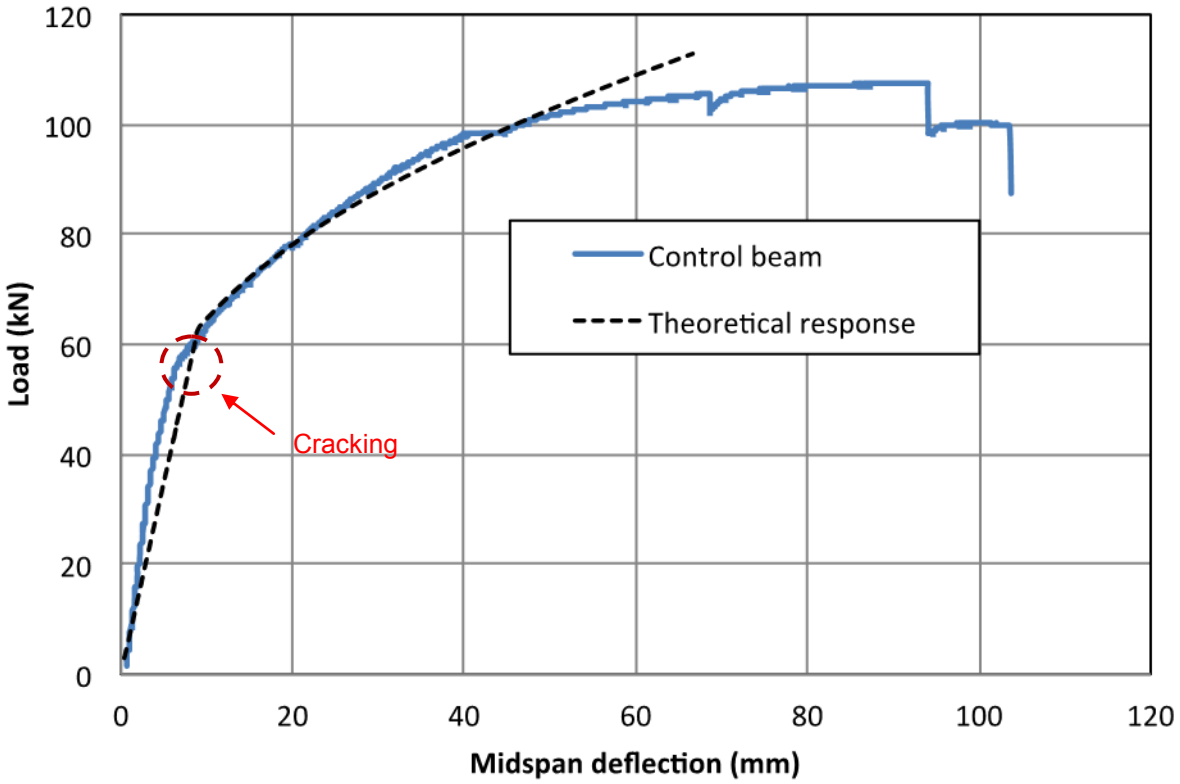

Figure 4-26 – Experimental vs. theoretical deflection response for beams with 2 strands

The concrete midspan compressive strain was monitored and similar observations to those made for the beams with one (1) strand were obtained. The concrete midspan compressive strain had a typical trend, increasing as the midspan deflection increased. In addition, the measured ultimate midspan compressive strain increased with increasing ultimate load and midspan deflection; the ultimate midspan deflection and the concrete compressive strain at failure decreased as the corrosion level increased. Beams with 2.5%, and 10% (L-shaped cathode) corrosion levels exhibited a 24.55% and a 38.8% reduction in concrete compressive strain at failure, which correlates well with the reduction in midspan deflection.

However, the ultimate concrete compressive strain for the beam with 10% corrosion and with a straight cathode (ST-2S-10%-NW-SC) appears to be an outlier. This may be attributed to the straight cathode acting as an additional longitudinal rebar and affecting the load deflection of the beam, which can be also observed in the beam's load-deflection curve as it exhibited an ultimate midspan deflection almost equal to that of the control beam. Figure 4-28 presents the applied load versus the measured midspan concrete compressive strain for beams with two strands at different corrosion levels. Table 4-8 presents a summary of the measured ultimate midspan concrete compressive strain values.

Table 4-8 – Summary of measured ultimate midspan concrete compressive strain for beams with two prestressing strands

Corrosion level	Ultimate			
	Compressive strain	% Reduction concrete compressive strain	Deflection (mm)	% Reduction in deflection
0.0%	2393	-	104.0	-
2.5%	2303	3.8%	78.5	24.6%
10.0%-LC	2104	12.1%	63.7	38.8%
10.0%-SC	3515	N/A	88.0	15.4%

The crack opening widths of the first three (3) flexure cracks due to loading were measured, and the cumulative crack opening versus load is presented in Figure 4-29. In addition, the average tensile strain within the centre 600mm constant moment zone was measured by an OSMOS fibre

optic sensor (FOS) and plotted against the applied load, Figure 4-30. The average tensile strain at the prestressing strand level decreased with an increased corrosion level, this is due to the decrease in monotonic load capacity.

The failure mechanism of the control (uncorroded) beam with two prestressing strands was similar to that of the control beam with a single strand. It failed by strand yielding followed by multiple wire rupture at a single location. In the corroded beams with 2.5% and 10% corrosion levels with L-shaped cathodes, the failure initiated by one or two wires rupturing at one location then shortly thereafter another wire rupturing at a nearby location. All failures of the corroded beams took place at a severe corrosion pit along the strand. However, the beam with a straight cathode and with 10% corrosion level (ST-2S-10%-NW-SC) failed by concrete crushing as shown in Figure 4-31. Three factors may have contributed to this change in beam failure; this beam was part of the pour that had the lowest concrete strength (41.26 ± 3.49 MPa) prior to testing of all the beams. Also a visual inspection of the exposed strands after failure revealed that the pitting was not as severe for this beam as that for the remaining beams. The strands did not seem to achieve the theoretical 10% mass loss due to corrosion. The location of the stainless steel tube in between and in close proximity to the two strands, together with corrosion led to a debonding of the strands within the flexure zone. This would have triggered the beam to behave as a tied arch, which would cause the stress in the concrete to flow directly from supports to the loading points causing very high concrete compressive stresses resulting in concrete crushing at midspan.

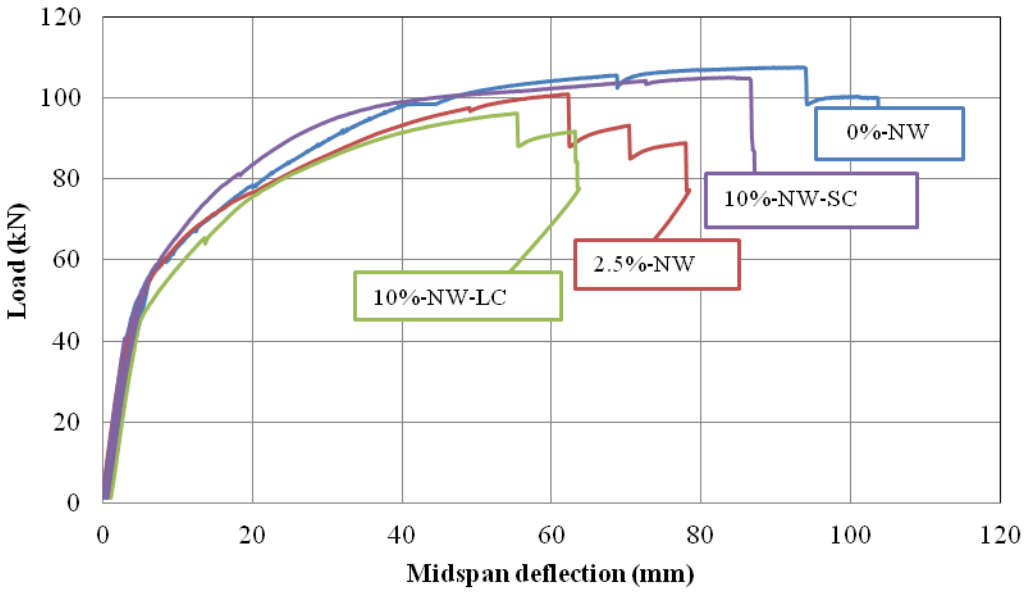

Figure 4-27 – Load vs. midspan deflection at different corrosion levels for beams with 2 strands

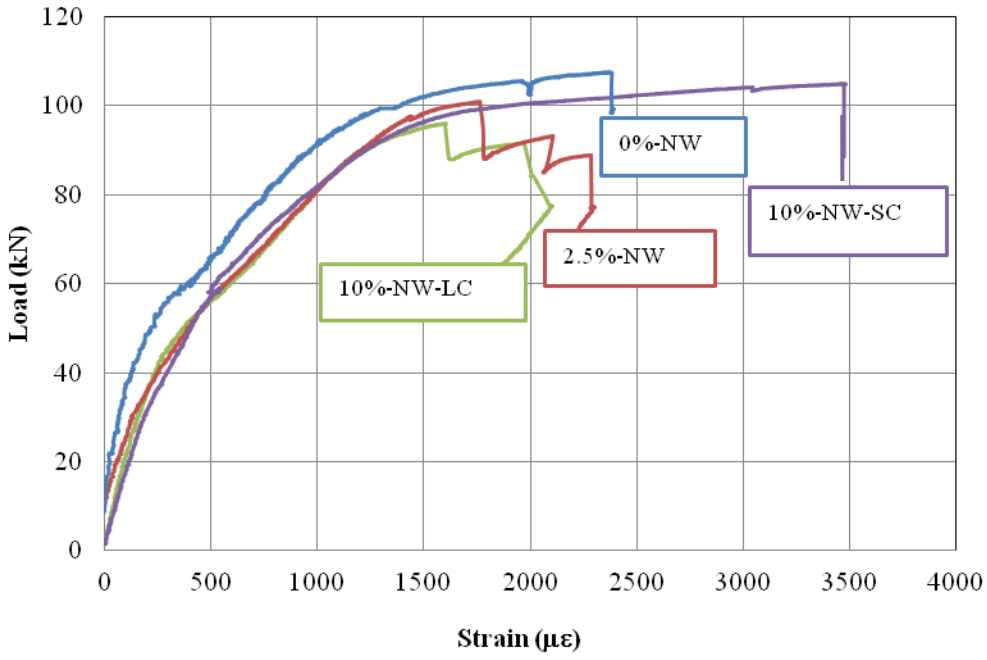

Figure 4-28 – Load vs. midspan concrete compressive strain for beams with two strand

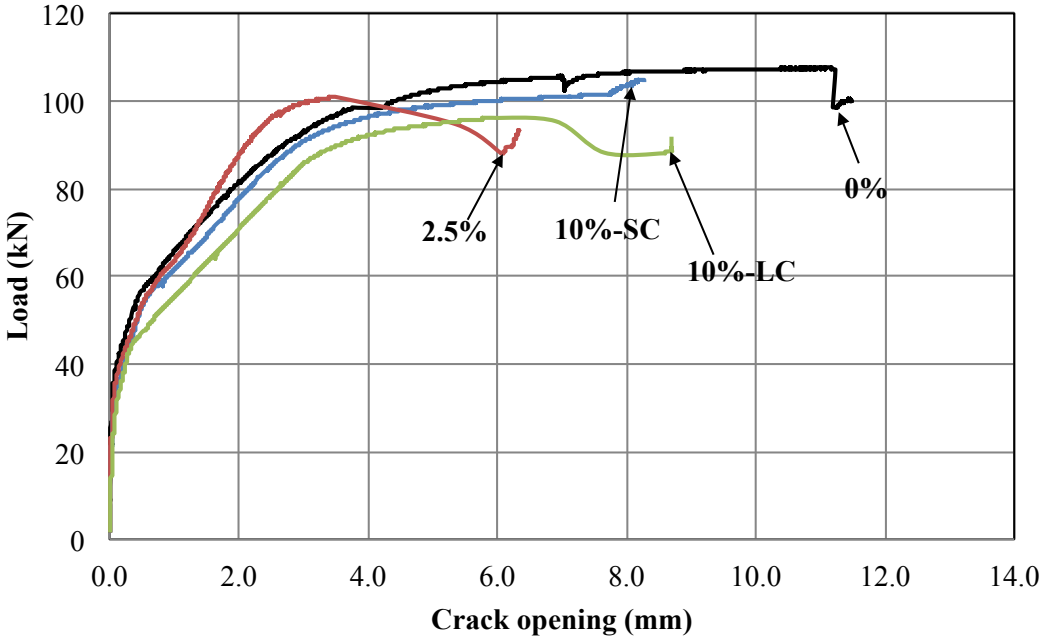

Figure 4-29 – Cumulative crack opening within the constant moment zone vs. load

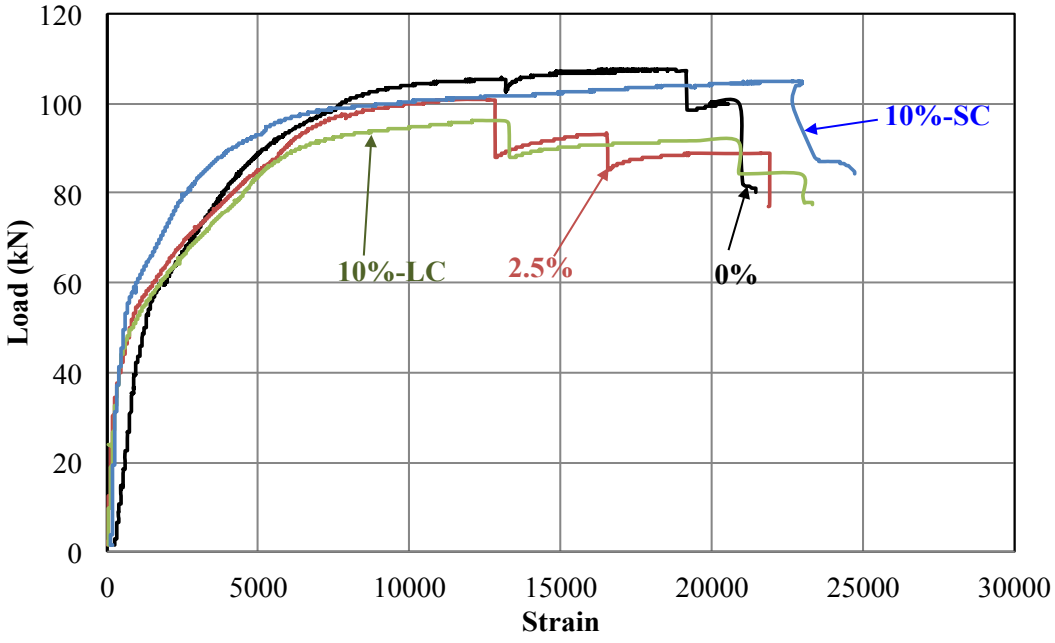

Figure 4-30 – Average tensile strand strain vs. load at different corrosion levels

Figure 4-31 – Failure by concrete crushing of beam ST-2S-10%-NW-SC

Beams repaired with CFRP sheets

Two beams prestressed with a single strand and corroded to a 5% and 10% corrosion level by mass losses were repaired using CFRP sheets. The beams' surface was prepared by grinding the surface to open the concrete pores, and the concrete edges were rounded. The beam surface was cleaned from dust and a layer of Sikadur® 330 epoxy was applied. The CFRP sheets (SikaWrap® Hex 230C) were then applied on top of the epoxy layer and all the excess epoxy was squeezed out by using a metal roller allowing the epoxy to fully impregnate the CFRP sheet in the process. The CFRP sheets were placed according to the manufacturer's instructions as per the configuration presented in Section 3.8, Figure 3-8.

Upon installation of the CFRP sheets onto the beams, they were allowed to cure at room temperature for 7 days, after which the beams were tested to failure in four-point bending under a monotonically increasing load.

Table 4-9 summarizes the test results for the repaired beams, the unrepaired beams, and the control beam. Figure 4-32 shows the load-deflection response of repaired and unrepaired beams. The load deflection response for all the beams was bi-linear with a distinct change in slope (stiffness) beyond the cracking load and then gradually changing to a nonlinear curve. Test results showed that the repaired beams had higher stiffness, and that the repairs restored the reduction in load capacity due to corrosion.

Table 4-9 – Test result summary for CFRP repaired, unrepaired, and control beams

Corrosion level	Concrete Strength (MPa)	Cracking		Ultimate			
		Load (kN)	Deflection (mm)	Load (kN)	% Reduction in load	Deflection (mm)	% Reduction in deflection
0.0%	48.69 ± 3.49	33.6	3.0	65.3	-	141.4	-
5.0%	49.89 ± 4.66	24.0	2.0	58.8	9.9%	78.6	44.4%
5.0% repaired	48.69 ± 3.49	38.7	3.8	70.3	-7.6%	42.8	69.8%
10.0%	49.89 ± 4.66	23.0	1.8	48.3	26.0%	33.3	76.4%
10.0% repaired	49.89 ± 4.66	31.6	2.6	63.2	3.1%	43.5	69.3%

The concrete compressive strain and the CFRP tensile strain at midspan were monitored. It was observed that the concrete ultimate compressive strain decreased while the CFRP ultimate tensile strain increased with an increase in the corrosion level. This indicates that as the corrosion level increased corrosion pitting becomes more severe and further reduces the strand's load bearing capacity, therefore in order to maintain the overall beam resistance the CFRP sheet has to resist a bigger portion of the applied load.

Figure 4-33 shows load versus concrete compressive strain curves, and Figure 4-34 presents the applied load versus CFRP and concrete midspan strains for the corroded and the repaired beams. The repaired beams both failed in flexure by strand rupture followed shortly thereafter by rupture of the CFRP sheet. Figure 4-35 shows a typical repaired beam at failure. These results show that repair of corroded beam with CFRP sheets, up to a corrosion level of 10% by mass loss, is capable of restoring the beam's uncorroded monotonic capacity.

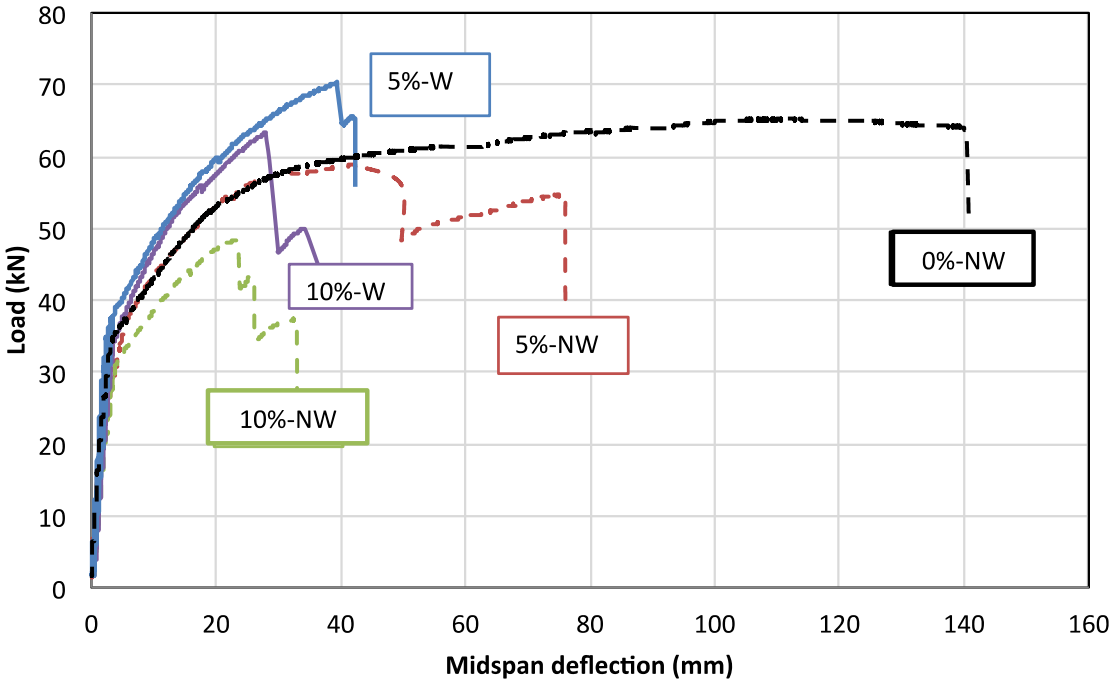

Figure 4-32 – Load vs. midspan deflection comparison of the repaired and unrepaired beams

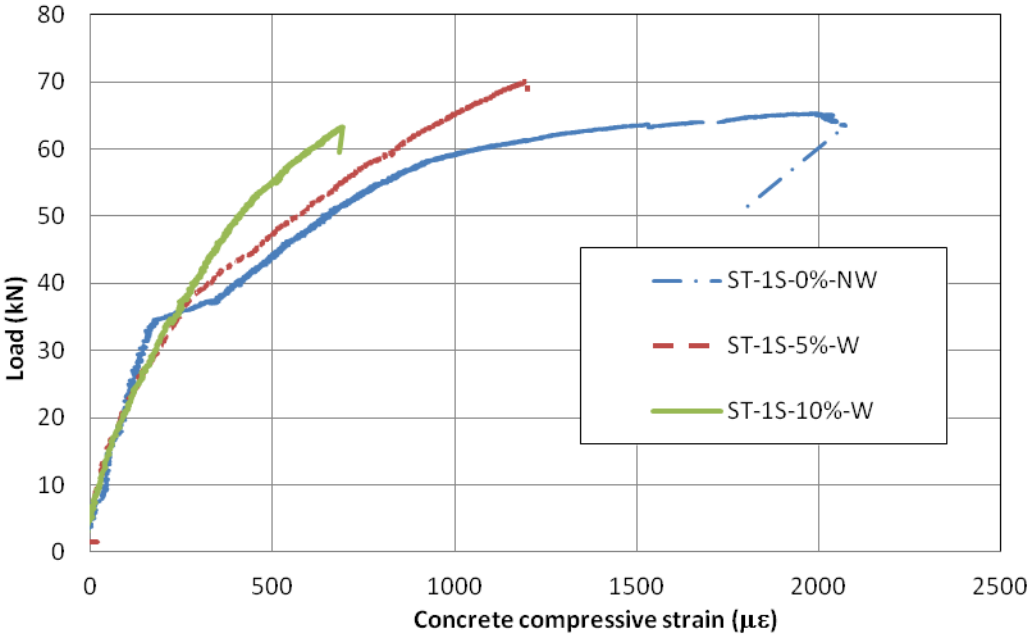

Figure 4-33 – Load vs. concrete midspan compressive strain for corroded and repaired beams

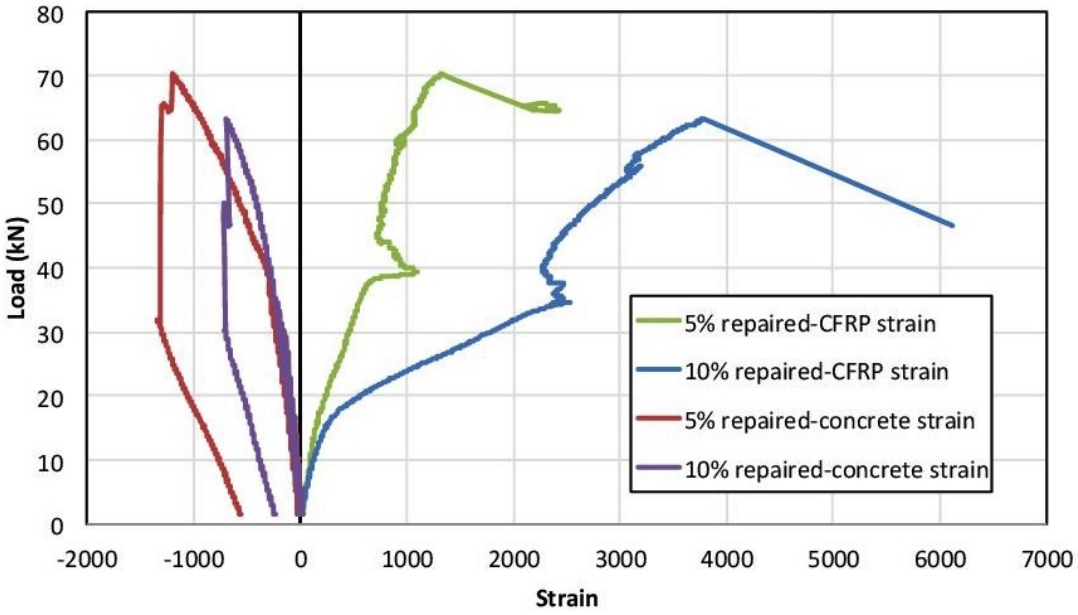

Figure 4-34 – Load vs. CFRP strain at midspan for corroded and repaired beams

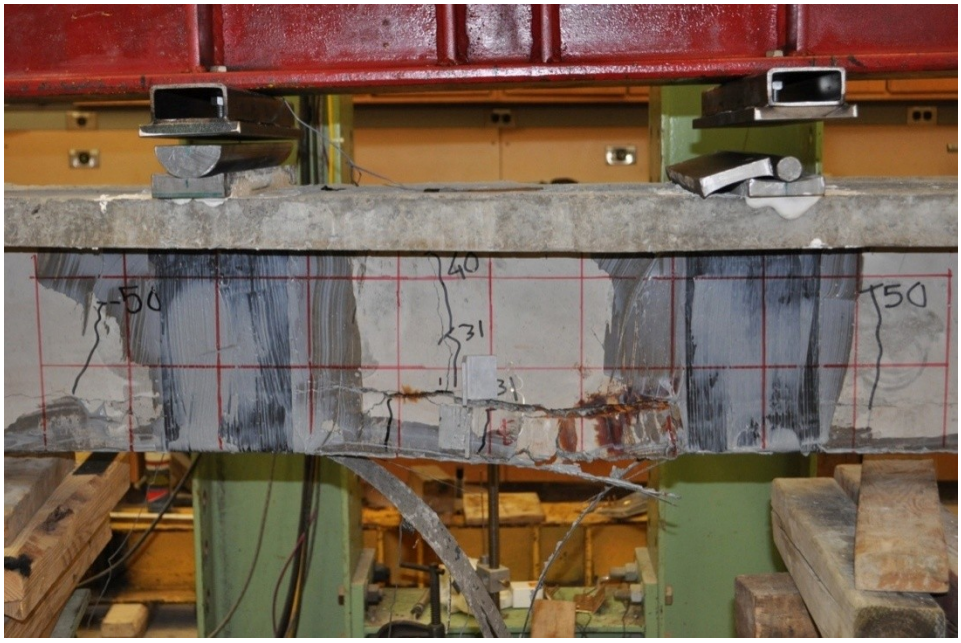

Figure 4-35 – Typical failure of a prestressed beam repaired by CFRP sheets

Both repaired beams that were corroded to a 5% and a 10% corrosion by mass loss showed capacities close to their repair design capacity calculated in accordance with ACI 440.2R-08 without applying the corresponding material reduction factors. Figure 4-36 presents the load deflection response for the control beam, and the repaired and unrepaired beams with a 5% corrosion level. Figure 4-37 presents the load deflection response for the control beam, and the repaired and the unrepaired beams with a 10% corrosion level.

For the beam corroded to a 5% corrosion repaired with CFRP the load capacity exceeded that of the control (uncorroded) beam by 7.64%, while the midspan deflection was further decreased by an additional 25% in comparison to the reduction of the unrepaired beam corroded to the same corrosion level, adding up to a total reduction of 70% for the ultimate midspan deflection. In addition, the cracking load of the repaired beam increased in comparison to that of the unrepaired beams. This is attributed to the increased post-cracking stiffness of the beam due to the CFRP sheets.

For the beam corroded to a 10% mass loss and repaired with CFRP, the load capacity was restored to a level only 3% below that of the control (uncorroded) beam, while the ductility remained roughly the same as the unrepaired corroded beam with the same corrosion level.

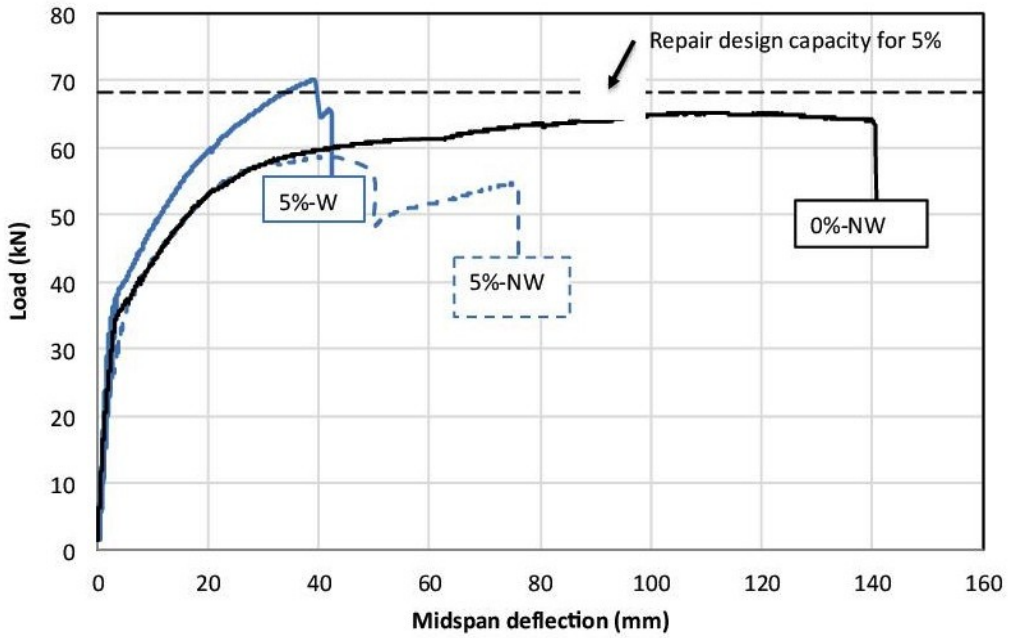

Figure 4-36 – Design repair load capacity compared to experimental response of the beam corroded to 5% by mass loss

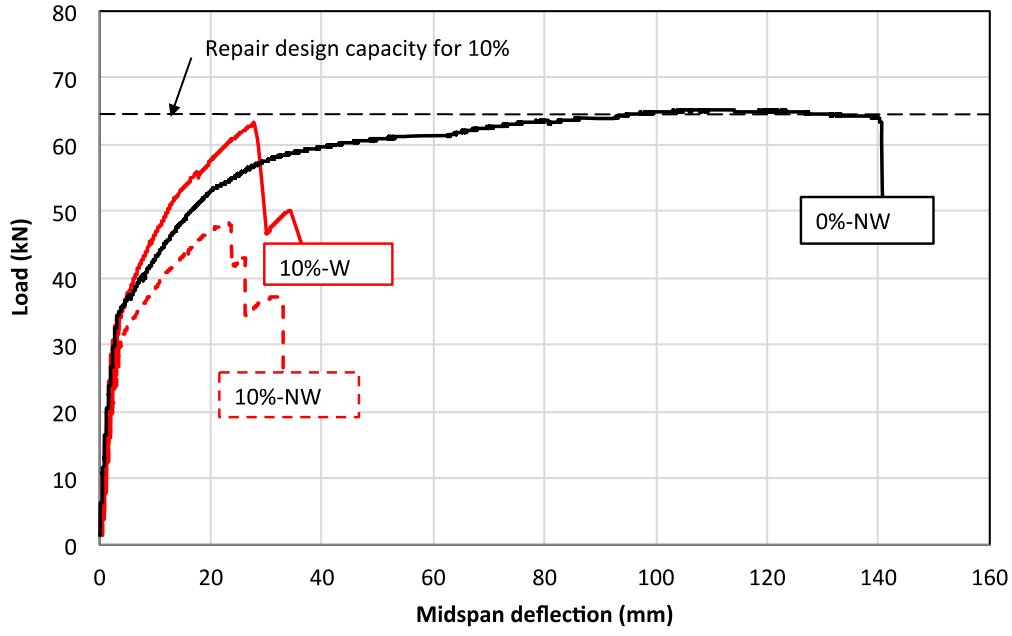

Figure 4-37 – Design repair load capacity compared to experimental response for the beam corroded to 5% by mass loss

4.5 Fatigue Testing

The fatigue/cyclic loading testing phase of the experimental program (Phase III-Chapter 3) included twenty-five (25) prestressed T-beams. Table 4-10 gives the experimental matrix for the fatigue testing phase. All beams in this phase were prestressed using a single prestressing wire and the same L-shaped stainless bar (cathode) for the accelerated corrosion setup as previously described. The twenty-five beams were divided into three groups. Five (5) beams were left uncorroded, ten (10) beams were corroded to a 5% mass loss, and the final ten (10) beams were corroded to a 10% mass loss. Each set of ten (10) corroded beams is divided into two sets of five (5) beams. Five (5) beams were corroded and unrepaired, and five (5) beams were corroded and then repaired using CFRP sheets as described in Section 3.8.

Table 4-10 – Fatigue testing matrix

Number of specimens	Corrosion Level	Repair Condition
25 Beams	0% - 5 Beams	N/A
	5% - 10 Beams	5 Beams-repaired using CFRP
		5 Beams-unrepaired
	10% - 10 Beams	5 Beams-repaired using CFRP
		5 Beams-unrepaired

Beams were tested under fatigue load cycling between peak and a valley values determined as a percentage of the monotonic static capacity of their respective groups. For example, the monotonic static capacity of uncorroded prestressed beam was 65.3 kN, so when a similar beam

is tested under cyclic loading from valley to a peak values of 10% to 70% of the monotonic capacity, which corresponds to cycling between 6.5 kN to 45.7 kN. Each beam within a set of five (5) beams was tested under a different load range in order construct a complete load versus fatigue life curve. The applied load range was varied by changing the value of the peak (maximum) load, while the valley (minimum) load value was kept constant at 10% of the monotonic load capacity.

The peak load was applied manually then the load was decreased to the mean load value before cycling, after which the 407 Material Testing System (MTS) controller took over and started cycling at a chosen frequency. The maximum cycling frequency used was 2.5 Hz. Beam failure was defined by rupture of a prestressing strand, rupture of the CFRP sheet, or concrete crushing. Fatigue tests were run to a maximum of 1 million cycles (2 million reversals).

Instrumentation for the fatigue beam tests included: midspan deflection measurement by an external LVDT, a 280 kN load cell to monitor the applied load, a 60 mm strain gauge to monitor the compressive strain at the concrete's top fibre, and two 10 mm strain gauges to monitor the tensile strain in the CFRP sheets within the constant moment region. A national instruments data acquisition system (DAQ) was used to record all the instrumentation's readings.

Table 4-11 presents a summary of the fatigue testing data including: the maximum and minimum cyclic load values, the testing load ranges, and the corresponding fatigue life for all the beams tested under cyclic loading. Figure 4-38 presents the load range versus fatigue life curves for each group.

Table 4-11 – Summary of fatigue testing of prestressed T-beams

	Peak		Valley	Range	Life	Notes
	%Pu	kN	kN	kN	# Cycles	
Control (Pu=65.28)	0.70	45.7	6.5	39.2	31000	
	0.70	45.7	6.5	39.2	54000	
	0.65	42.4	6.5	35.9	44950	
	0.65	42.4	6.5	35.9	89300	
	0.60	39.2	6.5	32.6	276000	
	0.60	39.2	6.5	32.6	1000000	Runout
	0.55	35.9	6.5	29.4	1000000	Runout
5% (Pu=58.8)	0.70	41.2	5.9	35.3	12730	
	0.65	38.2	5.9	32.3	30530	
	0.60	35.3	5.9	29.4	58600	
	0.55	32.3	5.9	26.5	208000	
	0.50	29.4	5.9	23.5	1000000	Runout
10% (Pu=48.29)	0.83	40.1	4.8	35.3	82.5	Outlier
	0.83	40.1	4.8	35.3	15300	
	0.77	37.2	4.8	32.4	66000	
	0.68	32.8	4.8	28.0	185500	
	0.60	29.0	4.8	24.1	385000	
	0.60	29.0	4.8	24.1	1000000	Runout
5%-W (Pu=70.26)	0.75	52.7	7.0	45.7	3900	
	0.61	42.9	7.0	35.9	65740	
	0.56	39.7	7.0	32.6	91000	
	0.56	39.7	7.0	32.6	62920	
	0.52	36.4	7.0	29.4	851000	
10%-W (Pu=63.24)	0.67	42.2	6.3	35.9	55600	
	0.62	39.0	6.3	32.6	214044	
	0.56	35.7	6.3	29.4	243500	
	0.51	32.4	6.3	26.1	328076	

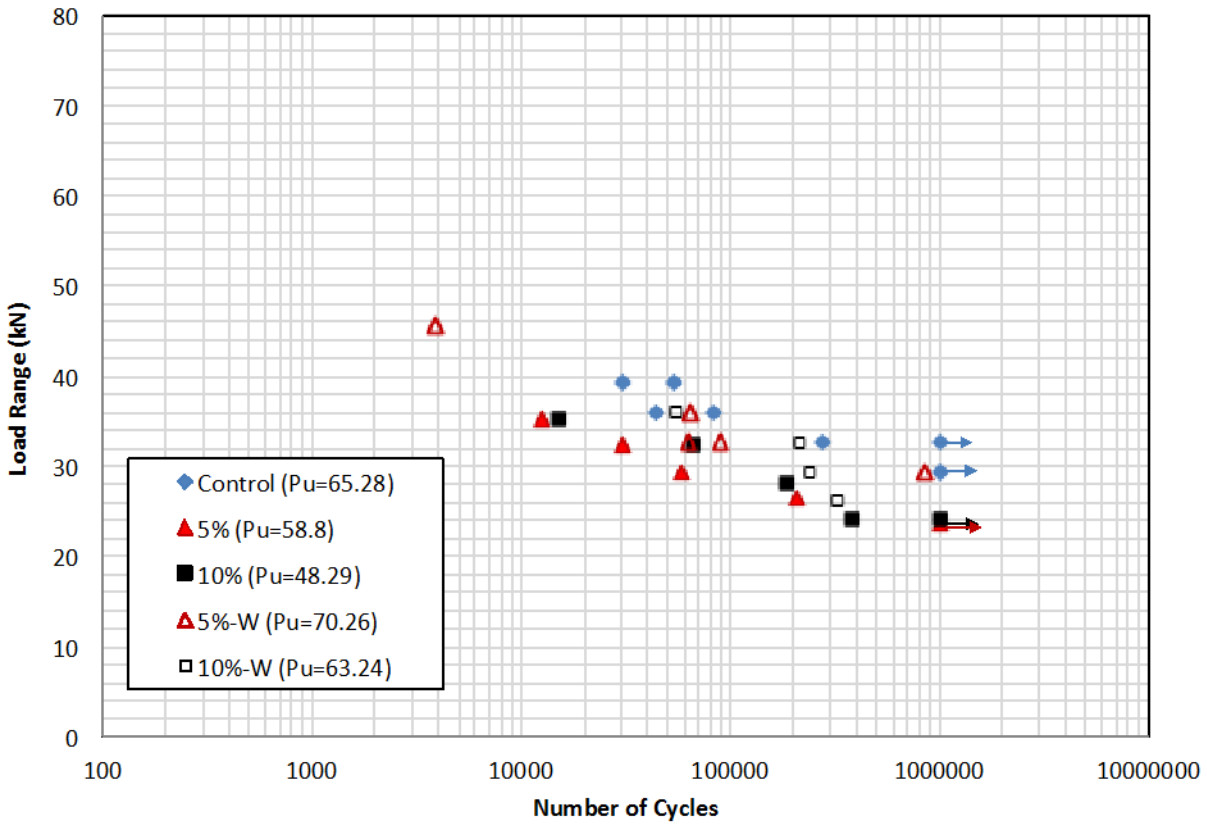

Figure 4-38 – Load range versus life of T-beams at different corrosion levels

By examining Figure 4-38 the effect of corrosion on the fatigue life of the prestressed beams is evident. This can be observed by comparing the load range versus fatigue life experimental data of the beam corroded to 5% by mass loss to that of the non-corroded control beams. The deterioration results in a downward shift in the load range versus fatigue life data so that for a given load range the fatigue life resistance of the corroded beam is less than that of the control beam. However, while a drop in fatigue resistance of the corroded beams with 5% corrosion by mass loss in comparison to that of the non-corroded beams is observed; additional deterioration of the beams with 10% corrosion levels is not observed.

For the beams corroded and then repaired using CFRP sheets an improvement in their fatigue resistance is observed compared to the fatigue resistance of the corroded/non-repaired beams. By comparing the repaired and non-repaired beams with a 5% corrosion level, an upward shift is observed almost restoring the fatigue resistance to the same level as that of the non-corroded control beams. An improvement is also observed in the fatigue resistance of the repaired beams with a 10% corrosion level in comparison to that of the non-repaired beams with a 10% corrosion level; however, the fatigue resistance of the control beam was not restored. It is also observed that beams corroded to 10% by mass loss exhibited more scatter/variation in their response compared to both non-repaired and repaired beams with a 5% corrosion level.

Figure 4-39 presents the midspan deflection versus the fatigue life for the control beams and the non-repaired beams with 5% and 10% corrosion levels. It should be noted here that because the applied load ranges were calculated as a percentage of the monotonic load capacity of each set, the load ranges are different for each set of beams (control, 5% & 10% corrosion), and therefore the midspan deflection values are not comparable. However, midspan deflection versus fatigue life curves for all the beams are grouped into a low, a medium, and a high load range categories. As expected, the midspan deflection increased with the increased applied load range, and more importantly, the midspan deflection versus fatigue life curves for all three load range categories remained flat throughout the fatigue life indicating that no significant prestress loss due to creep occurred.

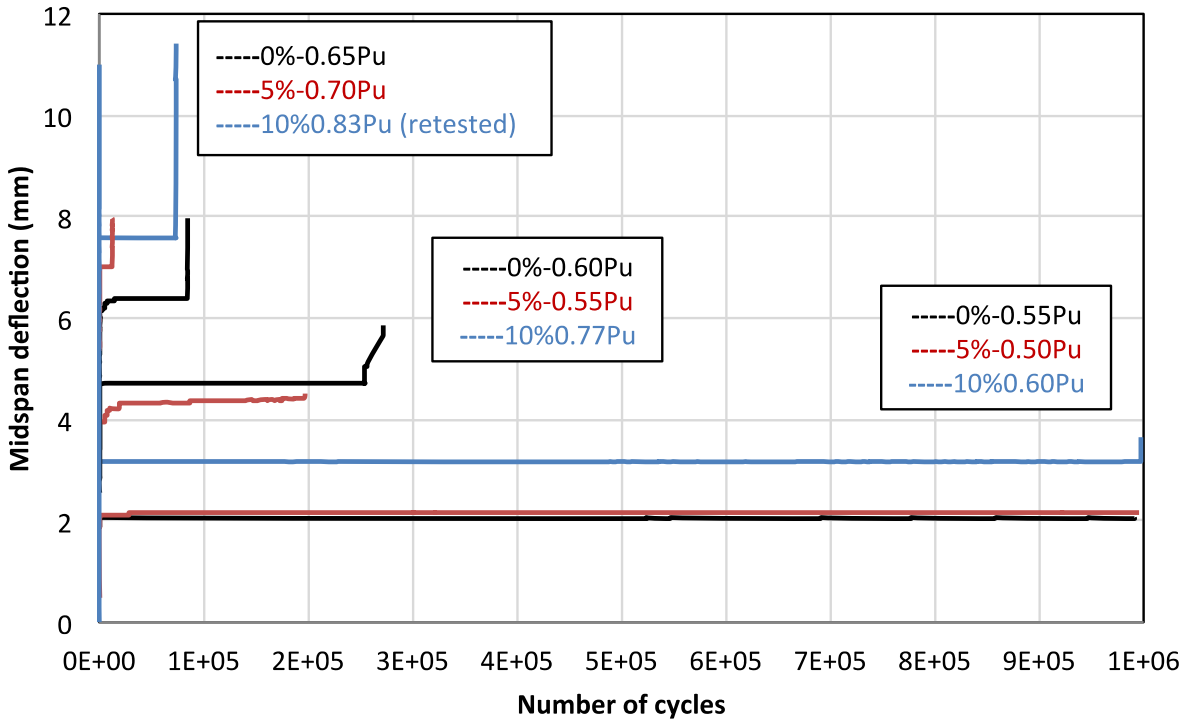

Figure 4-39 –Midspan deflection versus fatigue life response of non-repaired beams with different corrosion levels

Chapter 5
Fatigue Analysis and Discussion

A wide range of testing was conducted in this study, ranging from beam testing to material fatigue testing of a single wire taken from a 7-wire prestressing strand. The objective of this chapter is to develop a mechanistic model to predict the overall beam fatigue behaviour by accurately modelling the failure mechanism of a prestressing strand. In-depth discussions of the experimental results, followed by a mechanistic modelling of the fatigue behaviour are presented in this chapter.

A prestressing strand failure is initiated by the fracture of a single wire; therefore the applied stress or strain on a single wire versus fatigue life experimental data is used when evaluating the fatigue life models. The nominal prestressing strand stress is calculated based on the applied load data, presented in Section 4.5. Once the nominal strand stress is known, the individual wire stress is calculated based on the calculated, and experimentally verified, force distribution amongst the seven (7) individual wires.

5.1 Nomenclature

In this chapter for the purpose of focusing on the type of specimen (strand or wire) and the medium within which it is tested; beam specimens are referred to as strand-in-beam specimens, and single wire specimens are referred to as wire-in-air specimens.

5.2 Prestressing strand nominal stress

Using the applied peak and valley loads, the specimen's cross sectional geometry, the initial prestressing level, and the calculated prestress losses, conventional beam sectional analysis was used to calculate the applied force in the prestressing strand. For the corroded beams, the cross sectional area of the prestressing strand was considered to have an overall reduction equals to the percent of actual mass loss due to corrosion. For example, at 10% corrosion by mass loss the strand's cross sectional area is reduced from 98.7 mm^2 to 88.8 mm^2. Figure 5-1 presents a calculation flow chart for the strand nominal stresses. A summary of the experimental results and the calculated nominal strand stresses are presented in Table 5-1.

5.2.1 Calculation of prestress loss

A certain amount of the initial applied prestressing loss is lost during and after the force being transferred to the concrete member. Multiple factors contribute to the total prestress loss such as; anchorage seating loss, elastic shortening of the concrete, creep and shrinkage of concrete, and relaxation of the tendons. An accurate determination of the magnitude of the lost prestressing force is very important in determining the actual level of strand stresses under applied loads.

Field measurements of the actual prestress losses were not possible; as the pretensioned beams were constructed at an off-campus facility and needed to be transported back our structures laboratory. The prestress losses were calculated in accordance with the Canadian Precast Prestressed Concrete Institute (CPCI) Design Manual 4, which indicates losses in the range of 200-350 MPa are typical for normal density concrete members and recommends a value of 240 MPa (or 21% of initial prestress force) for preliminary design purposes. Two methods are given to calculate the level of prestress losses; the simplified method and the detailed method.

The Simplified Method accounts for the level of concrete stress, type of prestressed reinforcement and ratio of volume to surface area, while the detailed methods accounts for additional factors affecting concrete creep and shrinkage. The simplified method is meant for calculating the prestress loss for an initial prestress level of 75% of the strand's ultimate tensile capacity.

For the pretensioned beams in the present study the prestress loss was calculation using both the simplified and the detailed methods, and was found to be 300 MPa and 252 MPa respectively. Since the initial prestress level was 70% and not 75% of the strand's ultimate tensile capacity; the prestress loss based on the detailed method (252 MPa) was used in determining the strand's stress levels under applied loads.

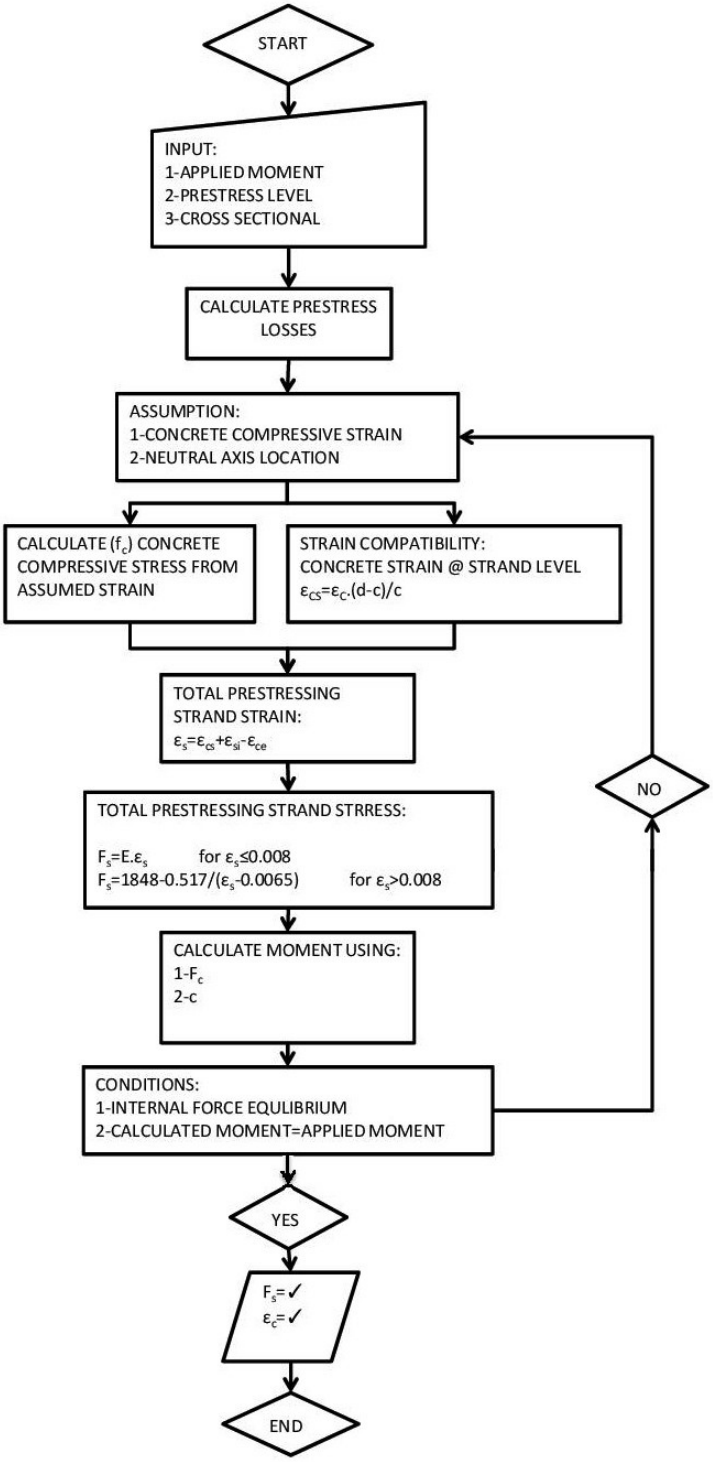

Figure 5-1 – Calculation flowchart for calculating the prestressing strand stress level due to moment applied on the beam

Table 5-1 – Summary of beam fatigue results and calculated nominal strand stresses

	Peak		Valley		Strand Stress (MPa)			Life	Notes
	%Pu	kN	%Pu	kN	Peak	Valley	Range	# Cycles	
Control (Pu=65.28)	70	45.7		6.5	1435	1011	424	31000	
	70	45.7		6.5	1435	1011	424	54000	
	65	42.4		6.5	1340	1011	329	44950	
	65	42.4	10	6.5	1340	1011	329	89300	
	60	39.2		6.5	1248	1010	238	276000	
	60	39.2		6.5	1248	1010	238	1000000	Runout
	55	35.9		6.5	1163	1009	154	1000000	Runout
5% Corrosion (Pu=58.8)	70	45.7		5.9	1363	1010	353	12730	
	65	42.4		5.9	1275	1010	265	30530	
	60	39.2	10	5.9	1191	1009	182	58600	
	55	35.9		5.9	1119	1009	111	208000	
	50	32.6		5.9	1071	1008	63	1000000	Runout
10% Corrosion (Pu=48.29)	83	54.2		4.8	1396	1010	386	82.5	
	83	54.2		4.8	1304	1010	294	15300	
	77	50.3	10	4.8	1172	1009	163	66000	
	68	44.4		4.8	1084	1008	76	185500	
	60	39.2		4.8	1084	1008	76	385000	
5% Corrosion Wrapped (Pu=70.26)	75	49.0		7.0	1597	1013	585	3900	
	61	39.8		7.0	1352	1011	342	65740	
	56	36.6	10	7.0	1271	1010	261	91000	
	56	36.6		7.0	1271	1010	261	62920	
	52	33.9		7.0	1193	1009	184	851000	
10% Corrosion Wrapped (Pu=63.24)	67	43.7		6.3	1389	1011	379	55600	
	62	40.5	10	6.3	1210	1010	200	214044	
	56	36.6		6.3	1141	1009	131	243500	
	51	33.3		6.3	1086	1009	77	328076	

5.3 Force Distribution for the 7-wire Strand

As previously discussed and experimentally investigated in Section 4.2, the first step in the fatigue life modelling is to analyze the force distribution in the strand to quantify the force/stress within individual wires. In this chapter an analytical approach suggested by Costello (1997) is used to identify the forces within the individual wires of a strand. This analytical approach is compared to our experimental results.

This approach considers the change in the helix angle due to loading, and uses trigonometry to describe the change in helix geometry during loading. Figure 5-2 presents a schematic of (a) the 7-were strand under axial load and (b) the various forces acting upon an individual external wire due an axial nominal load on the strand, and (c) the change of the external wire helix geometry (rotation and length) due to loading.

Based on the change in the helix geometry due to loading, the number of external wires in the strand, and the material's poisson's ratio, the wire strain is related to the strand's nominal strain. This approach relates the strand strain to the centre wire strain, and formulates the strains in the external wires as a function of the centre wire strain and strand geometry. Equations (5-1) and (5-2) define the final steps in calculating the forces for the centre and external wires respectively. The reader should refer to Castello's Theory of Wires (1997) for the complete detailed procedure of calculating the individual wire force.

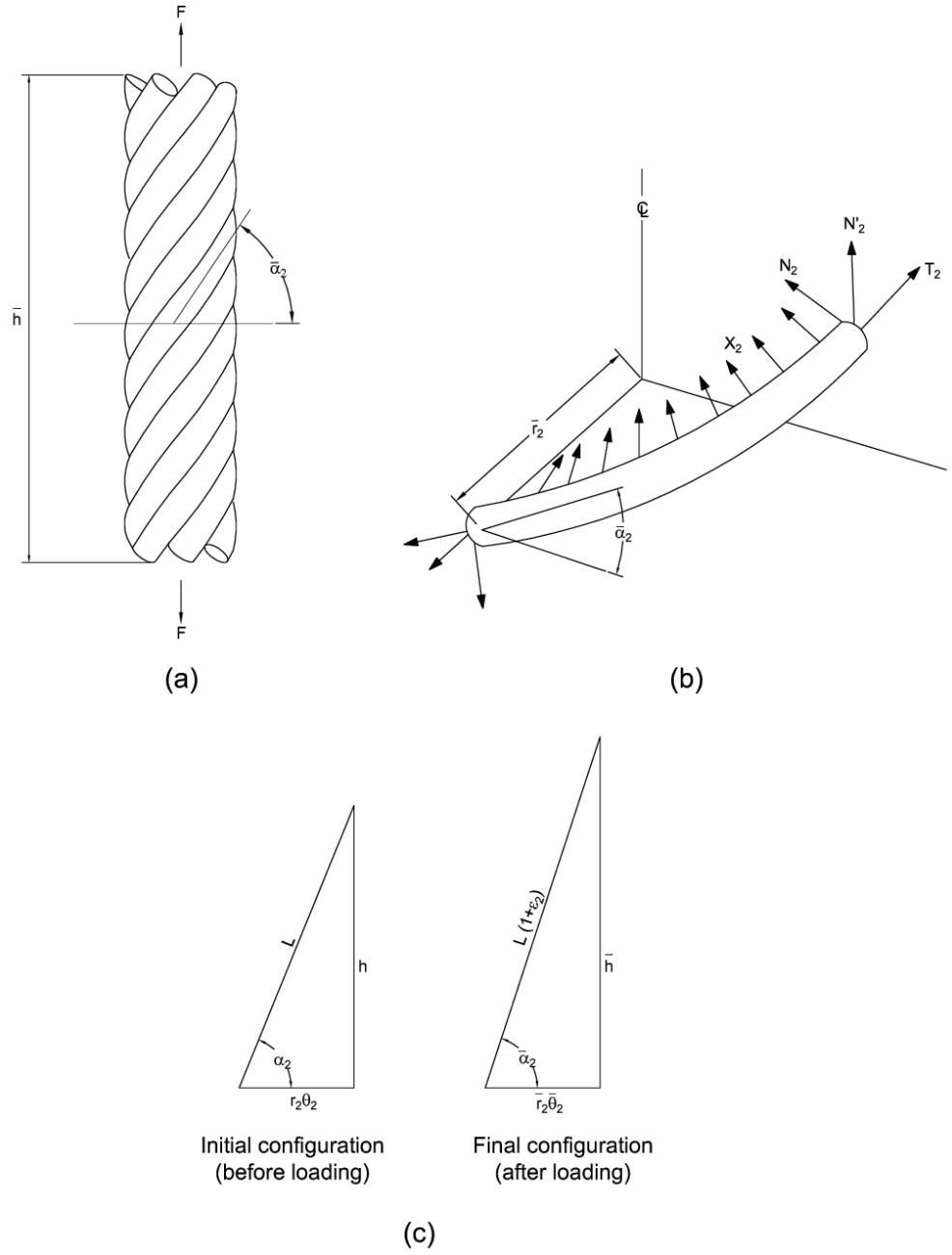

Figure 5-2 – (a) Schematics of 7-wire strand (b) Force diagram for an external wire, and (c) change in geometry (length and rotation) due to applied load F (Castello, 1997)

$$\frac{F_1}{ER_1^2} = \pi\varepsilon_1 \tag{5-1}$$

$$\frac{F_2}{ER_2^2} = m_2\left[\frac{T_2}{ER_2^2}\sin\alpha_2 + \frac{N_2'}{ER_2^2}\cos\alpha_2\right] \tag{5-2}$$

Where,

F_1	Force in the centre wire
F_2	Force in the external wires
m_2	Number of external wires in the lay
R_1	Radius of the centre wire
R_2	Radius of external wire
T_2	External wire axial tension
N_2	Shear component in an external wire in the y-direction
E	Modulus of elasticity
α	Helix angle
ε_1	Strain in centre wire = Nominal strand strain

The analytical model predicts a load carrying contribution for each of the external wires to be 14% of the total applied load on the strand assembly. This is slightly higher than the experimentally obtained external wire load carrying contribution, presented in Section 4.2, which ranged from 10.2% to 13.2% of the total applied load. However, the experimental results are based on a monotonic tension test up to only 80 kN. In addition, an evident trend was observed

of continuing force redistribution amongst the individual wires with increasing total load. The average load carrying contribution of the external wires increased at a decreasing rate, and load carrying contribution of the centre wire decreased at a decreasing rate (see Figure 4-5). Given that the maximum load of 80 kN is lower than the initial prestressing load (approximately 128 kN, which represented 70% of the ultimate stress of the strand of 1860 MPa), and the observed force redistribution trends, it is reasonable to assume that had the monotonic tension test of the strand assembly reached the initial prestressing level, the load carrying contribution of the external wire would have reached 14% of the total applied load predicted by the analytical model.

5.4 Discussion of the Stress Range or Strain Range versus Fatigue Life Results

Figure 5-3 presents the strain range versus fatigue life for all beam and non-corroded and corroded single wire testing. The strain range presented for the beam specimens is the calculated strain range in the external wire due to the applied loading.

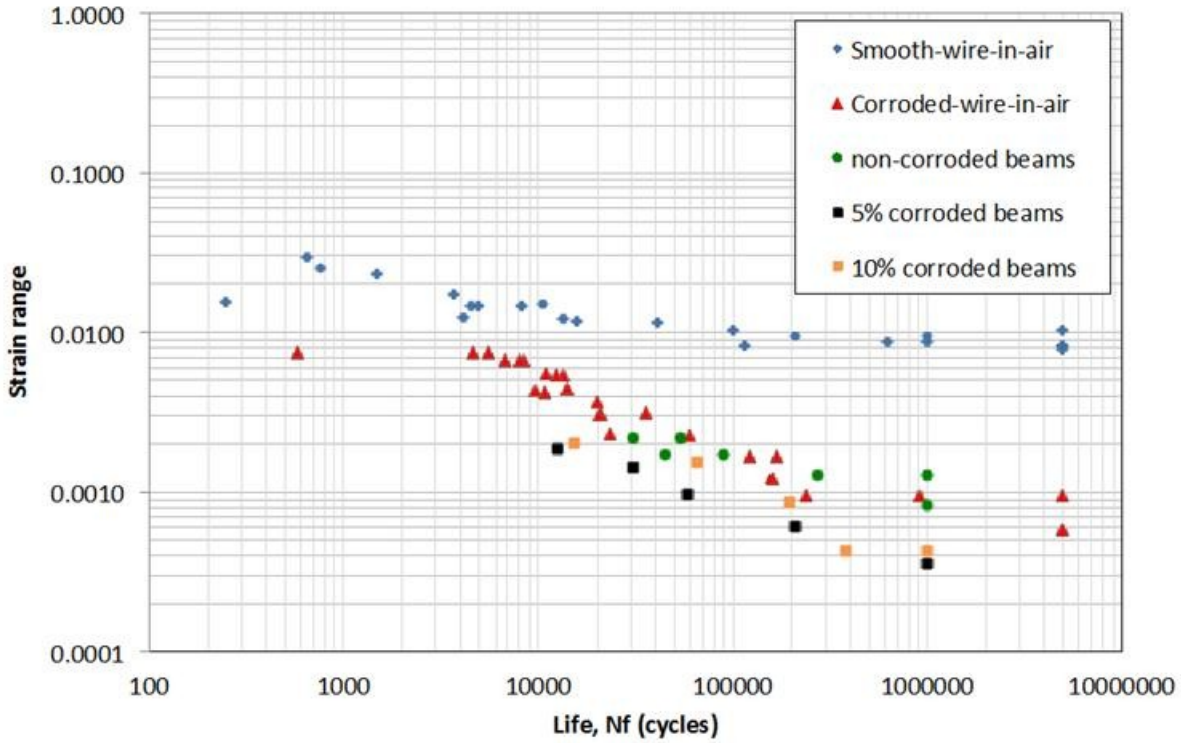

Figure 5-3 – Strain range versus fatigue life data for all the fatigue tests

5.4.1 Fatigue resistance of a non-corroded wire in air, strand in air and a strand inside a beam specimens

Figure 5-4 shows fatigue test results from the current study together with the fatigue results for strand specimens collected by Paulson et al. (1983) as presented in Section 2.4.1. The smooth wire-in-air specimens have a relatively flat curve that is typical of the behaviour of cold drawn steels, Dowling (1993).

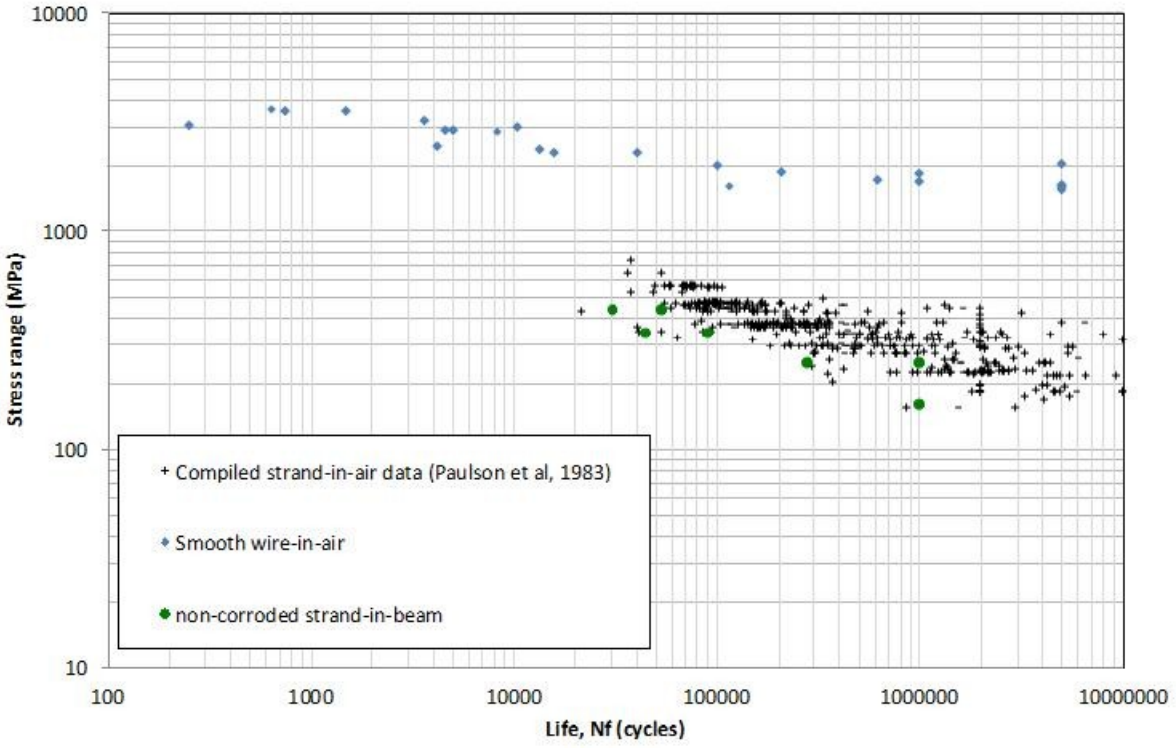

Figure 5-4 – wire-in-air, strand-in-air, and strand-in-beam versus fatigue life

Before discussing Figure 5-4, it is worth reiterating that all of the experimental data compiled by Paulson et al. (1983) from the literature was for prestressing strands as isolated elements, meaning that the strands were tested in air. The fatigue strength of the strand-in-air and strand-in-beam specimens is much lower than the smooth wire-in-air specimens at long lives. The mean fatigue resistance of the strand-in-beam specimens suffers a greater deterioration in fatigue strength compared to the mean fatigue resistance of the strand-in-air specimens. The strand-in-air specimens differ from the wire-in-air specimens in only one way; the strand specimen comprises of 7-wire, a central straight wire with six (6) external wires helically wrapped around it.

A single smooth wire-in-air specimen has no external forces acting upon it other than the applied axial load. However, under axial loading of the strand the helically wrapped external wires extend and attempt to straighten, only to be resisted by the adjacent wires and the centre wire. This resistance results in a contact/clamping force between adjacent external wires, and between the external wires and centre wire causing rubbing/friction along the contact band. When cyclic fatigue loading is introduced, the oscillation in the contact/clamping force can cause inter-wire fretting damage from which fatigue cracks are likely to originate, grow and finally lead to wire fracture. This mechanism can be reasonably assumed to be causing the reduction in the fatigue resistance of the strand-in-air specimens in comparison to the fatigue resistance of the wire-in-air specimens.

Since the strand-in-beam specimens have a lower fatigue resistance than the strand-in-air specimens; therefore a mechanism more severe than inter-wire fretting must govern the fatigue resistance. It is suggested that this mechanism is wire to concrete fretting adjacent to cracks in the concrete. When the bond is maintained between the strand in a beam and the surrounding concrete the strain compatibility is maintained and there is no relative slip between the strand and the concrete. However, when the beam is subjected to bending moment tensile stresses are introduced in the beam soffit causing the concrete to crack (flexural cracks) when tensile stresses exceed the tensile strength of the concrete. As a result, stress raisers in the prestressing strand are created at flexural crack locations causing debonding of the strand from the concrete on either sides of the crack. Relative slip may now occur at these locations giving rise to fatigue cracks that grow and finally lead to wire fracture.

To further investigate this inference non-corroded full 7-wire strand samples were extracted from the beams that were tested to failure and closely inspected for signs of fretting. Figure 5-5 shows a close up of a 7-wire strand sample extracted from the beam after failure. One of the external helical wires was removed to reveal the inter-wire contact zone. Obvious signs of abrasion along an inter wire contact band along the length of the wires can be observed between adjacent external wires and between an external and centre wire.

Then the extracted strand samples were unwound so that each individual wire could be closely inspected at the fracture location. Figure 5-6 shows a 15x magnification of the fracture location in a centre wire. Again the markings of a contact band, approximately measuring 0.6 mm wide, on the side of an external wire is evident. Figure 5-7 and Figure 5-8 are both close-ups of fracture locations on opposite sides of the same external wire. Figure 5-7 shows the more aggressive abrasion/fretting signs on the wire at the wire-concrete interface. The strand-concrete fretted wire had typical elliptical shape observed by Pantucek (1977) and Blakeborough and Cullimore (1984) as presented in the literature review in Section 2.4.2, Figure 2-12.

Figure 5-8 shows inter-wire abrasion/fretting. The fracture profile shown in Figure 5-8 and Figure 5-9 is consistent with the fracture profile observed by Toribio and Ovejero (2005) due to hydrogen assisted cracking of heavily cold drawn wires, shown in Figure 2-18. The difference between the two fretting interfaces (inter-wire and concrete-wire) can be distinguished by the continuous contact band on the inter-wire fretting side, while the signs of fretting on the concrete-wire interface are localized around the fracture location (at a concrete crack location).

Figure 5-9 and Figure 5-10 show close-ups of the fracture plane for the same wire shown in Figure 5-8. The fracture plane shown in shown Figure 5-10 shows a typical penny shaped fatigue crack propagation zone followed by a brittle fracture zone. An x200 magnification of the fracture planes are presented in Figure 5-11 and Figure 5-12, which reveal that the fatigue crack initiated from a surface flaw. These figures present physical evidence that failure under cyclic loading occurs due to the initiation of fatigue cracks from fretting induced surface damage.

Figure 5-5 – Close up of a 7-wire strand as extracted from the beam after fatigue failure

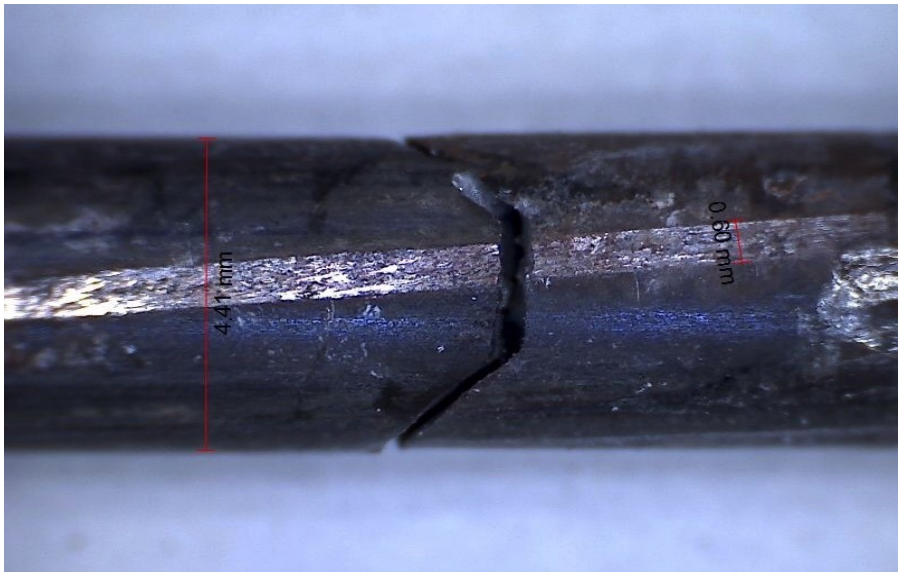

Figure 5-6 – Close of the centre wire of a 7-wire prestressing strand at the failure location as extracted from the beam after failure

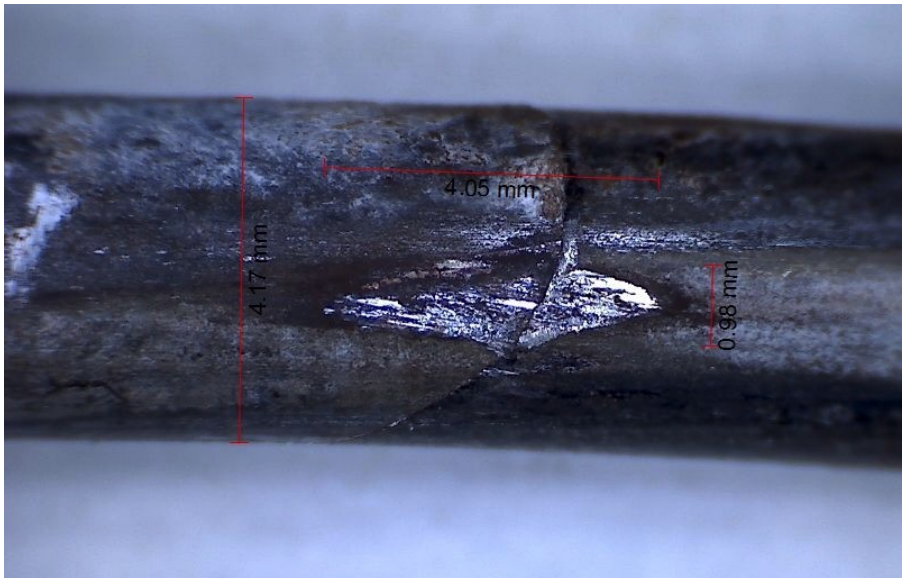

Figure 5-7 – Close-up of concrete-wire fretting damage on an external wire of the 7-wire prestressing strand as extracted from the beam after failure

Figure 5-8 – Close-up of inter-wire fretting damage on an external wire of a 7-wire prestressing strand as extracted from the beam after failure

Figure 5-9 – Close up of the fracture surface of the wire shown in Figure 5-7 & Figure 5-8

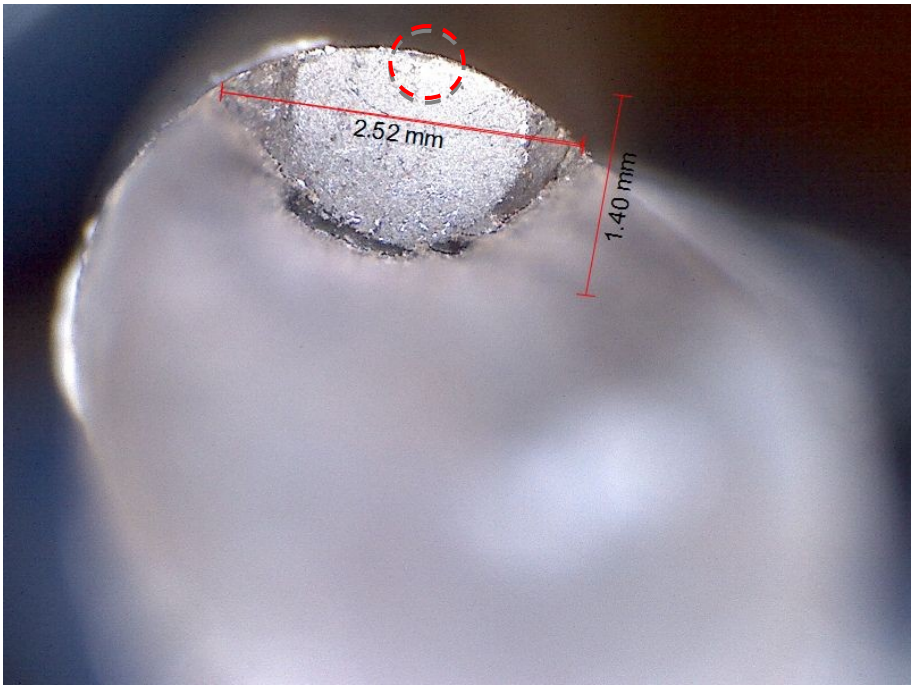

Figure 5-10 – Fatigue fracture plane of the wire shown in Figure 5-7 & Figure 5-8

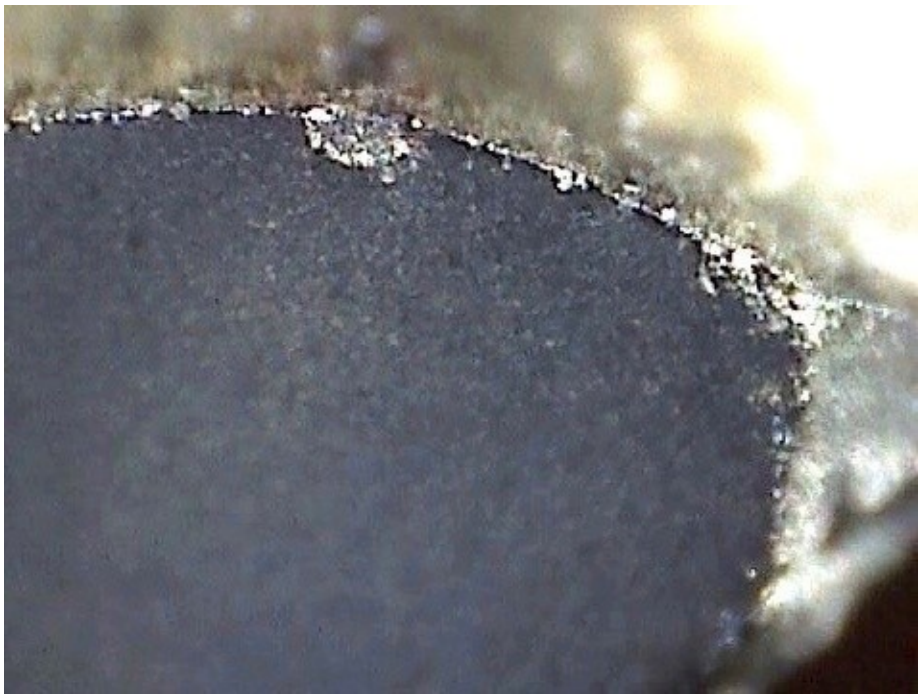

Figure 5-11 – 200× magnification of the fretting damage circled in Figure 5-10

Figure 5-12 – 200× magnification of a sample the fretting damage

5.4.2 Fatigue resistance of a corroded single wire-in-air and a corroded strand-in-a beam

A second feature from Figure 5-3 is the significant degradation in the fatigue life resistance of corroded wire-in-air specimens compared to the resistance of the smooth wire-in-air specimens. For clarity of presentation Figure 5-13 shows these two data sets together with the wire in air data but without the remaining experimental results.

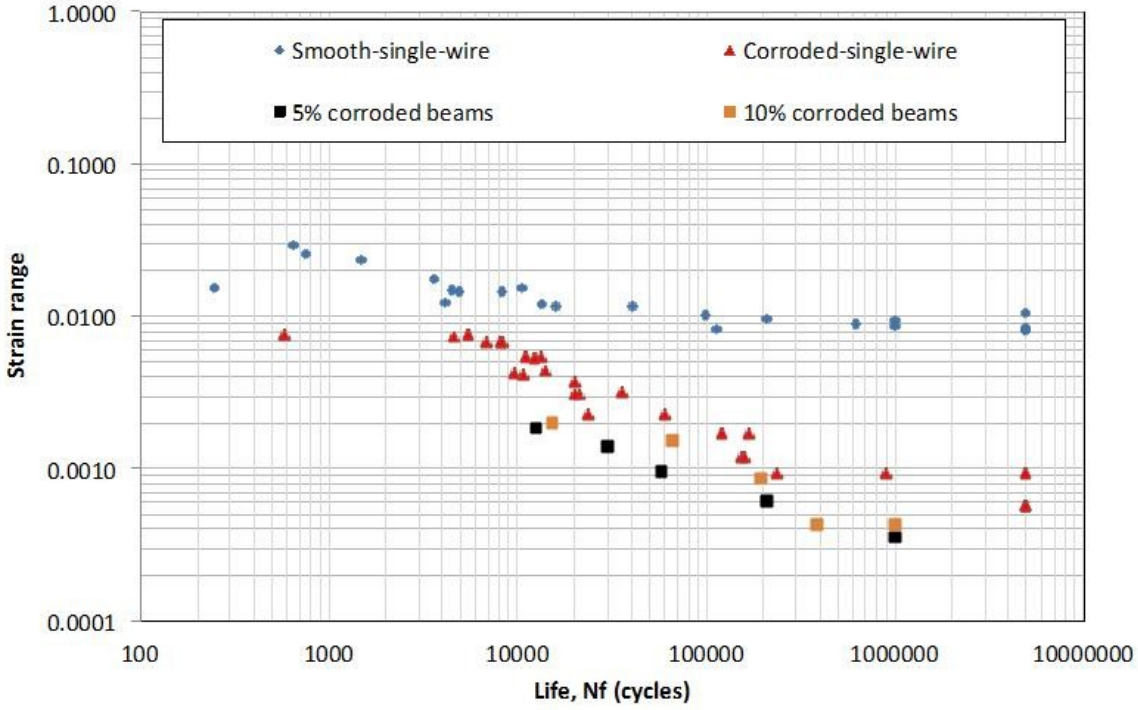

Figure 5-13 – Strain range-fatigue life behaviour of wire-in-air, corroded-wire-in-air & (5% & 10%) corroded strand-in-a beam

At short fatigue lives the difference in behaviour between the wire-in-air specimens and the remaining data sets is small, but at long lives a the fatigue limit of the corroded wire-in-air and corroded strand-in-beam specimens drops almost 10 fold and 20 fold respectively in comparison to the smooth wire-in-air specimens. In addition, the corroded strand-in-beam specimens

exhibited further deterioration in comparison to the corroded wire-in-air specimens. An initial examination of the corroded wires reveals corrosion damage in the form of bold overall surface degradation and distinct corrosion pitting. Inspection of the fracture locations showed that the failures occurred at pit locations, and the fracture plane passed through pitted cross sections.

Pitted cross-sections were inspected under a microscope to study the variations in pit shape and geometry. The observed pits were irregular in shape, with similar irregularities for different specimens but the pitting dimensions (depth and width) varied widely. The pitting surface was observed to be rough with many visible imperfections. Figure 5-14 and Figure 5-15 show a general view of corrosion pitting on a wire and on a strand specimen respectively. Figure 5-16 (a to f) presents six (6) samples of pitted cross sections with pit depths varying from approximately 0.3 mm to 1.15 mm, with an average pit depth of 0.6 mm. It is worth noting here that the original (non-corroded) single wire diameter is approximately 4.2 mm, and the measured corroded wire diameter ranged approximately between 3.65 mm to 4.13 mm.

Based on the above observations, it is reasonable to assume that the deteriorated fatigue resistance of corroded wire-in-air specimens is caused by a stress concentration due to corrosion pitting coupled with an amplification of the stress concentration due to an internal imperfection inside the pit probably due to stress corrosion cracking as reported in the review of the literature, in Section 2.5.1. As for the additional fatigue resistance degradation exhibited by the corroded strand-in-beam, this is the result of the combined impact of the corrosion pitting and concrete fretting. This impact can be observed by comparing the strain range-fatigue life data of the corroded-strand-in-beam to the corroded-wire-in-air data.

Figure 5-14 – Failure at a corrosion pit location on a wire specimen

Figure 5-15 – Failure at a corrosion pit location on a strand specimen

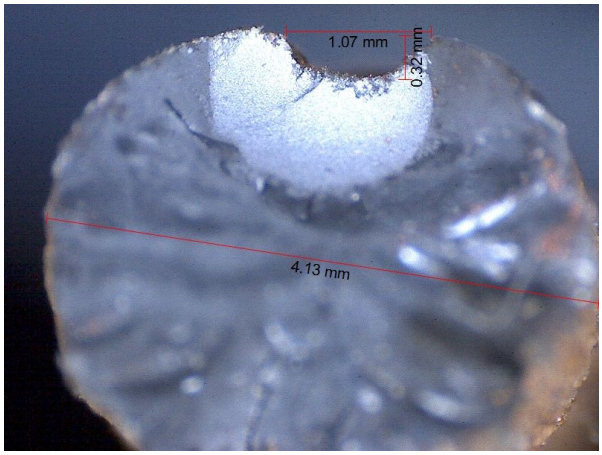

(a)

(b)

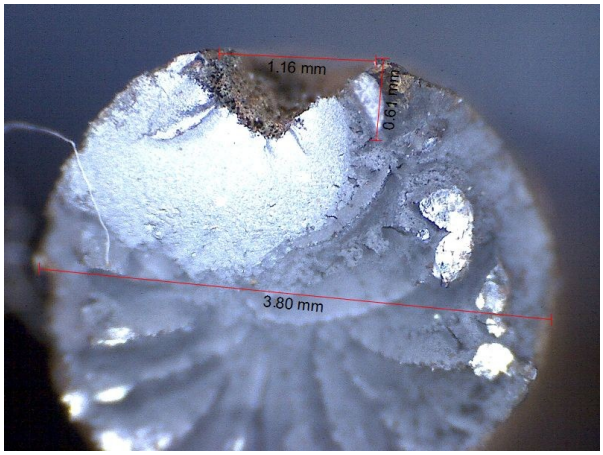

(c)

(d)

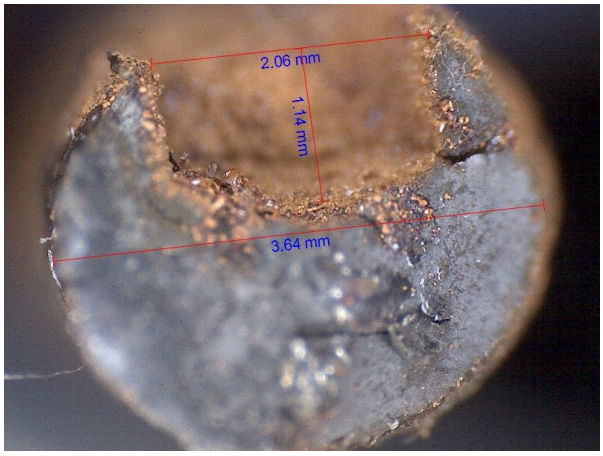

(e)

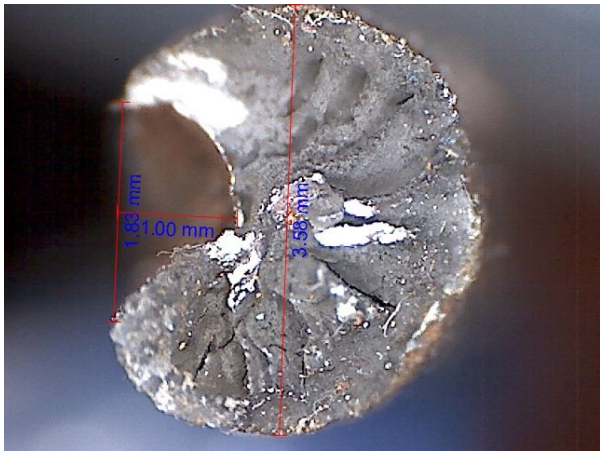

(f)

Figure 5-16 – Pitting cross section through the failure plain on corroded single wire specimens

5.4.3 Comparison of the fatigue resistance of non-corroded and corroded strand-in-beam specimens

In this section the impact of corrosion on the fatigue resistance of the corroded strands-in-beam specimens in comparison to the non-corroded strand-in- beam specimens is discussed. Figure 5-17 presents the experimental data for the non-corroded and corroded strand-in-beam specimens. By comparison it is evident that corrosion further degraded the fatigue resistance of the strand-in-beam specimens. This is attributed to the added stress concentration due to corrosion pitting coupled by wire to concrete surface fretting for the corroded strand-in-beam data.

Based on this observation it should be expected that the strand-in-beam specimens with the higher corrosion level (10% by mass loss) should exhibit more degradation in comparison to the strand-in-beams specimens with 5% corrosion level. However, this is not observed, rather the experimental data for the strand-in-beam specimens indicates that the strand-in-beam specimens with 10% corrosion level exhibit an improvement in their fatigue resistance in comparison to the stand-in-beam specimens with a 5% corrosion level. Further discussion about the cause of this apparent improvement is presented later in this chapter.

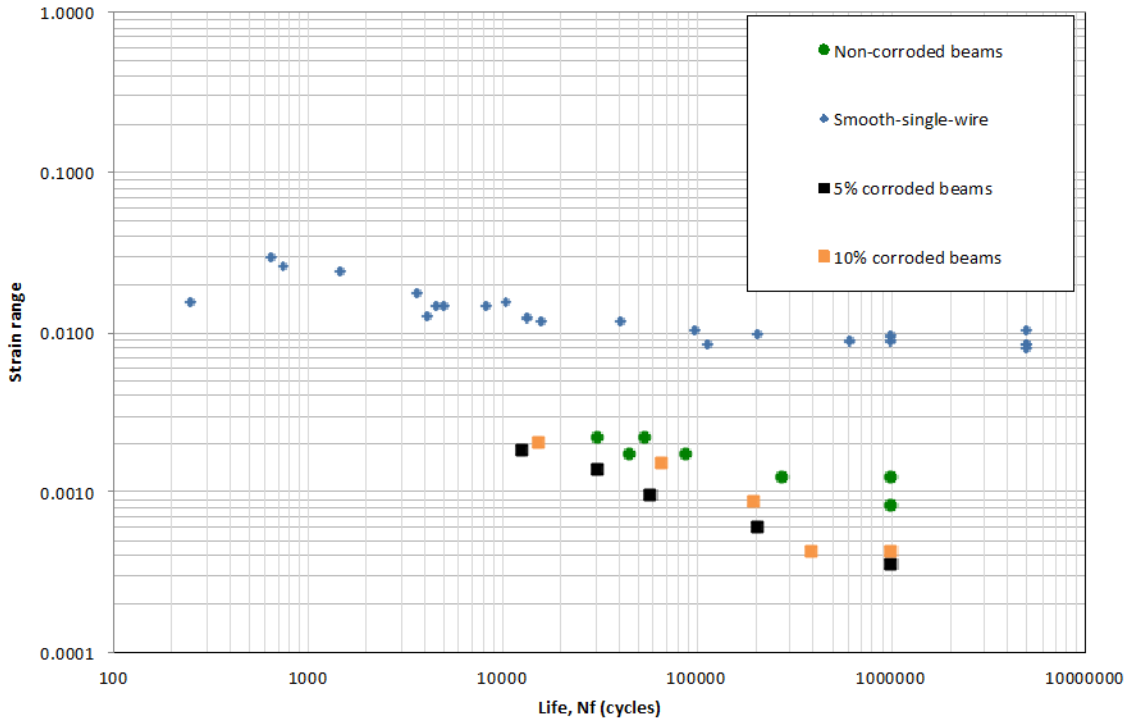

Figure 5-17 – Comparison of the Strain range-Life behaviour of non-corroded strand-in-beam & (5% & 10%) corroded strand-in-beam

5.4.4 Fatigue resistance of corroded strand-in-beams repaired with CFRP

Finally in this section in the impact of the using CFRP to repair corroded beams is discussed. Carbon Fibre Reinforced Polymer sheets typically contribute to the flexure strength of a member by acting as a supplementary reinforcement to the existing ones. The CFRP contributes in resisting the tensile stresses developed at the soffit of the beam, and therefore reduces the stress in the original reinforcement in comparison to what would have been applied in its absence.

Figure 5-18 presents the strain range versus the fatigue life data for the corroded strand-in-beam repaired with CFRP specimens, and the data for the non-repaired corroded ones. For the specimens corroded to 5% by mass loss the improvement is evident and the fatigue resistance is

restored to that of the non-corroded strand-in-beam specimens. However, for the specimens corroded to 10% by mass loss the fatigue response of the repaired specimen exhibits similar scatter to that of the non-repaired specimens that it is unclear to whether any improvement occurred.

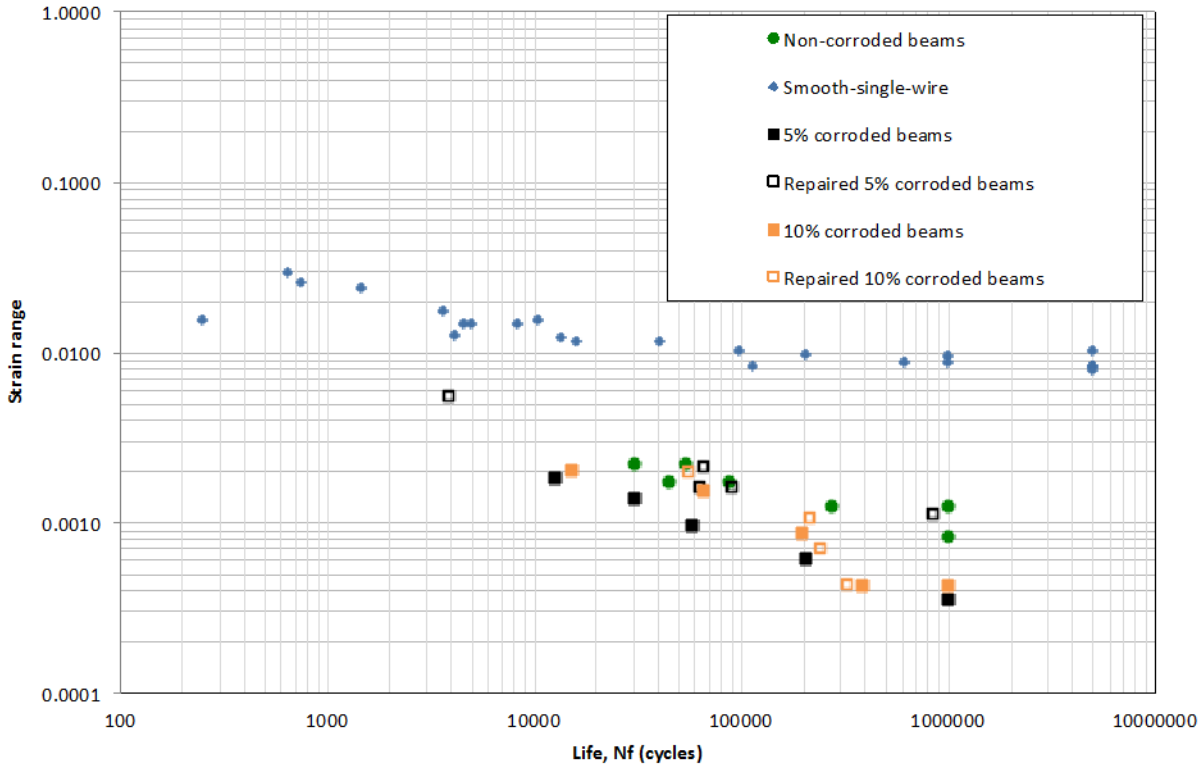

Figure 5-18 – Strain range versus the fatigue life data for the corroded strand-in-beam non-repaired and repaired with CFRP specimens

5.5 Fracture Mechanics of Fatigue Crack Propagation

It is widely known that notches or flaws in a component are the usual sources of fatigue crack initiation. A component's fatigue life is spent growing/propagating a crack from initiation in a crack or flaw until it reaches the critical/failure crack length (a_f) at which sudden fracture occurs. The impact of a notch or flaw on the fatigue life of a component depends on multiple factors; the notch or flaw geometry, the applied fatigue stress range, and the fatigue crack growth characteristics of the material. In order to analyze and model the fatigue behaviour of individual wires and the prestressing strand; fatigue crack propagation using fracture mechanics combined with simulated flaws representing the stress concentration due to the corrosion pitting and/or fretting due inter-wire contact and wire contact with concrete are utilized in this chapter.

Before presenting an analysis of the results, basic fatigue and fracture mechanics terms that are used in the analysis of crack growth are introduced. Terms that define cycling loading are defined below and are presented graphically for constant amplitude load cycling, in Figure 5-19.

- *Mean nominal stress*, is the average of the maximum and minimum nominal stress during a loading cycle, Equation (5-3)

$$S_{mean} = \frac{S_{max} + S_{min}}{2} \tag{5-3}$$

- *The nominal stress range* is the difference between the maximum and minimum nominal stress during a loading cycle, Equation (5-4).

$$\Delta S = S_{max} - S_{min} \tag{5-4}$$

- *The nominal stress amplitude* is one half the stress range, Equation (5-5).

$$S_{ampl} = \frac{S_{max} - S_{min}}{2} \tag{5-5}$$

- *The stress ratio* is the ratio of the minimum nominal stress to the maximum nominal stress, Equation (5-6).

$$\mathrm{R} = \frac{S_{min}}{S_{max}} \tag{5-6}$$

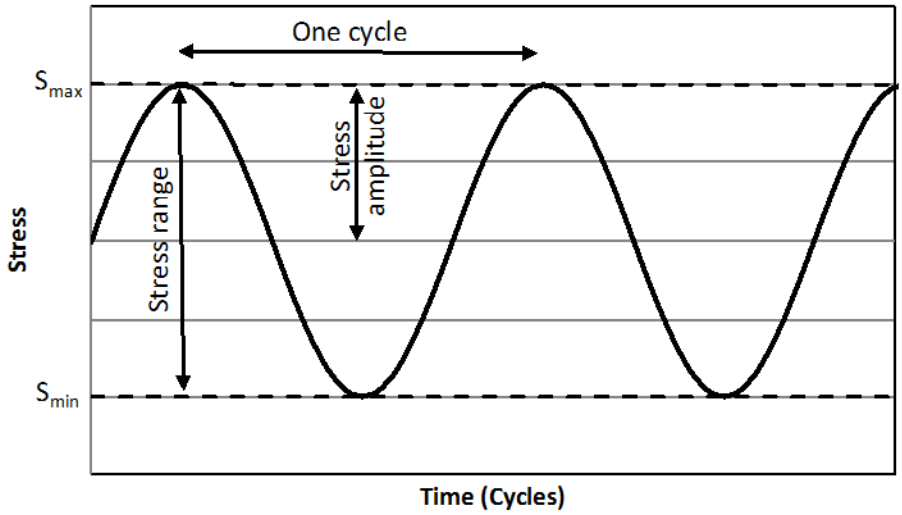

Figure 5-19 – Constant amplitude cyclic loading

The range of the stress intensity factor ΔK is a measurement of the severity of a crack or a crack-like flaw and is the main variable affecting the growth rate. Using Fracture Mechanics (FM) *ΔK* is given by Equation (5-7) for a linear elastic solution, or by Equation (5-8) for a plastic-elastic solution where it is given in terms of the strain range:

$$\Delta K = F \Delta S \sqrt{\pi a} \tag{5-7}$$

$$\Delta K = FE\Delta\varepsilon\sqrt{\pi a} \quad (5\text{-}8)$$

F: a dimensionless shape factor

E: modulus of elasticity

ΔS: Stress range

$\Delta\varepsilon$: Strain range

a: Crack length

Since K and S are proportional for a given crack length; then the range of the stress intensity factor can be written as follows:

$$\Delta K = K_{max} - K_{min} = FS_{max}\sqrt{\pi a} - FS_{min}\sqrt{\pi a} \quad (5\text{-}9)$$

$$= F\varepsilon_{max}\sqrt{\pi a} - F\varepsilon_{min}\sqrt{\pi a} \quad (5\text{-}10)$$

It should be noted that due to the dependence of ΔK on the crack length (a) the crack propagation rate increases as the crack length increases. The fatigue crack growth is defined as an incremental increase in crack length (Δa) due to application of number of loading cycles (ΔN), and therefore is the ratio of (Δa/ΔN). If the crack length is plotted against the number of load cycles on logarithmic scales we have a curve such as the one shown in Figure 5-20.

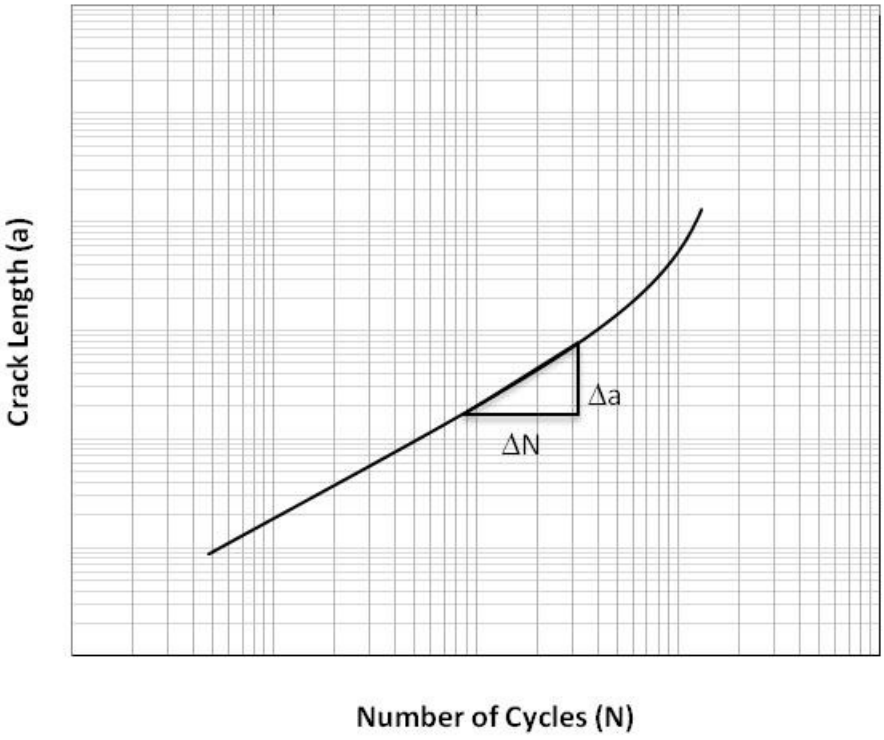

Figure 5-20 – Graphical representation of the fatigue crack growth rate

5.5.1 Fatigue crack growth rate

Expressions defining the crack growth rate date back to the early 1960s. These expressions relate the crack growth rate (da/dN) to the stress intensity range (ΔK) in the form of Equation (5-11), Paris (1964).

$$\frac{da}{dN} = A\Delta K^m \tag{5-11}$$

The crack growth rate versus stress intensity range curve is considered to be a material property for a given stress ratio. Once defined it can be used, for given test conditions, to numerically propagate a crack within the specimen/component to a critical crack length (a_f) which will cause failure either by brittle fracture or by plastic yielding. By knowing the crack growth rate, the

crack growth life can be obtained by means of a numerical integration of the crack growth rate equation for a range of the crack length, ranging between the initial crack/crack-like-flaw length (a_i) to the failure crack length (a_f). The fatigue life (crack growth life) is defined as the area under the curve of the dN/da versus the crack length (a) and expressed by the integral presented in Equation (5-12).

$$N_f = \int_{a_i}^{a_f} \left(\frac{dN}{da}\right) da \qquad (5\text{-}12)$$

A typical fatigue crack growth rate versus stress intensity curve would consist of an initial slow growth rate region followed by an intermediate rate (steady rate) region, and then a third region of rapid growth rate just before fracture.

Figure 5-21 shows a graphical representation of the fatigue crack growth expression, Equation (5-11), by plotting (da/dN) on the y-axis against stress intensity range (ΔK) on the x-axis on a log-log scale. For the low growth rate region the slope becomes vertical at the stress intensity range threshold value, denoted ΔK_{th} in Figure 5-21. The stress intensity range threshold is defined as the value of ΔK below which the crack does not grow for a given stress ratio, which brings us to the effect of the stress ratio on the fatigue crack growth rate

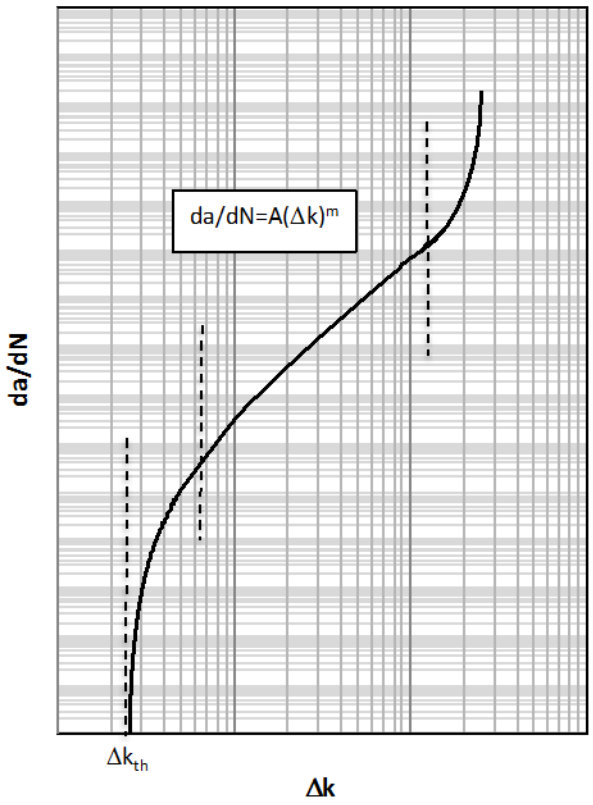

Figure 5-21 – Schematic of the different stages of fatigue crack growth

5.5.2 Effect of the stress ratio (R) on the fatigue crack growth rate

This effect is similar to the mean stress effect on the stress-life curves of some materials. The stress ratio increases with increasing mean stress, resulting in an increase in the fatigue crack growth rate and a decrease in fatigue life (i.e. the S-N curve shifts downwards). For fatigue crack propagation, as the mean stress increases a larger portion of the stress range becomes effective as the crack remains open for a larger portion of the applied stress range, and therefore the crack spends a greater portion of the fatigue life in a growing state. As the mean stress or stress intensity increases it reaches a stage at which the full stress range becomes effective (closure free

state, $\Delta\sigma_{eff}$). This is known as the intrinsic crack growth state, in which the stress intensity range threshold (ΔK_{th}) becomes the intrinsic stress intensity range (ΔK_i), see Figure 5-22.

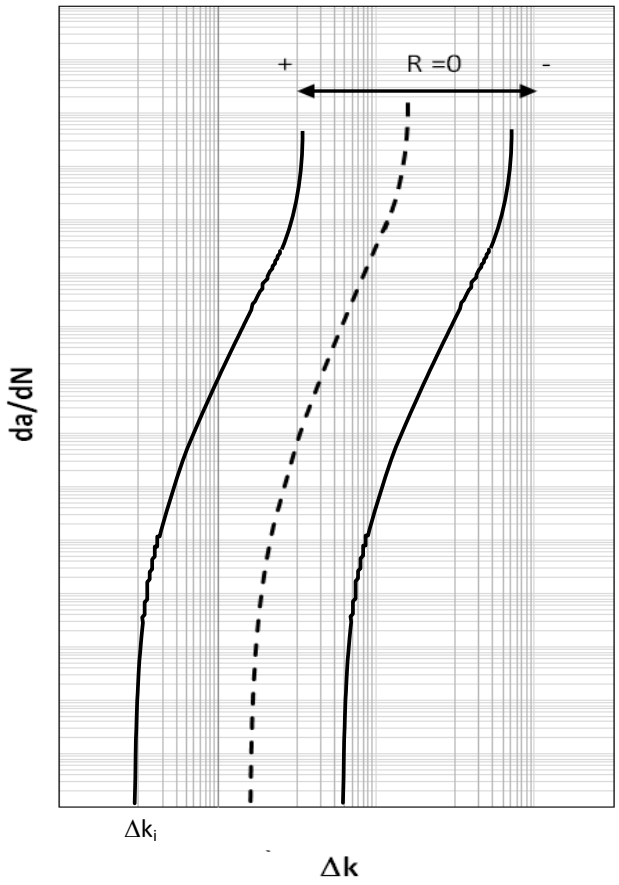

Figure 5-22 – Schematic showing the effect of the stress ratio on the fatigue crack growth rate

DuQuesnay el al. (1993) demonstrated that the strain-life data for all stress ratios fall on a single curve when the closure free strain range (the effective strain range, $\Delta\varepsilon_{eff}$) is plotted versus the fatigue life. The authors also observed that if the applied minimum stress is greater than a certain stress level for each material; then the stress range at the fatigue limit becomes constant for

further increases in mean stress. They thought of this stress level as a material constant describing the intrinsic material fatigue resistance similar to the intrinsic stress intensity threshold presented by Beevers (1981), ΔK_i. Another term introduced by the authors is $\Delta\varepsilon^*$, which represents the portion of the effective strain range responsible for causing damage and crack propagation. The relation between the effective strain range, intrinsic strain range, and $\Delta\varepsilon^*$ is presented by Equation (5-13):

$$\Delta\varepsilon_{eff} = \Delta\varepsilon_i + \Delta\varepsilon^* \tag{5-13}$$

$\Delta\varepsilon_{eff}$: is the effective strain range

$\Delta\varepsilon_I$: is the intrinsic strain range

$\Delta\varepsilon^*$: is the portion of the effective strain range causing damage

Historically researchers have found that when fatigue fracture is initiated from an uncracked site (usually a notch) or by very small flaws crack growth rates for small cracks are higher than those predicted from long crack data, Shijve and Jacobs (1964), Pearson (1975), and Dowling (1976).

In addition, it was observed that for very short cracks a transition occurs in which the critical stress for a crack to propagate becomes the fatigue limit stress rather than the threshold stress intensity.

To account for the behaviour of short cracks with the crack tip near a free surface, El Haddad et al. (1979) proposed a modification factor that increases the effective crack length by adding a constant length that depends on the applied stress ratio the material and its condition. This constant, referred to as an intrinsic crack length (a_o), is derived based on the premise that the

stress threshold for fatigue crack growth approaches the fatigue limit of a material for very short cracks. The above authors proposed the following expression:

$$\Delta K_{eff} = FE\Delta\varepsilon_{eff}\sqrt{\pi(a + a_{o)}} \tag{5-14}$$

$$a_o = \frac{1}{\pi}\left(\frac{\Delta K_i}{F\Delta\varepsilon_i E}\right)^2 \tag{5-15}$$

$$\frac{da}{dN} = A(\Delta K - \Delta K_i)^m \tag{5-16}$$

Where a_o : intrinsic crack length

ΔK : is the applied stress range

ΔK_i : is the intrinsic stress range

A : a material constant

m: a material constant

5.5.3 Effect of a notch on fatigue life

Fatigue failure of a component occurs as a result of a fatigue crack that initiates from an area of stress concentration and continues to grow throughout the fatigue life. Such an area of stress concentration can be a notch, a surface imperfection, a casting flaw or any other sort discontinuity in the component. Imperfections may be simulated by notches with various shapes based on their geometry.

One of two approaches, the strain-life approach or the fracture mechanics approach, usually are used employed to model the effect of a notch on the fatigue life of a component. The strain-life

approach is a simplified approach and is typically adequate when modelling a blunt notch (not a sharp radius) with a smooth geometry and no interior flaws. A stress concentration factor is used to account for the stress amplification based on the notch geometry and dimensions. This results in a constant reduction in the fatigue resistance for medium to long fatigue lives. This phenomenon results in an S-N curve that is parallel to the stress or strain versus fatigue life curve of a smooth specimen. Figure 5-23 presents a schematic of the effect of a blunt notch on the fatigue resistance of a component.

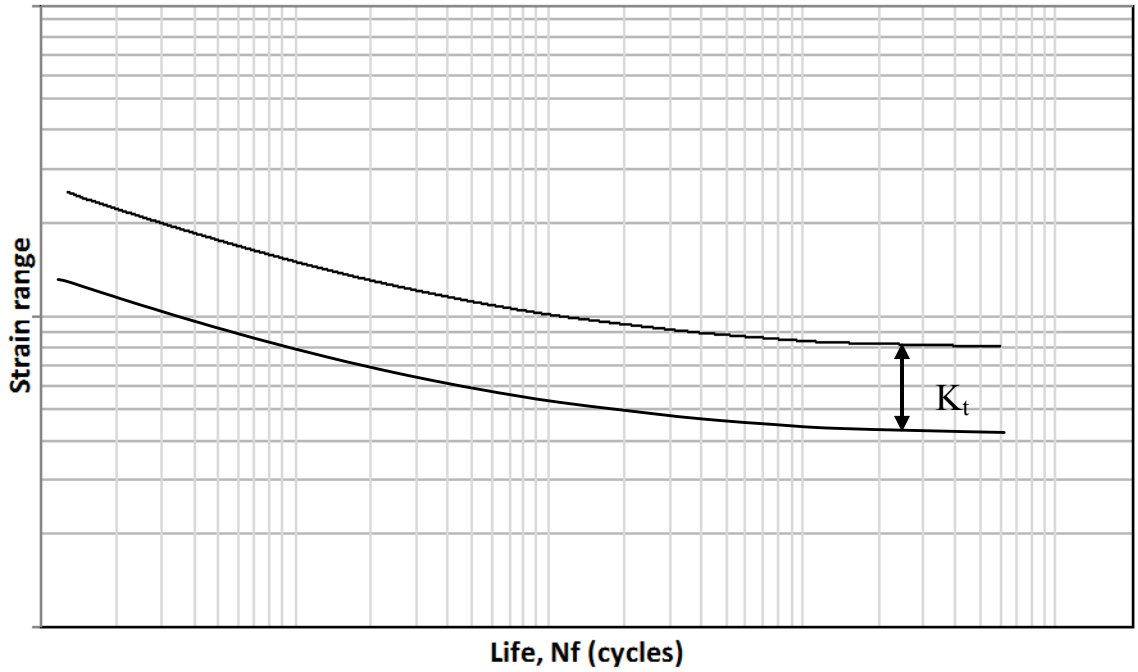

Figure 5-23 – Effect of a notch on the fatigue resistance

Many researchers have employed the strain-life approach in their analysis of the fatigue behaviour of corroded reinforced concrete beams and found it to yield good agreement to experimental data, with a fatigue notch factor (K_t) varying based on the pit geometry between 2

to 3 (Masoud et al., 2005; Soudki et al., 2007; and Al-Hammoud et al., 2011). Figure 5-24 presents the load range versus the fatigue life curves for non-corroded and corroded reinforced concrete beams by Soudki et al. (2007). The parallel downward shift in the fatigue response as described above can be observed by comparing the corroded beam response to the non-corroded one.

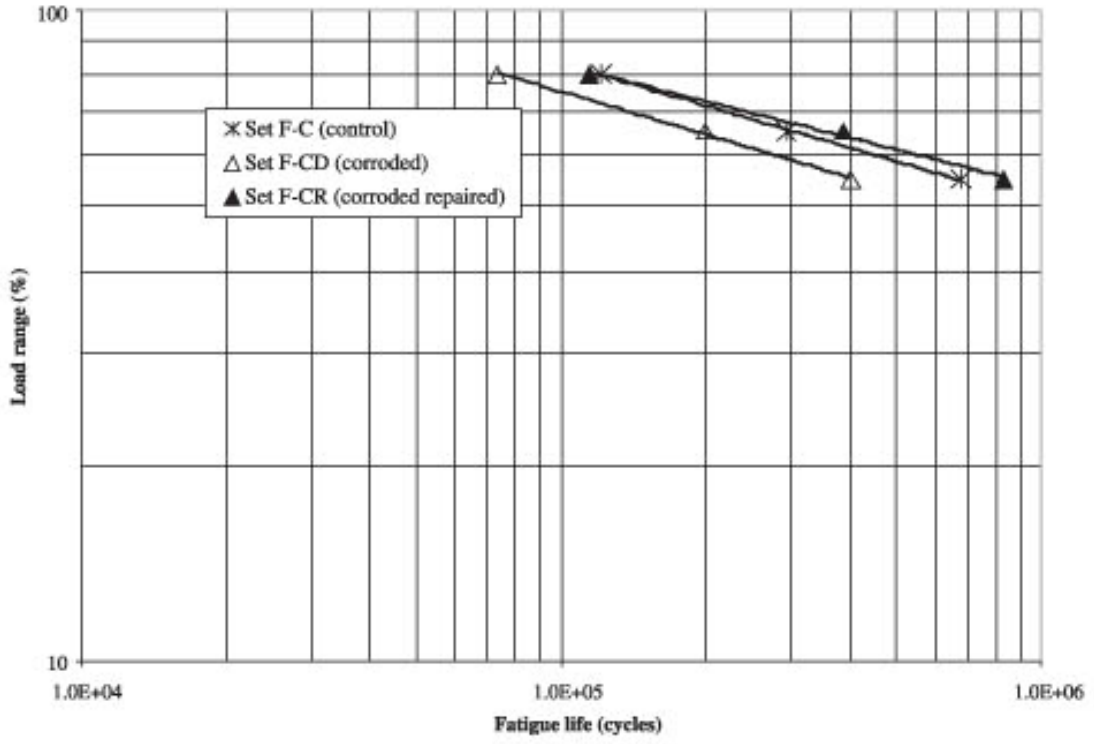

Figure 5-24 – Load range vs. fatigue life for non-corroded and corroded concrete reinforced beams (Soudki et al., 2007)

Alternatively, if the notch is not blunt or has internal flaws using the strain-life approach is no longer adequate, since the imperfection within the notch acts as a secondary notch/flaw with the primary notch, resulting in additional stress amplification. Furthermore, as the fatigue crack

continues to propagate and grow out of the notch zone the stress concentration at the crack tip due to the secondary notch rapidly reduces to the stress concentration factor for the primary notch so that its influence is felt only for small crack sizes.

The impact of a small notch or flaw within a larger notch on a crack is captured by the stress concentration factor for a flaw in a notch, which accounts for the geometry of the stress raiser and the length of the fatigue crack. An S-N curve for a specimen or component with a small flaw in a notch will show a decrease in its reduction in fatigue strength from that of a smooth specimen as the fatigue life decreases as schematically shown in Figure 5-25.

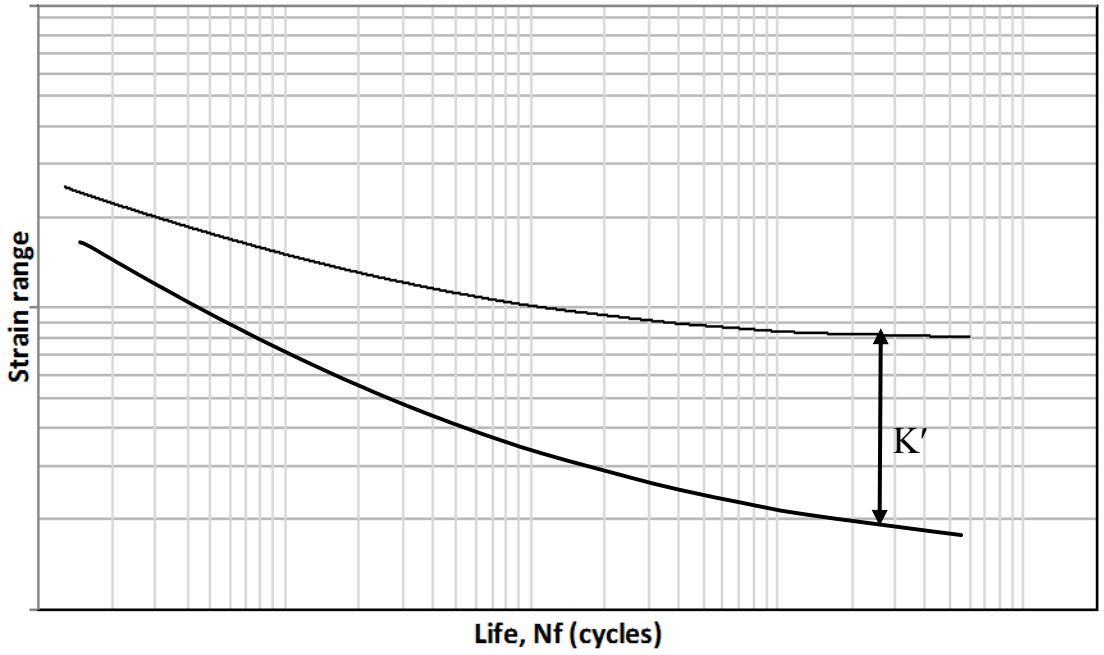

Figure 5-25 – Schematic of the impact of notch/crack within a notch on fatigue resistance

A fatigue response similar to that discussed above for a flaw within a notch was observed by Nurnberger and presented in Section 2.5.1, Figure 2-22 Nurnberger's comparison of the fatigue

resistance of cold drawn prestressing steel wires tested in air and in corrosion promoting aqueous medium (tap-water and sea-water) Figure 2-22 is presented again below as Figure 5-26.

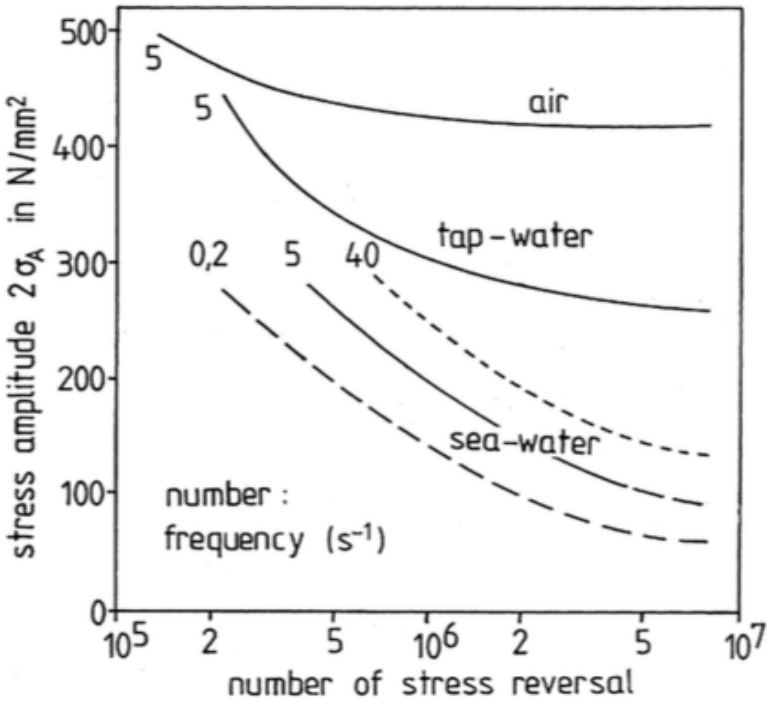

Figure 5-26 – Fatigue behaviour of cold drawn prestressing steel wire tested in air, tap-water and sea-water, (Nurnberger, 2002)

Referring back to the observations made from comparing the experimental fatigue behaviour of the non-corroded strand-in-beam specimens to the behaviour of the smooth wire-in-air specimens; the above-described effect of a notch/crack within a notch on the fatigue behaviour of a component is representative of the observed experimental response. In the next section a fatigue crack growth analysis using fracture mechanics is employed to analyze and model the fatigue behaviour of the fatigue tests presented earlier in this chapter.

5.6 Derivation of the Closure-free Crack Growth Rate Curve

A brief background summary of the fracture mechanics analysis of fatigue crack propagation was presented in the previous section. In this section deriving the closure-free crack propagation rate curve for the prestressing strand is discussed.

The derivation of the closure-free crack growth curve procedure used in this study is based on the procedure presented by Lam et al. (1998) using effective strain-life data. This procedure is suitable for this study as it takes an inverse problem approach by identifying a crack growth rate versus stress intensity range curve that would fit the observed experimental data. Lam et al. (1998) employed a value of 2.5 MPa for the intrinsic stress range (ΔK_i) for steels based on a large number of stress intensity factors collected by Taylor (1985). In this study that same value will be used.

Prior to presenting the derivation procedure it is worth re-mentioning the observation that the prestressing strand material exhibited no/insignificant mean stress effect during the fatigue testing, recall Section 4.3 (Figure 4-8). This is important as it leads to the conclusion that the stress range applied during the fatigue material testing of the smooth-wire-in-air is representative of an effective strain range (i.e. closure-free state).

Using the experimental strain-life data of the smooth-wire-in-air testing; the first step towards determining the fatigue crack growth rate is to assume an intrinsic strain range $\Delta\varepsilon_i$ that would result in a linear log-log curve of $\Delta\varepsilon^*$ versus N_f. Refer to Figure 5-27 which presents a schematic of the three curves of the $\Delta\varepsilon_{eff,}$, $\Delta\varepsilon_i$, and $\Delta\varepsilon^*$ against the fatigue life.

Knowing $\Delta\varepsilon_i$ and ΔK_i, the intrinsic crack length (a_o) can be calculated using Equation (5-15). Then assuming initial values of the material constants (A & m) and using numerical integration of Equation (5-16) for a = 0 to a = a_f, the crack growth life (fatigue life) is obtained. Where a_f can be conservatively assumed to be a value equal to half the specimen diameter. The diameter of the smooth-specimen-in-air was 2.2mm; therefore a_f was set to 1.1 mm.

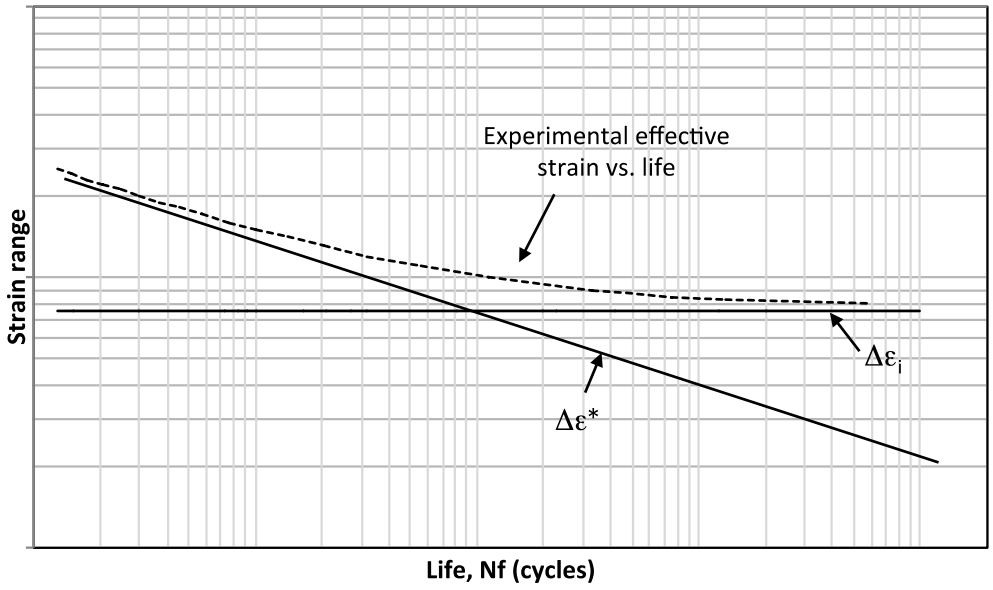

Figure 5-27 – Schematic showing fitting the experimental Strain-Life data by an assumed intrinsic strain range (Δεi)

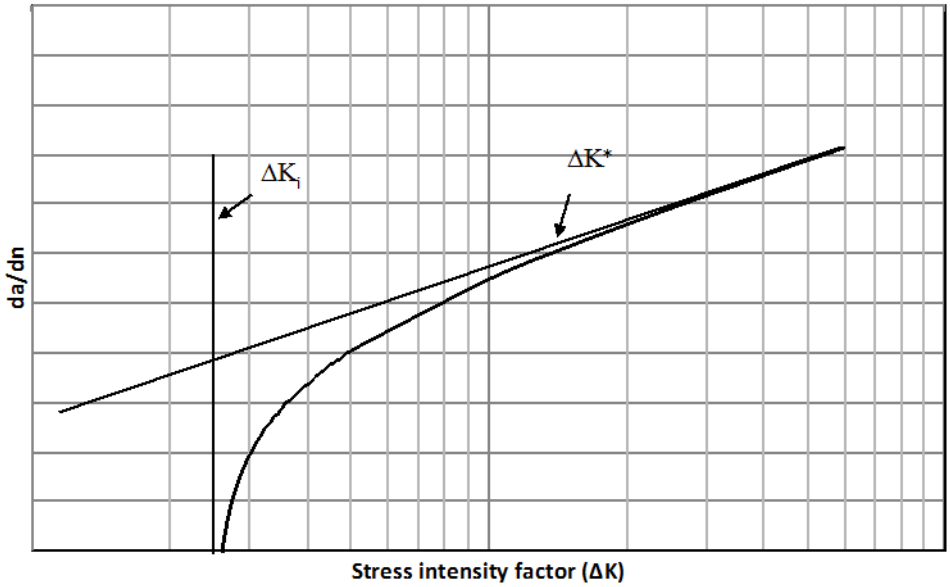

Figure 5-28 – Schematic of fatigue crack growth rate versus the stress intensity factor

The calculated fatigue life is compared to the experimentally observed values; if the values are not in good agreement then the initial values of the material constants (A & m) are changed, where (A) affects the vertical position rate and (m) affects the slope of the calculated strain life curve. It is easiest to attempt fitting two data points, one at a short/medium targeted fatigue life and the second at a targeted long fatigue life. For the first point the value of (m) should be kept constant, typically a value of 2 is a reasonable starting point McEvily (1969), while varying the value of (A) to fit the experimental date (the target fatigue life). If the calculated life is longer than the experimental life then (A) should be decreased to decrease the growth rate and therefore shorten the calculated fatigue life, and vice versa. Once the first data point is in good agreement with the experimental data, the second point is fitted to the experimental data by varying the

value of (m) while maintaining the value of (A). It is worth noting that more than one iteration may be required to achieve a good fit to the experimental data.

Finally, the crack is propagated using numerical integration for a range of values for the effective strain range ($\Delta\varepsilon_{eff}$), and the calculated strain range versus life curve for smooth specimens is compared to experimentally obtained data to ensure that the calculated curve accurately represents the experimental data.

The procedure described above along with an intrinsic strain range $\Delta\varepsilon_i = 0.0075$, and a crack shape factor (F) = 0.65 for a semi-circular crack were used to derive the crack growth rate versus stress intensity range curve of the prestressing wire from fully reversed (R=-1) constant amplitude smooth-wire-in-air fatigue data. Figure 5-29 presents the derived crack propagation curve, while Table 5-2 presents the crack growth rate parameters. The derived crack growth rate was then used to derive a complete strain-life curve, which (as expected) shows a good correspondence to the experimental data since the "A" and "m" where selected so that the derived strain-life curve fits the smooth wire-in-air experimental data, Figure 5-30.

Table 5-2 – Fatigue crack growth rate parameters

A=	9.0E-12	
m=	3.3	
Δk_i=	2.5	MPa
$\Delta \varepsilon_i$=	0.0075	

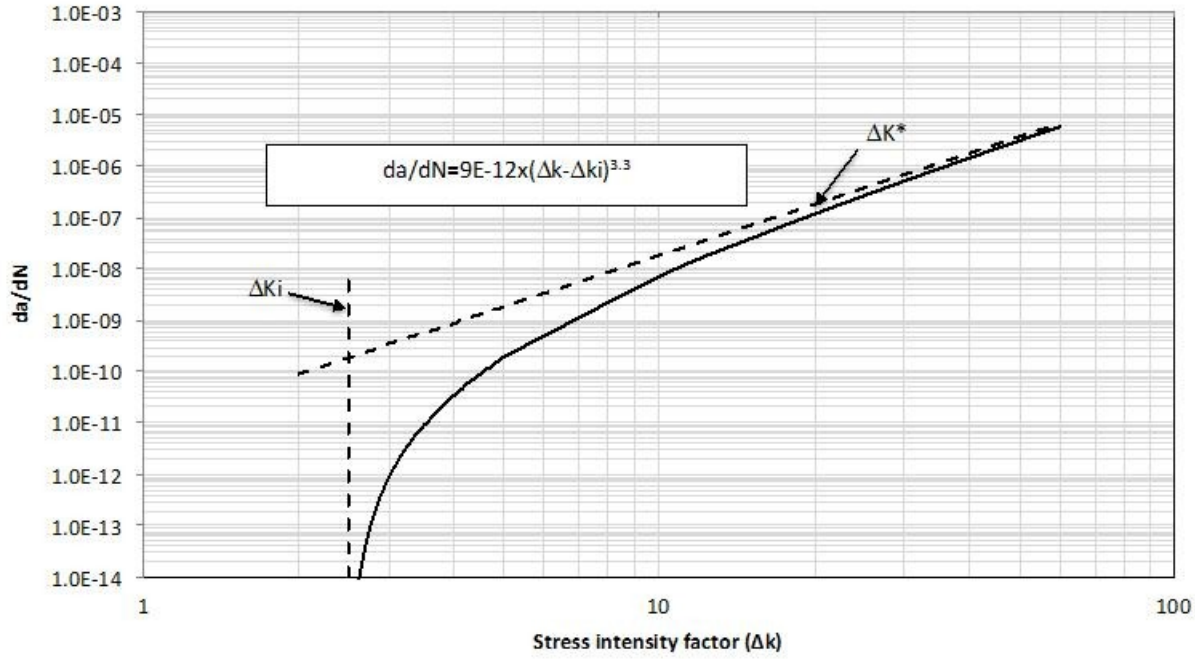

Figure 5-29 – Derived crack growth rate for 7-wire prestressing strand steel

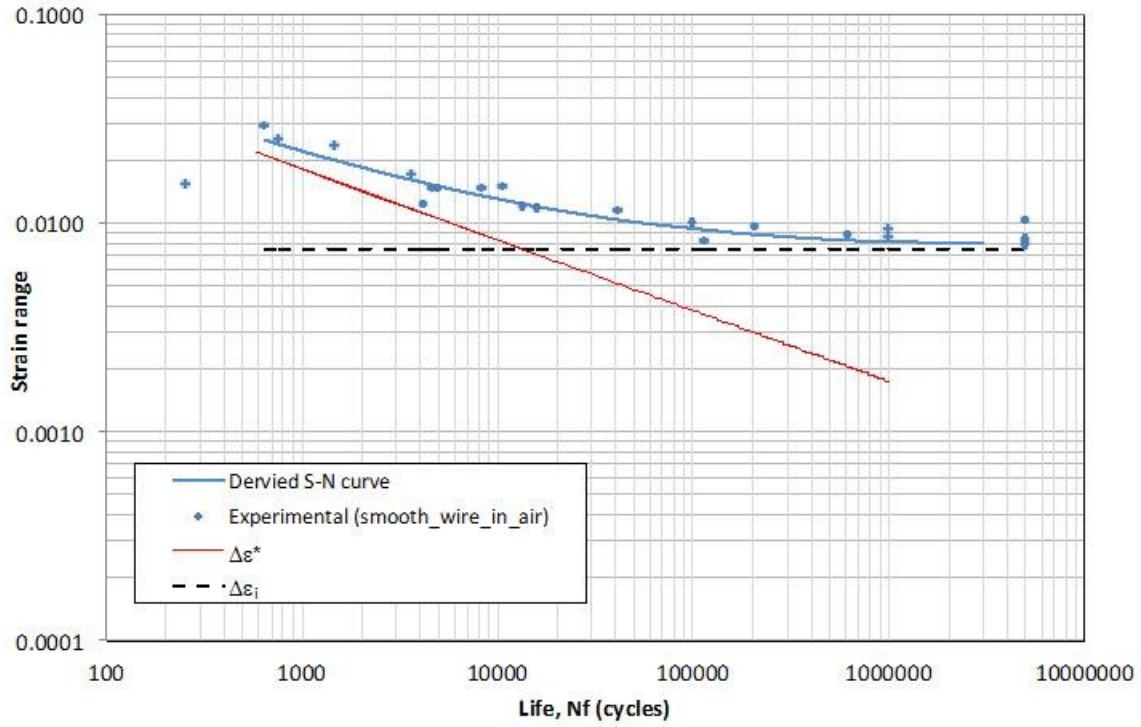

Figure 5-30 – Comparison of the Strain-Life curve based on the fracture mechanics analysis of small fatigue cracks to the smooth specimen fatigue data

5.7 Modelling of Deterioration of the Fatigue Resistance Due to Fretting Induced Flaws

As previously discussed in Section 5.4 the experimentally observed deterioration of the fatigue resistance between the single-wire-in-air data and the strand-in-air data was attributed to inter-wire fretting induced damage. Moreover, further deterioration of strand-in-beam data in comparison to the strand-in-air data was attributed to a more detrimental fretting between the concrete and the strand at concrete crack locations. In addition, the observed trend of an increase in the reduction in fatigue resistance as the fatigue life increases; is attributed to the fatigue crack spending an increasing fraction the fatigue life propagating out the notch zone at a near fatigue limit stress level.

In this section, the hypothesis described above is analytically examined by introducing an initial edge crack length of 0.001 mm into the smooth wire specimen to simulate fretting damage. The corresponding fatigue life is obtained by numerical integration of Equation (5-14) from a = 0.001 mm to a = a_f = 1.1 mm, using the fatigue crack growth rates presented in Figure 5-29. A schematic of the fatigue crack propagation from the fretting induced flaw is presented in Figure 5-31.

For very short fatigue lives, there would be no fretting damage, and as the number of cycles increases the fretting damage will increase. Therefore, the expected response would give rise to a strain-fatigue life curve with an increased slope for shorter lives converging with the stain-fatigue life curve of the smooth single-wire specimens. Hence simulating the fretting damage by introducing an initial crack at the beginning of the fatigue life (i.e. zero cycles) would not accurately represent the effect on fatigue life of the fretting damage mechanism at short lives. A

simple approach to incorporate the fretting damage in fatigue crack growth was utilized, and the modelled strain range versus fatigue life curve for the non-corroded-strand in beam specimens together with the experimental data is presented in Figure 5-32.

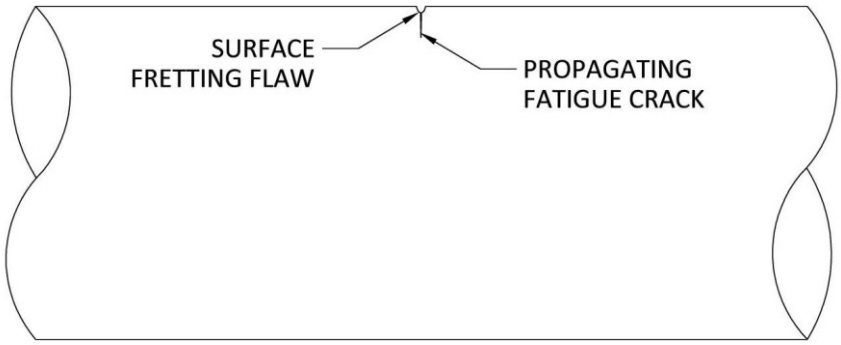

Figure 5-31 – Schematic of the fatigue crack propagation from the fretting induced flaw is presented

This approach assumes a linear correlation between the crack growth due to fretting damage and fatigue life (number of cycles). This was implemented in the fatigue life modelling by introducing an incrementally increasing initial crack size representing the fretting induced damage over the first 10,000 cycles (at zero cycles the initial fretting crack length is equal to zero and it linearly increases to a_i = 0.001 mm at 10,000 cycles). Although there is no short life strand-in-beam experimental data for comparison, it can be seen in Figure 5-32 that this approach is representative of the expected fretting induced damage response at short lives as explained above.

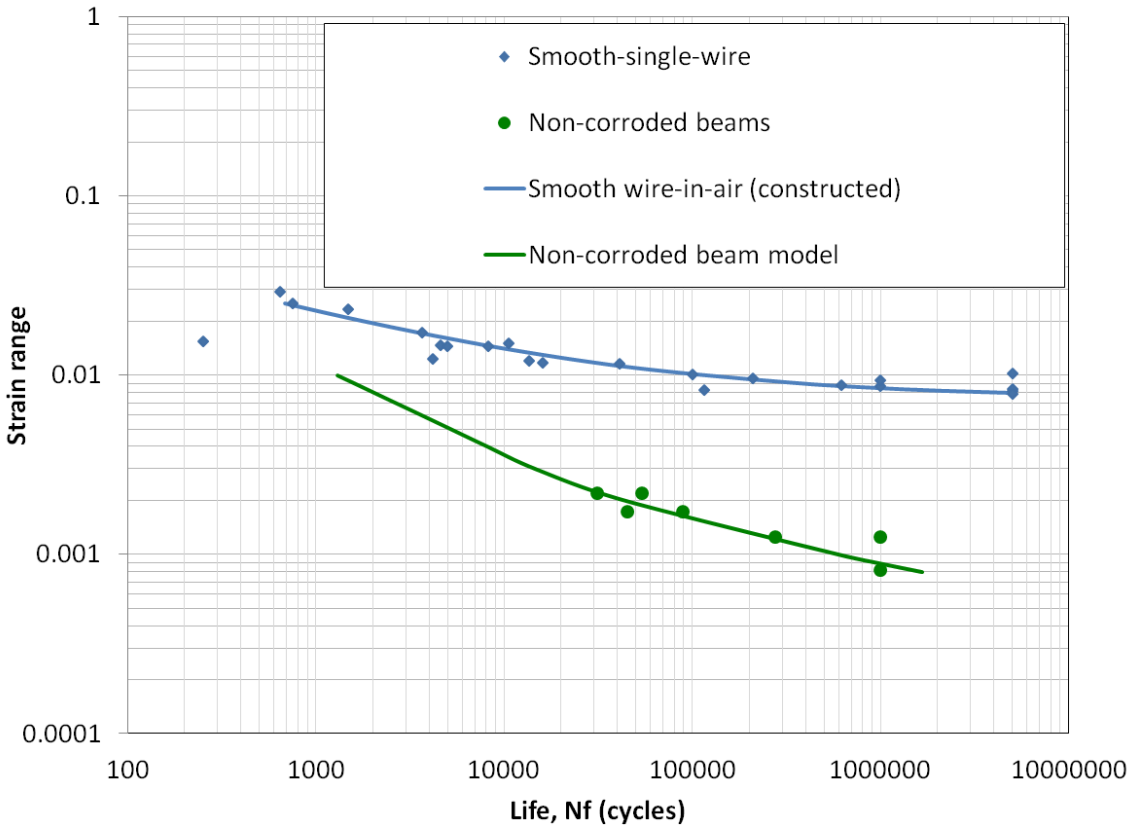

Figure 5-32 – Strain versus fatigue life comparison of experimental and modelled non-corroded-strand-in-beam specimens

The modelled fatigue life response represented by the solid green line in Figure 5-32 reasonably represents the experimental results as it falls within the experimental scatter band. To further evaluate the goodness of fit, a Two One-Sided Test (TOST) equivalence test was conducted. It is worth noting the run-out experimental results were not included in the goodness of fit assessment. The lower and upper bounds for the TOST were based on the 95% confidence interval on the difference between the mean of the experimental results and the mean of a power regression trend line. The TOST results showed that the experimental and modelled fatigue

responses are equivalent, with the significance level set at 5% and therefore with a confidence interval on the difference between the means of 90%.

The curve given by our fatigue life model is compared to the present experimental results and those previously presented in Section 2.4.3, by Ozell (1962), Rabbat et al. (1978), and Overman et al. (1984), see Figure 5-33. Although the majority the experimental results aggregated from the literature fall within a fatigue life region beyond our results (2 to 10 million cycles); by extending our modelled fatigue response, it is visually apparent that it is in a good agreement with the experimental data aggregated from the literature as it remains within their scatter band.

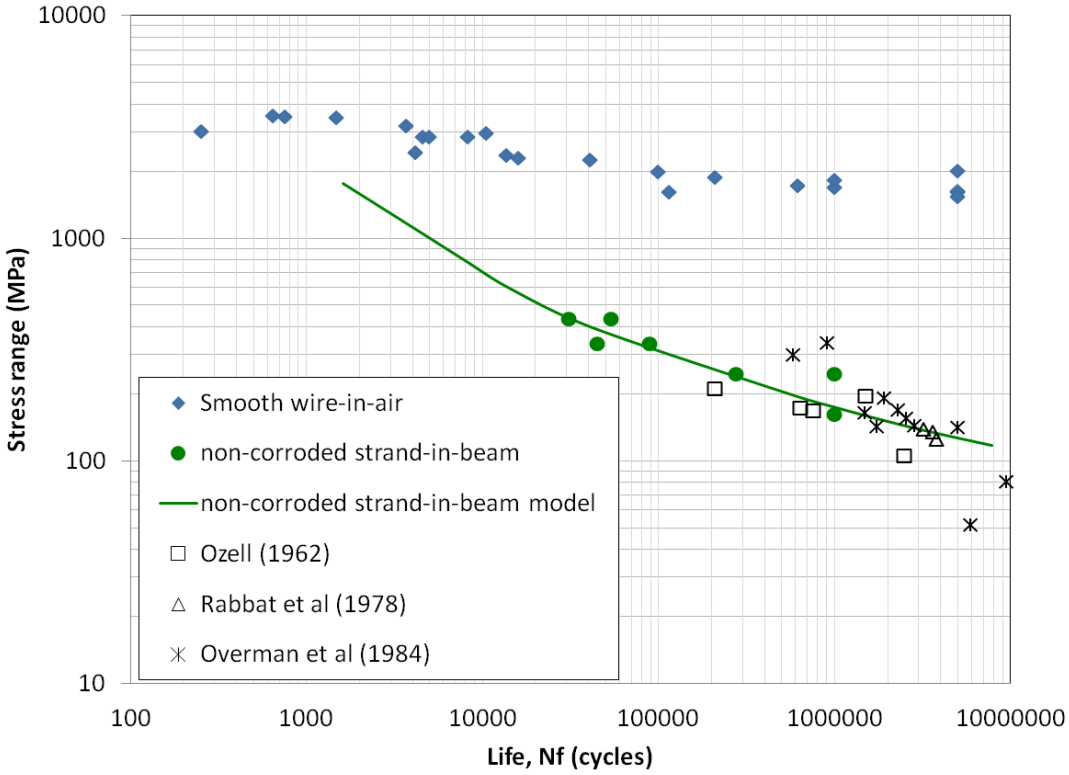

Figure 5-33 – Experimental results from the literature for pretensioned beams and fatigue life results and modelling from the present study

Referring back to the previous work presented in the background, Section 2.4.1, on fatigue testing of full 7-wire strand-in-air collected by Paulson et al. (1983); the predicted fatigue responses of the non-corroded strand-in-air and non-corroded-strand-in-beam specimens are compared to the Paulson et al.'s compiled experimental results from the literature for strand-in-air specimens, and the present fatigue data for our strand-in-beam tests Figure 5-34.

Figure 5-34 presents the modelled fatigue response of strand-in-air specimens fitted to the mean of the experimental data by Paulson et al. (1983), and also presents the prediction model by Naaman (1989). The strain-in-air model uses the same modelling approach used for the strand-in-beam predictions with an initial crack length of 0.0002 mm that was found to reasonably represent the mean strand-in-air experimental data of Paulson.

It is evident that Paulson's strand-in-air data and Naaman's model are unconservative estimates if used to model the behaviour of our prestressing strand inside a beam fatigue data (pretensioned beam behaviour). This is in agreement with a similar statement by Wollmann et al. (1996) about post-tensioned beams, but contradicts Overman et al.'s (1984) conclusion that Paulson's strand-in-air model could be used to model the fatigue behaviour of pretensioned beams. This contradiction is easily explained; as Overman et al. (1984) did not account for the fact that Paulson's model is a lower bound for fatigue life model of strand-in-air behaviour and not the mean. In order to accurately compare the strand-in-air fatigue model to the strand-in-beam behaviour, a model of the mean response of the strand-in-air specimens should be the reference rather than the lower bound one.

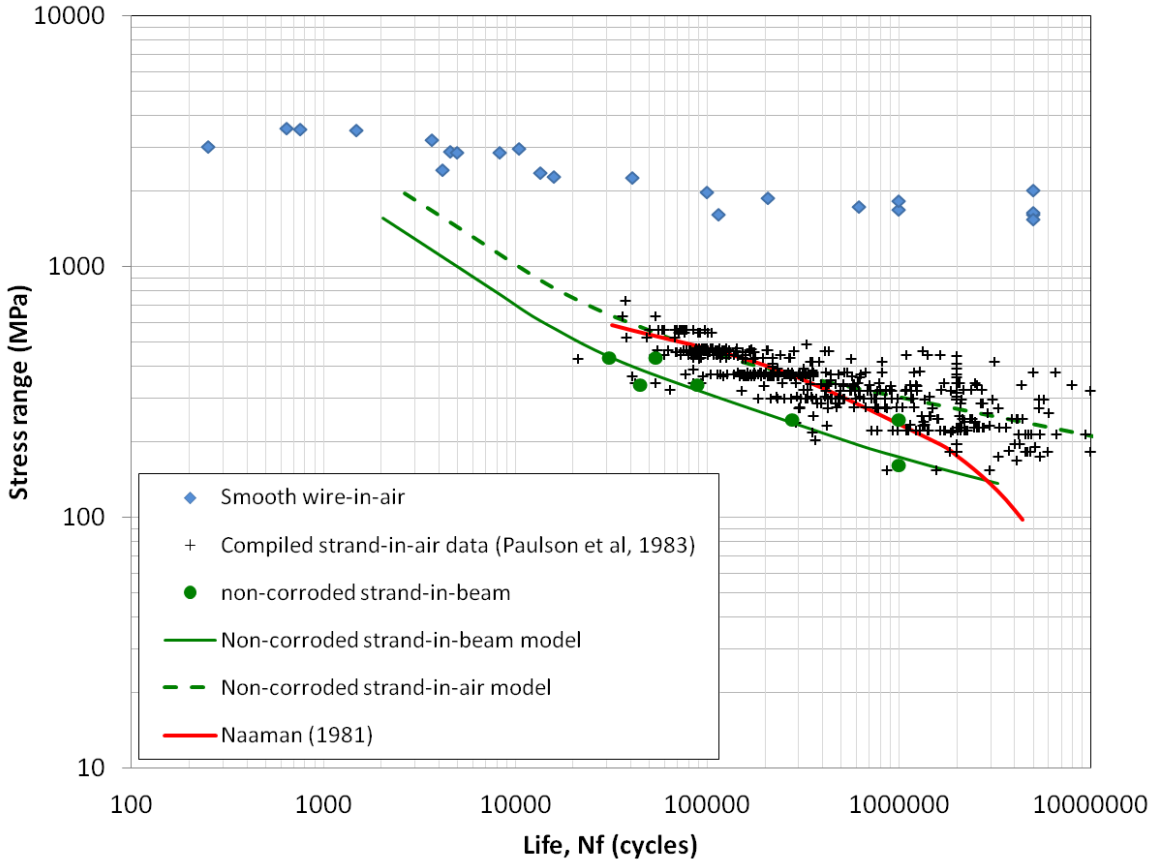

Figure 5-34 – Comparison of the modelled Strain-Fatigue life curve to Paulson et al. (1983) data using an incremental introduction of the fretting damage

5.8 Modelling of the Deteriorated Fatigue Resistance Due to Corrosion Pitting

In this section modelling of the deteriorated fatigue resistance due to corrosion pitting is presented. There are two components of the modelling presented herein. This first, is modelling of the fatigue resistance of corroded-single-wire in air specimens, and the second is the modelling of the fatigue resistance of corroded-strand-in-beam specimens.

5.8.1 Corroded single wire-in-air specimens

The cause of the deteriorated fatigue resistance of corroded-wire-in-air specimens is corrosion induced pitting. Referring back to Section 5.4.2, the observed pit cross sections had pit depths varying from approximately 0.3 mm to 1.15 mm, with an average pit depth of 0.6 mm. For modelling of the fatigue resistance of corroded-wire-in-air specimens the corrosion pitting is modelled by a hemispherical notch with a depth and notch root radius equal to the measured average pit depth of 0.6 mm and a flaw at the notch root. The notch geometry is used to determine the stress intensity factor of a crack emerging from a corrosion pit.

As previously discussed a component with a notch may be accurately modelled using strain-life approach by utilizing a stress concentration factor (K_t) to account the amplified stress at the notch location; which would result in a strain-fatigue life curve parallel to that of the smooth specimens (without a notch) strain-life curve but shifted downwards by division of the strain values by K_t (i.e. constant reduction is the fatigue resistance)

Figure 5-35 presents modelled fatigue life curves for corroded-wire-in-air-specimens using the strain-life approach with a notch factors (K_t) = 2.19, as presented in Peterson's Stress Concentration Factors, Pilkey (2008), to represent the average corrosion pit as a hemispherical

edge notch, and another curve with a notch factor (K_t) = 10 to fit the long fatigue life experimental data.

It is evident that the experimental fatigue behaviour of the corroded-wire-in-air specimens cannot be modelled using the strain-life approach and the corrosion pit as a blunt notch, since the predictions are extremely unconservative for medium to long fatigue lives. A K_t = 10 value that fits the long life fatigue data implies a, the corrosion pit that is very sharp which does not represent the observed pit shape. Moreover, the modelled curve based on a K_t = 10 is overly conservative and does not represent the experimentally observed fatigue response.

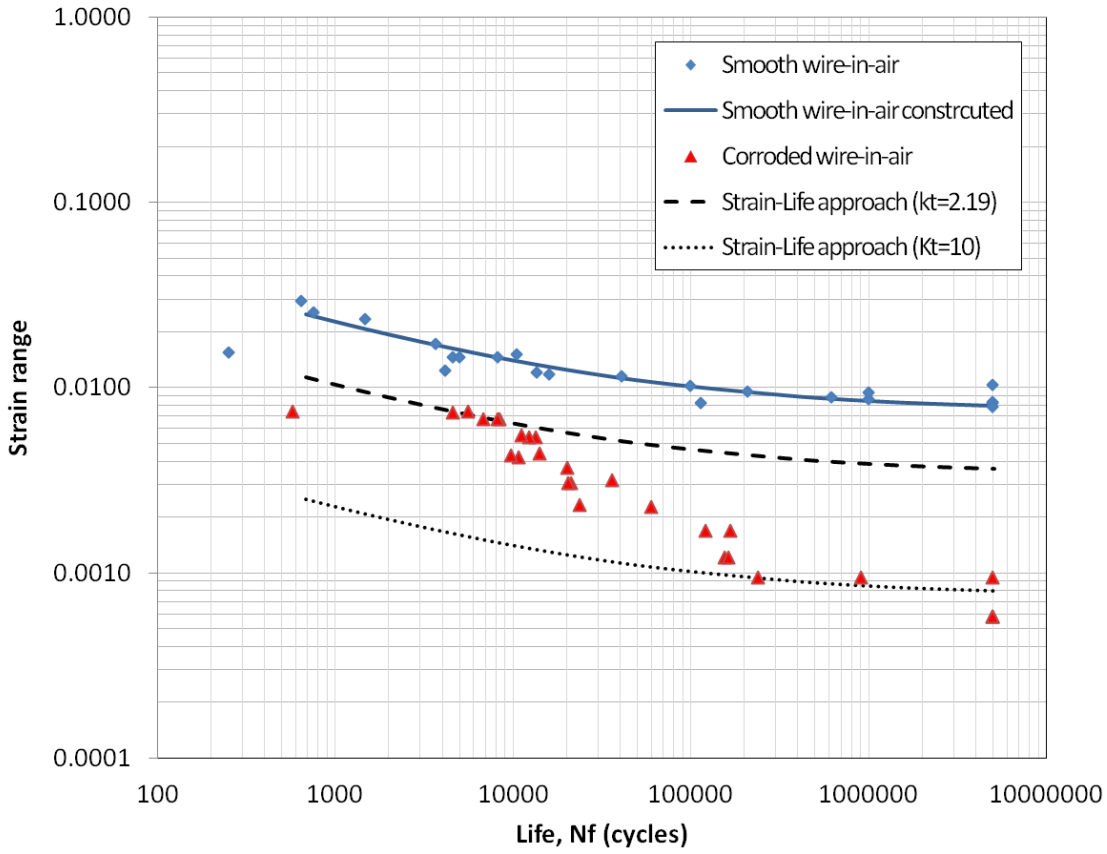

Figure 5-35 – Strain-fatigue life modelling using a strain-life approach (K_t=2.19 and 10)

Stress amplification at long fatigue lives of this magnitude, can only be explained by an initial crack or a flaw at the notch root, as previously discussed in Section 5.5.3. This leads to the second observation presented in Section 5.4.2 in regards to the observed roughness of the corrosion pit surface, which can be modelled as flaw at the notch (pit) root which can be accurately modelled using short crack strain based fracture mechanics solution for a fatigue crack propagating from a secondary interior notch at the root of the primary notch, see Figure 5-36.

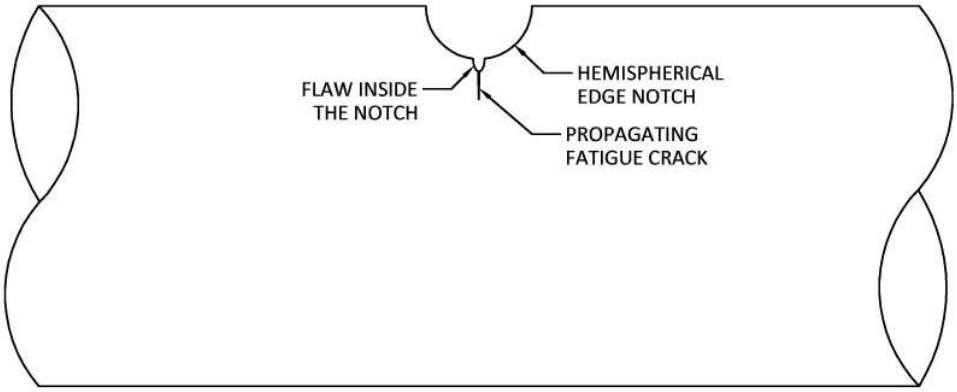

(a) Longitudinal section

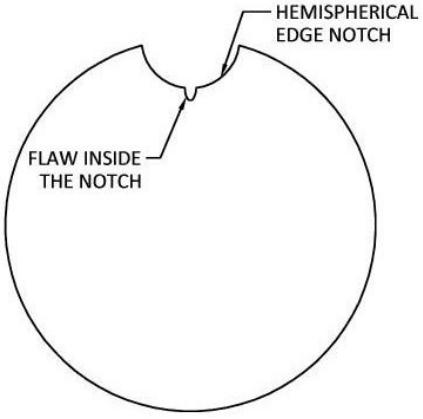

(b) Transverse section

Figure 5-36 – Schematic for a fatigue crack propagating from a secondary notch at the root of the primary notch

Multiple solutions for the stress intensity factor equations of a fatigue crack propagating from the notch root are available in the literature. In this study the solution by Xu et al. (1997) is used combined with a fatigue stress concentration factor (K_t) for a hemispherical notch of 2.19, and an initial flaw with an assumed depth of 0.0001mm is used to simulate the presence of a flaw at the notch root.

Numerical integration of Equation (5-14) is used to compute the modelled fatigue life for a full range of applied strain ranges using the solution of the stress intensity factor for crack propagating from the notch root by Xu et al. (1997) as defined by Equations (5-18) to (5-23). The modelled strain range versus fatigue life response is presented in Figure 5-37.

$$K_c = \frac{1}{2} g \left(1 + \frac{l}{\alpha\rho}\right)^{-1/2} \left[1 + \left(1 + \frac{l}{\alpha\rho}\right)^{-1}\right] \quad (5\text{-}17)$$

$$\alpha = 0.4629 + 0.0089K_t \quad (5\text{-}18)$$

$$\beta = 0.0639 + 0.1036K_t \quad (5\text{-}19)$$

$$g = 1 \qquad for\ {}^{l}/_{\rho} < \beta \quad (5\text{-}20)$$

$$g = 1 + \frac{\tan\left({}^{\pi}/_{2K_t}\right)}{1.7429 + 0.2136K_t}\left(\frac{l}{\rho} - \beta\right) \qquad for\ {}^{l}/_{\rho} \geq \beta \quad (5\text{-}21)$$

$$K_e = K_c \left[1 + 0.1215\left({}^{l}/_{l_t}\right)\right] \quad (5\text{-}22)$$

$$\Delta K_{eff} = FK'E\Delta\varepsilon_{eff}\sqrt{\pi(a + a_{o)}} \quad (5\text{-}23)$$

Where ρ : notch root radius (mm)

l : fatigue crack length (mm)

K_t : surface stress concentration factor based on notch geometry

K_c : stress concentration factor for symmetric cracks at the end of an elliptical hole (MPa√m)

K_e : stress concentration factor for a crack at the root of an edge notch (MPa√m)

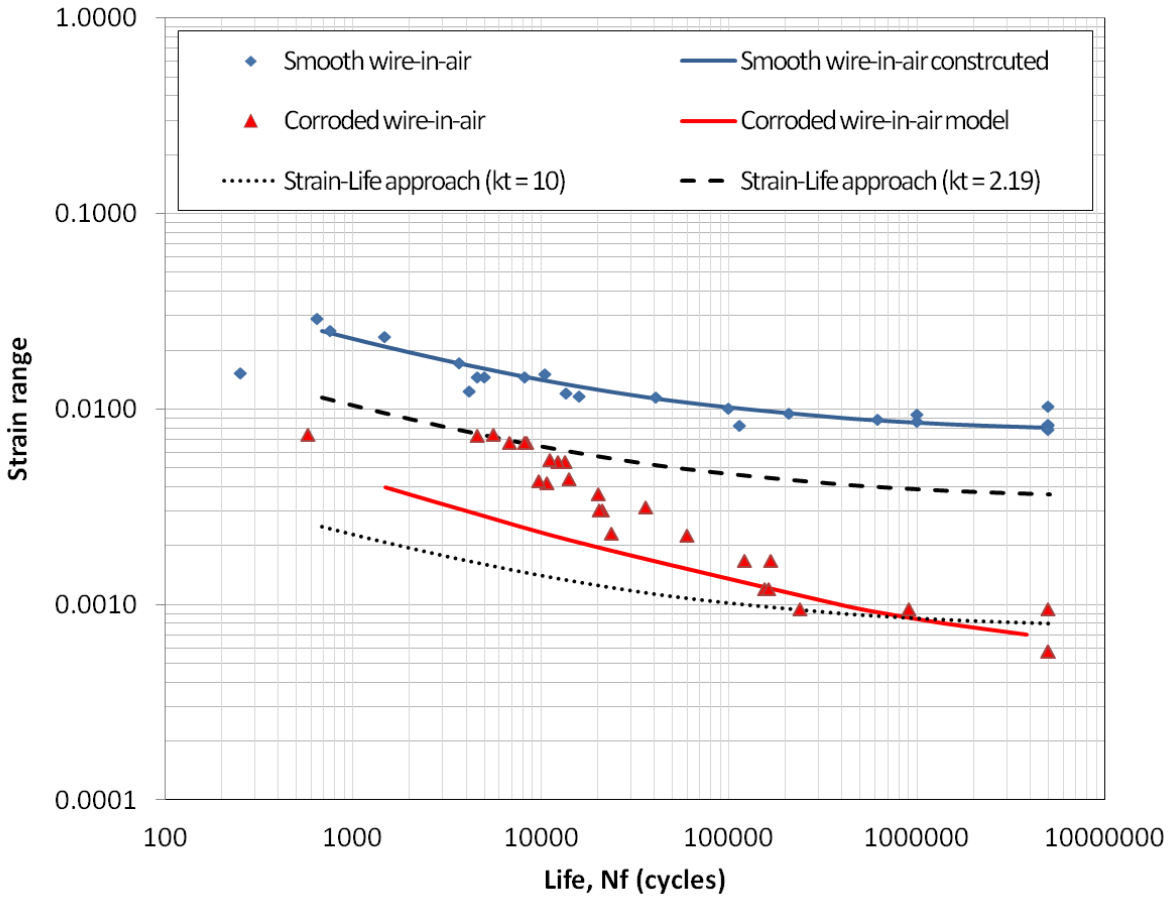

Figure 5-37 – Strain-fatigue life model of corroded-wire-in-air specimens

The modelled fatigue life presented in Figure 5-37 is a reasonable representation of the experimental results for mid to long fatigue lives, but it is conservative in comparison to the short life experimental data and falls outside the experimental scatter band.

Short fatigue lives corresponds to larger strain ranges, and respectively higher stresses. Coupled with the observation from Figure 5-35 that the modelled fatigue response using the strain life approach (that only accounts for the corrosion pit, K_t = 2.19) captures the experimental fatigue behaviour at short lives; it may reasonably concluded the effect of the flaw inside the corrosion

pit diminishes at higher strains. At the high nominal stresses that prevail at short lives, this can be explained by the high values of K_t due to the internal flaw at the notch (pit) root, which would cause local strains higher than the yield strain, and the resulting cyclic creep would deform/stretch the internal flaw out of shape therefore reducing its stress concentration factor.

This will lead to a reduction in the impact of the flaw at the notch root, and in turn lead to longer fatigue lives than those modelled for the original geometry. To implement this hypothesis, the value of the initial K_t is increased linearly from the value of a pit without an internal flaw to the value of a pit with an internal flaw over the range of lives where an increase in the fatigue life above that modelled by the pit plus flaw model is observed.

The effectiveness of this simple approximation is examined in Figure 5-38, which presents a comparison of the modelled strain-life curve for corroded-wire-in-air specimens with the measured fatigue data. The dashed line represents specimens with a constant geometry of the flaw at the notch root, and the solid line represents the specimens with the altered flaw geometry due to high plastic strains. It is visually evident that using an incremental introduction of the flaw at the notch root as described above yields an improved modelling of the strain range versus fatigue life of the corroded-wire-in-air specimens, since the modelled curve falls within the experimental scatter band throughout the fatigue lives.

The goodness of fit for the modelled fatigue curve was evaluated as previously described in Section 5.7 by conducting a Two One-Sided Test (TOST) equivalence test. The TOST results showed that the experimental and modelled fatigue responses are equivalent, with the

significance level set at 5% and therefore with a confidence interval on the difference between the means of 90%.

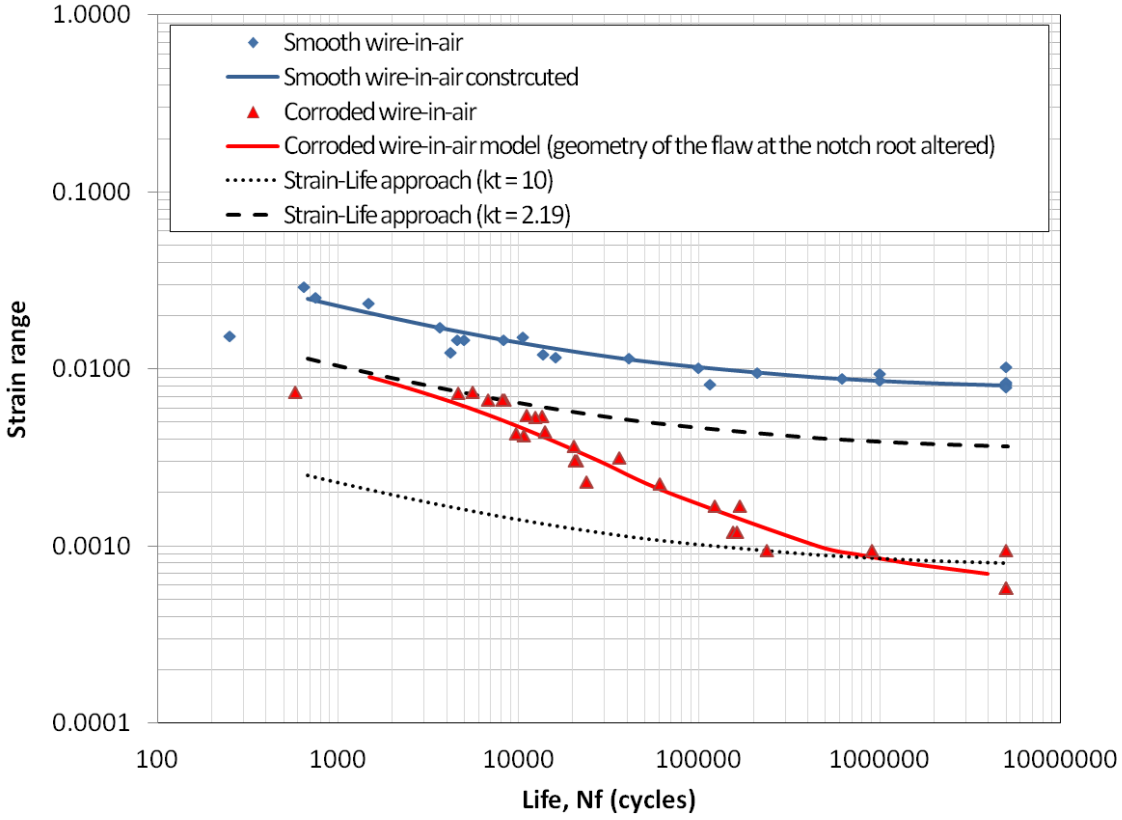

Figure 5-38 – Strain-fatigue life modelling of corroded-wire-in-air specimens (incremental introduction of the flaw at the notch root)

5.8.2 Corroded strand-in-beam specimens

In this section the same modelling approach used for the fatigue resistance of a corroded-wire-in-air is employed in modelling the fatigue resistance of the corroded-strand-in-beam specimens. However, unlike the corroded-wire-in-air specimens this is a strand inside a beam and therefore exhibits both inter-wire and strand to concrete fretting. A hemispherical edge notch of 0.6 mm in depth is used to simulate the observed average corrosion pit size, and an initial crack is used to

simulate a surface fretting flaw that intersects the edge of the pit. A value of $K_t = 3$ is used for the stress concentration at the notch edge. Since the fatigue crack is propagating from the edge and not the notch root, the shape of the crack is quarter-circular and not semi-circular. The same a crack shape correction factor for a semicircular crack (F = 0.65) was used as an approximation for the quarter-circular crack. Figure 5-39 presents a schematic of the flaw geometry.

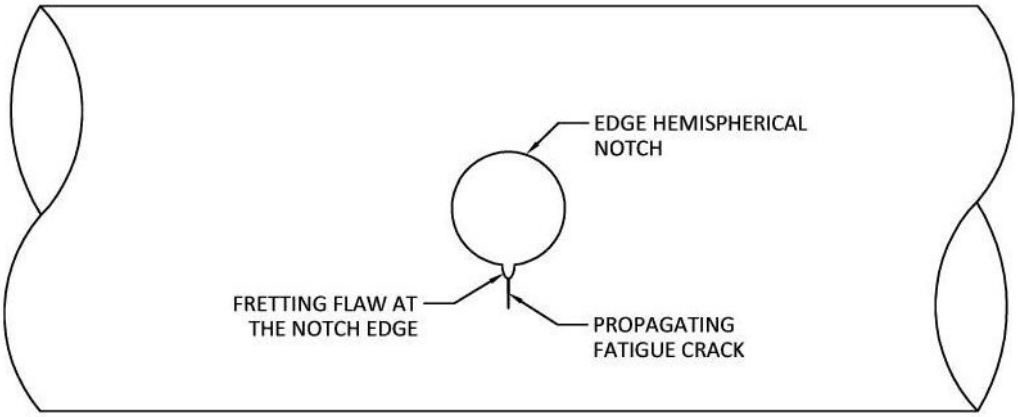

(a) Top view

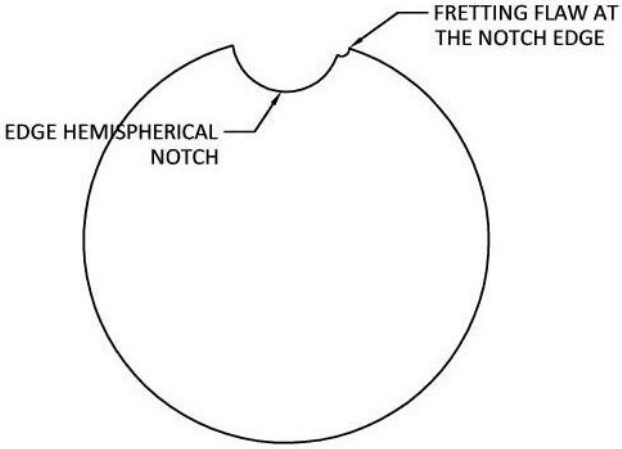

(b) Transverse section

Figure 5-39 – Schematic showing a fatigue crack propagating from a fretting induced flaw intersecting the edge of a pit for a corroded strand-in-beam specimen

As previously discussed in Section 5.7 the fretting induced damage was modelled by introducing an initial crack into the smooth wire specimen, consequently, in order to account for the combined impact of the fretting and a flaw at the notch edge the initial crack length used in modelling the fatigue resistance of the corroded-strand-in-beam specimens was longer than the crack length used in modelling the fatigue resistance of the corroded-wire-in-air specimens to account for the severe concrete fretting damage. Multiple iterations were conducted with various crack lengths, and an initial crack length of 0.02mm was found to yield a good correlation of the fatigue model with the experimental results.

Moreover, the same incremental approach of linearly introducing the flaw at the notch root and the fretting damage was used, however, an introductory period of the first 100,000 cycles was found to correlate well with the experimental results. Figure 5-40 presents the experimental and modelled strain range versus fatigue life data for the corroded-strand-in-beam (corroded beam) specimens in comparison to those for the corroded-wire-in-air specimens.

The goodness of fit for the modelled fatigue curve was evaluated as previously described in Section 5.7, by conducting a Two One-Sided Test (TOST) equivalence test. The TOST results showed that the experimental and modelled fatigue responses are equivalent, with the significance level set at 5% and therefore with a confidence interval on the difference between the means of 90%. The modelled fatigue response is also visually representative of the experimental data and falls within their scatter band.

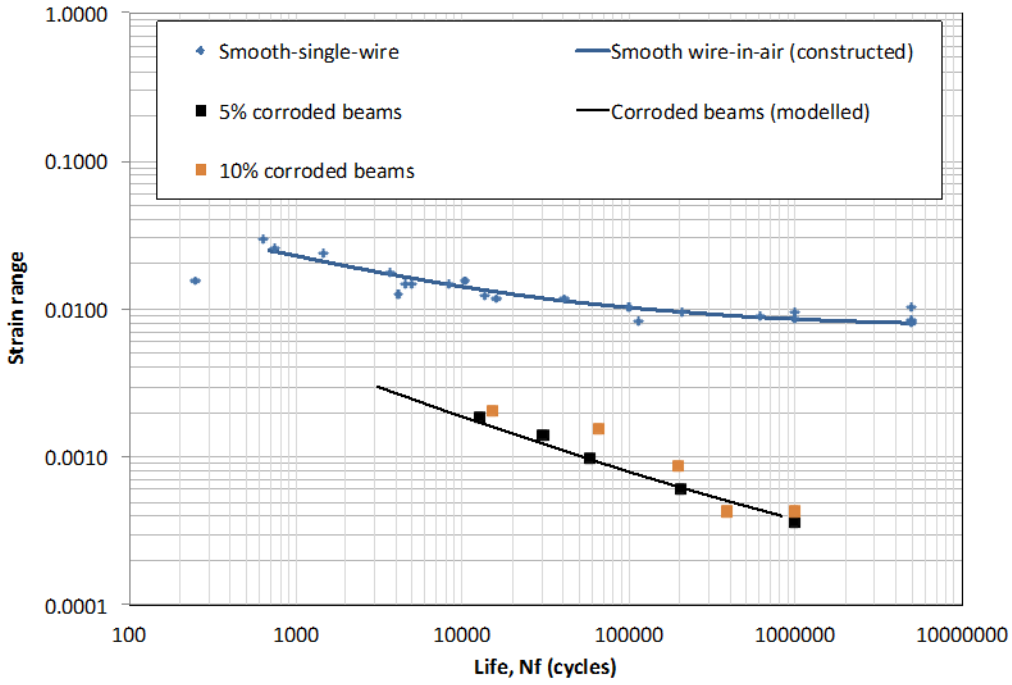

Figure 5-40 – Strain-fatigue life model of corroded-strand-in-beam specimens Adham correct spelling

The improvement in the fatigue resistance of the corroded strand-in-beam with a 10% corrosion level in comparison to that of the corroded strand-in-beam specimens with 5% corrosion was previously mentioned in Section 5.4.3. Since the representation of the deterioration mechanism due to corrosion by a fatigue crack propagating from a secondary notch within the primary notch was shown to accurately model the observed experimental behaviour; the observed improvement at the higher corrosion level may be due to a smoother notch surface and smaller internal flaws for the larger corrosion value.

5.8.3 Corroded strand-in-beam repaired with CFRP

For the corroded strand-in-beam in a beam repaired with CFRP the same modelling approach and crack initiation assumptions for the corroded/non-repaired strand-in-beam specimens are

employed. The only difference is the applied stress range for the strand; due to the load resistance contribution of the CFRP sheet the reduced strand stress is calculated using sectional analysis and used in modelling the fatigue life. Figure 5-41 shows the modelled strain range versus fatigue life curves for the corroded strand-in-beam repaired with CFRP and corroded/non-repaired strand-in-beam specimens in comparison to the experimental data.

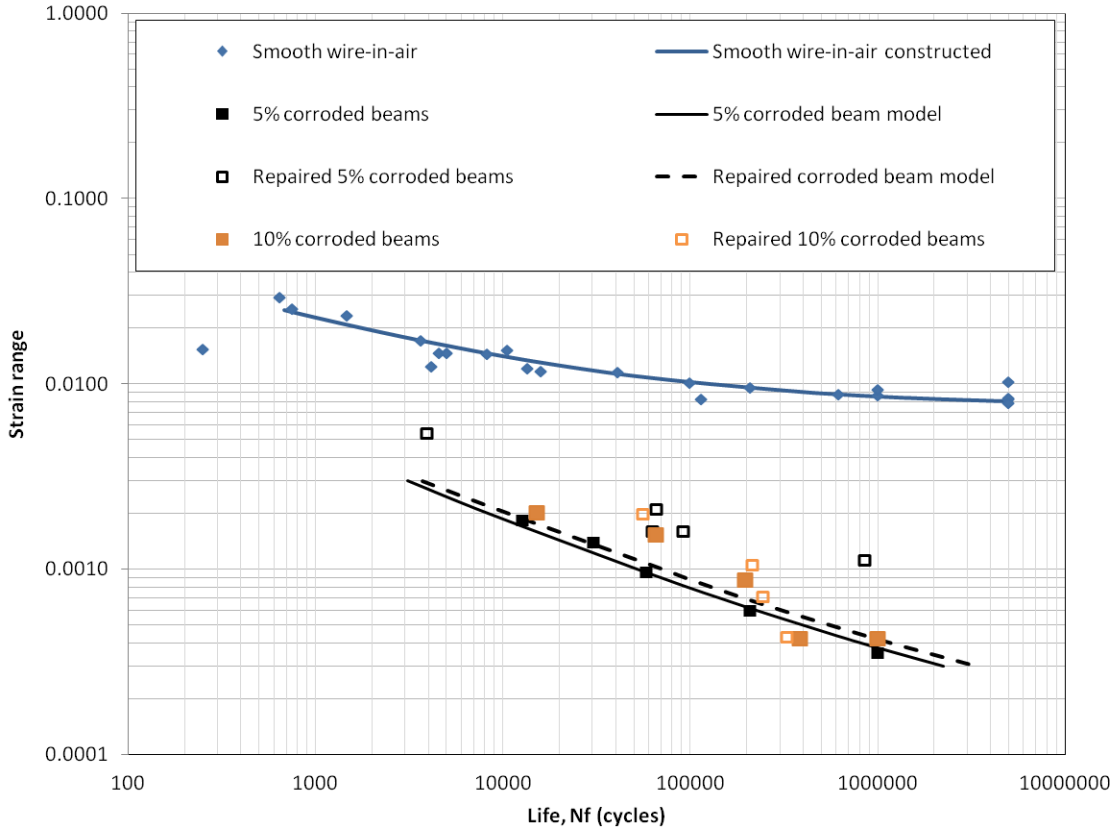

Figure 5-41 – Modelled and experimental strain range vs. fatigue life data for non-repaired and repaired corroded strand-in-beam specimens

The modelled curve shows only a marginal improvement in the predicted fatigue resistance of corroded strand-in-beam repaired with CFRP in comparison to the predicted fatigue resistance of corroded/non-repaired strand-in-beams specimens, and is not representative of the experimental data; this indicates that there is another factor that contributes to the improved fatigue resistance of the beams repaired with CFRP other than just simply reducing the applied strand stress.

To analyse this behaviour we refer back to the observations made from the monotonic testing results for the corroded beam repaired with CFRP in Section 4.4.2. Figure 4-32 is presented here again for clarity as Figure 5-43, and presents the applied load versus midspan deflection for non-repaired beams and repaired beams.

Notice the increased post-cracking stiffness (reduced midspan deflection for a given load) of the repaired beams beyond cracking load. A reduction in deflection leads to a reduction in crack opening and therefore a reduced concrete fretting of the strand. All of the strand-in-beam specimens we pre-cracked on the first load cycling during fatigue testing. This is consistent with the observations of researchers presented in Section 2.6.3, who reported that post-cracking stiffness increases and crack opening widths decreases with CFRP strengthening, Soudki and Sherwood (2000), Hassan and Rizkalla (2002), Rosenboom et al. (2006).

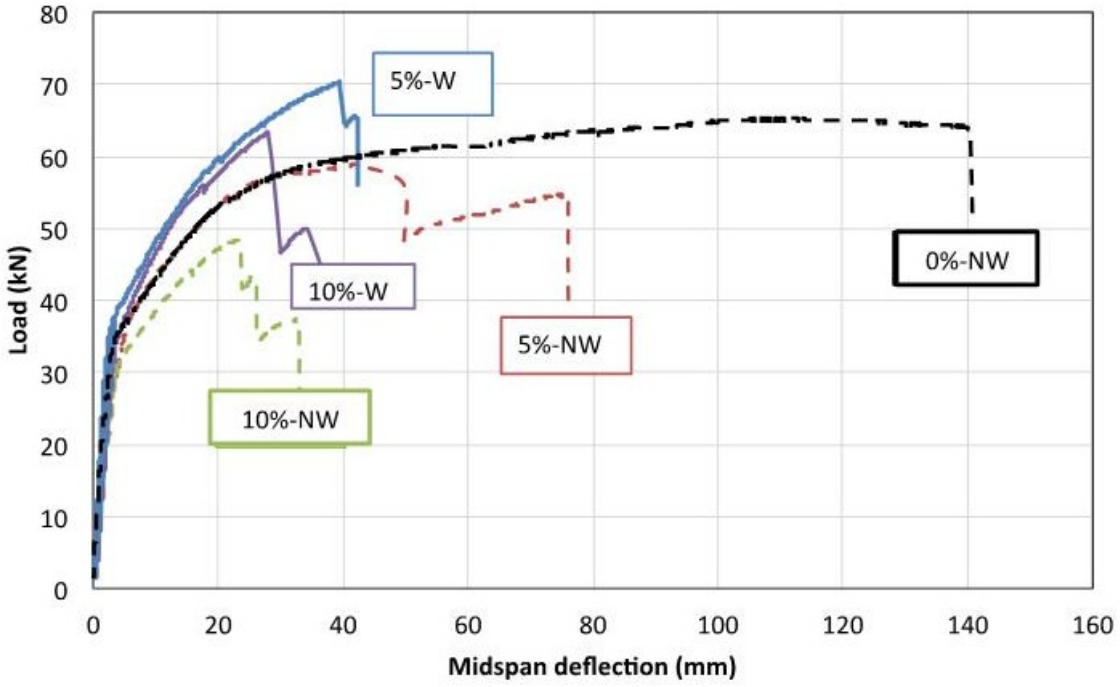

Figure 5-42 – Load vs. midspan deflection comparison of the repaired and unrepaired beams

To simulate the effect of a reduction in the fretting damage due to the repair using CFRP sheet, the initial crack length of 0.02 mm that was used to simulate the fretting damage of the non-repaired corroded strand-in-beam specimens was reduced to 0.001 mm for the corroded strand-in-beam repaired with CFRP specimens.

Figure 5-43 presents the predicted strand range versus fatigue life curve with a reduced fretting initial crack length due to the repair using CFRP. The modelled fatigue resistance of the corroded strand-in-beam specimens repaired with CFRP shows good representation of the experimental results, which confirms the hypothesis that CFRP repair improved the fatigue resistance not only by reducing the strand stress range but also increasing the stiffness of the cracked section; therefore the FRP reduces the crack width and consequently reduces fretting damage.

The goodness of fit for the modelled fatigue curve was evaluated as previously described in Section 5.7, by conducting a Two One-Sided Test (TOST) equivalence test. The TOST results showed that the experimental and modelled fatigue responses are equivalent, with the significance level set at 5% and therefore with a confidence interval on the difference between the means of 90%. The modelled fatigue response is also visually representative of the experimental data and falls within their scatter band.

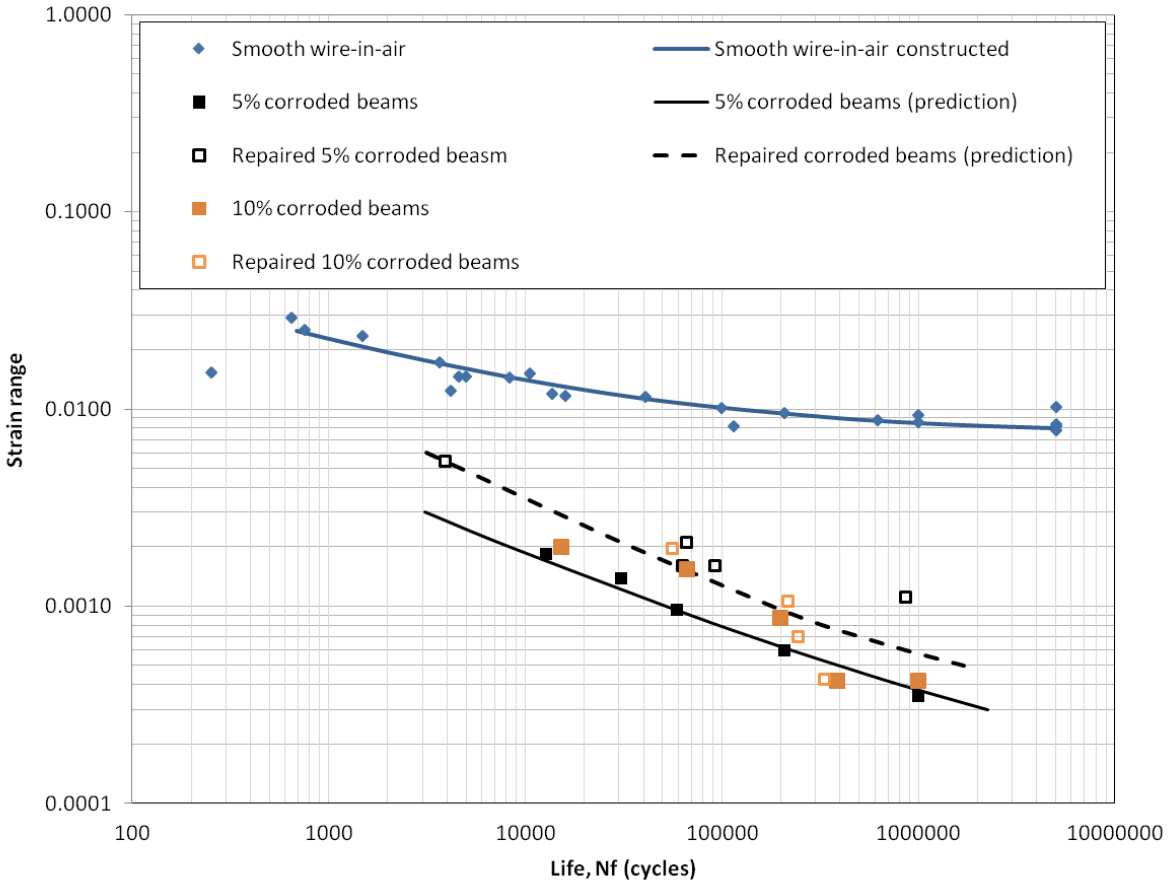

Figure 5-43 – Modelled strange range vs. fatigue life curve non-repaired and repaired corroded strand-in-beam specimens (assuming a reduced concrete fretting damage)

5.9 Summary

In this chapter an in depth analysis was presented that mechanistically explains the fatigue life and failure behaviour of the 7-wire prestressing strand. The analysis presented in Chapter 4 was based on studying the behaviour by identifying the fatigue material properties and fatigue crack propagation response of a single wire. These properties were identified through an extensive experimental program comprised of testing a total of 61 single wire specimens (25 smooth wire specimens and 31 corroded wire specimens).

Experimental samples from the single wire specimens as well as the full strands extracted from beams tested to failure were closely examined to identify the flaws that caused the fatigue fracture. Visually obvious signs of inter-wire fretting and wire to concrete fretting were observed and presented. Wire-in-air experimental results were compared to up to 700 strand-in-air fatigue tests results compiled by Paulson et al. (1983). Significant deterioration was observed at long fatigue lives, which was attributed to inter-wire fretting. Additional deterioration was observed for non-corroded strand-in-beam specimens in comparison to the strand-in-air specimens; indicating that concrete fretting is more detrimental than inter-wire fretting. On the other hand, for the corroded strands corrosion induced pitting was observed and a wide range of the pit geometries were found.

Using a short crack strain based Fracture Mechanics approach the fatigue crack propagation rate was calculated, and then combined with a solution by Xu et al. (1997) for the stress intensity factor for a crack propagating from a notch root to model the fatigue resistance.

The smooth wire in air had an initial zero crack length. The strand in air had a fretting crack. Moreover, an incremental introduction of the initial crack was utilized to simulate the time delay

(number of cycles) that are expected to be physically required for the full fretting damage to be manifested.

Alternatively for the corroded wire-in-air specimens, corrosion induced pitting was represented by a hemispherical edge notch of a depth and a notch root radius of 0.6 mm based on the average physically measured corrosion pit dimensions. In addition, an initial crack length of 0.0001mm was incrementally introduced to simulate a flaw at the notch root. Similarly modelling of the corroded strand in beam utilized the same approach with the same notch geometry. However, an initial crack length of 0.02 mm was used to simulate the combined fretting and corrosion induced damage. Figure 5-44 presents all of the experimental data in comparison to their corresponding modelled fatigue resistance. The modelled fatigue behaviour is in good agreement with the experimental data indicating that an accurate mechanistic analysis of the fatigue behaviour of the prestressing strand is representative of the beam response.

Finally the fatigue resistance of the corroded strand-in-beam specimens repaired with CFRP was modelled using the same modelling approach, notch geometry, and crack initiation assumption; but with a lower strand stress due to the CFRP contribution in resisting the applied stress, and a reduced initial crack length of 0.001 mm simulating the reduction in concrete fretting damage as a result of the increased cracked section stiffness due to the application of the CFRP repair. Figure 5-43 presented the predicted strand range versus fatigue life curve with a reduced fretting initial crack length due to the repair using CFRP, the predicted fatigue resistance was in good agreement with the experimental results of the 5% corroded/repaired strand-in-beam specimens repaired with CFRP. However for the specimens corroded to 10% by mass loss, scatter in the experimental results made it harder to quantify the difference in response between the non-

repaired and repaired specimens. Figure 5-44 presents all of the modelled fatigue response and there corresponding experimental data sets.

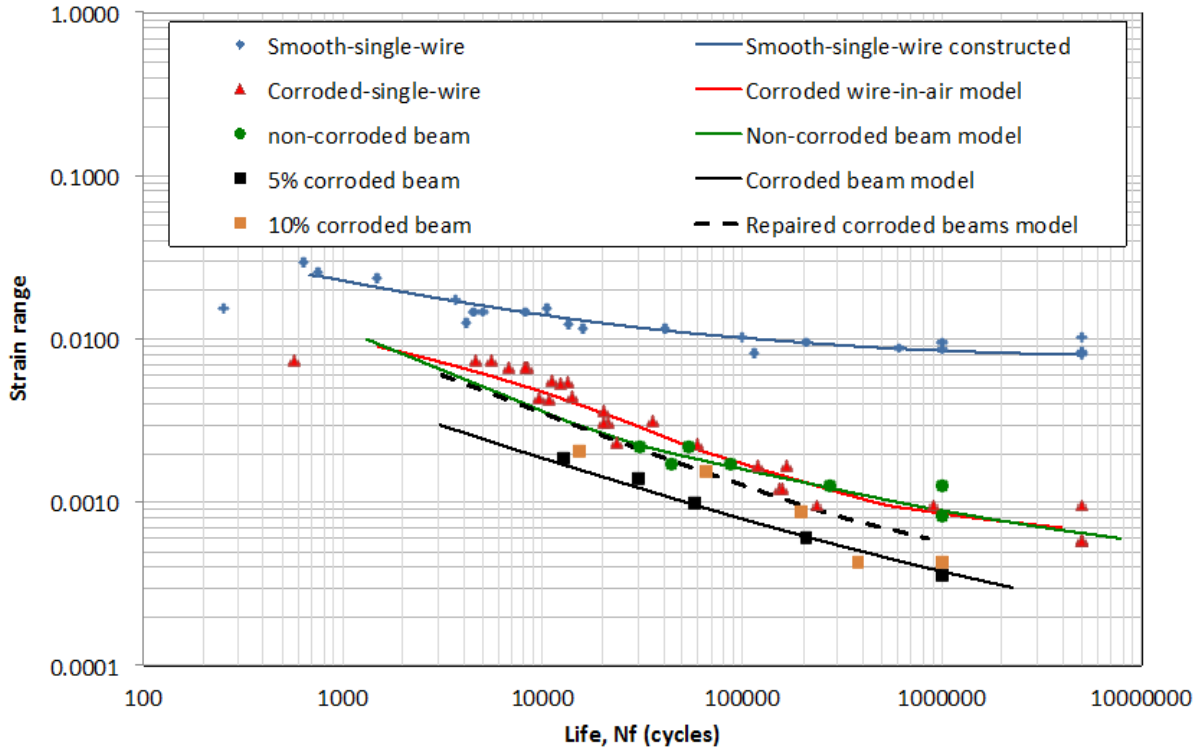

Figure 5-44 – Summary of fatigue resistance models versus experimental behaviour

Finally, it is important to summarize the assumptions, the parameters and the limitation of the modelling approach. Assumptions were made in order to identify the material fatigue properties and to model the fatigue response; namely a) the material fatigue response is not affected by mean stresses b) an intrinsic strain range $\Delta\varepsilon_i = 0.0075$ based on the smooth wire-in-air fatigue test results and c) the fatigue crack shape is semi-circular or quarter-circular.

In addition, the primary fitting parameter for the modelled fatigue response was the initial crack length and shape used to simulate various flaw geometries that we were unable to get physical

measurements for. The initial crack lengths used ranged from 0.0001 mm to 0.02 mm. Although, the crack lengths are arbitrary fitting parameters, a pretensioned beam with a similar configuration and steel strand is expected to replicate the modelled fatigue response presented in this study

Chapter 6
Summary, Conclusions and Recommendations

This study presented an in depth investigation of the fatigue performance of pretensioned T-beams subjected to different level of corrosion, and examined the effectiveness of using externally applied Carbon Fibre Reinforced Polymer (CFRP) sheets to repair and restore their monotonic and fatigue load carrying capacities.

6.1 Summary

The study comprised of an extensive experimental program and an in depth analysis. The experimental program consisted of multiple phases; a material testing phase, and a beam testing phase. For the material testing phase, a total of sixty-one (61) material samples under carious configuration were fatigue tested to identify the material's monotonic and fatigue properties, the impact of corrosion pitting, and were the basis of the mechanics analysis and modelling. For the beam-testing phase, a total thirty-seven (37) pretensioned concrete beams measuring 3.6m in length were tested under monotonic and fatigue loading. The beams were subjected to different corrosion levels and repair configurations to compare the behaviour of the prestressing strand inside a beam to the fatigue life models.

In this chapter findings of the study are presented followed by recommendation for future work. The findings are divided as follows; experimentalbeam testing, material testing, and mechanics analysis and modelling.

6.1.1 Beam Testing

Conclusions presented in this section are based on the experimental test results of thirty-seven (37) pretensioned concrete T-beams. Twelve (12) beams were testing under monotonic testing in four-point bending, and twenty-five (25) beams were tested under fatigue loading. Conclusions in this section are presented as monotonic and fatigue behaviour.

Monotonic behaviour

- Corrosion significantly affected the behaviour of the pretensioned T-beams, with significant reductions in their ultimate load carrying capacity and midspan deflection.
- Beams with a 2.5% corrosion level by mass loss exhibited a 6.5% reduction in ultimate load and a 26.4% reduction in midspan deflection.
- Beams with a 5% corrosion level by mass loss suffered reductions of 44% and 10% in load carrying capacity and midspan deflection, respectively.
- The beams with the high corrosion level of 10% mass loss had 76% and 26% reductions in its load carrying capacity and midspan deflection, respectively.
- The cumulative flexure crack widths and average strand tensile strains increased with increased corrosion levels, while the concrete midspan compressive strain decreased with an increased corrosion level.
- Failure was characterized by rupture of the strand in all beams, but the rupture pattern differed between non-corroded and corroded beams.

- For the non-corroded beams a rupture of multiple wires occurred at the same location, while for the corroded beams wire failures occurred at adjacent locations depending on the pit location.
- CFRP repair was effective in restoring the load carrying capacity of corroded pretensioned beams. The stiffness of the strengthened members increased in comparison to their unstrengthened counterparts. However, the reduction in ductility was not reversible.

Fatigue behaviour

- Corroded beams exhibited deterioration in their fatigue resistance in comparison to the non-corroded beams.
- Beams corroded to a 5% by mass loss showed a uniform deterioration at different load ranges.
- Beams corroded to a 10% mass loss did not exhibit an additional deterioration in fatigue resistance in comparison to beams corroded to a 5% mass loss.
- Beams corroded to a 10% by mass loss showed more scatter in their fatigue response than the beams corroded to a 5% mass loss with the mean experimental response indicating a slight improvement in fatigue resistance in comparison to beams corroded to 5%.
- Beams corroded to a 5% mass loss and repaired using CFRP sheets exhibited a uniform improvement in fatigue resistance, and the fatigue resistance was restored to the level of the non-corroded beams.

- Beams corroded to 10% by mass loss and repaired using CFRP showed a scatter in their fatigue response similar to that of the non-repaired beams with a 10% corrosion level.
- The mean experimental fatigue response of the beams corroded to a 10% mass loss improved in comparison to that of the non-repaired beams, but the fatigue resistance level of the non-corroded beams was not restored.

Material Testing

This section presents conclusions derived from material testing of a total of sixty-one (61) single wire tests. Material testing samples were made out of a single wire of a 7-wire prestressing strand. Twenty-five (25) non-corroded specimens and thirty-six (36) corroded specimens were tested. Corroded specimens wire specimens were taken from a complete strand corroded inside a concrete prism. Actual corrosion levels by mass loss achieved were 8% and 10%.

- Fatigue response of non-corroded wire specimens was typical of cold drawn steel.
- Non-corroded wire specimens tested under cyclic loading with an average positive mean stress of 500 MPa had a similar fatigue response to that of non-corroded wire specimens tested under zero mean (R = -1) cyclic loading.
- No difference in fatigue response was observed between wire specimens corroded to 8% by mass loss and specimens corroded to 10% by mass loss.
- Corroded wire specimens showed a deteriorated fatigue response in comparison to non-corroded wire specimens.

Analysis and Modelling

Samples from the single wire specimens as well as the full strands extracted from beams tested to failure were closely examined to identify the flaws that caused the fatigue fracture.

- Inter-wire fretting was identified as the cause of the deterioration in the fatigue resistance for non-corroded strand-in-air specimens in comparison to that of the smooth wire-in-air specimens. Visible signs of inter-wire fretting induced damage were presented.
- Concrete fretting was identified as the cause of the flaws causing fatigue fracture for non-corroded strands-in-beam, and signs of concrete fretting induced damage were presented.
- A comparison of experimental results compiled by Paulson et al. (1983) and an equation by Naaman (1989) for strand-in-air specimens to those of the strand-in-beam specimens from this study reveals an additional deterioration of the fatigue resistance for the strand-in-beam specimens; indicating that concrete fretting is more detrimental than inter-wire fretting.
- The fatigue crack propagation rate was calculated using a short crack strain-based fracture mechanics approach, and the constructed fatigue response of the smooth wire-in-air specimens accurately represented of the experimental response.
- Smooth wire-in-air specimens had a zero initial crack length, while the non-corroded strand specimens had an initial crack that simulated a fretting induced flaw.
- Strand-in-air specimens had an assumed initial crack length of 0.0002 mm, and non-corroded strand-in-beams specimens had an assumed initial crack length of 0.001 mm.

- A simplified approach of incrementally introducing the initial crack to simulate the time delay (number of cycles) that are physically required for the full fretting damage to be manifested resulted in a good correlation of modelling to the experimental results.
- In the corroded specimens, corrosion induced pitting was observed, and a wide range of the pit geometries were found.
- A short crack strain-based fracture mechanics approach, the average corrosion pit geometry and assumed flaw sizes were used to model the fatigue resistance of corroded wire-in-air and corroded strand-in-beam specimens.
- A solution for the stress intensity factor for a crack propagating from a notch root by Xu et al. (1997) was used to model the fatigue resistance of the corroded wire-in-air specimens.
- Corrosion induced pitting was represented by a hemispherical edge notch of a depth of 0.6 mm based on the average physically measured corrosion pit, and an initial crack of length of 0.0001 mm was incrementally introduced to simulate a flaw at the notch root.
- The strand-in-repaired-beam specimens had a reduced strand stress range due to the contribution to the moment resistance of the beam by the CFRP sheet.
- Corroded strand-in-repaired-beam specimens had higher cracked section stiffness and smaller flexural crack widths in comparison to corroded strand-in-beam specimens, which reduced the cyclic displacement at the cracks and the fretting induced damage.

- Modelling of the corroded strand-in-beam specimens utilized the same approach with the same notch geometry as that for the corroded strands. However, an initial crack length of 0.02 mm was used to simulate the combined fretting and corrosion induced damage for a non-repaired beam, and crack length of 0.001 mm was used for the repaired beams.
- The modelled fatigue behaviour is a good representation of the experimental data indicating that the crack growth analysis of the fatigue behaviour of the prestressing strand is representative of the beam response.
- The fatigue behaviour of non-corroded and corroded pretensioned beams can be accurately modelled by using short crack strain-based fracture mechanics and an appropriate description of fretting and corrosion flaws to construct the strand fatigue life curves.

6.2 Conclusions

This study has presented an extensive body of experimental work along with an in depth mechanistic analysis of the deterioration mechanisms of the primary prestressing reinforcement, the 7-wire strand, used for pretensioning applications. This study's primary contribution is presenting a mechanistic understanding of the failure process of pretensioned beams, and demonstrating a modelling approach that is built on material properties obtained through simple material testing that accurately predicts the fatigue behaviour of non-corroded and corroded pretensioned concrete beams. Notable conclusions are summarized and presented below:

- Corrosion significantly affected the behaviour of pretensioned beam; under monotonic loading reductions in load capacity and midspan deflection of 26% and 76% respectively

were observed at 10% corrosion by mass loss. Under cyclic loading a significant reduction in fatigue resistance was also observed.

- Repair of corroded pretensioned beams using Carbon Fibre Reinforced Polymer Sheet (CFRP) successfully restored the monotonic ultimate load capacity and fatigue resistance to those of the non-corroded pretensioned beams.
- The fatigue behaviour of the 7-wire prestressing strand-in-air was shown experimentally not to be representative of its fatigue behaviour inside a beam.
- Various deterioration mechanisms were identified for the 7-wire prestressing strand subjected to cyclic loading under different conditions. The resulted in a major deterioration in the material's fatigue resistance as a strand assembly in comparison to that of the single wire.
- Employing short-crack strain based fracture mechanics along with the identified 7-wire prestressing strand deterioration mechanisms accurately modelled the fatigue response of non-corroded and corroded pretensioned beams.

6.3 Recommendations for Future Work

In this section, recommendations are made for future work that would expand on the findings of this thesis and contribute to a deeper understanding of parameters that were outside the scope of this study:

- A study investigating the fatigue behaviour of beams with multiple corroded strands.
- An investigation on the effect of overloads and variable amplitude cyclic loading on the fatigue behaviour of corroded pretensioned beams.
- An experimental program to evaluate fretting induced surface damage in 7-wire strands and to quantify the fretting force in relation to the applied stress level.
- A study aimed at to providing design recommendations based on a statistical analysis of the distribution of fatigue strengths of cyclically loaded beams with corrosion and fretting induced flaws.
- A study to statistically quantify the depth of cracks due to stress corrosion in prestressing wires.

Bibliography

ACI committee 215, (1974) "Considerations for Design of Concrete Structures Subjected to Fatigue Loading ACI (215R-74)" American Concrete Institute, Farmington Hills, MI.

ACI Committee 222, (2010) "Protection of Metals in Concrete Against Corrosion (ACI 222R-10)" American Concrete Institute, Farmington Hills, MI.

ACI Committee 222, (2014) "Report on Corrosion of Prestressing Steels (ACI 222 2R-14)" American Concrete Institute, Farmington Hills, MI.

ACI Committee 318 (2014) "Building Code Requirements for Structural Concrete (ACI 318-14) and Commentary" American Concrete Institute, Farmington Hills, MI.

ACI-ASCE Committee 423 (2005)."Recommendations for Concrete Members Prestressed With Unbonded Tendons (ACI-ASCE 423.3R-05)" American Concrete Institute, Farmington Hills, MI.

Aidoo J, Harries KA, Petrou MF. 2004. Fatigue behavior of CFRP-strengthened reinforced concrete bridgegirders. Journal of Composites for Construction 8(6): 501-518

Al-Hammoud, R. (2006). "Fatigue flexural behaviour of corroded reinforced concrete beams repaired with CFRP sheets." Masters Abstracts International.

Al-Hammoud, R., Soudki, K., & Topper, T. H. (2010). Fatigue flexural behavior of corroded reinforced concrete beams repaired with CFRP sheets. Journal of Composites for Construction, 15(1), 42-51.

Alonso, M. C., Procter, R. P. M., Andrade, C., & de Santa Maria, M. S. (1993). Susceptibility to stress corrosion cracking of a prestressing steel in NaHCO 3 solutions. Corrosion science, 34(6), 961-973.

Andrade, C., Alonso, C., and Molina, F. J. (1993). "Cover cracking as a function of bar corrosion: Part I - Experimental test." Materiaux Et Constructions, 26(162), 453-464.

ASTM A1061M. (2009). "Standard Test Methods for Testing Multi-Wire Steel Strand." ASTM International, West Conshohocken, PA, USA.

ASTM A416M. (2010). "Standard Specification for Steel Strand, Uncoated Seven-Wire for Prestressed Concrete." ASTM International, West Conshohocken, PA, USA.

ASTM A931. (2008). "Standard Test Method for Tension Testing of Wire Ropes and Strand." ASTM International, West Conshohocken, PA, USA.

ASTM G1. (2003). "Standard Practice for Preparing, Cleaning, and Evaluating Corrosion Test Specimens." ASTM International, West Conshohocken, PA, USA.

Badawi, M. A. (2007). "Monotonic and fatigue flexural behaviour of RC beams strengthened with prestressed NSM CFRP rods." PhD thesis, University of Waterloo, Waterloo, Ont.

Bahke, E. (1980). "Principles Defining the Strength of Wire Ropes and Chains - 2." Wire, v 30, n 3, p 168-176, May-Jun 1980.

Bannantine, J. (1990). "Fundamentals of metal fatigue analysis." Prentice Hall, 1990, 273.

Baus, R., and Brenneisen, A. (1968). "The Fatigue Strength of Prestressing Steel" Steel for Prestressing, 95-117.

Beeby, A. W. (1983). "Cracking, Cover and Corrosion of Reinforcement" Concrete International, 5(2), 35-40.

Beevers, C. J. (1981). "Some Aspects of the Influence of Microstructure and Environment on Delta K Thresholds" In Int. Symposium on Fatigue Thresholds, (Vol. 1, p. 17).

Bentur, A. (1997). Steel corrosion in concrete : fundamentals and civil engineering practice. E & FN Spon, London.

Blakeborough, A., & Cullimore, M. S. G. (1984). "Fretting in the fatigue of wire rope" Advances in Fracture Research (Fracture 84)., 3, 2133-2141.

Bonacci, J. F., & Maalej, M. (2001). "Behavioral trends of RC beams strengthened with externally bonded FRP" Journal of Composites for Construction, 5(2), 102-113.

Bondy, K. (1970). "Realistic Requirements for Unbonded Post-Tensioning Tendons" PCI Journal, v 15, n 1, p. 50-59.

Broomfield, J. P. (2007). Corrosion of steel in concrete: understanding, investigation and repair. Spons Architecture Price Book.

Burton, K. T., and Hognestad, E. (1967). "Fatigue tests of reinforcing bars-Tack welding of stirrups." ACI Journal Proceedings, ACI.

Clear, K. C. (1974). Time to corrosion of reinforcing steel in concrete slabs (No. 500).

Costello, G. A. (. A. (1997). Theory of wire rope. Springer, New York.

CPCI (2008). Design Manual, 4th Edition. Canadian Precast/Prestressed Concrete Institute, 100-196 Bronson Avenue, Ottawa, Ontario Canada.

Darmawan, M. S., and Stewart, M. G. (2007). "Effect of Pitting Corrosion on Capacity of Prestressing Wires" Magazine of Concrete Research, 59(2), 131-139.

Derecho, A. T., & Munse, W. H. (1966). Stress Concentration at External Notches in Members Subjected to Axial Loadings (No. Ihr-64).

Dowling, N. E. (1977). Crack growth during low-cycle fatigue of smooth axial specimens. ASTM-STP 637, 97-121.

Dowling, N. E. (1993). Mechanical Behavior of Materials: Engineering Methods for Deformation, Fracture, and Fatigue. Prentice Hall Englewood Cliffs, NJ.

DuQuesnay, D. L., Pompetzki, M. A., & Topper, T. H. (1993). "Fatigue life prediction for variable amplitude strain histories." SAE Technical Paper, No. 930400, Society of Automotive Engineers, Warrendale, PA, USA.

El-Hacha, R., Green, M. F., & Wight, R. G. (a) (2004). Flexural behaviour of concrete beams strengthened with prestressed carbon fibre reinforced polymer sheets subjected to sustained loading and low temperature. Canadian Journal of Civil Engineering, 31(2), 239-252.

El-Hacha, R., Wight, R. G., & Green, M. F. (b) (2004). Prestressed carbon fiber reinforced polymer sheets for strengthening concrete beams at room and low temperatures. Journal of composites for construction, 8(1), 3-13.

El Haddad, M. H., Smith, K. N., & Topper, T. H. (1979). "Fatigue crack propagation of short cracks". Journal of Engineering Materials and Technology, 101(1), 42-46.

El Maaddawy, T. A., and Soudki, K. A. (2003). "Effectiveness of impressed current technique to simulate corrosion of steel reinforcement in concrete." J.Mater.Civ.Eng., 15(1), 41-47.

El Menoufy, A., and Soudki, K. (2014). Flexural behavior of corroded pretensioned girders repaired with CFRP sheets. PCI Journal, 59(2).

Evans, U. R. (1961). The Corrosion and Oxidation of Metals; Scientific Principles and Practical Applications. London, E. Arnold (1961).

Ford, J. V. L. (2004). Effects of Freeze/Thaw Cycling on The Fatigue Behaviour of Prestressed Concrete Beams Strengthened With Prestressed CFRP Sheets (Master dissertation, Queen's University).

Goins, D. (2000). "Motor speedway bridge collapse caused by corrosion" Material Performance, 36(7), 18-19.

Goto, S., and Roy, D. M. (1981a). "Diffusion of Ions Through Hardened Cement Pastes" Cement and Concrete Research, 11(5-6), 751-757.

Goto, S., and Roy, D. M. (1981b). "Effect of w/c Ratio and Curing Temperature on The Permeability of Hardened Cement Paste." Cement and Concrete Research, 11(4), 575-579.

Harder, J., and Rogowsky, D. (1999). "Inspection and Monitoring of Buildings with Unbonded Prestressing" Proceedings of the International Conference of Structural Faults and Repair, MC Forde, ed., Engineering Technics Press, Edinburgh, Scotland.

Hansson, C. M., and Sorensen, B. (1990). "Threshold Concentration of Chloride in Concrete for The Initiation of Reinforcement Corrosion." ASTM Special Technical Publication, (1065), 3-16.

Heffernan, P. J. (1998). "Fatigue Behaviour of Reinforced Concrete Beams Strengthened with CFRP Laminates" Royal Military College of Canada.

Heffernan, P. J., and M. A. Erki (2004). "Fatigue behavior of reinforced concrete beams strengthened with carbon fiber reinforced plastic laminates." Journal of Composites for Construction 8.2 (2004): 132-140

Helgason, T., Hanson, J. M., Somes, N. F., Corley, W., and Hognestad, E. (1976). "Fatigue strength of high-yield reinforcing bars." NCHRP Report, (164).

Hilmes, J. B. (1965). Statistical Analysis of the Fatigue Characteristics of Underreinforced Prestressed Concrete Flexural Members.

Hosford, W. F. (2005). Mechanical behavior of materials. Cambridge Univ Pr.

Jones, D. A. (1996). Principles and prevention of corrosion. Prentice Hall, Upper Saddle River, N.J.

Kokubu, M., and Okamura, H. (1965). "Fundamental Study on Fatigue Behavior of Reinforced Concrete Beams Using High Strength Deformed Bars." Transactions, 1-28.

Lam, T. S., Topper, T. H., & Conle, F. A. (1998). "Derivation of crack closure and crack growth rate data from effective-strain fatigue life data for fracture mechanics fatigue life predictions." International journal of fatigue, 20(10), 703-710.

Larson, K. H., Peterman, R. J., & Rasheed, H. A. (2005). Strength-fatigue behavior of fiber reinforced polymer strengthened prestressed concrete T-beams. Journal of Composites for Construction, 9(4), 313-326.

MacDougall, C. and Bartlett, F.M. (2002) “Tests of corroded unbonded 7-wire tendon with wire breaks.” American Concrete Institute Structural Journal, Vol. 99, No. 6, November/December, pp. 803 - 810

MacGregor, J. G., Jhamb, I., and Nuttall, N. (1971). "Fatigue strength of hot rolled deformed reinforcing bars." ACI Journal Proceedings, ACI.

Mansfeld, F., Kendig, M. W., and Tsai, S. (1982). "Recording and analysis of AC impedance data for corrosion studies. II. Experimental approach and results." Corrosion, 38(11), 570-80.

Masoud, S., Soudki, K., & Topper, T. (2001). CFRP-strengthened and corroded RC beams under monotonic and fatigue loads. Journal of composites for construction.

Masoud, S. G. A. (2002). "Behaviour of corroded reinforced concrete beams repaired with FRP sheets under monotonic and fatiue loads." PhD thesis, University of Waterloo [Dept. of Civil Engineering], Waterloo, Ontario.

Masoud, S., Soudki, K., & Topper, T. (2005). Postrepair fatigue performance of FRP-repaired corroded RC beams: Experimental and analytical investigation. Journal of Composites for Construction, 9(5), 441-449.Mehta, P. K. (1980). "Durability of concrete in marine environment-a review." Performance of Concrete in Marine Environment, 1-20.

McEvily, A. J. (1969, December). Fatigue crack growth and the strain intensity factor. In Air Force Conf. on Fatigue and Fracture of Aircraft Structures and Materials, Miami Beach (pp. 451-458).

Mordock, J. (1965). "A Critical Review of Research on the Fatigue of Plain Concrete." Illinois Univ Eng Exp Sta Bulletin.

Naaman, A.E. (1989). "Fatigue Of Reinforcement In Partially Prestressed Beams" Structural Materials: Proceedings of the sessions related to structural materials at Structures Congress '89, p 377-381, San Francisco Hilton, San Francisco, CA,. New York, N.Y.

Neuber, H. (1946). Theory of notch stresses: Principles for exact stress calculation. JW Edwards.

Neville, A. M. (1996). Properties of concrete. John Wiley and Sons, New York.

Ngoc, A. V., Castel, A., and Francois, R. (2009). "Effect of stress corrosion cracking on stress-strain response of steel wires used in prestressed concrete beams." Corrosion Science, 51(6), 1453-9.

Nurnberger, U. (2002). "Corrosion induced failure mechanisms of prestressing steel." Materials and Corrosion, 53(8), 591-601.

Overman, T. R., Breen, J. E., & Frank, K. H. (1984). Fatigue Behavior of Pretensioned Concrete Girders (No. FHWA/TX-85/39+ 300-2F).

Oudah F, El-Hacha R. 2013. Research progress on the fatigue performance of RC beams strengthened in flexure using Fiber Reinforced Polymers. Journal of Composite Part B: Engineerig 47: 82-95

Ozell, A. M. (1962). Fatigue tests of prestressed concrete I beams with depressed strands. In 4th Congress of the FIP (pp. 128-135).

Page, C. L., Short, N. R., Holden, W. R., & Materials Research Group. (1986). "The influence of different cements on chloride-induced corrosion of reinforcing steel" Cement and Concrete Research, 16(1), 79-86.

Pakniat, P., and Hammad, A. (2008). "Optimizing bridge decks maintenance strategy based on probabilistic performance prediction using genetic algorithm." Annual Conference of the Canadian Society for Civil Engineering 2008 - "Partnership for Innovation", June 10, 2008 - June 13, Canadian Society for Civil Engineering, Quebec City, QC, Canada, 2057-2067.

Pantucek, P. (1977). Pressung von Seildraht unter statischer und dynamischer Beanspruchung. Doktor Dissertation Universitat Karlsuhe.

Paris, P. C. (1964). The fracture mechanics approach to fatigue. Sagamore Army Materials Research Conference, p 107-132, 1963.

PCI Bridge Design Manual Steering Committee. (2011). Precast Prestressed Concrete Bridge Design Manual. Precast/Prestressed Concrete Institute, 209 W. Jackson Blvd., Chicago IL.

Pearson, S. (1975). Initiation of fatigue cracks in commercial aluminium alloys and the subsequent propagation of very short cracks. Engineering Fracture Mechanics, 7(2), 235-247.

Pfister, J. F., and Hognestad, E. (1964). High strength bars as concrete reinforcement, part 6: fatigue tests. Portland Cement Association, Research and Development Laboratories, .

Phillips, J. M. P. (1993). The effect of corrosion on the structural performance of new and repaired one-way slabs.

Pilkey, W., Pilkey, Deborah F, & Peterson, Rudolph Earl. (2008). Peterson's stress concentration factors (3rd ed.). Hoboken, N.J.: John Wiley.

Poursaee, A., and Hansson, C. M. (2009). "Potential pitfalls in assessing chloride-induced corrosion of steel in concrete." Cem.Concr.Res., 39(5), 391-400.

Proverbio, E., and Ricciardi, G. (2000). "Failure of a 40 years old post-tensioned bridge near seaside." Proc. Int. Conf. Eurocorr 2000.

El-Hacha, R., & Soudki, K. (2013). Prestressed near-surface mounted fibre reinforced polymer reinforcement for concrete structures—a review 1. Canadian Journal of Civil Engineering, 40(11), 1127-1139.

Rabbat, B. G., Kaar, P. H., Russell, H. G., & Bruce Jr, R. N. (1978). Fatigue Tests of Full Size Prestressed Girders (No. FHWA-LA-78-206P Final Report.).

Rehm, G. (1967). Contribution to the Problem of Fatigue Strength of Steel Bars for Concrete Reinforcement. Portland Cement Association.

Rinaldi, Z., Imperatore, S., and Valente, C. (2010). "Experimental evaluation of the flexural behavior of corroded P/C beams." Constr.Build.Mater., 24(11), 2267-2278.

Roberts, M. (1981). "Carbonation of concrete made with dense natural aggregates." BRE-IP--6/81 Information Paper, 6 81

Rosenboom, O., Hassan, T. K., & Rizkalla, S. (2006). Flexural behavior of aged prestressed concrete girders strengthened with various FRP systems. Construction and building materials, 21(4), 764-776.

Rosenboom, O., & Rizkalla, S. (2006). Behavior of prestressed concrete strengthened with various CFRP systems subjected to fatigue loading. Journal of Composites for Construction, 10(6), 492-502.

Ryals, K. K., Breen, J. E., & Kreger, M. E. (1992). Fretting Fatigue in External Post-Tensioned Tendons. Centre for Transportation Research, Bureau of Engineering Research, University of Texas at Austin.

Schonlin, K., and Hilsdorf, H. (1988). "Permeability as a Measure of Potential Durability of Concrete Development of a Suitable Test Apparatus." Permeability of Concrete, 99-115.

Schijve, J., & Jacobs, F. A. (1964) "Fatigue Crack Propagation in Unnotched and Notched Aluminum Alloy Specimens." NLR-TR M. 2128, Nat. Aero-Astronaut. Res. Inst.(Amsterdam).

Schijve, J. (1967). Significance of fatigue cracks in micro-range and macro-range. ASTM-STP 415. 1967, 415-459.

Shahawy, M., and T. E. Beitelman. (1999). "Static and Fatigue Performance of RC Beams Strengthened with CFRP Laminates." Journal of Structural Engineering 125(6): 613–621.

Smith, K. N., Topper, T., and Watson, P. (1970). "A stress-strain function for the fatigue of metals(Stress-strain function for metal fatigue including mean stress effect)." Journal of Materials, 5 767-778.

Soudki, K., and Sherwood, T.G. (2000). "Behaviour of reinforced concrete beams strengthened with carbon fibre reinforced polymer laminates subjected to corrosion damage." Canadian journal of civil engineering 27.5 (2000): 1005-1010.

Soudki, K., E. El-Salakawy, and B. Craig. (2007). "Behavior of CFRP Strengthened Reinforced Concrete Beams in Corrosive Environment." Journal of Composites for Construction 11(3): 291–298.

Soudki, K. A., Rteil, A. A., Al-Hammoud, R., & Topper, T. H. (2007). Fatigue strength of fibre-reinforced-polymer-repaired beams subjected to mild corrosion. Canadian Journal of Civil Engineering, 34(3), 414-421.

Stratfull, R. F., Clear, K. C., Crumpton, C. F., Bukovatz, J. E., Weed, R. M., Pike, R. G., Hay, R. E., Clifton, J. R., Beeghly, H. F., Mathey, R. G., and Todd, P. L. (1974). "Corrosion and corrosion protection." Transp.Res.Rec., (50),.

Structures, D. C. (1992). CEB Design Guide for Durable Concret Structures.

Takács, P. F., & Kanstad, T. (2000). Strengthening prestressed concrete beams with Carbon Fiber Reinforced Polymer plates. Nordic Concrete Research-Publications, 25, 21-34.

Taylor, D. (1984). "Analysis on data on fatigue crack propagation thresholds." Engineering Materials Advisory Services Ltd, v 1, p 327-337, 1984

Tilly, G. P. (1979). "Fatigue of steel reinforcement bars in concrete: a review." Fatigue of Engineering Materials and Structures, 2(3), 251-68.

Toribio, J., & Ovejero, E. (2005). Failure analysis of cold drawn prestressing steel wires subjected to stress corrosion cracking. Engineering failure analysis, 12(5), 654-661.

Tuutti, K. (1977). "Corrosion of Steel in Concrete." EUROCOR '77, Eur Congr on Met Corros, 92nd Event of the Eur Fed of Corros, 655-661.

Waterhouse, R. B. (Ed.). (1981). Fretting fatigue. Elsevier Science & Technology.

Wollmann, G. P., Yates, D. L., JOHN, E. B., & Kreger, M. E. (1996). Fretting Fatigue in Post-Tensioned Concrete Beams (SP-161). ACI structural journal, 93(2).

Xu, R. X., Topper, T. H., & Thompson, J. C. (1997). "Mode I stress intensity factor equations for cracks at notches and cavities." Fatigue & Fracture of Engineering Materials & Structures, 20(9), 1351-1361.

Young, J. (1988). "A review of the pore structure of cement paste and concrete and its influence on permeability." Permeability of Concrete, 1-19.

Yuan, Y., Ji, Y., and Shah, S. P. (2007). "Comparison of two accelerated corrosion techniques for concrete structures." ACI Structural Journal., 104(3), 344-7.